BIODEGRADABLE POLY(LACTIC ACID) NANOCOMPOSITES: SYNTHESIS AND CHARACTERIZATION

by

YONGHUI LI

B.S., Zhejiang University, Hangzhou, China, 2005
M.S., Zhejiang University, Hangzhou, China, 2007

AN ABSTRACT OF A DISSERTATION

submitted in partial fulfillment of the requirements for the degree

DOCTOR OF PHILOSOPHY

Department of Grain Science and Industry
College of Agriculture

KANSAS STATE UNIVERSITY
Manhattan, Kansas

2011

Abstract

Biobased polymers derived from renewable resources are increasingly important due to acute concerns about the environmental issues and limited petroleum resources. Poly(lactic acid) (PLA) is such a polymer that has shown great potential to produce biodegradable plastics. However, low glass transition temperature (T_g), low thermal stability, slow biodegradation rate, and high cost limit its broad applications. This dissertation seeks to overcome these limitations by reinforcing PLA with inorganic nanoparticles and low-cost agricultural residues.

We first synthesized PLA nanocomposites by *in situ* melt polycondensation of L-lactic acid and surface-hydroxylized nanoparticles (MgO nanocrystals and TiO_2 nanowires) and investigated the structure-property relationships. PLA grafted nanoparticles (PLA-g-MgO, PLA-g-TiO_2) were isolated from the bulk nanocomposites via repeated dispersion/centrifugation processes. The covalent grafting of PLA chains onto nanoparticle surface was confirmed by Fourier transform infrared spectroscopy and thermalgravimetric analysis (TGA). Transmission electron microscopy and differential scanning calorimetry (DSC) results also sustained the presence of the third phase. Morphological images showed uniform dispersion of nanoparticles in the PLA matrix and demonstrated a strong interfacial interaction between them. Calculation based on TGA revealed that more than 42.5% PLA was successfully grafted into PLA-g-MgO and more than 30% was grafted into PLA-g-TiO_2. Those grafted PLA chains exhibited significantly increased thermal stability. The T_g of PLA-g-TiO_2 was improved by 7 °C compared with that of pure PLA.

We also reinforced PLA with low-value agricultural residues, including wood flour (WF), soy flour (SF), and distillers dried grains with solubles (DDGS) by thermal blending. Tensile measurements and morphological images indicated that methylene diphenyl diisocyanate (MDI) was an effective coupling agent for PLA/WF and PLA/DDGS systems. MDI compatibilized PLA/WF and PLA/DDGS composites showed comparable tensile strength and elongation at break as pure PLA, with obviously increased Young's modulus. Increased crystallinity was observed for PLA composites with SF and DDGS. Such PLA composites have similar or superior properties compared with pure PLA, especially at a lower cost and higher biodegradation rate than pure PLA.

The results from this study are promising. These novel PLA thermoplastic composites with enhanced properties have potential for many applications, such as packaging materials, textiles, appliance components, autoparts, and medical implants.

BIODEGRADABLE POLY(LACTIC ACID) NANOCOMPOSITES: SYNTHESIS AND CHARACTERIZATION

by

YONGHUI LI

B.S., Zhejiang University, Hangzhou, China, 2005
M.S., Zhejiang University, Hangzhou, China, 2007

A DISSERTATION

submitted in partial fulfillment of the requirements for the degree

DOCTOR OF PHILOSOPHY

Department of Grain Science and Industry
College of Agriculture

KANSAS STATE UNIVERSITY
Manhattan, Kansas

2011

Approved by:

Major Professor
Xiuzhi Susan Sun

Copyright

Abstract

Biobased polymers derived from renewable resources are increasingly important due to acute concerns about the environmental issues and limited petroleum resources. Poly(lactic acid) (PLA) is such a polymer that has shown great potential to produce biodegradable plastics. However, low glass transition temperature (T_g), low thermal stability, slow biodegradation rate, and high cost limit its broad applications. This dissertation seeks to overcome these limitations by reinforcing PLA with inorganic nanoparticles and low-cost agricultural residues.

We first synthesized PLA nanocomposites by *in situ* melt polycondensation of L-lactic acid and surface-hydroxylized nanoparticles (MgO nanocrystals and TiO_2 nanowires) and investigated the structure-property relationships. PLA grafted nanoparticles (PLA-g-MgO, PLA-g-TiO_2) were isolated from the bulk nanocomposites via repeated dispersion/centrifugation processes. The covalent grafting of PLA chains onto nanoparticle surface was confirmed by Fourier transform infrared spectroscopy and thermalgravimetric analysis (TGA). Transmission electron microscopy and differential scanning calorimetry (DSC) results also sustained the presence of the third phase. Morphological images showed uniform dispersion of nanoparticles in the PLA matrix and demonstrated a strong interfacial interaction between them. Calculation based on TGA revealed that more than 42.5% PLA was successfully grafted into PLA-g-MgO and more than 30% was grafted into PLA-g-TiO_2. Those grafted PLA chains exhibited significantly increased thermal stability. The T_g of PLA-g-TiO_2 was improved by 7 °C compared with that of pure PLA.

We also reinforced PLA with low-value agricultural residues, including wood flour (WF), soy flour (SF), and distillers dried grains with solubles (DDGS) by thermal blending. Tensile measurements and morphological images indicated that methylene diphenyl diisocyanate (MDI) was an effective coupling agent for PLA/WF and PLA/DDGS systems. MDI compatibilized PLA/WF and PLA/DDGS composites showed comparable tensile strength and elongation at break as pure PLA, with obviously increased Young's modulus. Increased crystallinity was observed for PLA composites with SF and DDGS. Such PLA composites have similar or superior properties compared with pure PLA, especially at a lower cost and higher biodegradation rate than pure PLA.

The results from this study are promising. These novel PLA thermoplastic composites with enhanced properties have potential for many applications, such as packaging materials, textiles, appliance components, autoparts, and medical implants.

Table of Contents

List of Figures

List of Tables

Acknowledgments

Upon completing this dissertation, I owe my deepest gratitude and appreciation to so many people for their immense assistance. First and foremost, I am heartily thankful to my major advisor, Dr. Xiuzhi Susan Sun, for her patient supervision, continuous encouragement, and constant support throughout the completion of this degree. For the past four years, Dr. Sun has not only been my model of profound, rigorous scholarship, but also an exemplar for integrity and kindness. I believe her influence will last throughout my life. Sincere appreciation is extended to Dr. Donghai Wang, Dr. Jun Li, Dr. Praveen Vadlani, and Dr. Mohammad Hosni for serving on my supervisory committee. Special thanks to Dr. Jun Li for his valuable instructions and suggestions on some experiments.

I would like to thank all the members in Dr. Sun's group for their constant help, valuable discussions, and cordial friendship, particularly Dr. Karthik Venkateshan, Dr. Jeanne Shera, Dr. Amy Mo, and Dr. Biaobing Wang for their precious suggestions when conducting this research. Special thanks to Ms. Susan Kelly for her unreserved support and help all the time. Further thanks to all the other faculties, staffs, and graduate students in the Department of Grain Science and Industry at Kansas State University (KSU) for their assistance, support, and friendship during my study here.

I am grateful to all my friends in U.S. and China, whose friendship, support, and inspiration make my life be smoother and more joyful. I am also indebted to the KSU community for making it a memorable and joyous journey during my stay in Manhattan, KS.

Last but not least, my deepest appreciation goes to my parents Chunsheng Li and Junlan Li, my sister Dandan Li, and my wife Wenting Qian. Without their everlasting love, support, and encouragement, I could never go this far.

Chapter 1 - Introduction

1.1 General Background

Plastics based on synthetic polymers from petroleum resources have been widely used in many fields, including packaging, textiles, service utensils, appliance components, construction materials, agriculture, etc. However, we are facing severe environmental issues due to their non-biodegradability. Besides, petroleum resources are finite. Therefore, there is a great interest in the development of alternative and biodegradable polymers from renewable resources. Depending on the origins and synthesis processes, renewable resources derived biodegradable polymers can be classified into three categories (Averous, 2004; Yang et al., 2007): (1) polymers extracted from agro-resources, e.g., starch, protein, cellulose; (2) polymers produced by microorganisms, e.g., poly(hydroxyalkanoate)s; (3) chemically synthesized polymers with monomers obtained from agro-resources, e.g., poly(lactic acid) (PLA). There are also some biodegradable polymers based on petroleum derived monomers, e.g., poly(vinyl alcohol), poly(ε-caprolactone), poly(butylenes succinate), poly(butylene adipate-*co*-terephthalate). Among these numerous biodegradable polymers, PLA is the most attractive and useful one.

PLA has many advantages: (1) lactic acid can be easily produced by the fermentation of renewable sugar based resources, such as starch, sugar cane, cellulose, etc.; (2) PLA can be processed by conventional thermoplastic processing techniques like extrusion, injection molding, blow molding, and thermoforming; (3) PLA has shown great potential to produce biomedical materials, textiles, films, auto parts, appliance components, service utensils, and packaging materials; (4) the production of PLA improves the agricultural economy. However, similar to other biopolymers, PLA has several unsatisfactory characteristics, including low strength and modulus above glass transition/heat distortion temperatures around 60 ºC, low thermal stability, rigidity, poor gas barrier properties, and slow biodegradation rate,

which limited its broad commodity applications. Numerous efforts, such as copolymerization, plasticization, blending, composites and nanocomposites fabrication have been attempted to modify the properties of PLA (Bhardwaj & Mohanty, 2007; Grijpma & Pennings, 1994; Martin & Averrous, 2001; Ray & Bousmina, 2005; Zhang et al., 2006; Zhang & Sun, 2004).

Inspired by the research of Toyota in early 1990s that addition of 4.7% nano-clay into nylon 6 resulted in 50% increase in strength/modulus and 87 ºC increase in heat distortion temperature (Kojima et al., 1993, Usuki et al., 1993), synthesizing polymer nanocomposites provides a new approach to enhance the properties of pristine polymers. Polymer nanocomposites combine the advantages of the inorganic nanoparticles (e.g., rigidity, thermal stability) and the organic polymers (e.g., flexibility, dielectric, ductility, and processability). Besides, the small size of nanoparticles leads to a significant increase in interfacial area, which creates a large volume fraction of interfacial polymers with dramatically enhanced physical, thermal-mechanical, and processing characteristics (Liu & Brinson, 2006). Generally, only less than 5 wt% nanoparticles are needed for fabrication of polymer nanocomposites with satisfactory properties, while conventional composites require a much higher loading of microfillers about 20-60 wt% (Nielsen & Landel, 1994). Therefore, polymer nanocomposites are far lighter in weight than conventional composites, and they are more competitive with other materials for specific applications.

Over the last decade, PLA has been reinforced with various nanoparticles, including clays, carbon based nanofillers, metal oxides, polysaccharide nanoparticles, etc. (Gnanasekaran et al., 2009; Kim et al., 2010; Nakayama & Hayashi, 2007; Petersson et al., 2007; Ray et al., 2003; Wang et al., 2009; Wu & Liao, 2007; Yan et al., 2007), and improved mechanical properties, heat distortion temperature, thermal stability, and gas barrier properties were reported. Natural biofillers are abundant, relatively inexpensive, renewable, and biodegradable. Therefore, various natural fillers, including starch (Jacobsen & Fritz, 1996; Ke & Sun, 2000; Wu, 2008; Zhang & Sun, 2004), protein (Zhang et al., 2006), wood flour and fibers (Huda et al., 2006;

Jiang et al., 2007; Takatani et al., 2008) have been incorporated into PLA to reduce its cost and increase biodegradability. Moreover, the thermal-mechanical properties may be reinforced with appropriate formulation and processing techniques.

Grand challenges to develop PLA nanocomposites/composites with targeted properties are the difficulties to achieve homogeneous dispersion and strong interfacial interactions between PLA matrix phase and filler phase (Akcora et al., 2009; Balazs et al., 2006; Mackay et al., 2006; Oh & Green, 2008). We hypothesized that ester bonding could be formed between carboxyl groups of lactic acid and hydroxyl groups of hydroxylized nanoparticles, and uniform dispersion of nanoparticles and strong interfacial covalent bonding between inorganic nanoparticles and organic PLA matrix could be achieved through *in situ* surface polymerization. We also hypothesized that high-performance/low cost PLA composites with biofillers could be obtained with appropriate coupling agents.

1.2 Objectives

The overall objectives of this dissertation were to overcome the drawbacks of PLA, including low glass transition temperature, low thermal stability, slow biodegradation rate, and high cost via reinforcement with inorganic nanoparticles and low-cost agricultural residues, and to investigate the structure-property relationships of newly developed PLA composites. The specific objectives were to:

(1) synthesize PLA nanocomposites by *in situ* melt polycondensation of L-lactic acid and surface-hydroxylized MgO nanocrystals and investigate the structure, morphology, and thermal properties of the nanocomposites;

(2) develop PLA nanocomposites with original MgO and PLA grafted MgO nanocrystals through thermal compounding and compression molding and investigate the thermal, mechanical, and morphology properties;

(3) synthesize PLA nanocomposites by *in situ* melt polycondensation of L-lactic acid and high aspect ratio TiO_2 nanowires and investigate the structure and properties;

(4) study the isothermal crystallization kinetics and melting behaviors of PLA/TiO_2 nanowire nanocomposites prepared through *in situ* melt polycondensation and easy solution-mixing approaches, respectively;

(5) develop high performance PLA composites incorporated with low-value agricultural residues (wood flour, soy flour, distillers dried grains with solubles) and investigate the thermal, mechanical, and morphology properties.

1.3 References

Akcora, P., Liu, H., Kumar, S. K., Moll, J., Li, Y., Benicewicz, B. C., Schadler, L. S., Acehan, D., Panagiotopoulos, A. Z., Pryamitsyn, V., Ganesan, V., Ilavsky, J., Thiyagarajan, P., Colby, R. H., & Douglas J. F. (2009). Anisotropic self-assembly of spherical polymer-grafted nanoparticles. Nature Mater., 8, 354–359.

Averous, L. (2004). Biodegradable multiphase systems based on plasticized starch: A review. J. Macromol. Sci. C, 44, 231–274.

Balazs, A. C., Emrick, T., & Russell, T. P. (2006). Nanoparticle polymer composites: where two small worlds meet. Science, 314, 1107-1110.

Bhardwaj, R., & Mohanty, A. K. (2007). Advances in the properties of polylactides based materials: A review. J Biobased Mater. Bioenergy, 1, 191-209.

Gnanasekaran, D., Madhavan, K., & Reddy, B. S. R. (2009). Developments of polyhedral oligomeric silsesquioxanes (POSS), POSS nanocomposites and their applications: a review. J. Sci. Ind. Res., 68, 437-464.

Grijpma, D. W. and Pennings, A. J. (1994), (Co)polymers of L-lactide, 1. Synthesis, thermal properties and hydrolytic degradation. Macromol. Chem. Phys., 195, 1633–1647.

Huda, M. S., Drzal, L. T., Misra, M., & Mohanty, A. K. (2006). Wood-fiber-reinforced poly(lactic acid) composites: Evaluation of the physicomechanical and morphological properties. J. Appl. Polym. Sci., 102, 4856-4869.

Jacobsen, S., & Fritz, H. G. (1996). Filling of poly(lactic acid) with native starch. Polym. Eng. Sci., 36, 2799-2804.

Jiang, L., Wolcott, M. P., Zhang, J. W., & Englund, K. (2007). Flexural properties of surface reinforced wood/plastic deck board. Polym. Eng. Sci., 47, 281-288.

Ke, T. Y., & Sun, X. S. (2000). Physical properties of poly(lactic acid) and starch composites with various blending ratios. Cereal Chem., 77, 761-768.

Kim, H., Abdala, A. A., & Macosko, C. W. (2010). Graphene/polymer nanocomposites. Macromolecules, 43, 6515-6530.

Kojima, Y., Usuki, A., Kawasumi, M., Okada, A., Fukushima, Y., Kurauchi, T., & Kamigaito, O. (1993). Mechanical properties of nylon 6-clay hybrid. J. Mater. Res., 8, 1185-1189.

Liu, H., & Brinson, L. C. (2006). A hybrid numerical-analytical method for modeling the viscoelastic properties of polymer nanocomposites. Trans. ASME, 73, 758-768.

Mackay, M. E., Tuteja, A., Duxbury, P. M., Hawker, C. J., Horn, B. V., Guan, Z., Chen, G., & Krishnan, R. S. (2006). General strategies for nanoparticle dispersion. Science, 311, 1740-1743.

Martin, O., & Avérous, L. (2001). Poly (lactic acid): plasticization and properties of biodegradable multiphase systems. Polymer, 42, 6209-6219.

Nakayama, N., & Hayashi, T. (2007). Preparation and characterization of poly(L-lactic acid)/TiO2 nanoparticle nanocomposites films with high transparency and efficient photodegradability. Polym. Degrad. Stab., 92, 1255-1264.

Nielsen, L. E., & Landel, R. F. (1994). Mechanical Properties of Polymers and Composites. 2nd edition, New York, Marcel Dekker, Inc. pp 377-505.

Oh, H., & Green, P. F. (2009). Polymer chain dynamics and glass transition in athermal polymer/nanoparticle mixtures. Nat. Mater., 8, 139-143.

Petersson, L., Kvien, I., & Oksman, K. (2007). Structure and thermal properties of poly(lactic acid)/cellulose whiskers nanocomposite materials. Compos. Sci.Tech., 67, 2535-2544.

Ray, S. S., & Bousmina, M. (2005). Biodegradable polymers and their layered silicate nanocomposites: in greening the 21st century materials world. Prog. Mater. Sci., 50, 962-1079.

Ray, S. S., Yamada, K., Okamoto, M., & Ueda, K. (2003). New polylactide/layered silicate nanocomposites. 2. Concurrent improvements of material properties, biodegradability, and melt rheology. Polymer, 44, 857-866.

Takatani, M., Ikeda, K., Sakamoto, K., & Okamoto, T. (2008). Cellulose esters as compatibilizers in wood/poly(lactic acid) composite. J. Wood Sci., 54, 54-61.

Usuki, A., Kojima, Y., Kawasumi, M., Okada, A., Fukushima, Y., Kurauchi, T., & Kamigaito, O. (1993). Synthesis of nylon 6-clay hybrid. J. Mater. Res., 8, 1179-1184.

Wang, B., Sun, X. S., Klabunde, K. J. (2009). Poly(lactic acid)/multi-hydroxyl magnesium oxide nanocomposites prepared by melt compounding. J. Biobased Mater. Bioenergy, 3, 130-138.

Wu, C. S. (2008). Characterizing biodegradation of PLA and PLA-g-AA/starch films using a phosphate-solubilizing Bacillus species. Macromol. Biosci., 8, 560-567.

Wu, C. S., & Liao, H. T. (2007). Study on the preparation and characterization of biodegradable polylactide/multi-walled carbon nanotubes nanocomposites. Polymer, 48, 4449-4458.

Yan, S., Yin, J., Yang, Y., Dai, Z., Ma, J., & Chen, X. (2007). Surface-grafted silica linked with L-lactic acid oligomer: a novel nanofiller to improve the performance of biodegradable poly(L-lactide). Polymer, 48, 1688-1694.

Yang, K., Wang, X., & Wang, Y. (2007). Progress in nanocomposite of biodegradable polymer. J. Ind. Eng. Chem., 13, 485-500.

Zhang, J. F., & Sun, X. S. (2004). Mechanical properties of poly(lactic acid)/starch composites compatibilized by maleic anhydride. Biomacromolecules, 5, 1446-1451.

Zhang, J. W., Jiang, L., & Zhu, L. Y. (2006). Morphology and properties of soy protein and polylactide blends. Biomacromolecules, 7, 1551-1561.

Chapter 2 - Preparation and Characterization of Polymer-Inorganic Nanocomposites by *in situ* Melt Polycondensation of L-lactic acid and Surface-Hydroxylated MgO[1]

2.1 Abstract

Compared with pristine polymers, bionanocomposites derived from biopolymers and inorganic nanoparticles have significantly improved electrical/magnetic properties, mechanical properties, thermal stability, gas barrier properties, and fire retardance. In this study, poly(lactic acid) (PLA) nanocomposites were prepared by *in situ* melt polycondensation of L-lactic acid with different loading ratios of surface-hydroxylated magnesium oxide (MgO) nanocrystals. Molecular weight, structure, morphology, and thermal properties of the nanocomposites were characterized. PLA-grafted MgO (PLA-g-MgO) was isolated from free PLA for the nanocomposite with 3% MgO via repeated dispersion/centrifugation processes and characterized. The weight-average molecular weight of the PLA-0.01%MgO nanocomposite was 55,500, which was 30% higher than that of pure PLA. Discoloration of PLA was obviously depressed in the presence of MgO nanocrystals. Formation of hydrogen bonding between PLA chains and surface –OH groups from MgO was detected by Fourier transform infrared spectroscopy. Morphological images showed uniform dispersion of MgO nanocrystals in the PLA matrix and demonstrated a strong interfacial interaction between the PLA matrix and MgO nanocrystals. PLA-MgO nanocomposites exhibited improved thermal stability compared with pure PLA.

---

[1] Results have been published. Li, Y., & Sun, X. S. (2010). Preparation and characterization of polymer-inorganic nanocomposites by in situ melt polycondensation of L-lactic acid and surface-hydroxylated MgO. *Biomacromolecules*, 11, 1847-1855. (Reuse by permission of American Chemical Socity).

Calculations based on thermogravimetric analysis revealed that more than 42.5% PLA was successfully grafted into PLA-g-MgO.

2.2 Introduction

Poly(L-lactic acid) (PLA), a biodegradable and compostable polymer made from renewable resources such as corn starch, has been extensively studied in recent years as an alternative to petrochemical plastics. It has shown great potential to produce biomedical materials, textiles, films, vehicle interiors, appliance components, service utensils, and packaging materials (Anderson et al., 2008; Gupta & Kumar, 2007; Ljungberg & Wesslen, 2005; Zhang & Sun, 2004). However, unsatisfactory characteristics of PLA such as modest strength and modulus, brittleness, low modulus at glass transition temperature around 60 ºC, poor gas barrier properties, and slow crystallization rate have limited its use. The study of polymer-inorganic nanocomposites is of great interest to both industry and academia because these nanocomposites exhibit significantly improved properties compared with pristine polymers, including electrical/magnetic properties, mechanical properties, thermal stability, gas barrier properties, and fire retardance (Alexandre & Dubois, 2000; Gacitua et al., 2005; Ray & Bousmina, 2005; Ray & Okamoto, 2003; Tingaut et al., 2010; Vaia et al., 1996; Yang et al., 2007; Zou et al., 2008;). The development of nanoscale dispersion of inorganic nanoparticles in the polymer matrix and specific interactions between them are two keys to achieving the best combination of nanocomposite properties (Haque et al., 2007; Luo et al., 2009; Zou et al., 2008).

Currently, most PLA nanocomposites are prepared by melt blending (Chen et al., 2005; Ray et al., 2002; Wang et al., 2009) or *in situ* ring-opening polymerization of lactide (Feng et al. 2008; Hong et al. 2004; Paul et al. 2005). However, effective dispersion of nanoparticles in the polymer matrix has been a challenge because nanoparticles agglomerate. The nanoparticle surface is often modified to promote dispersion (Rong et al., 2006; Zou et al., 2008), which frequently results in extra cost and use of toxic organic solvents. *In situ* ring-opening polymerization of lactide

involves the formation and purification of lactide from the oligocondensation of lactic acid, which also increases the cost of PLA production (Garlotta et al., 2001; Mehta et al., 2005) and prevents its application in various commodities. A breakthrough technology has recently been reported to produce PLA with moderate molecular weight; this technology is based on the direct melt polycondensation of lactic acid and uses a tin (Sn(II)) catalyst system activated by proton acids (Moon et al., 2000; Moon & Kimura, 2003). It has also been reported that the molecular weight of PLA can further increase to several hundred thousand when the melt polycondensation is subjected to another solid-state post-polycondensation process (Moon et al., 2001). Therefore, in this study, we proposed an *in situ* melt polycondensation strategy to prepare PLA nanocomposites using L-lactic acid (LA) and inorganic nanocrystals (surface-hydroxylated magnesium oxide, MgO) as starting materials.

Of all inorganic nanoparticles, metal oxides (magnesium, aluminum, iron, titanium, silicon, etc.) have attracted much attention because a layer of hydroxyl (-OH) groups that results from water dissociation covers the outmost surface of oxide nanocrystals (Al-Abadleh & Grassian, 2003; Henderson, 2002; Richards et al., 2000). Silicon dioxide (SiO_2) (Wu et al., 2008; Yan et al., 2007; Yao et al., 2009) and titanium dioxide (TiO_2) (Lu et al., 2008) have been studied recently. However, MgO has a much smaller crystal size ($\leq$ 4 nm) than SiO_2 (~12 nm) and TiO_2 (~20 nm) and thus should have more surface defects and higher reactivity that should result in higher efficiency of water dissociation, which usually occurs only at defects on oxide surfaces such as corners, edges, steps, kinks, and vacancies (Kim et al., 2002; Langel & Parrinello, 1994). In regard to MgO, for each type of defect, two main categories of -OH groups are generally expected from heterolytic dissociation of water (Chizallet et al., 2006; Chizallet et al., 2007; Huang et al., 2009): (1) -OH groups produced by hydroxylation of surface Mg^{2+} cations (called mono-coordinated hydroxyls because they are bonded to only one Mg^{2+} cation) and (2) -OH groups generated by protonation of surface oxide ions (referred to as multi-coordinated hydroxyls because they are bonded to several Mg^{2+} cations). Generally, only the low-coordinated (mono-

and di-) -OH groups on the edge and corner sites can be more reactive and are responsible for the reactivity of hydroxylated MgO (Chizallet et al., 2006; Richards et al., 2000).

The MgO used in this study was provided by NanoScale Co. (NanoActive Magnesium Oxide Plus®) following the aerogel method developed by Klabunde and his coworkers (Itoh et al., 1993; Utamapanya et al., 1991). The MgO exhibited a polyhedral shape with a much larger surface area ($\geq$ 600 m^2/g) and percentage of corner and edge ions (21%) than commercial cubic-shaped MgO (surface area: 30 m^2/g, corner and edge ions: 0.4%) (Lucas et al., 2001). The MgO contains about nine –OH groups/nm^2 at 100 ºC; the surface –OH group concentration decreased progressively with heat treatment temperature but still possessed an average of 3.6 surface –OH groups/nm^2 after heat treatment at 500 ºC under vacuum (Itoh et al., 1993). Some attention has been paid to the reactivity of this highly hydroxylated MgO in the area of catalysts and adsorbents studies (Lucas et al., 2001; Neal et al., 2009); however, limited studies have been conducted for polymer nanocomposites (Beavers et al., 2009; Wang et al., 2009). In our previous study, surface-hydroxylated MgO (NanoActive Magnesium Oxide®) was used as filler to prepare PLA nanocomposites by melt blending (Wang et al., 2009). At an MgO loading ratio of 0.4 wt% or less, mechanical properties were significantly improved, which was mainly attributed to the nano-reiforcement of a large amount of surface –OH groups of MgO. However, satisfying dispersion of MgO in the melt PLA matrix was still not achieved.

In this study, we hypothesized that carboxyl groups from LA could polymerize with hydroxyl groups from surface-hydroxylated MgO crystals to form PLA-MgO nanocomposites (as illustrated in Figure 2.1) to create better interfacial interaction and dispersion of MgO crystals in the PLA matrix and that interfacial interaction between the PLA matrix and MgO could further be improved through formation of hydrogen bonding (H-bonding) between remaining surface -OH groups of MgO and ester groups in the PLA chains (Figure 2.1). This study had three specific objectives: (1) synthesize PLA/MgO nanocomposites via *in situ* melt polycondensation from LA

with different MgO loading ratios; (2) characterize the molecular weight, structure, morphology, and thermal properties of bulk nanocomposites; and (3) characterize the properties of PLA-grafted MgO (PLA-g-MgO) isolated from free PLA from the PLA-3%MgO nanocomposite to confirm the surface polymerization.

2.3 Experimental Section

2.3.1 Materials

L-lactic acid was supplied as a 90 wt% aqueous solution by Acros Organics. MgO with an extremely high surface area, small crystal size (≤ 4 nm), and rough surface morphology was obtained from NanoScale Co. (NanoActive Magnesium Oxide Plus®, Manhattan, KS). Tin (II) chloride dihydrate ($SnCl_2 \cdot H_2O$) (98%, reagent grade) and *p*-toluenesulfonic acid monohydrate (TSA) (98.5+%, ACS reagent grade) were purchased from Sigma-Aldrich Co. All materials were used as received.

2.3.2 Dehydration/Oligomerization

Our preliminary studies showed that the desirable MgO loading level for bulk nanocomposite preparation was less than 0.2%; this value was used to determine the experimental MgO loading levels (0.005%, 0.01%, 0.05%, and 0.2% based on the weight of pure LA).The MgO was added gradually to 100 g of a 90 wt% aqueous solution of LA and stirred with a magnetic stirrer until it was uniformly dispersed. The mixture was then charged into a 250-ml three-neck flask and dehydrated at 110 ℃ under atmospheric pressure for 2 h, then at 130 ℃ under a reduced pressure of 100 torr for 3 h, and finally at 150℃ under a reduced pressure of 10 torr for another 4 h. Then a viscous oligomer with MgO was obtained. Oligomer without MgO was also prepared as a control following the same procedures. The degree of polymerization (DP) of the oligomers was determined to be about 6 through ^1H NMR.

2.3.3 Polymerization

A 100-mL three-neck flask was equipped with a mechanical stirrer and a reflux condenser that was connected with a vacuum system through a liquid nitrogen

cold trap. Twenty grams of oligomer was charged into the flask and then mixed with $SnCl_2 \cdot H_2O$ (0.4% wt relative to oligomer) and TSA (an equimolar ratio to $SnCl_2 \cdot H_2O$) as a binary catalyst (Moon et al., 2000). The mixture was gradually heated to 180 °C with stirring. The pressure was reduced gradually to 10 torr in 1.5 h. Then the reaction was continued at 180 °C/10 torr for 10 h. At the end of the reaction, the flask was cooled, and the product was dissolved in chloroform and subsequently precipitated into methanol. The resulting solid was filtered and dried under vacuum at 80 °C for 24 h. Bulk nanocomposites were labeled according to MgO loading ratio as PLA-0.005%MgO, PLA-0.01%MgO, PLA-0.05%MgO, and PLA-0.2%MgO. Pure PLA without MgO was prepared following the same procedures and used as a control. Because both PLA-g-MgO and free PLA in the bulk nanocomposites at 0.2% MgO or lower are dissolved/dispersed completely in chloroform, we prepared a PLA-3%MgO nanocomposite to isolate enough PLA-g-MgO for characterization purposes. To prepare the PLA-3%MgO nanocomposite, pure LA oligomer was first prepared following the same dehydration/oligomerization procedures. The 3% MgO was added into 20 g of oligomer and then mixed with the same amount of catalysts and polymerized at the same conditions as other nanocomposites. The 3% MgO was added to the LA oligomer rather than to LA to obtain a higher yield of PLA-g-MgO.

2.3.4 Isolation of PLA-g-MgO

When the PLA-3%MgO nanocomposite was dispersed into excessive chloroform, free PLA was completely dissolved and some PLA-g-MgO remained. The PLA-g-MgO was isolated from free PLA via centrifugation at 8500 rpm for 1 h and washed with excessive chloroform repeatedly five times to completely remove the free PLA. Free PLA from the first centrifugation was precipitated into methanol and collected. A control sample (t-MgO) was also prepared by mixing 1 g MgO with a chloroform solution of PLA for 10 h and then repeating the dispersion/centrifugation cycles. The photographs of PLA-g-MgO/free PLA/chloroform and t-MgO/PLA/chloroform suspensions before and after centrifugation are shown in Figure 2.2. It is clear that t-MgO was precipitated at the

bottom of the tube and PLA-g-MgO was suspended at the top after centrifugation. This indicates there always will be a certain amount of PLA-g-MgO dissolved/dispersed in PLA/chloroform solution and remaining with free PLA after precipitation. Finally, the PLA-g-MgO, t-MgO, and free PLA were dried in a vacuum oven at 80 °C for 24 h to remove the residual solvent.

2.3.5 Gel Permeation Chromatography (GPC) Analysis

The weight- (M_w) and number-average molecular (M_n) weight as well as the polydispersity index (PDI, equals to M_w/M_n) were determined through GPC (Waters 2695 Separation Module). Samples were dissolved in tetrahydrofuran at a concentration of 5 mg/ml. The measurement was performed at room temperature and a flow rate of 1 ml/min. The molecular weight was calibrated according to a polystyrene standard.

2.3.6 Nuclear Magnetic Resonance (NMR) Spectroscopy

^{1}H NMR and ^{13}C NMR spectra were acquired at room temperature for PLA and bulk nanocomposites on a Varian Inova 400 MHz spectrometer in $CDCl_3$ containing tetramethylsilane as the internal reference. All spectra were recorded using a spinning rate of 20 kHz with a relaxation delay of 1 s for ^{1}H NMR for and 3 s for ^{13}C NMR. Solid-state ^{1}H NMR and ^{13}C NMR spectra were obtained for PLA-g-MgO and free PLA isolated from the PLA-3%MgO nanocomposite on a Bruker IPSO 500 MHz WB NMR spectrometer. The ^{1}H NMR was carried out with a single 90-degree pulse of 1.3 μs under ultrahigh magic-angle spinning (MAS) at 60 kHz. The ^{13}C NMR was performed with cross-polarization MAS under the following conditions: sample spinning rate 10 kHz, contact time 2 ms, relaxation delay 3 s, and two-pulse phase modulation proton decoupling during acquisition.

2.3.7 Fourier-transform Infrared (FTIR) Spectroscopy

FTIR spectra were acquired with a PerkinElmer Spotlight 300 spectrometer. Spectra were collected in the region of 4000 to 800 cm^{-1} with a spectral resolution of 8 cm^{-1} and 64 scans co-added.

2.3.8 Scanning Electron Microscopy (SEM) and Transmission Electron Microscopy (TEM) Analysis

SEM (Hitachi S-3500N, Hitachi Science Systems, Ltd., Japan) and TEM (H-7100, Hitachi Co.) were used to study morphology of the samples. For SEM, a piece of each sample was mounted on an aluminum stub, and the surface was coated with a mixture of 60% gold particles and 40% palladium with a sputter coater (Desk II Sputter/ Etch Unit, NJ) before observation. For TEM, fine powders of each sample were absorbed onto Formvar/Carbon-coated 200-mesh copper grids (Electron Microscopy Sciences, Fort Washington, PA, USA) and observed without staining.

2.3.9 Differential Scanning Calorimetry (DSC) Analysis

Thermal transitions of the samples were measured with a TA DSC Q200 instrument. About 5 mg of dried powder was sealed in an aluminum pan. An empty sealed pan was used as a reference. The sample was heated from 0 °C to 190 °C at a rate of 10 °C/min, isothermally conditioned at 190 °C for 3 min, quenched to 0 °C, isothermally conditioned at 0 °C for 3 min, and then heated again to 190 °C at the same rate. The sample was characterized in an inert environment by using nitrogen with a gas flow rate of 50 ml/min. Results were obtained from the second DSC heating scan. Heat capacity (ΔC_p), glass transition temperature (T_g), melting temperature (T_m), heat of melting (ΔH_m), and heat of crystallization (ΔH_c) were determined from the DSC thermograms. Crystallinity (X_m) was estimated according to the equation:

$$X_m(\%) = \frac{\Delta H_m}{\Delta H_0} \times 100 \qquad (1)$$

where ΔH_m and ΔH_0 are heats (J/g) of melting of PLA nanocomposites and PLA crystals of infinite size with a value of 93.6 J/g (Fischer et al., 1973), respectively.

2.3.10 Thermogravimetric Analysis (TGA)

Decomposition characteristics of the samples were determined with a PerkinElmer Pyris1 TGA (Norwalk, CT). About 5 mg of each sample was placed in

the pan and heated from 40 °C to 700 °C at a heating rate of 20 °C/min under a nitrogen atmosphere. Pure MgO was dried in a vacuum oven at 80 °C for 24 h before TGA measurement.

2.4 Results and Discussion

2.4.1 Molecular Weight

Molecular weights of PLA and bulk nanocomposites are summarized in Table 2.1. The M_w and M_n of pure PLA were 42,500 and 23,300, respectively. The M_w and M_n of PLA-0.005%MgO were similar to those of pure PLA, whereas the M_w and M_n of PLA-0.01%MgO were significantly higher than those of pure PLA. When the loading ratio of MgO further increased to 0.05% and 0.2%, M_w decreased sharply by 39% and 78%, respectively, compared with pure PLA. First, the intrinsic balance of carboxyl and hydroxyl groups in lactic acid (-COOH/-OH = 1) was broken by the presence of extra hydroxyl groups on the surface of MgO nanocrystals (-COOH/-OH < 1); therefore, the theoretical molecular weight was reduced at a complete conversion of -COOH. Second, it is known that PLA chains grow from two end groups during polycondensation; however, in the case of nanocomposites, one end group was covalently bonded to the MgO surface, and the chain could grow only from the other end. Third, when several polymer chains grew on the surface of the same MgO nanocrystal, the steric hindrance from neighbor polymer chains increased as the polymer grew (Zhao et al., 2005). Moreover, the molecular mobility decreased compared with a single free polymer chain, leading to a decrease in chain growth. The increased molecular weight of the PLA-0.01%MgO nanocomposite could be because the decreased size of grafted polymer chains was counterbalanced by the total number of chains on each MgO nanocrystal surface showing a larger hydrodynamic volume at the optimal MgO loading ratio of 0.01%. The PDI for PLA and nanocomposites ranged between 1.5 and 2.0 as measured from GPC; these values are similar to those for PLA obtained from the melt polycondensation method (Moon et al., 2000; Moon & Kimura, 2003).

The molecular weight of free PLA isolated from PLA-g-MgO in the PLA-3%MgO nanocomposite was also measured (M_w = 10,100 and M_n = 6,000). The isolated PLA-g-MgO was not very soluble in any solution because of its complicated composition (i.e., aggregates resulted from highly concentrated unreacted MgO nanocrystals, partially reacted MgO nanocrystals, MgO nanocrystals with different sizes, and distribution of grafted PLA chains). Therefore, we failed to measure its molecular weight through GPC. Efforts were made to measure the polymer chain length of PLA-g-MgO through solid-state ^{1}H NMR. However, because of the relatively low resolution of solid-state ^{1}H NMR and broad peaks from methyl and methine proton resonances, signals from resonances of methyl or methine protons next to the terminal hydroxyl groups were not detected. Thus, the chain length of PLA-g-MgO was not calculated.

Discoloration of PLA is usually a serious problem in melt polycondensation of lactic acid and might be caused by high reaction temperatures, long reaction times, and by-products (Moon et al., 2000). However, the presence of MgO nanocrystals appears to depress discoloration. Melt polycondensation of lactic acid alone for 10 h resulted in a light black color. With the addition of 0.005% MgO, the color became only slightly black, and with MgO addition further increased to 0.01%, 0.05%, and 0.2%, the color of nanocomposites became totally white (Table 2.1). This is probably caused by the specific interaction (chemical grafting, H-bonding, etc.) between PLA and MgO and improved thermal stability of nanocomposites.

2.4.2 NMR

Figure 2.3A shows the typical ^{1}H NMR spectra of PLA and its bulk nanocomposites. The major peaks at 1.56 and 5.15 ppm were assigned to the methyl and methine proton resonances from the PLA main chain. The weak peak at 4.35 ppm was assigned to the methine proton next to the terminal hydroxyl group. Another weak peak at 1.35 ppm was assigned to the methyl proton next to the terminal hydroxyl group. Peaks assigned to the methyl and methine protons next to the terminal carboxyl group could be identified only for LA oligomers (DP<8) (Espartero

et al., 1996) because the intensity of these peaks decreased dramatically as molecular weight increased and could not be detected. The ^{13}C NMR spectrum was used in a qualitative analysis of the structure of PLA polymers. The result was in accordance with the ^{1}H NMR analysis (Figure 2.4A). The peaks assigned to the methyl (16.85 ppm), methine (69.21 ppm), and carbonyl (169.81 ppm) groups of the LA repeat units were observed. The three-peak pattern centered at 77 ppm is due to the solvent $CDCl_3$. Resonances associated with methyl, methine, and carbonyl groups next to the terminal hydroxyl or carboxyl groups were not observed because of the relatively long chain length (DP ~165 units, determined from ^{1}H NMR) (Song et al., 2008). All the PLA nanocomposites showed ^{1}H NMR and ^{13}C NMR spectra similar to those of pure PLA; the typical spectra of PLA-0.05%MgO is presented in Figures 2.3A and 2.4A. Shifts of any peaks attributed to the PLA chains polymerized on the MgO surface were not detected for these PLA nanocomposites. The same phenomena occurred in multi-walled carbon nanotubes-PLA telechelic prepolymers (Song et al., 2008).

The solid-state ^{1}H NMR spectra for free PLA and PLA-g-MgO are shown in Figure 2.3B. Two broad resonance peaks at 1.41 and 5.03 ppm were attributed to the methyl and methine proton resonances from the main chain of free PLA. In the spectrum of PLA-g-MgO, the methyl and methine proton characteristic peaks shifted upfield to 1.16 and 4.13 ppm, respectively, indicating that the chemical environments of methyl and methine protons in the LA repeat units had been changed after being grafted onto the electron-rich MgO surface. A new peak at 8.53 ppm observed only for PLA-g-MgO was assigned to the proton resonances from multi-coordinated hydroxyl groups of MgO (Chizallet et al., 2007), which possess much lower reactivity. Such differences were also observed in solid-state ^{13}C NMR spectra for free PLA and PLA-g-MgO (Figure 2.4B). The resonances of each of the carbon groups in free PLA were split into two or three distinct peaks, whereas in PLA-g-MgO, almost no split peaks were observed, indicating that a certain degree of racemization occurred for free PLA but little occurred for PLA-g-MgO (Kricheldorf et al., 1992; Moon et al., 2000; Thakur et al., 1997). The peaks at 169.4, 170.8, and

171.3 ppm that stemmed from carbonyl groups for free PLA shifted to 178 ppm for PLA-g-MgO. Another weak peak at 181.4 ppm was probably associated with the terminal carbonyl groups next to the MgO surface. The downfield shift of carbonyl groups might be caused by covalent grafting of PLA chains onto the MgO surface or H-bonding between carbonyl groups and –OH groups from MgO (Ando et al., 1988). The peaks at 15.7 and 16.9 ppm assigned to methyl groups for free PLA shifted downfield to 19.9 ppm for PLA-g-MgO. NMR results revealed a great possibility that PLA chains were chemically grafted onto the MgO surface, which was also confirmed by other techniques as described in the following paragraphs.

2.4.3 FTIR

The FTIR spectra of pure PLA and bulk nanocomposites are presented in Figure 2.5A. Pure PLA showed a strong absorption band at 1751 cm^{-1} (Figure 2.5A, a) corresponding to the stretching vibration of carbonyl groups (–C=O) from the repeated ester units. The –C–O– stretching vibrations from the ester units were observed at 1180, 1129, and 1082 cm^{-1}. The bands at 2996 and 2877 cm^{-1} were assigned to the –C–H asymmetric and symmetric stretching vibrations of CH_3 groups in the side chains, whereas their bending vibration was observed at 1454 cm^{-1}. The band at 2948 cm^{-1} was attributed to the stretching of –CH– groups in the main chain of PLA, and its symmetric and asymmetric bending vibrations appear at 1382 and 1358 cm^{-1} (Auras et al., 2004).

Similar FTIR bands were observed for PLA bulk nanocomposites, except for the –C=O region around 1751 cm^{-1} (Figure 2.5A). In the nanocomposites (b-e), the stretching vibrations of –C=O were all split into two distinct peaks, unlike the single carbonyl peak of pure PLA (Figure 5A, a). One of the split peaks at about 1751 cm^{-1} was still assigned to the original –C=O vibration, which is free and not H-bonding with MgO nanocrystals; the other peak shifted to a lower wavenumber around 1745 to 1747 cm^{-1} and was caused by the formation of intermolecular H-bonding, as illustrated in Figure 2.1. The H-bonding involves –C=O groups from both grafted and free PLA chains, which are often regarded as H-bonding acceptors, together with

some remaining -OH groups from the MgO nanocrystal surface, which are usually considered H-bonding donors. The abundance of surface –OH groups of MgO nanocrystals provided a favorable condition for formation of H-bonding. The H-bonding between PLA and other –OH rich materials observed through FTIR was also reported in other studies (Lin et al., 2007; Zhou et al., 2007).

Compared with MgO, PLA-g-MgO showed new absorption bands at 1751, 2990, and 2940 cm^{-1} (Figure 2.5B). These peaks were attributed to the –C=O, $–CH_3$, and –CH– groups, respectively, from PLA chains grafted onto the MgO nanocrystals. The spectrum of t-MgO was in accordance with that of pure MgO, and no characteristic peaks of PLA were observed. The –OH absorption band of PLA-g-MgO was different from that of MgO and t-MgO. In particular, the 3500-3800 cm^{-1} signal disappeared after surface grafting. This was caused by selective grafting of PLA with the mono- and di-coordinated –OH groups (Chizallet et al., 2007) because of their higher reactivity, which was discussed previously. These results confirm that PLA chains were chemically grafted onto the MgO surface.

2.4.4 Morphology

The SEM images of MgO, pure PLA, bulk nanocomposites, and PLA-g-MgO are shown in Figure 2.6. The bare MgO crystals existed in compact aggregate forms with an average size of 10 to 15 μm. PLA exhibited incontinuous particular morphology with a flat, smooth surface (Figure 2.6, a). All the bulk nanocomposites exhibited continuous morphology with small, uniformly distributed convexities (Figure 2.6, b-e). As MgO loading ratio increased, the number of convexities per unit area in the nanocomposite matrix obviously increased. At 0.2% MgO, the convexities grew and aggregated together, resulting in a more irregular and uneven surface. The convexities resulting from PLA-g-MgO nanocomposites were uniformly dispersed in the matrix with a remarkably reduced size (100 to 500 nm), which indicates that initial MgO aggregates were effectively broken down to nanoscale through *in situ* polymerization. In addition to nanoscale uniform dispersion, interfacial interaction is another key factor for nanocomposite preparation. As seen from Figure 2.6 (b-e), the

smooth, continuous feature at the interface between the PLA matrix and convexities indicates that a chemical reaction occurred between PLA and MgO. In general, chemical grafting of polymer chains that are compatible with the polymer matrix on the inorganic particles provides strong interfacial interaction between the inorganic and organic phases (Hong et al., 2005). Moreover, the formation of H-bonding between organic PLA chains and inorganic nanocrystals contributes to the unique continuousness observed only in the bulk nanocomposites and further improves the interfacial interaction. PLA-g-MgO exhibited a unique loose and porous morphology (Figure 2.6), indicating that the compact aggregation of original MgO crystals was greatly inhibited after surface grafting with PLA chains.

TEM is more a powerful technique than SEM for penetrating the surrounding polymer environment and provides information about how MgO nanocrystals were distributed inside each convexity observed in the SEM images. Before polymerization, bare MgO crystals severely aggregated, and it was difficult to distinguish a single crystal (Figure 2.7, MgO). After it was grafted with PLA, the surface-grafted MgO was almost homogeneously dispersed in the polymer matrix without obvious aggregation and kept its nanostructures with individual MgO crystals (pointed arrows in Figure 2.7, b). These results indicate that agglomeration of nanocrystals was prevented by the surface grafting and H-bonding between PLA chains and surface hydroxyl groups of MgO, which also afforded the uniform dispersion. When MgO incorporation increased to 0.01% and 0.05%, the abundant OH groups were prone to interact with themselves because of the stronger intramolecular hydroxyl-hydroxyl bonding (Lin et al., 2007); this led to a small amount of aggregation of several MgO crystals, but the aggregation was slight and incompact (Figure 2.7, c and d). When MgO loading ratio further increased to 0.2%, much denser and thicker black spots were observed (pointed arrow in Figure 2.7, e), indicating that large, compact aggregates of MgO crystals were formed. PLA-g-MgO exhibited a unique fibril structure due to the surface-grafted polymer chains (Figure 2.8, left), which was obviously different from the morphology of pure MgO (Figure

2.7, MgO). At higher magnification, uniform distribution of MgO crystals in the PLA-g-MgO system was also observed (Figure 2.8, right).

2.4.5 Thermal Properties

Figure 2.9A shows the DSC thermograms of pure PLA and bulk nanocomposites, and quantified results are summarized in Table 2.2. Pure PLA and bulk nanocomposites showed similar T_g values, except for PLA-0.2%MgO. The T_g of PLA-0.2%MgO was about 4 ºC lower than that of other nanocomposites because of its smaller molecular weight (Jamshidi et al., 1988).

Cold crystallization was observed for PLA and the bulk nanocomposites. Compared with PLA, the cold crystallization of bulk nanocomposites occurred at lower temperatures. The depression of cold crystallization temperature in the bulk nanocomposites was probably induced by the MgO nanocrystals, which acted as nucleation agents for the system. No obvious change of crystallinity was observed between PLA and bulk nanocomposites, except for PLA-0.01%MgO, which showed relatively lower crystallinity. As discussed previously, the PLA-0.01%MgO nanocomposite had the highest molecular weight because optimal size and number of grafted PLA chains were obtained. However, a 0.01% MgO nanocrystal core might hinder mobility of the grafted PLA chain and limit the effective diffusion of chains to the growing crystalline lamella, resulting in crystals with reduced grain size, more defects, and, therefore, lower crystallinity. Both PLA and bulk nanocomposites exhibited double melting behavior, which can be explained by the melt-recrystallization model (Yasuniwa et al., 2004). The melting temperatures of bulk nanocomposites were all lower than that of pure PLA, especially that of PLA-0.2%MgO, which was 10 ºC lower. The sharp reduction of melting temperature for PLA-0.2%MgO was caused by its lower molecular weight (Ikada & Tsuji, 2000).

DSC thermograms of free PLA and PLA-g-MgO isolated from the PLA-3%MgO nanocomposite are presented in Figure 2.9B, and the results are also summarized in Table 2.2. PLA-g-MgO showed a broad melting peak with peak value of 117.8 ºC. For free PLA, besides the normal double melting peaks at 133.7 and

141.6 ºC, another small melting peak was observed at 116.4 ºC, indicating there were still some PLA-g-MgO residues dissolved/dispersed in the chloroform solution with free PLA during the isolation process.

The TGA thermograms of pure PLA and bulk nanocomposites are presented in Figure 2.10 (A), and the thermogravimetric data are summarized in Table 2.3. The onset, end, and maximum rate of decomposition temperatures (T_{onset}, T_{end}, and T_{max}) of PLA and PLA-0.005%MgO were similar. PLA-0.01%MgO exhibited increased thermal stability compared with pure PLA. The thermal stability of PLA-0.05%MgO was the lowest, with T_{onset}, T_{end}, and T_{max} about 10 ºC lower than those for pure PLA. The T_{max} for PLA-0.2%MgO was 324 ºC, which was the highest among all samples. These results indicate that addition of MgO could increase thermal stability of PLA. The decreased thermal stability of PLA-0.05%MgO could be explained by the competition between the addition of MgO and decrease of molecular weight.

The TGA thermograms of intensively dried pure MgO, PLA-g-MgO, and free PLA are presented in Figure 2.10 (B), and thermogravimetric data are summarized in Table 2.3. The weight loss of MgO (W_{MgO}) and PLA-g-MgO ($W_{PLA\text{-}g\text{-}MgO}$) were 33.3% and 75.8%, respectively. The amount of PLA grafted onto the MgO surface (W_g) for PLA-g-MgO was roughly calculated as:

$$W_g = W_{PLA-g-MgO} - W_{MgO} = 75.8\% - 33.3\% = 42.5\% \qquad (2)$$

The amount of -OH groups on the MgO surface involved in the surface grafting was neglected in this calculation, which indicates that more than 42.5% PLA was successfully grafted. The decomposition range of MgO and PLA-g-MgO both exhibited three stages, with T_{max} at 73, 184, and 351 ºC for MgO and 271, 376, and 485 ºC for PLA-g-MgO. The detailed mechanism for the decomposition of PLA-g-MgO remains unclear. However, we can conclude that when PLA was grafted onto MgO, its thermal stability was greatly improved. Moreover, because free PLA has some PLA-g-MgO not separated thoroughly, the T_{max} was 34 ºC higher than that of pure PLA, even though the molecular weight of free PLA was much lower than that of pure PLA.

2.5 Conclusions

PLA-MgO nanocomposites were synthesized by *in situ* melt polycondensation of LA and surface-hydroxylated MgO nanocrystals at a low MgO loading level. Molecular weight of the PLA-0.01%MgO reached 55,500, which was 30% higher than that of pure PLA. The color of PLA-MgO nanocomposite was almost white, whereas that of pure PLA was slightly black.

PLA-MgO nanocomposites exhibited continuous morphology with small convexities uniformly distributed in the matrix because of surface grafting and H-bonding between PLA chains and hydroxylated MgO. Pure PLA exhibited an incontinuous particle morphology with a flat, smooth surface. MgO crystals acted as nucleation agents to induce and accelerate crystallization of the PLA-MgO nanocomposite. Decomposition of the PLA-MgO nanocomposite was significantly increased compared with that of pure PLA. Results indicate this is a promising approach to preparing PLA/MgO nanocomposites.

2.6 Acknowledgments

Financial support was provided from U.S. Department of Agriculture/National Research Initiative and U.S. Department of Energy. Contribution No. 10-278-J from the Kansas Agricultural Experiment Station. The authors gratefully acknowledge the following individuals for their contributions: Dr. Krystyna Brzezinska and Dr. Jerry Hu (Materials Research Laboratory at UCSB) for performing GPC and solid-state NMR analysis, Dr. David Wetzel (Department of Grain Science and Industry, Kansas State University) for use of the FTIR instrument, Mr. Kent Hampton (Department of Entomology, Kansas State University) for performing SEM analysis, and Dr. Dan Boyle (Department of Biology, Kansas State University) for performing TEM analysis.

2.7 References

Al-Abadleh, H. A., & Grassian, V. H. (2003). Oxide surfaces as environmental interfaces. Surf. Sci. Rep., 52, 63-161.

Alexandre, M., & Dubois, P. (2000). Polymer-layered silicate nanocomposites: preparation, properties and uses of a new class of materials. Mat. Sci. Eng. R., 28, 1-63.

Anderson, K. S., Schreck, K. M., & Hillmyer, M. A. (2008). Toughening polylactide. Polym. Rev., 48, 85-108.

Ando, S., Ando, I., Shoji, A., & Ozaki, T. (1988). Intermolecular hydrogen-bonding effect on carbon-13 NMR chemical shifts of glycine residue carbonyl carbons of peptides in the solid state. J. Am. Chem. Soc., 110, 3380-3386.

Auras, R., Harte, B., & Selke, S. (2004). An overview of polylactides as packaging materials. Macromol. Biosci., 4, 835-864.

Beavers, E. M., Klabunde, K. J., Wang, B., & Sun, X. S. (2009). Lactic acid-magnesium oxide nanocrystal interactions: how nanoparticles size and shape effect chemistry and template oligomerization. New J. Chem., 33, 1951-1959.

Chen, G., Kim, H., Shim, J., & Yoon, J. (2005). Role of epoxy groups on clay surface in the improvement of morphology of poly(l-lactide)/clay composites. Macromolecules, 38, 3738-3744.

Chizallet, C., Costentin, G., Che, M., Delbecq, F., & Sautet, P. (2007). Infrared characterization of hydroxyl groups on MgO: a periodic and cluster density functional theory study. J. Am. Chem. Soc., 129, 6442-6452.

Chizallet, C., Costentin, G., Lauron-Pernot, H., Che, M., Bonhomme, C., Maquet, J., Delbecq F., & Sautet P. (2007). Study of the structure of OH groups on MgO by 1D and 2D 1H MAS NMR combined with DFT cluster calculations. J. Phys. Chem. C, 111, 18279-18287.

Chizallet, C.; Costentin, G.; Lauron-Pernot, H.; Krafft, J. M., Bazin, P.; Saussey, J.; Delbecq, F.; Sautet, P.; Che, M. Role of hydroxyl groups on the basic reactivity of MgO: a theoretical and experimental study. Oil Gas Sci. Technol. 2006, 61, 479-488.

Espartero, J. L., Rashkov, I., Li, S. M., Manolova, N., & Vert, M. (1996). NMR analysis of low molecular weight poly(lactic acid)s. Macromolecules, 29, 3535-3539.

Feng, J., Cai, W., Sui, J., Li, Z., Wan, J., & Chakoli, A. N. (2008). Poly(L-lactide) brushes on magnetic multiwalled carbon nanotubes by in-situ ring-opening polymerization. Polymer, 49, 4949-4994.

Fischer, E. W., Sterzel, H. J., & Wegner, G. (1973). Investigation of the structure of solution grown crystals of lactide copolymers by means of chemical reactions. Kolloid Z. Z. Polym., 251, 980-990.

Gacitua, W., Ballerini, A. A., & Zhang, J. (2005). Polymer nanocomposites: synthetic and natural fillers a review. Maderas. Ciencia y tecnología, 7, 159-178.

Garlotta, D. (2001). A literature review of poly(lactic acid). J. Polym. Environ., 9, 63-84.

Gupta, A. P., & Kumar, V. (2007). New emerging trends in synthetic biodegradable polymers – polylactide: a critique. Eur. Polym. J., 43, 4053-4074.

Haque, S., Rehman, I., & Darr, J. A. (2007). Synthesis and characterization of grafted nanohydroxyapatites using functionalized surface agents. Langmuir, 23, 6671-6676.

Henderson, M. A. (2002). The interaction of water with solid surfaces: fundamental aspects revisited. Surf. Sci. Rep., 46, 1-308.

Hong, Z., Qiu, X., Sun, J., Deng, M., Chen, X., & Jing, X. (2004). Grafting polymerization of L-lactide on the surface of hydroxyapatite nano-crystals. Polymer, 45, 6699-6706.

Hong, Z., Zhang, P., He, C., Qiu, X., Liu, A., Chen, L., Chen, X., & Jing, X. (2005). Nano-composte of poly(L-lactide) and surface grafted hydroxyapatite: mechanical properties and biocompatibility. Biomaterials, 26, 6296-6304.

Huang, C. C., Hohn, K. L., & Schlup, J. R. (2009). The influence of surface hydroxyls on catalyzed tetrakis(dimethylamino)ethylene chemiluminescence. J. Phys. Chem C, 113, 11050-11059.

Ikada, Y., & Tsuji, H. (2000). Biodegradable polyesters for medical and ecological applications. Macromol. Rapid Comm., 21, 117-132.

Itoh, H., Utamapanya, S., Stark, J. V., Klabunde, K. J., & Schlup, J. R. (1993). Nanoscale metal oxide particles as chemical reagents. Intrinsic effects of particle size on hydroxyl content and on reactivity and acid/base properties of ultrafine magnesium oxide. Chem. Mater., 5, 71–77.

Jamshidi, K., Hyon, S. H., & Ikada, Y. (1988). Thermal characterization of polylactides. Polymer, 29, 2229-2234.

Kim, Y. D., Stultz, J., & Goodman, D. W. (2002). Dissociation of water on MgO(100). J. Phys. Chem. B, 106, 1515-1517.

Kricheldorf, H. R., Boettcher, C., & Tonnes, K. U. (1992). Polylactones: 23. Polymerization of racemic and mesod,l-lactide with various organotin catalysts—stereochemical aspects. Polymer, 33, 2817-2824.

Langel, W., & Parrinello, M. (1994). Hydrolysis at stepped MgO surfaces. Phys. Rev. Lett., 73, 504-507.

Lin, Y., Zhang, K., Dong, Z., Dong, L., & Li, Y. (2007). Study of hydrogen-bonded blend of polylactide with biodegradable hyperbranched poly(ester amide). Macromolecules, 40, 6257-6267.

Ljungberg, N., & Wesslen, B. (2005). Preparation and properties of plasticized poly(lactic acid) films. Biomacromolecules, 6, 1789-1796.

Lu, X., Lv, X., Sun, Z., & Zheng, Y. (2008). Nanocomposites of poly(L-lactide) and surface-grafted TiO2 nanoparticles: synthesis and characterization. Eur. Polym. J., 44, 2476-2481.

Lucas, E., Decker, S., Khaleel, A., Seitz, A., Fultz, S., Ponce, A., Li, W., Carnes, C., & Klabunde, K. J. (2001). Nnocrystalline metal oxides as unique chemical reagents/sorbents. Chem.-Eur. J., 7, 2505-2510.

Luo, Y., Wang, X., Xu, D., & Wang, Y. (2009). Preparation and characterization of poly(lactic acid)-grafted TiO_2 nanoparticles with improved dispersions. Appl. Surf. Sci., 255, 6795-6801.

Mehta, R., Kumar, V., Bhunia, H., & Upadhyay, S. (2005). Synthesis of poly(lactic acid): a review. J. Macromol. Sci.-Pol. Rev., 45, 325-349.

Moon, S. I., & Kimura, Y. (2003). Melt polycondensation of L-lactic acid to poly(L-lactic acid) with Sn(II) catalysts combined with various metal alkoxides. Polym Int., 52, 299-303.

Moon, S. I., Lee, C. W., Miyamoto, M., & Kimura, Y. (2000). Melt polycondensation of L-lactic acid with Sn(II) catalysts activated by various proton acids: a direct manufacturing route to high molecular weight poly(L-lactic acid). J. Polym. Sci. Pol. Chem., 38, 1673-1679.

Moon, S. I., Lee, C. W., Taniquchi, I., Miyamoto, M., & Kimura, Y. (2001). Melt/solid polycondensation of L-lactic acid: an alternative route to poly(L-lactic acid) with high molecular weight. Polymer, 42, 5059-5062.

Neal, L. M., Hernandez, D., & Hagelin-Weaver, H. E. (2009). Effects of nanoparticle and porous metal oxide supports on the activity of palladium catalysts in the oxidative coupling of 4-methylpyridine. J. Mol. Catal A-Chem., 307, 29–36.

Paul, M. A., Delcourt, C., Alexandre, M., Degée, P., Monteverde, F., Rulmont, A., & Dubois, P. (2005). (Plasticized) polylactide/(organo-)clay nanocomposites by in situ intercalative polymerization. Macromol. Chem. Phys., 206, 484-498.

Ray, S. S., & Bousmina, M. (2005). Biodegradable polymers and their layered silicate nanocomposites: in greening the 21st century materials world. Prog. Mater. Sci., 50, 962-1079.

Ray, S. S., Maiti, P., Okamoto, M., Yamada, K., & Ueda, K. (2002). New polylactide/layered silicate nanocomposites. 1.preparation, characterization, and properties. Macromolecules, 35, 3104-3110.

Ray, S. S., & Okamoto, M. (2003). Polymer/layered silicate nanocomposites: a review from preparation to processing. Prog. Polym. Sci., 28, 1539-1641.

Richards, R., Li, W., Decker, S., Davidson, C., Koper, O., Zaikovski, V., Volodin, A., Rieker, T., & Klabunde, K. J. (2000). Consolidation of metal oxide nanocrystals. Reactive pellets with controllable pore structure that reprent a new family of porous, inorganic materials. J. Am. Chem. Soc., 122, 4921-4925.

Rong, M. Z., Zhang, M. Q., & Ruan, W. H. (2006). Surface modification of nanoscale fillers for improving properties of polymer nanocomposites: a review. Mater. Sci. Technol., 22, 787-796.

Song, W., Zheng, Z., Lu, H., & Wang, X. (2008). Incorporation of multi-walled carbon nanotubes into biodegradable telechelic prepolymers. Macromol. Chem. Phys., 209, 315-321.

Thakur, K. A. M., Kean, R. T., Hall, E. S., Kolstad, J. J., Lindgren, T. A., Doscotch, M. A., Siepmann, J. I., & Munson, E. J. (1997). High-Resolution 13C and 1H Solution NMR Study of Poly(lactide). Macromolecules, 30, 2422-2428.

Tingaut, P., Zimmermann, T., & Lopez-Suevos, F. (2010). Synthesis and Characterization of Bionanocomposites with Tunable Properties from Poly(lactic acid) and Acetylated Microfibrillated Cellulose. Biomacromolecules, 11, 454-464.

Utamapanya, S., Klabunde, K. J., & Schlup, J. R. (1991). Nanoscale metal oxide particles/clusters as chemical reagents. Synthesis and properties of ultrahigh surface area magnesium hydroxide and magnesium oxide. Chem. Mater., 3, 175-181.

Vaia, R. A., Jandt, K, D., Kramer, E. J., & Giannelis, E. P. (1996). Microstructural evolution of melt intercalated polymer-organically modified layered silicates nanocomposites. Chem. Mater., 8, 2628-2635.

Wang, B., Sun, X. S., Klabunde, K. J. (2009). Poly(lactic acid)/multi-hydroxyl magnesium oxide nanocomposites prepared by melt compounding. J. Biobased Mater. Bioenergy, 3, 130-138.

Wu, L., Cao, D., Huang, Y., & Li, B. (2008). Poly(L-lactic acid)/SiO2 nanocomposites via in situ melt polycondensation of L-lactic acid in the presence of acidic silica sol: preparation and characterization. Polymer, 49, 742-748.

Yan, S., Yin, J., Yang, Y., Dai, Z., Ma, J., & Chen, X. (2007). Surface-grafted silica linked with L-lactic acid oligomer: a novel nanofiller to improve the performance of biodegradable poly(L-lactide). Polymer, 48, 1688-1694.

Yang, K., Wang, X., & Wang, Y. (2007). Progress in nanocomposite of biodegradable polymer. J. Ind. Eng. Chem., 13, 485-500.

Yao, X., Tian, X., Xie, D., Zhang, X., Zheng, K., Xu, J., Zhang, G., & Cui, P. (2009). Interface structure of poly(ethylene terephthalate)/silica nanocomposites. Polymer, 50, 1251-1256.

Yasuniwa, M., Tsubakihara, S., Sugimoto, Y., & Nakafuku, C. (2004). Thermal analysis of the double-melting behavior of poly(L-lactic acid). J. Polym. Sci. Pol. Phys., 42, 25-32.

Zhang, J., & Sun, X.S. (2004). Mechanical properties of poly(lactic acid)/starch composites compatibilized by maleic anhydride. Biomacromolecules, 5, 1446-1451.

Zhao, H., Kang, X., & Liu, L. (2005). Comb−coil polymer brushes on the surface of silica nanoparticles. Macromolecules, 38, 10619–10622.

Zhou, S., Zheng, X., Yu, X., Wang, J., Weng, J., Li, X., Feng, B., & Yin, M. (2007). Hydrogen bonding interaction of poly(D,L-Lactide)/hydroxyapatite nanocomposites. Chem. Mater., 19, 247-253.

Zou, H., Wu, S., & Shen, J. (2008). Polymer/silica nanocomposites: preparation, characterization, properties, and applications. Chem. Rev., 108, 3893-3957.

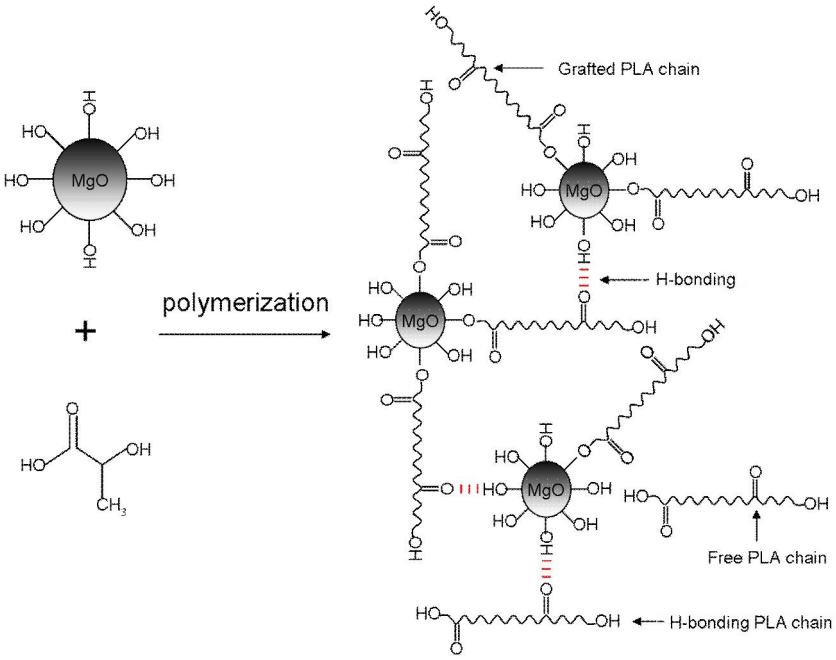

Figure 2.1 Scheme of the synthesis of PLA/MgO nanocomposites and formation of hydrogen bonding.

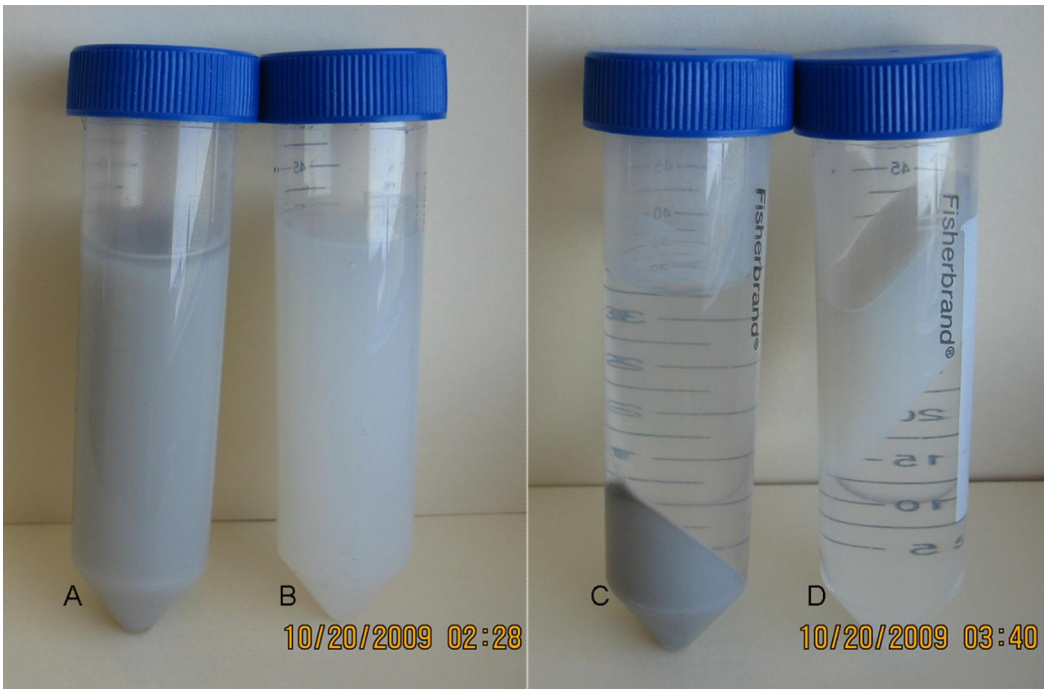

Figure 2.2 Photograph of t-MgO/PLA/chloroform suspension before (A) and after (C) centrifugation and PLA-g-MgO/free PLA/chloroform suspension before (B) and after centrifugation (D).

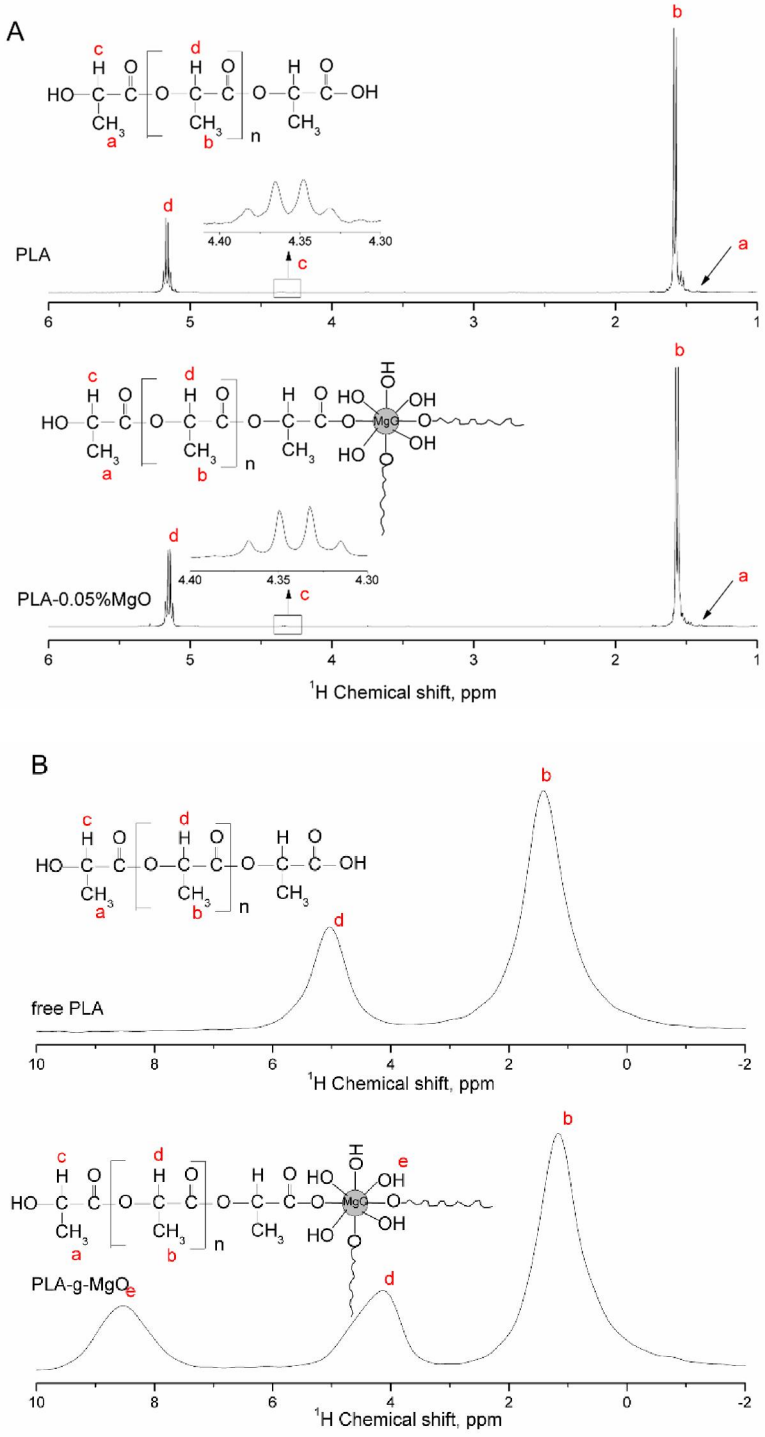

Figure 2.3 (A) Typical ^{1}H NMR spectra of PLA and nanocomposites; (B) Solid-state ^{1}H NMR spectra of free PLA and PLA-g-MgO.

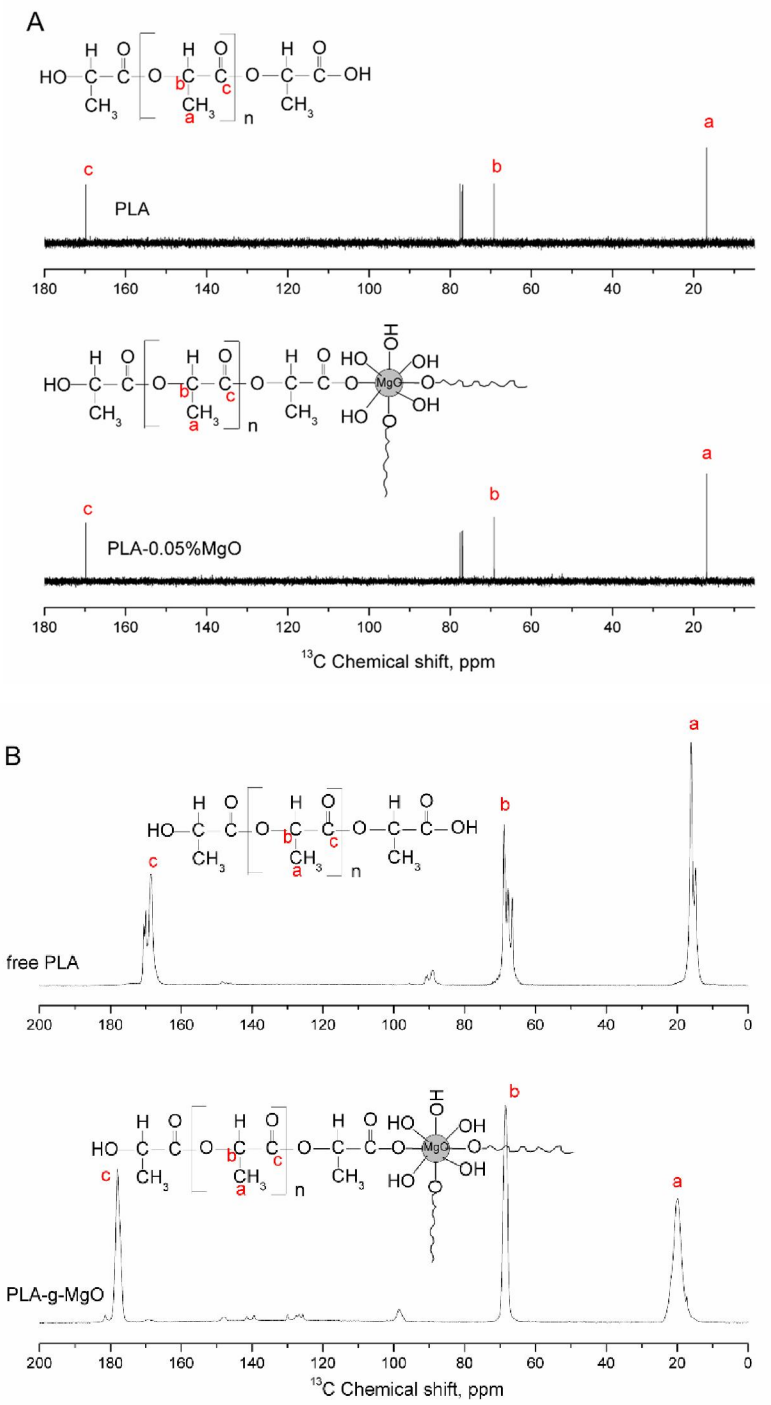

Figure 2.4 (A) Typical ^{13}C NMR spectra of PLA and nanocomposites; (B) Solid-state ^{13}C NMR spectra of free PLA and PLA-g-MgO.

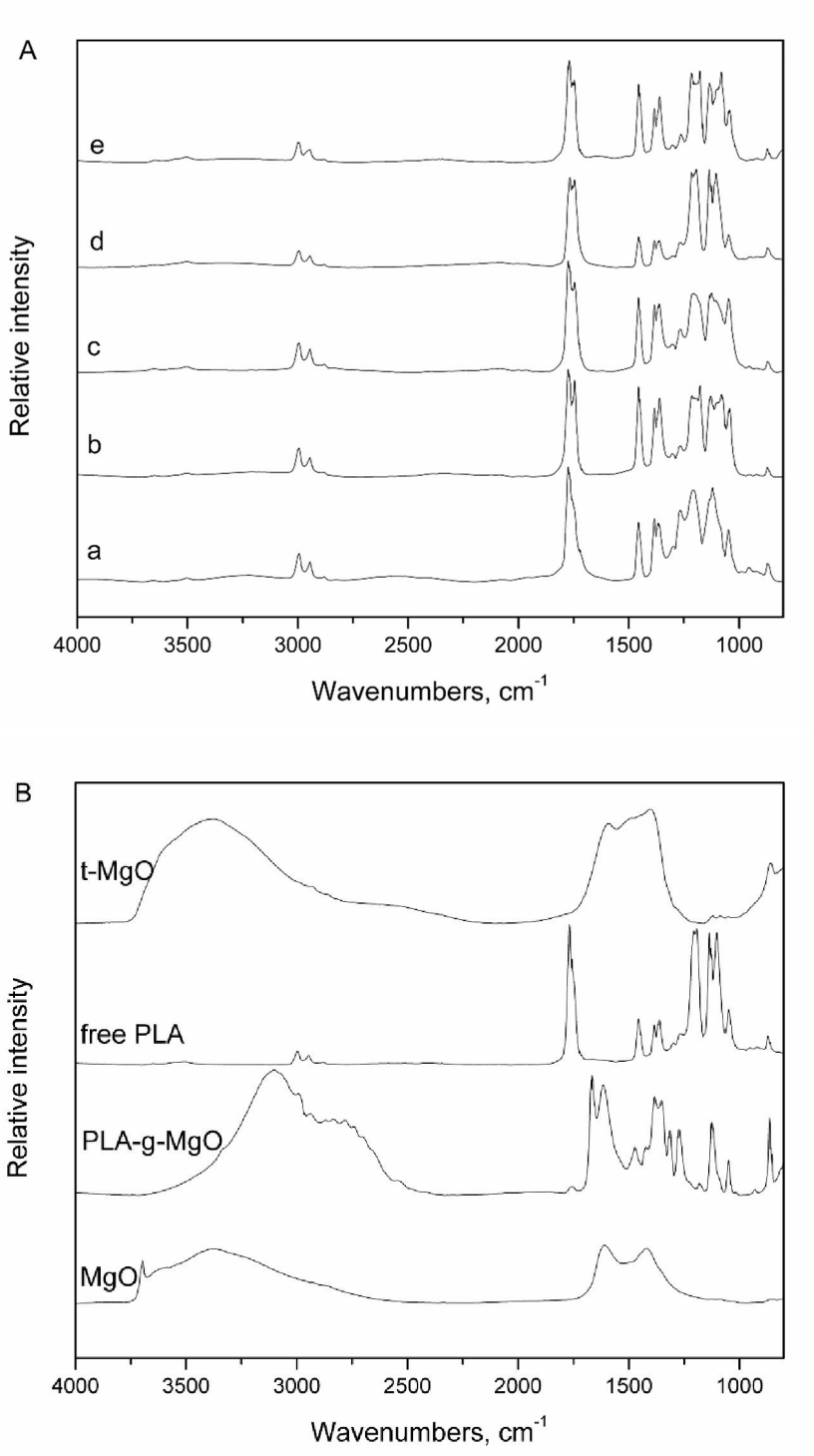

Figure 2.5 FTIR spectra of (A) PLA and nanocomposites (a, PLA; b, PLA-0.005%MgO; c, PLA-0.01%MgO; d, PLA-0.05%MgO; e, PLA-0.2%MgO); (B) MgO, PLA-g-MgO, free PLA, and t-MgO (a comparative sample, see text).

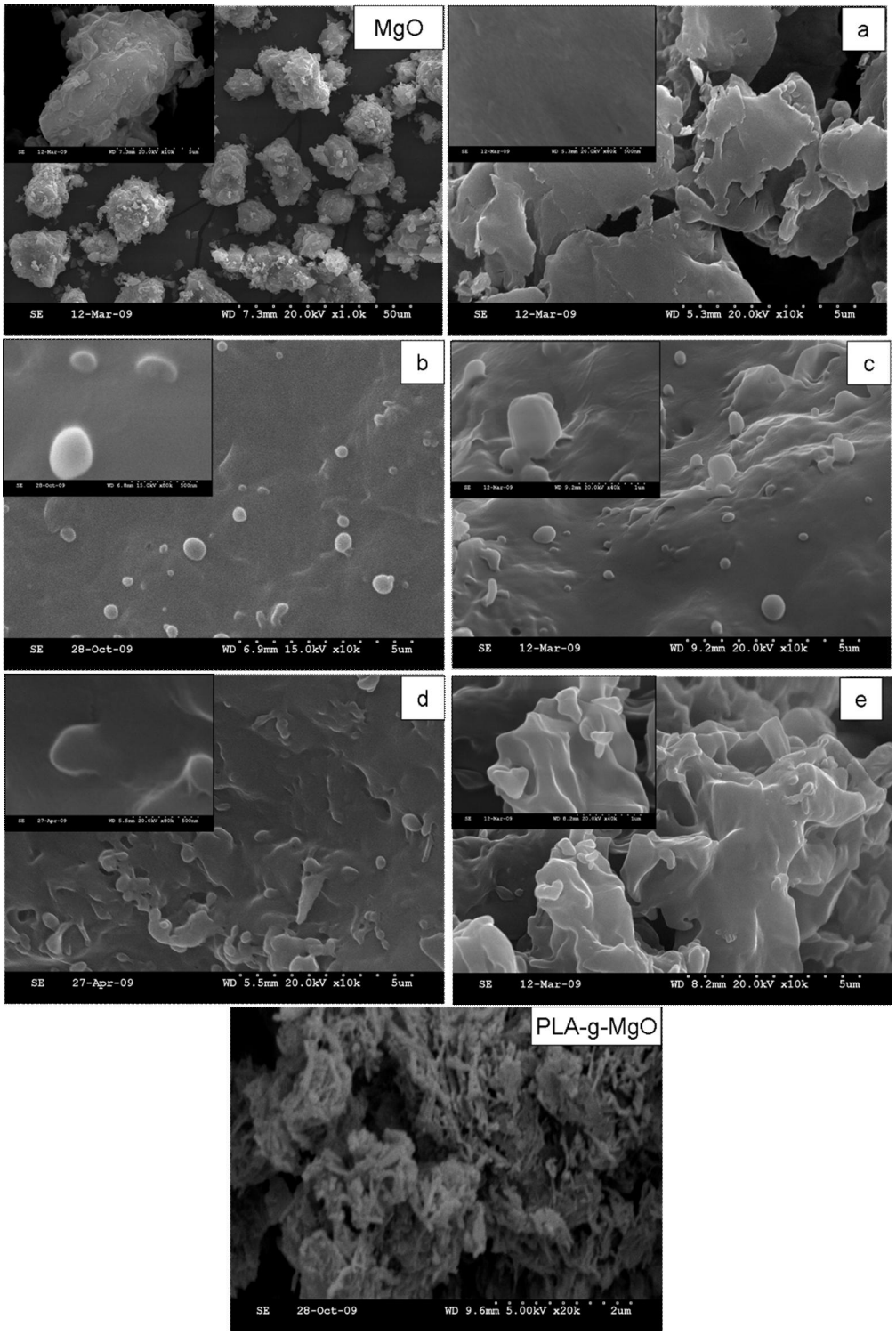

Figure 2.6 SEM images of MgO, PLA, nanocomposites (a, PLA; b, PLA-0.005%MgO; c, PLA-0.01%MgO; d, PLA-0.05%MgO; e, PLA-0.2%MgO), and PLA-g-MgO. (Scale bar is shown at the bottom of each image).

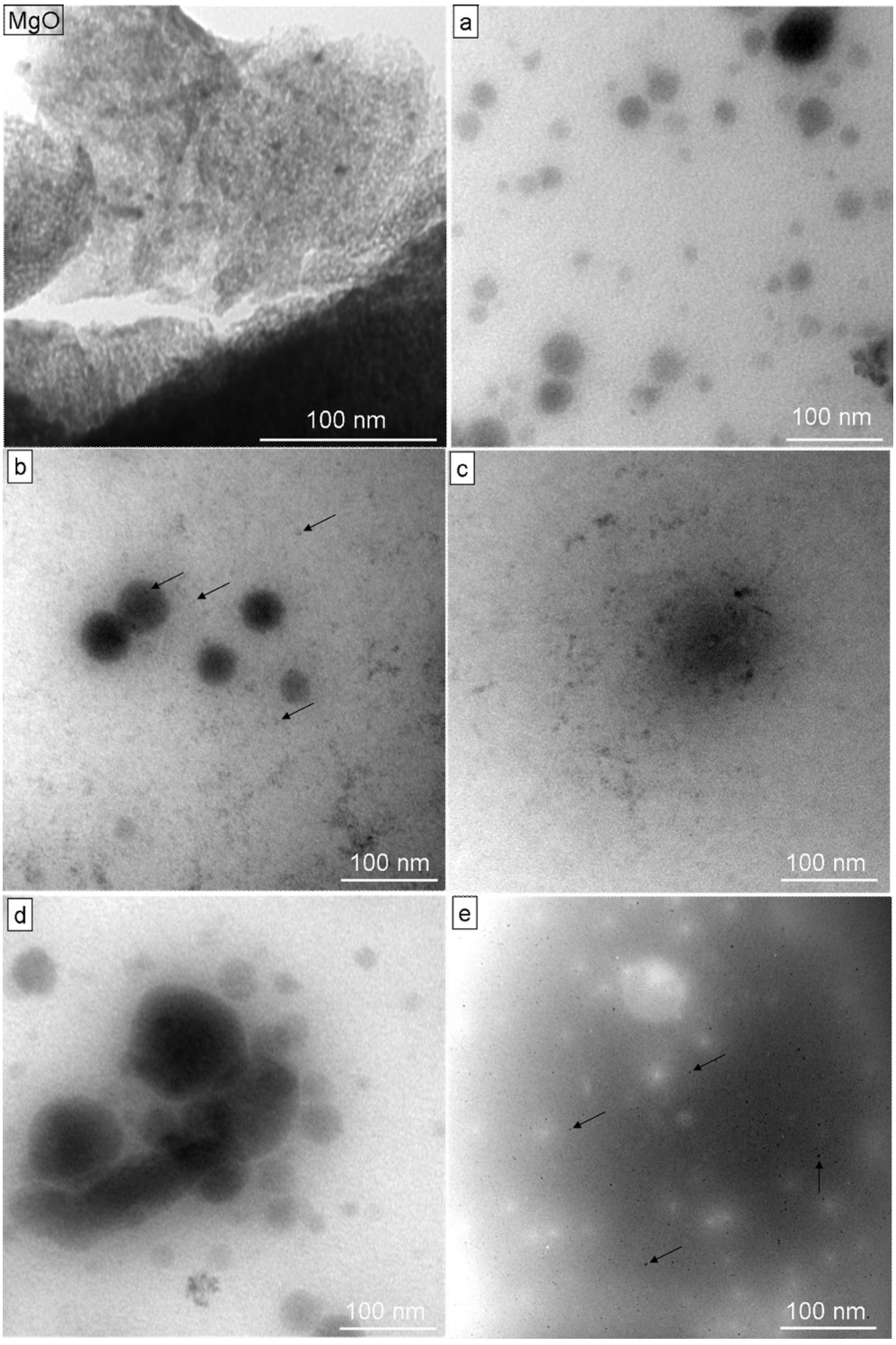

Figure 2.7 TEM images of MgO, PLA, and nanocomposites (a, PLA; b, PLA-0.005%MgO; c, PLA-0.01%MgO; d, PLA-0.05%MgO; e, PLA-0.2%MgO).

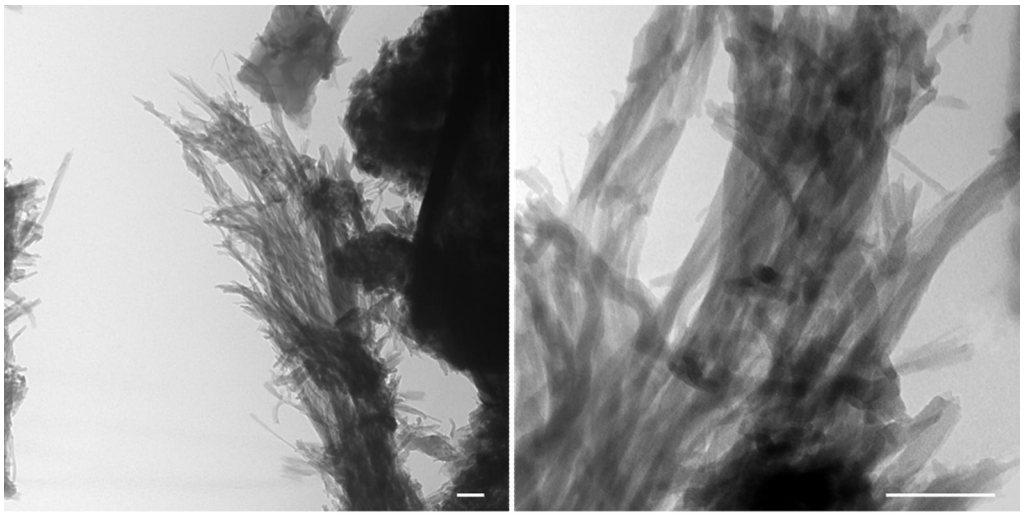

Figure 2.8 TEM images of PLA-g-MgO. (Left: lower magnification, 34000 X; Right: higher magnification, 130000 X. Scale bar: 100 nm).

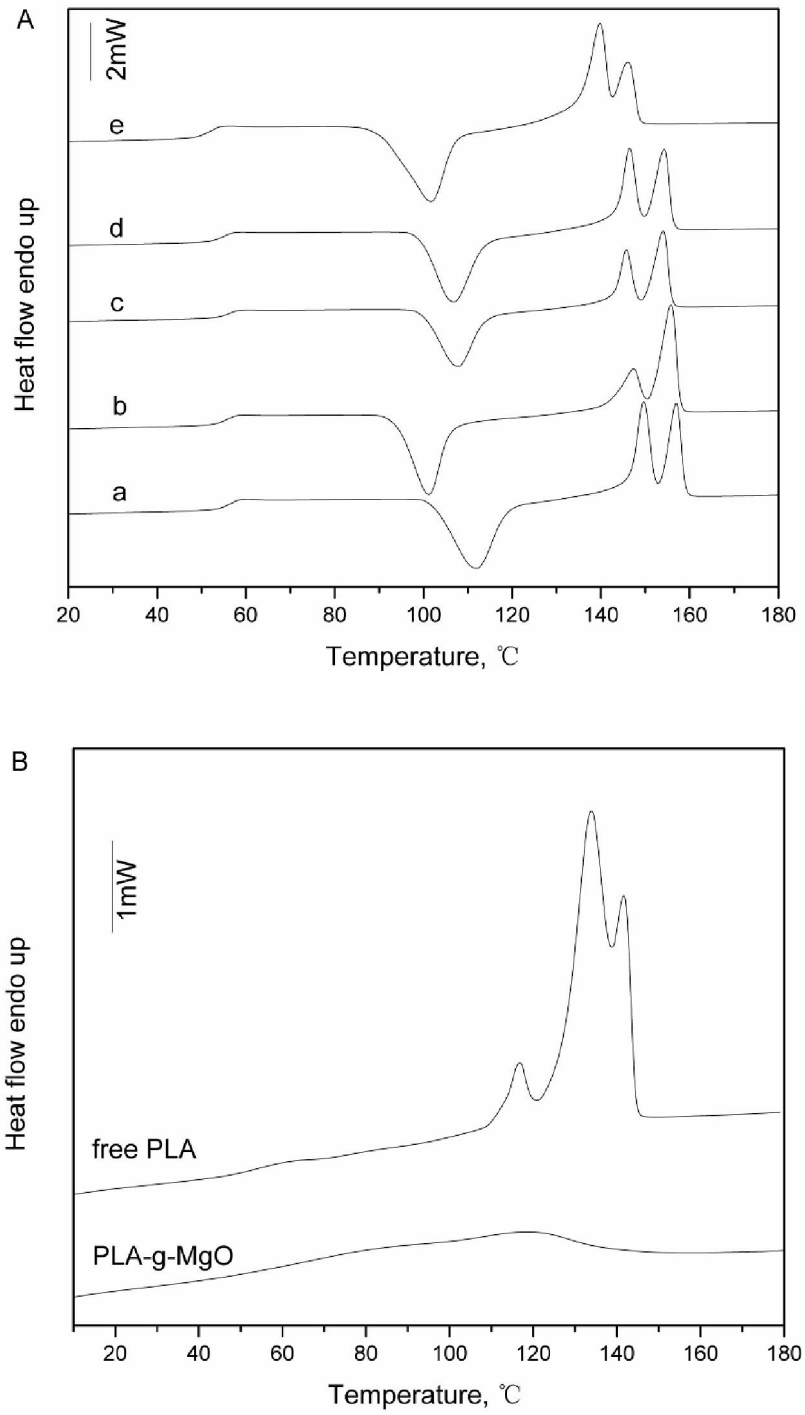

Figure 2.9 DSC thermograms of (A) PLA and nanocomposites (a, PLA; b, PLA-0.005%MgO; c, PLA-0.01%MgO; d, PLA-0.05%MgO; e, PLA-0.2%MgO); (B) free PLA and PLA-g-MgO.

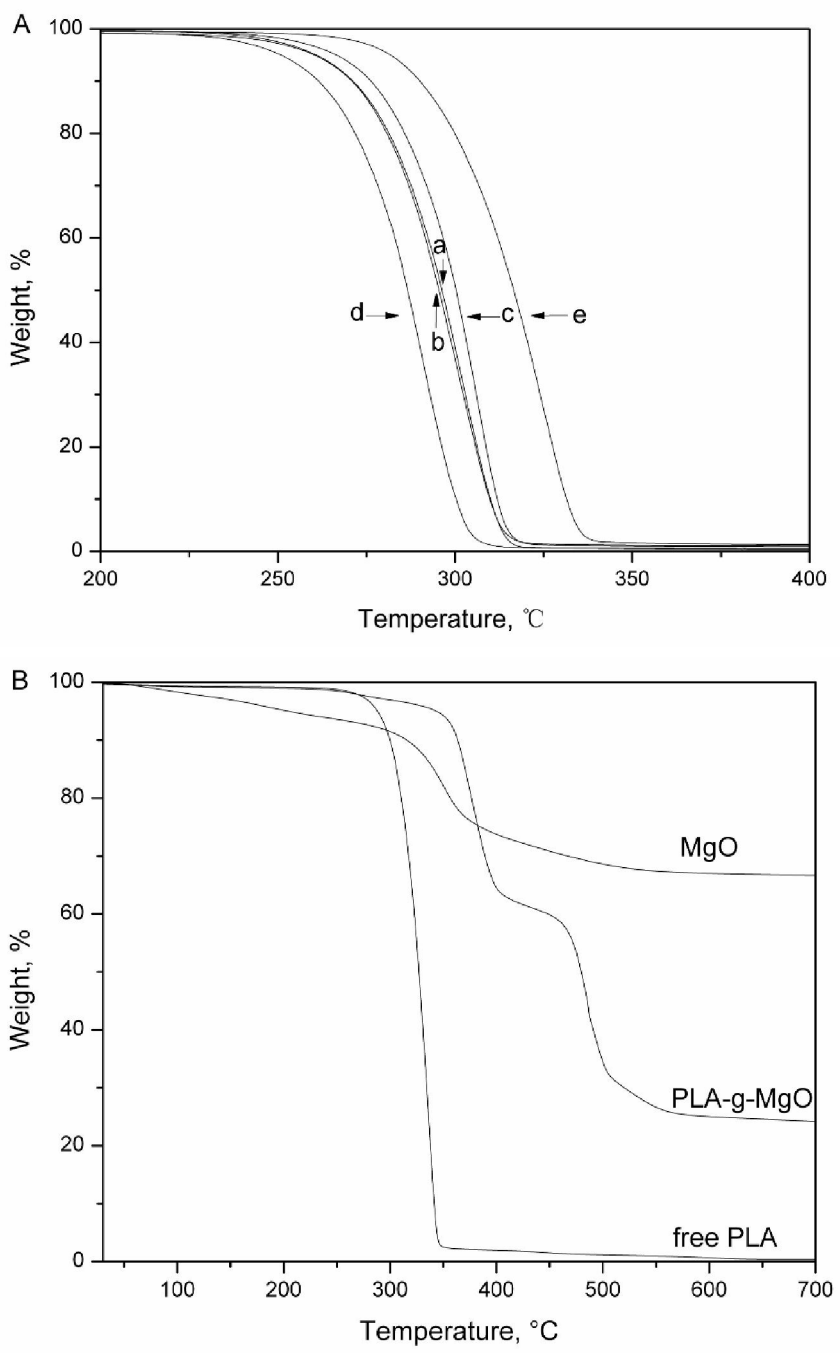

Figure 2.10 TGA of (A) PLA and nanocomposites (a, PLA; b, PLA-0.005%MgO; c, PLA-0.01%MgO; d, PLA-0.05%MgO; e, PLA-0.2%MgO); (B) MgO, PLA-g-MgO, and free PLA.

Table 2.1 Molecular weight and appearance of PLA, nanocomposites, and free PLA

Sample	M_w	M_n	[a]*PDI*	Appearance
PLA	42,500	23,300	1.8	Light black fibrils
PLA-0.005%MgO	41,900	20,000	2.0	Slight black fibrils
PLA-0.01%MgO	55,500	33,000	1.7	White fibrils
PLA-0.05%MgO	26,000	14,000	1.9	White solids
PLA-0.2%MgO	9,400	6,300	1.5	White solids
free PLA	10,100	6,000	1.7	White solids

[a]*PDI* -Polydispersity index (M_w/ M_n)

Table 2.2 Thermal properties of PLA, nanocomposites, free PLA, and PLA-g-MgO determined from DSC thermograms

Sample	T_g ºC	ΔC_p J/(g·ºC)	T_c ºC	ΔH_c J/g	T_m ºC	ΔH_m J/g	X_m %
PLA	55.9	0.63	112.0	-42.6	149.6, 157.0	44.2	47.2
PLA-0.005%MgO	55.3	0.62	101.2	-42.1	147.3, 155.8	44.2	47.3
PLA-0.01%MgO	55.9	0.59	107.8	-37.9	145.7, 154.0	38.5	41.1
PLA-0.05%MgO	54.6	0.59	106.8	-42.0	146.5, 154.3	42.2	45.0
PLA-0.2%MgO	51.4	0.62	101.7	-41.5	139.8, 146.2	43.3	46.3
free PLA	54.8	0.17	/	/	116.4, 133.7, 141.6	52.8	56.4
PLA-g-MgO	/	/	/	/	117.8	/	/

Table 2.3 Thermal decomposition temperatures of PLA, nanocomposites, free PLA, MgO, and PLA-g-MgO derived from TGA thermograms

Sample	T_{onset} ºC	T_{end} ºC	T_{max} ºC
PLA	278.5	317.1	302.4
PLA-0.005%MgO	278.8	316.5	301.4
PLA-0.01%MgO	287.3	317.2	306.5
PLA-0.05%MgO	268.5	307.2	292.1
PLA-0.2%MgO	296.2	338.0	324.0
free PLA	305.7	346.8	336.0
MgO	50.9, 160.7, 310.9	117.1, 213.9, 379.5	73.4, 184.4, 350.8
PLA-g-MgO	267.6, 353.3, 463.4	297.7, 404.9, 508.7	270.9, 376.2, 484.7

Chapter 3 - Nanocomposites of Poly(lactic acid) and Surface-grafted MgO Nanoparticles: Preparation and Characterization[2]

3.1 Abstract

Incorporating small amounts of rigid nanoparticles within a polymer host to prepare polymer nanocomposites has shown great potential to enhance the physical, thermomechanical, and processing characteristics of pristine polymers since the 1990s. In this study, we first prepared surface-grafted MgO (g-MgO) by *in situ* melt polycondensation of lactic acid and surface-hydroxylated MgO nanoparticles and then prepared poly(lactic acid) (PLA) nanocomposites through thermal compounding of PLA and g-MgO/MgO nanoparticles. The morphological, mechanical, and thermal properties of PLA/MgO and PLA/g-MgO nanocomposites were characterized. PLA/g-MgO nanocomposites exhibited higher tensile strength than neat PLA. Morphology of the fracture surfaces showed that stronger interfacial interaction was formed in PLA/g-MgO nanocomposites than in PLA/MgO nanocomposites. Surface grafting MgO with PLA chains likely results in enhanced chain entanglement and mechanical interlocking with the polymer matrix and, consequently, better adhesion. Increased thermal stability was observed for PLA/g-MgO nanocomposites with g-MgO loading levels lower than 0.05%, whereas decreased thermal stability was observed for all PLA/MgO nanocomposites.

[2] Results have been accepted to publish. Li, Y., & Sun, X. S. (2011). Nanocomposites of poly(lactic acid) and surface grafted MgO nanoparticles: preparation and characterization. *J. Biobased Mater. Bioenergy*, accepted.

3.2 Introduction

Polymer nanocomposites (PNCs), which are prepared by incorporating small amounts of rigid nanoparticles (typically less than 5% by weight) within a polymer host (Zhu & Wilkie, 2009), always exhibit properties significantly different from those of the host (Akcora et al., 2009; An et al., 2008; Balazs et al., 2006; Crosbya & Lee, 2007; Krishnamoorti & Vaia, 2007; Oh & Green, 2009; Ramanathan et al., 2008; Vaia & Maguire, 2007). Nanoparticles such as one-dimensional carbon nanotubes (Moniruzzaman & Winey, 2006; Swain & Jena, 2010), two-dimensional nanoclays (Chen et al., 2008; Ray & Okamoto, 2003), and three-dimensional silica spheres (Zou et al., 2008) have been widely studied as reinforcing agents for PNCs. Polymer nanocomposites are distinguished by the convergence of the dominant length scales associated with the average chain radius of gyration of the polymer matrix (R_g, ~2-20 nm), average size of the nanoparticles (nanoplate thickness and nanotube/nanosphere diameter, $2r$, < 100 nm), and average interparticle distance ($2d$). When these dimensions are of a comparable magnitude ($R_g \approx r \approx d$), geometrical considerations have a profound impact on the conventional underlying constructs of polymer behavior (Krishnamoorti & Vaia, 2007; Vaia & Maguire, 2007; Zou et al., 2008). Polymer nanocomposites can be prepared in several ways including direct mixing (melt mixing, solution mixing), sol-gel processing, and *in situ* graft polymerization. Melt processing is of greatest interest because this method is generally considered more economical and more flexible for formulation and involves compounding and fabrication facilities commonly used in commercial practice (Paul & Robeson, 2008).

Poly(lactic acid) (PLA) is a biodegradable and compostable polymer made from renewable resources; therefore, PLA nanocomposites have attracted intensive studies over the past decade (Chen et al., 2005; Drown et al., 2007; Feng et al., 2008; Hong et al., 2004; Kramschuster et al., 2007; Pan & Qiu, 2010; Paul et al., 2005; Parulekar et al., 2007; Ray et al., 2002; Wen et al., 2009; Xiang et al., 2009). PLA nanocomposites exhibit enhanced physical (e.g., barrier, erosion resistance, and reduced flammability), thermomechanical (e.g., heat distortion temperature, thermal expansion coefficient, and stiffness), and processing (e.g., surface finish and melt strength) characteristics compared with pristine polymers. Our

group has been working on PLA nanocomposites with surface-hydroxylated magnesium oxide (MgO) nanoparticles, including conventionally prepared NanoActive MgO (CP-MgO) and aerogel-prepared NanoActive MgO plus (AP-MgO) (Beavers et al., 2009; Li & Sun, 2010; Wang et al., 2009). These two types of MgO nanoparticles were developed by Dr. Klabunde and his co-workers (Itoh et al., 1993; Utamapanya et al., 1991) and have been commercialized. Compared with commercial MgO, these nanoparticles have a much smaller crystal size, higher surface area, more surface defects, and higher reactivity, which result in large numbers of surface hydroxyl groups because of water dissociation (Itoh et al., 1993; Lucas et al., 2001). We have prepared PLA nanocomposites with CP-MgO nanocrystals (hexagonal plate-like structure, 50 to 100 nm long, 5 nm thick, about 250 m^2/g surface area) through thermal compounding (Wang et al., 2009). At a CP-MgO loading ratio of 0.4 wt% or less, mechanical properties of nanocomposites were significantly improved, probably because of the affinity PLA segments have for the CP-MgO surface by hydrogen bonding. However, because inorganic nanoparticles typically agglomerate and are not always miscible with the organic polymer phase, it is usually a challenge to achieve better dispersion and strong interfacial interaction between nanoparticles and the polymer matrix. One strategy to overcome this difficulty is to shield the particle surface by grafting it with the same chains as the matrix polymer (Akcora et al., 2009).

In a previous study, we successfully prepared surface-grafted MgO with PLA chains (g-MgO) through *in situ* melt polycondensation of L-lactic acid (LA) and AP-MgO nanocrystals (polyhedral shape, crystal size $\leq$ 4 nm, surface area $\geq$ 600 m^2/g) (Li & Sun, 2010). Our goal for the present study was to prepare PLA nanocomposites with g-MgO nanoparticles (and with non-grafted MgO (AP-MgO) as a comparison) through thermal compounding and compression molding. We hypothesized that surface grafting MgO with PLA chains would improve nanoparticle dispersion and yield nanocomposites with enhanced interfacial interaction due to chain entanglement and mechanical interlocking between the polymer matrix and grafted PLA chains (Figure 3.1).

3.3 Experimental Section

3.3.1 Materials

PLA (2002D) (weight average molecular weight = 210 000) in pellet form was obtained from NatureWorks LLC (Minnetonka, MN). The LA was supplied as a 90 wt% aqueous solution by Acros Organics. MgO was obtained from NanoScale Co. (NanoActive Magnesium Oxide Plus (AP-MgO), Manhattan, KS). Tin (II) chloride dihydrate ($SnCl_2 \cdot H_2O$; 98%, reagent grade) and *p*-toluenesulfonic acid monohydrate (TSA; 98.5+%, ACS reagent grade) were purchased from Sigma-Aldrich Co. All materials were used as received.

3.3.2 Preparation of g-MgO

The g-MgO was prepared according to procedures described in our previous paper. Briefly, LA oligomer with degree of polymerization of about 6 was prepared at a gradually increasing temperature (110 to 150 °C) and vacuum level (100 to 10 Torr) during 9 h. The 3% MgO (based on the weight of LA oligomer) and binary catalysts ($SnCl_2 \cdot H_2O$, 0.4% wt relative to oligomer, and TSA, an equimolar ratio to $SnCl_2 \cdot H_2O$) were added to the LA oligomer. The mixture was gradually heated to 180 °C with stirring, and pressure was reduced stepwise to 10 Torr in 1.5 h to avoid LA bumping. The reaction was maintained at 180 °C/10 Torr for 10 h. At the end of reaction, the product was dispersed into chloroform. The g-MgO was isolated from free PLA via a repeated dispersion/centrifugation processes, dried in a vacuum oven at 80 °C for 24 h to remove the residual solvent, and stored for future use. The successful grafting of PLA onto MgO surface was confirmed by Fourier-transform infrared spectroscopy and thermal gravimetric analysis (TGA), and also supported by solid-state ^{1}H NMR, ^{13}C NMR, and differential scanning calorimetry (DSC) data, as reported in our previous paper (Li & Sun, 2010). TGA results indicated that more than 42.5% PLA was grafted for g-MgO (Li & Sun, 2010).

3.3.3 Preparation of PLA/MgO and PLA/g-MgO Nanocomposites

The PLA pellets were ground through a 2 mm screen in a laboratory mill (Thomas-Wiley Company, Philadelphia, PA). Ground PLA, MgO, and g-MgO were dried in a vacuum

oven at 80 ºC for 24 h. Ground PLA with various amounts of MgO and g-MgO (0.0125%, 0.025%, 0.05%, 0.2%, and 0.8%) were first mixed in a stand mixer (Ultra Power Kitchen Aid, St. Joseph, MI) for 10 min and then thermal compounded at 180 ºC and 130 rpm for 5 min in an intensive mixer (Rheomix 600, Haake, Paramus, NJ) equipped with two corotating rollers with a gap. After they cooled, the blends were ground into 2 mm powder. Pure PLA was treated with the same procedures used for the control. Dog-bone-type tensile bars were compression molded at 180 ºC and 8000 lb for 5 min with a Carver hot press (Model 3889, Carver Inc., Wabash, IN) according to ASTM Method D 638-03 (2003), cooled to room temperature in air, and then removed from the mold. At least five specimens were prepared for each type of nanocomposite.

3.3.4 Mechanical Measurements

The tensile bars of nanocomposites were conditioned at 25 ºC and 50% relative humidity for 48 h before mechanical testing. The mechanical tests were performed with an Instron testing system (model 4465, Canton, MA) at a crosshead speed of 5 mm/min with a 30 mm gauge length, according to ASTM Method D 638-03. Five replicates were tested for each sample type.

3.3.5 Scanning Electron Microscopy (SEM) Analysis

Morphology of the fractured surfaces of nanocomposites obtained from the tensile tests was observed via SEM (Hitachi S-3500N, Hitachi Science Systems, Ltd., Japan). The specimen was mounted on an aluminum stub, and the fractured surface was coated with an alloy of 60% gold and 40% palladium with a sputter coater (Desk II Sputter/ Etch Unit, NJ) before observation. A similar procedure was used to observe the morphology of MgO and g-MgO.

3.3.6 Thermal Properties Characterization

Thermal transitions of the nanocomposites were measured with a TA DSC Q200 instrument. About 5 mg of each sample obtained from the tensile bars was sealed in an aluminum pan. An empty pan was used as a reference. The sample was heated from 0 °C to 180 °C at a rate of 10 °C/min, equilibrated at 180 °C, quenched to 0 °C, equilibrated at 0 °C,

and then heated again to 180 °C at the same rate. The sample was characterized in an inert environment by using nitrogen with a gas flow rate of 50 mL/min. Heat capacity (ΔC_p), glass transition temperature (T_g), melting temperature (T_m), and heat of melting (ΔH_m) were determined from the DSC thermograms. Crystallinity (X_m) was estimated according to the following equation:

$$X_m(\%) = \frac{\Delta H_m}{\Delta H_0} \times 100 \qquad (1)$$

ΔH_m and ΔH_0 are the heats (J/g) of melting of PLA nanocomposites and a PLA crystal of infinite size with a value of 93.6 J/g (Fischer et al., 1973; Li & Sun, 2011), respectively.

Thermal stability of the nanocomposites was determined with a PerkinElmer Pyris1 TGA (Norwalk, CT). About 5 mg of each sample obtained from the tensile bars was placed in the pan and heated from 40 °C to 600 °C at a heating rate of 20 °C/min under a nitrogen atmosphere.

3.3.7 Flowability

Flowability of molten nanocomposites was measured with an MP600 Extrusion Plastometer (Tinius Olsen Testing Machine Company, INC. Horsham, PA) according to ASTM Method D 1238 – 04 (2004). About 8 g of each sample was charged into the cylinder. The melt flow index (MFI, g/10 min) value was determined as the amount of material extruded by a piston action through a standard orifice (diameter, 2.096 mm; length, 8.001 mm) at 190 °C and 2.16 kg load after preheating for 6 min.

3.4 Results and Descussion

3.4.1 Mechanical Properties

Both PLA and its nanocomposites showed brittle fracture behavior, with 5.3 to 6.3% elongation at break. PLA exhibited tensile strength (σ) of 64 MPa and Young's modulus (E) of 1.6 GPa (Figure 3.2). These values are lower than our previously reported values (σ = 76 MPa, E = 2 GPa) (Li et al., 2010); which is mainly due to the different thermal processing conditions used in each study. With the addition of 0.0125% MgO, σ and E were increased by

14% and 26%, respectively, compared with the values of PLA. The reinforcement of mechanical strength was probably caused by hydrogen bonding between ester groups in PLA chains and hydroxyl groups from the MgO surface. As the loading ratio of MgO further increased, σ and E decreased gradually but remained higher than the values of PLA. With 0.8% MgO, σ further decreased to 62 MPa.

For PLA/g-MgO nanocomposites, the maximum σ was observed with 0.025% g-MgO, and this value was 18% higher than the σ of PLA. Further increasing the g-MgO loading ratio to 0.05%, 0.2%, and 0.8% led to an obvious reduction in σ and a slight reduction in E. The σ of PLA/g-MgO nanocomposites was always slightly higher or similar to that of PLA/MgO nanocomposites, except for PLA/0.0125% g-MgO. The slight improvement in σ of the PLA/g-MgO nanocomposites could be a result of the enhanced penetration and interaction between the MgO nanoparticles and PLA matrix that occurred because of the surface grafting of MgO nanocrystals (Lu et al., 2008). However, when the loading ratios of MgO and g-MgO increased beyond the optimal value, the agglomeration of nanoparticles became dominant and suppressed the interfacial interaction effect. Those agglomerations acted as local stress concentrations during the tensile test, and the mechanical strength consequently decreased (Luo et al., 2009). Moreover, because of the large number of surface hydroxyl groups from MgO and g-MgO nanoparticles, hydrolysis effects became obvious at higher concentrations of fillers, which also led to the deterioration of mechanical strength (Wang et al., 2009).

3.4.2 Morphology

The morphological changes of MgO after surface grafting are shown in Figure 3.3. MgO crystals existed in compact agglomerate forms with an average size of 10 to 15 μm. After it was surface grafted with PLA chains, g-MgO exhibited a loose and porous morphology, indicating that the compact aggregation of the original MgO crystals was greatly inhibited (Li & Sun, 2010).

An examination of the fracture surface of PLA/MgO and PLA/g-MgO nanocomposites (e.g., at 0.025%) revealed an obvious difference in the interfacial interaction between the polymer matrix and the nanofiller in these two systems. Most MgO nanoparticles

protruded cleanly from the fracture surface (Figure 3.4, top), indicating a weak interfacial adhesion, whereas most g-MgO nanoparticles were thickly coated with PLA matrix or embedded within the matrix (Figure 3.4, bottom), indicating stronger PLA-g-MgO interactions. Surface grafting MgO with PLA chains likely results in enhanced chain entanglement and mechanical interlocking with the polymer matrix and, consequently, better adhesion. Moreover, for both PLA/MgO and PLA/g-MgO nanocomposites, formation of hydrogen bonding between the remaining surface hydroxyl groups of nanoparticles and carbonyl groups of the PLA matrix would also contribute to better interfacial adhesion (Ramanathan et al., 2008).

3.4.3 Thermal Properties

Figure 3.5 shows DSC thermograms of compression-molded PLA/MgO (A, first scan; C, second scan) and PLA/g-MgO (B, first scan; and D, second scan) nanocomposites, and DSC results are summarized in Table 3.1. The T_m and ΔH_m were obtained from the first heating scan to reveal the crystalline status of the compression-molded nanocomposites; the T_g and ΔC_p were obtained from the second heating scan to erase the physical aging effect during storage. Both PLA/MgO and PLA/g-MgO nanocomposites showed similar glass transition temperatures of about 59 ºC, and their heat capacity during glass transition [ΔC_p of 0.52 to 0.54 J/(g·ºC)] was similar to that of pure PLA, indicating that no strong chemical interactions were formed between the PLA matrix and nanoparticles. The melting temperature was also similar for all samples (148 to 149 ºC). The crystallinity of PLA was not obviously affected by addition of either MgO or g-MgO. For PLA/g-MgO nanocomposites with 0.025% or 0.8% nanoparticle loading levels, the decreased crystallinity might have been caused by processing variations.

TGA and derivative TGA thermograms of PLA/MgO and PLA/g-MgO nanocomposites are shown in Figures 3.6 and 3.7, respectively, and the temperatures at maximum decomposition rate are compared in Figure 3.8. Compared with the TGA thermogram curves of pure PLA, those of PLA/MgO nanocomposites shifted toward lower temperatures. As MgO loading ratio increased, the onset decomposition temperature, peak decomposition temperature (T_{max}), and end decomposition temperature decreased (Figure

3.6B). At 0.8% MgO, T_{max} was reduced by 48 ºC compared with that of pure PLA (Figure 3.8). Thermal stability of PLA/g-MgO nanocomposites with 0.0125%, 0.025%, and 0.05% g-MgO addition was slightly higher than that of pure PLA (Figure 3.8). As g-MgO addition further increased to 0.2%, T_{max} decreased slightly. At 0.8% g-MgO, T_{max} was reduced by 41 ºC compared with that of pure PLA. PLA/g-MgO nanocomposites showed improved thermal stability compared with PLA/MgO nanocomposites. As reported previously, when PLA was chemically grafted onto the MgO surface to form g-MgO, the grafted PLA chains showed greatly improved thermal stability compared with pure PLA (Li & Sun, 2010). During thermal compounding of PLA and g-MgO, strong entanglements formed between the PLA matrix and grafted PLA chains, which resulted in higher thermal stability for PLA/g-MgO nanocomposites. However, at higher g-MgO loading ratios (0.8%), the remaining hydroxyl groups on the g-MgO surface became dominant, which facilitated the random chain scission through hydrolysis and pyrolysis of the ester groups of PLA (Wang et al., 2009). In PLA/MgO nanocomposites, many surface hydroxyl groups from MgO were still available; therefore, decreased thermal stability was observed for all samples.

Measuring MFI is vital to anticipating and controlling polymer processing. Generally, polymers with higher MFI are used in injection molding, and polymers with lower MFI are used in blow molding or extrusion processes. Pure PLA had an MFI of 7.5 g/10 min (Figure 3.9), which was in accordance with the manufacturer's reported value (5 to 7 g/10 min). With addition of MgO, MFI values of PLA/MgO nanocomposites all increased to about 10 to 12 g/10 min. PLA/g-MgO nanocomposites showed MFI values of about 8 to 9 g/10 min; these values are slightly higher than those of pure PLA but lower than those of PLA/MgO nanocomposites. As discussed previously, many hydroxyl groups exist on the MgO and g-MgO surfaces, which facilitated the hydrolysis and pyrolysis of PLA during thermal processing and measuring and, therefore, increases MFI values. The g-MgO possesses fewer surface hydroxyl groups than MgO because it is surface grafted with PLA; therefore, PLA/g-MgO nanocomposites showed lower MFI values than PLA/MgO nanocomposites.

3.5 Conclusions

PLA/g-MgO nanocomposites with improved mechanical properties were prepared via thermal compounding. For PLA/MgO nanocomposites, maximum tensile strength and Young's modulus were obtained at a 0.0125% MgO loading level and increased by 14% and 26%, respectively, compared with values for pure PLA. For PLA/g-MgO nanocomposites, maximum tensile strength was obtained at a 0.025% g-MgO loading level and was slightly higher than the tensile strength value of the PLA/0.0125%MgO nanocomposite. Morphology of the fracture surfaces showed that PLA/g-MgO nanocomposites had stronger interfacial interaction than PLA/MgO nanocomposites. Compared with pure PLA, all PLA/MgO nanocomposites had decreased thermal stability and PLA/g-MgO nanocomposites with g-MgO loading levels lower than 0.05% had increased thermal stability. The mechanical properties between PLA/MgO and PLA/g-MgO nanocomposites are not significant, therefore, PLA/MgO may be more economically acceptable than PLA/g-MgO.

3.6 Acknowledgments

Financial support was provided from the U.S. Department of Agriculture/National Research Initiative and the U.S. Department of Energy. Contribution No. 11-017-J from the Kansas Agricultural Experiment Station.

3.7 References

Akcora, P., Liu, H., Kumar, S. K., Moll, J., Li, Y., Benicewicz, B. C., Schadler, L. S., Acehan, D., Panagiotopoulos, A. Z., Pryamitsyn, V., Ganesan, V., Ilavsky, J., Thiyagarajan, P., Colby, R. H., & Douglas J. F. (2009). Anisotropic self-assembly of spherical polymer-grafted nanoparticles. Nature Mater., 8, 354–359.

Allegra, G., Raos G., & Vacatello, M. (2008). Theories and simulations of polymer-based nanocomposites: From chain statistics to reinforcement. Prog. Polym. Sci., 33, 683–731.

An, L., Pan, Y., Shen, X., Lu, H., & Yang Y. (2008). Rod-like attapulgite/polyimide nanocomposites with simultaneously improved strength, toughness, thermal stability and related mechanisms. J. Mater. Chem., 18, 4928–4941.

ASTM D 638-03. (2003). Standard test method for tensile properties of plastics, ASTM International, West Conshohocken, PA, DOI: 10.1520/D0638-03, www.astm.org.

ASTM Standard, D1238-04. (2004). Standard test method for melt flow rates of thermoplastics by extrusion plastometer, ASTM International, West Conshohocken, PA, DOI: 10.1520/D1238-04, www.astm.org.

Balazs, A. C., Emrick, T., & Russell, T. P. (2006). Nanoparticle polymer composites: where two small worlds meet. Science, 314, 1107-1110.

Beavers, E. M., Klabunde, K. J., Wang, B., & Sun, X. S. (2009). Lactic acid-magnesium oxide nanocrystal interactions: how nanoparticles size and shape effect chemistry and template oligomerization. New J. Chem., 33, 1951-1959.

Chen, B., Evans, J. R. G., Greenwell, H. C., Boulet, P., Coveney, P. V., Bowden, A. A., & Whiting, A. (2008). A critical appraisal of polymer–clay nanocomposites. Chem. Soc. Rev., 37, 568–594.

Chen, G., Kim, H., Shim, J., & Yoon, J. (2005). Role of epoxy groups on clay surface in the improvement of morphology of poly(l-lactide)/clay composites. Macromolecules, 38, 3738-3744.

Crosbya, A. J., & Lee, J. Y. (2007). Polymer nanocomposites: the "nano" effect on mechanical properties. Polym. Rev., 47, 217-229.

Drown, E. K., Mohanty, A. K., Parulekar, Y., Hasija, D., Harte, B. R., Misra, M., & Kurian, J. V. (2007). The surface characteristics of organoclays and their effect on the properties of poly(trimethylene terephthalate) nanocomposites. Compos. Sci. Tech., 67, 3168-3175.

Feng, J., Cai, W., Sui, J., Li, Z., Wan, J., & Chakoli, A. N. (2008). Poly(L-lactide) brushes on magnetic multiwalled carbon nanotubes by in-situ ring-opening polymerization. Polymer, 49, 4949-4994.

Fischer, E. W., Sterzel, H. J., & Wegner, G. (1973). Investigation of the structure of solution grown crystals of lactide copolymers by means of chemical reactions. Kolloid Z. Z. Polym., 251, 980-990.

Hong, Z., Qiu, X., Sun, J., Deng, M., Chen, X., & Jing, X. (2004). Grafting polymerization of L-lactide on the surface of hydroxyapatite nano-crystals. Polymer, 45, 6699-6706.

Itoh, H., Utamapanya, S., Stark, J. V., Klabunde, K. J., & Schlup, J. R. (1993). Nanoscale metal oxide particles as chemical reagents. Intrinsic effects of particle size on hydroxyl content and on reactivity and acid/base properties of ultrafine magnesium oxide. Chem. Mater., 5, 71–77.

Kramschuster, A., Gong, S., Turng, L. S., & Li, T. (2007). Injection-molded solid and microcellular polylactide and polylactide nanocomposites. Biobased Mater. Bioenergy, 1, 37–45.

Krishnamoorti, R., & Vaia, R. A. (2007). Polymer Nanocomposites. J. Polym. Sci. Part B-Polym Phys., 45, 3252–3256.

Li Y., Venkateshan, K., & Sun, X. S. (2010). Mechanical and thermal properties, morphology, and relaxation characteristics of poly(lactic acid) and soy flour/wood flour blends. Polym. Int., 59, 1099-1109.

Li, Y., & Sun, X. S. (2010). Preparation and characterization of polymer−inorganic nanocomposites by in situ melt polycondensation of L-lactic acid and surface-hydroxylated MgO. Biomacromolecules, 11, 1847–1855.

Li, Y., & Sun, X. S. (2011). Mechanical and thermal properties of biocomposites from poly(lactic acid) and DDGS. J. Appl. Polym. Sci., n/a, doi: 10.1002/app.33681.

Lu, X., Lv, X., Sun, Z., & Zheng, Y. (2008). Nanocomposites of poly(L-lactide) and surface-grafted TiO2 nanoparticles: synthesis and characterization. Eur. Polym. J., 44, 2476-2481.

Lucas, E., Decker, S., Khaleel, A., Seitz, A., Fultz, S., Ponce, A., Li, W., Carnes, C., & Klabunde, K. J. (2001). Nnocrystalline metal oxides as unique chemical reagents/sorbents. Chem.-Eur. J., 7, 2505-2510.

Luo, Y. B., Li, W. D., Wang, X. L., Xu, D. Y., & Wang, Y. Z. (2009). Preparation and properties of nanocomposites based on poly(lactic acid) and functionalized TiO_2. Acta. Mater., 57, 3182-3191.

Moniruzzaman, M., & Winey, K. I. (2006). Polymer nanocomposites containing carbon nanotubes. Macromolecules, 39, 5194-5205.

Oh, H., & Green, P. F. (2009). Polymer chain dynamics and glass transition in athermal polymer/nanoparticle mixtures. Nat. Mater., 8, 139-143.

Pan, H., & Qiu, Z. (2010). Biodegradable poly(L-lactide)/polyhedral oligomeric silsesquioxanes nanocomposites: enhanced crystallization, mechanical properties, and hydrolytic degradation. Macromolecules, 43, 1499–1506.

Parulekar, Y., Mohanty, A. K., & Imam, S. H. (2007). Biodegradable nanocomposites from toughed polyhydroxybutyrate and titanate-modified montmorillonite clay. J. Nano. Nanotech., 7, 3580-3589.

Paul, D. R., & Robeson, L. M. (2008). Polymer nanotechnology: nanocomposites. Polymer, 49, 3187-3204.

Paul, M. A., Delcourt, C., Alexandre, M., Degée, P., Monteverde, F., Rulmont, A., & Dubois P. (2005). (Plasticized) polylactide/(organo-)clay nanocomposites by in situ intercalative polymerization. Macromol. Chem. Phys., 206, 484–498.

Ramanathan, T., Abdala, A. A., Stankovich, S., Dikin, D. A., Herrera-Alonso, M., Piner, R. D., Adamson, D. H., Schniepp, H. C., Chen, X., Ruoff, R. S., Nguyen, S. T., Aksay, I. A., Prud'Homme, R. K., & Brinson L. C. (2008). Nature Nanotech., 3, 327–331.

Ray, S. S., & Okamoto, M. (2003). Polymer/layered silicate nanocomposites: a review from preparation to processing. Prog. Polym. Sci., 28, 1539-1641.

Ray, S. S., Maiti, P., Okamoto, M., Yamada, K., & Ueda, K. (2002). New polylactide/layered silicate nanocomposites. 1.preparation, characterization, and properties. Macromolecules, 35, 3104-3110.

Swain, S. K., & Jena, I. (2010). Polymer/carbon nanotube nanocomposites: a novel material. Asian J. Chem., 22, 1–15.

Utamapanya, S., Klabunde, K. J., & Schlup, J. R. (1991). Nanoscale metal oxide particles/clusters as chemical reagents. Synthesis and properties of ultrahigh surface area magnesium hydroxide and magnesium oxide. Chem. Mater., 3, 175-181.

Vaia, R. A., & Maguire, J. F. (2007). Polymer nanocomposites with prescribed morphology: going beyond nanoparticle-filled polymers. Chem. Mater., 19, 2736-2751.

Wang, B., Sun, X. S., Klabunde, K. J. (2009). Poly(lactic acid)/multi-hydroxyl magnesium oxide nanocomposites prepared by melt compounding. J. Biobased Mater. Bioenergy, 3, 130-138.

Wen, X., Lin, Y., Han, C., Zhang, K., Ran, X., Li, Y., & Dong, L. (2009). Thermomechanical and optical properties of biodegradable poly(L-lactide)/silica nanocomposites by melt compounding. J. Appl. Polym. Sci., 114, 3379–3388.

Xiang, C., Joo, Y. L., & Frey, M. W. (2009). Nanocomposite fibers electrospun from poly(lactic acid)/cellulose nanocrystals. J. Biobased Mater. Bioenergy, 3, 147–155.

Zhu, J. & Wilkie, C. A. (2009). Flammability properties of polymer nanocomposites. In Polymer Nanocomposites Handbook, Edited Gupta R. K., Kennel E., and Kim K. J., CRC Press, New York, pp. 438.

Zou, H., Wu, S., & Shen, J. (2008). Polymer/silica nanocomposites: preparation, characterization, properties, and applications. Chem. Rev., 108, 3893-3957.

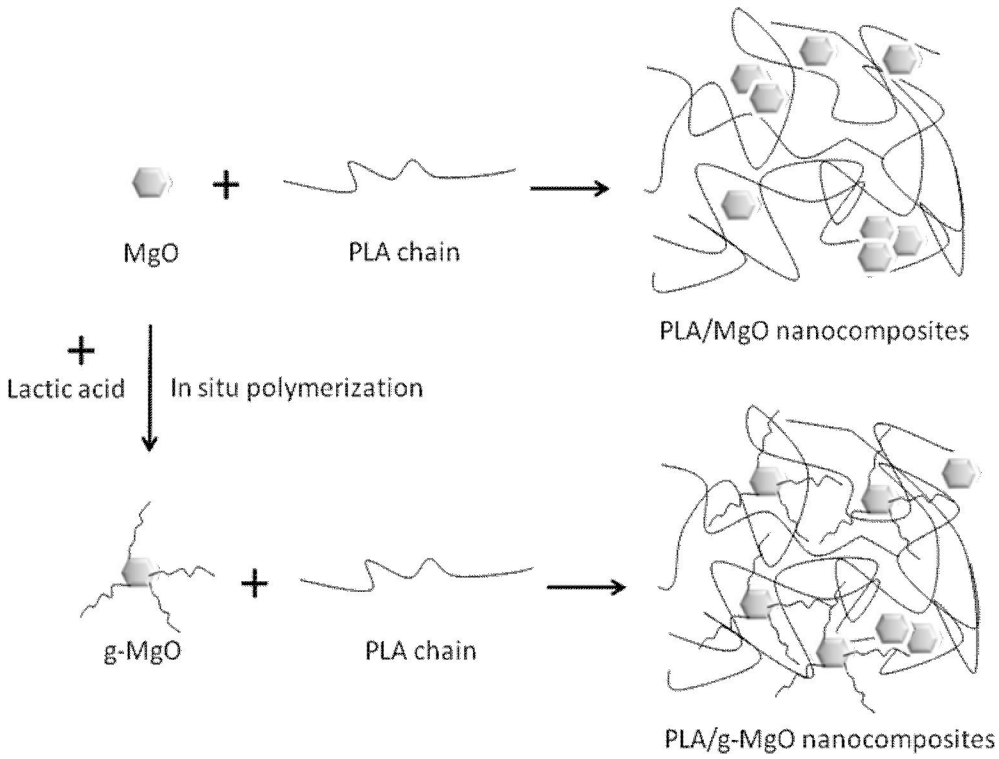

Figure 3.1 Schematic illustration of PLA/MgO and PLA/g-MgO nanocomposites.

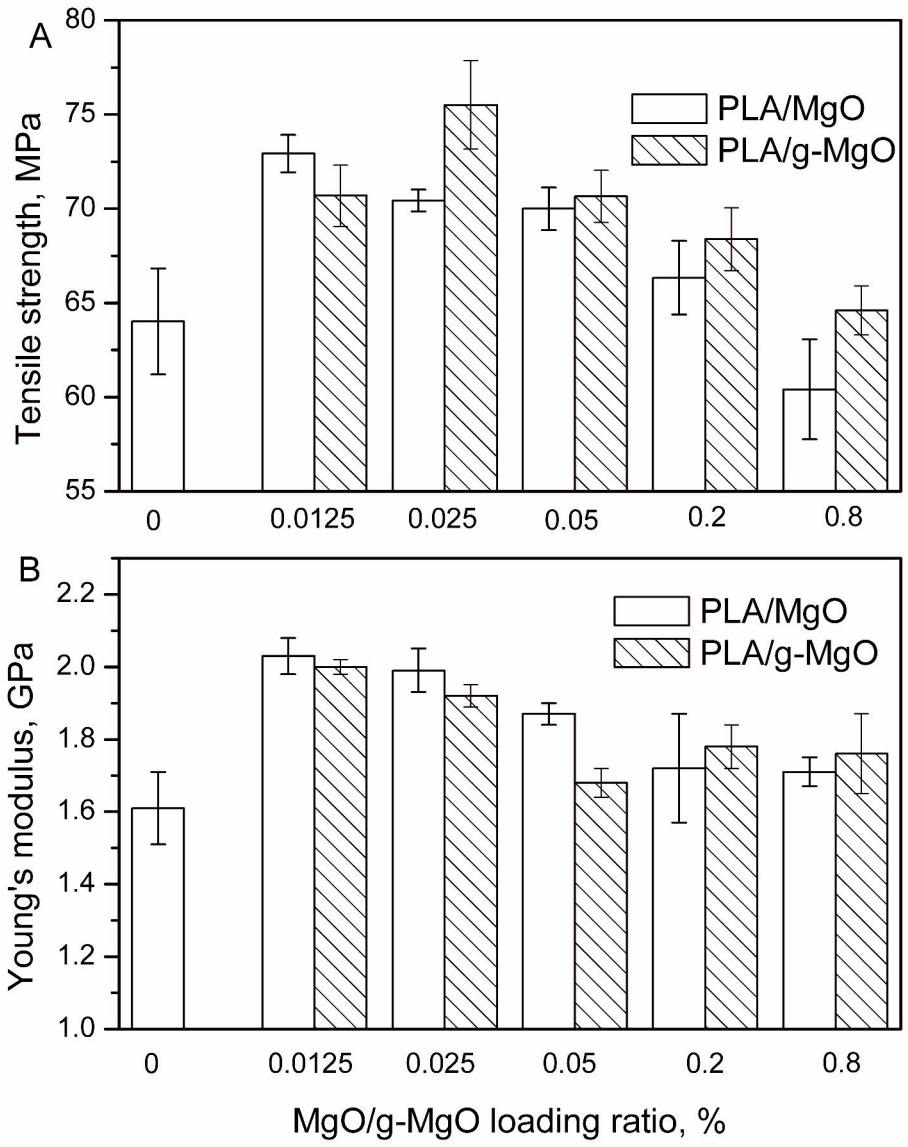

Figure 3.2 Tensile strength and Young's modulus of PLA/MgO and PLA/g-MgO nanocomposites.

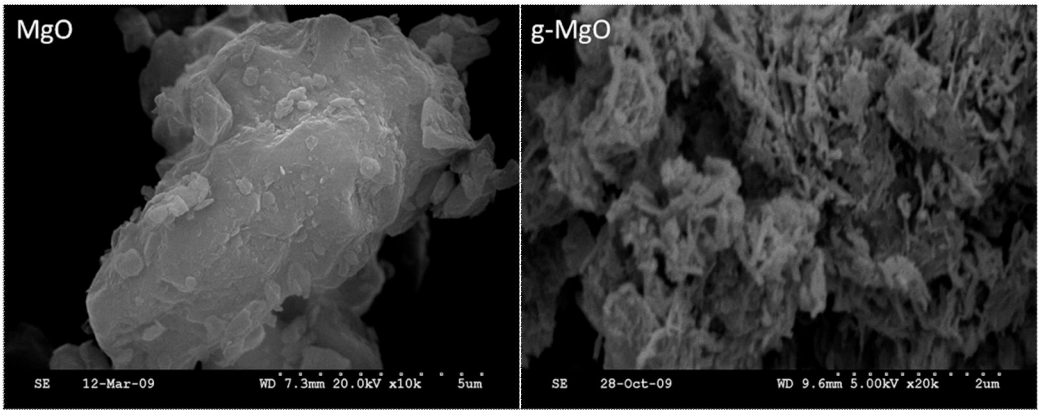

Figure 3.3 SEM images of MgO and g-MgO.

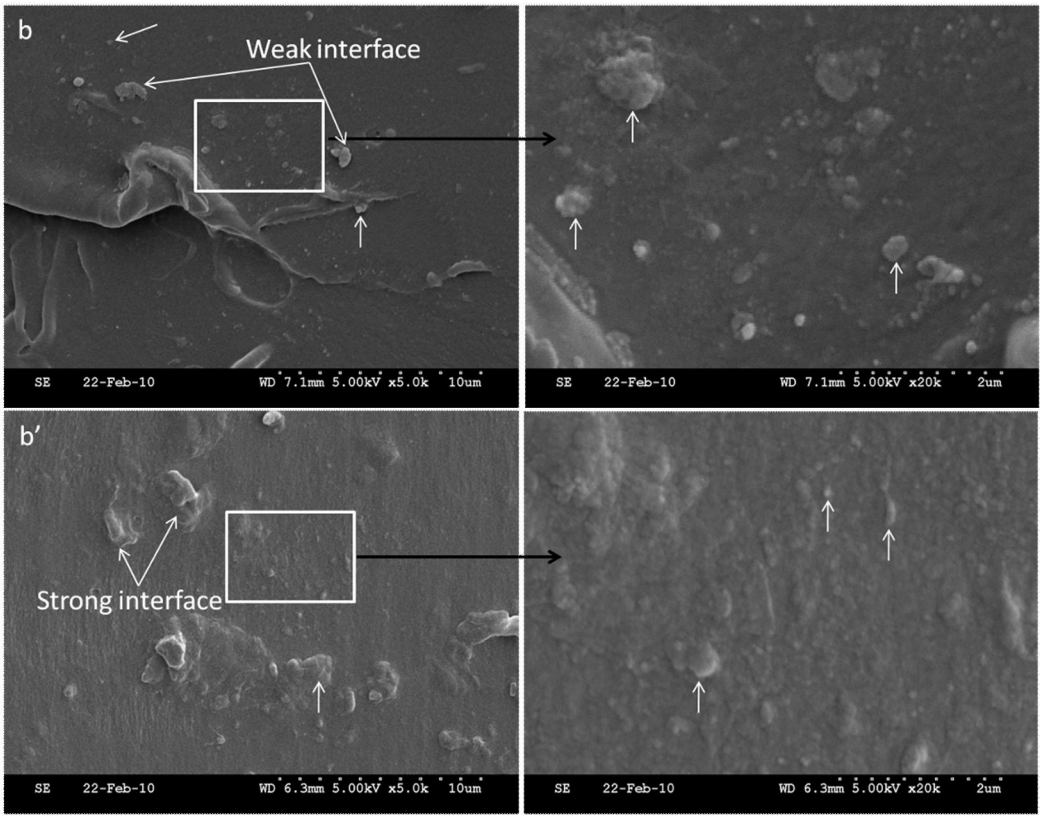

Figure 3.4 SEM images of PLA/MgO (top) and PLA/g-MgO (bottom) nanocomposites (nanoparticles are indicated with white arrows; right images are the squared section from left images with magnification).

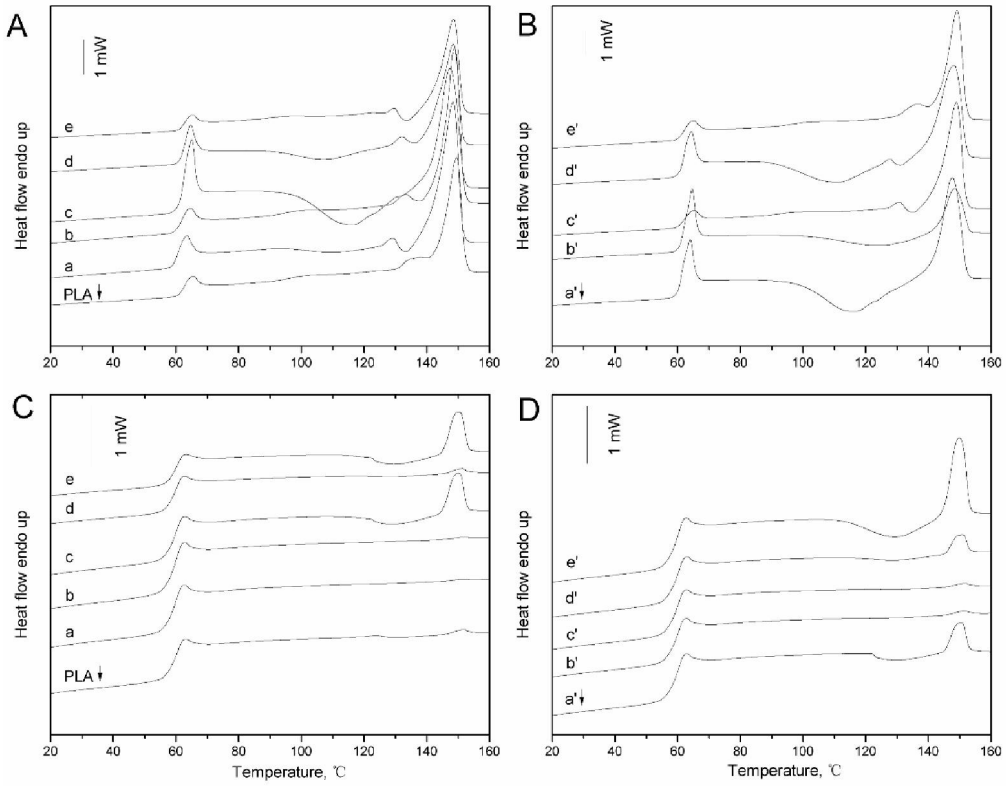

Figure 3.5 DSC thermograms of PLA/MgO (A, first scan; C, second scan) and PLA/g-MgO (B, first scan; D, second scan) nanocomposites with various nanoparticle loading levels (a/a', 0.0125%; b/b', 0.025%; c/c', 0.05%; d/d', 0.2%; e/e', 0.8%).

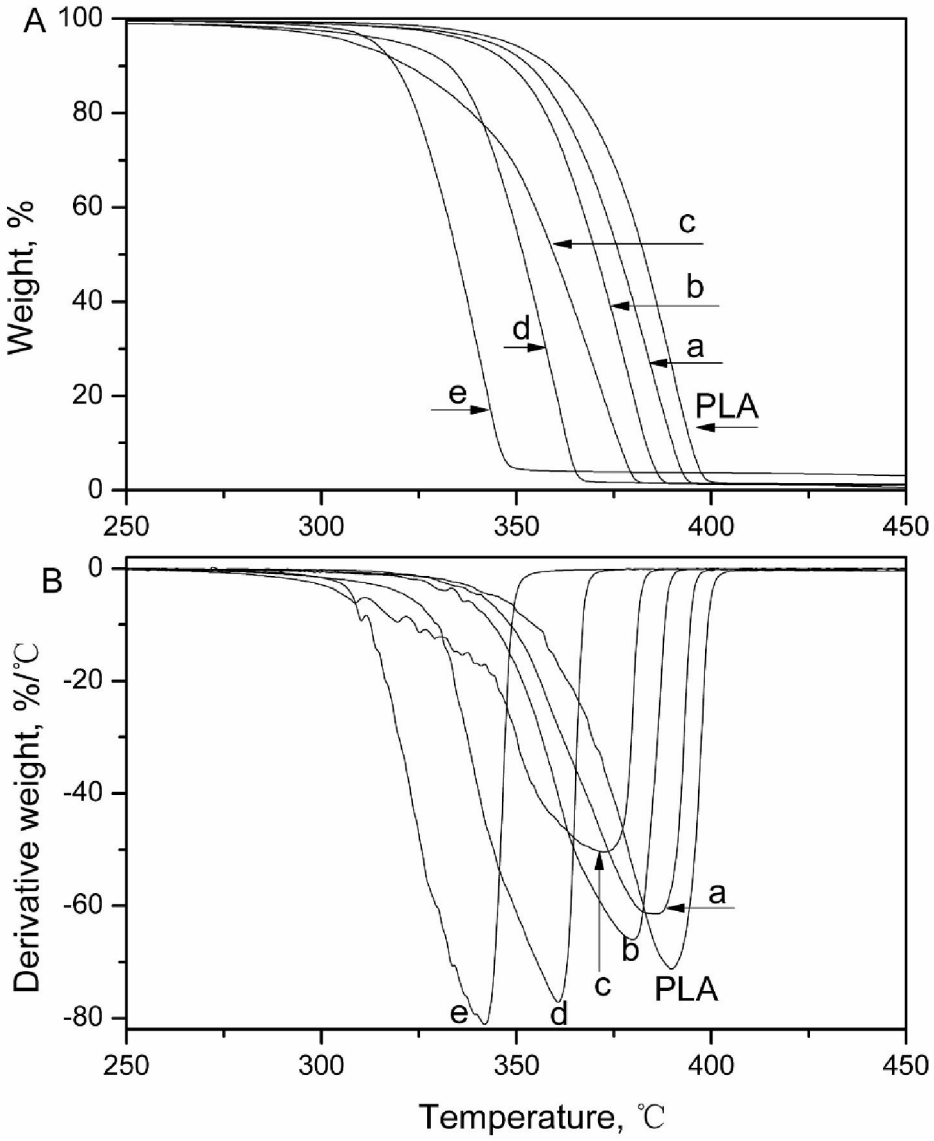

Figure 3.6 TGA (A) and derivative TGA (B) thermograms of PLA/MgO nanocomposites with various amounts of MgO (a, 0.0125%; b, 0.025%; c, 0.05%; d, 0.2%; e, 0.8%).

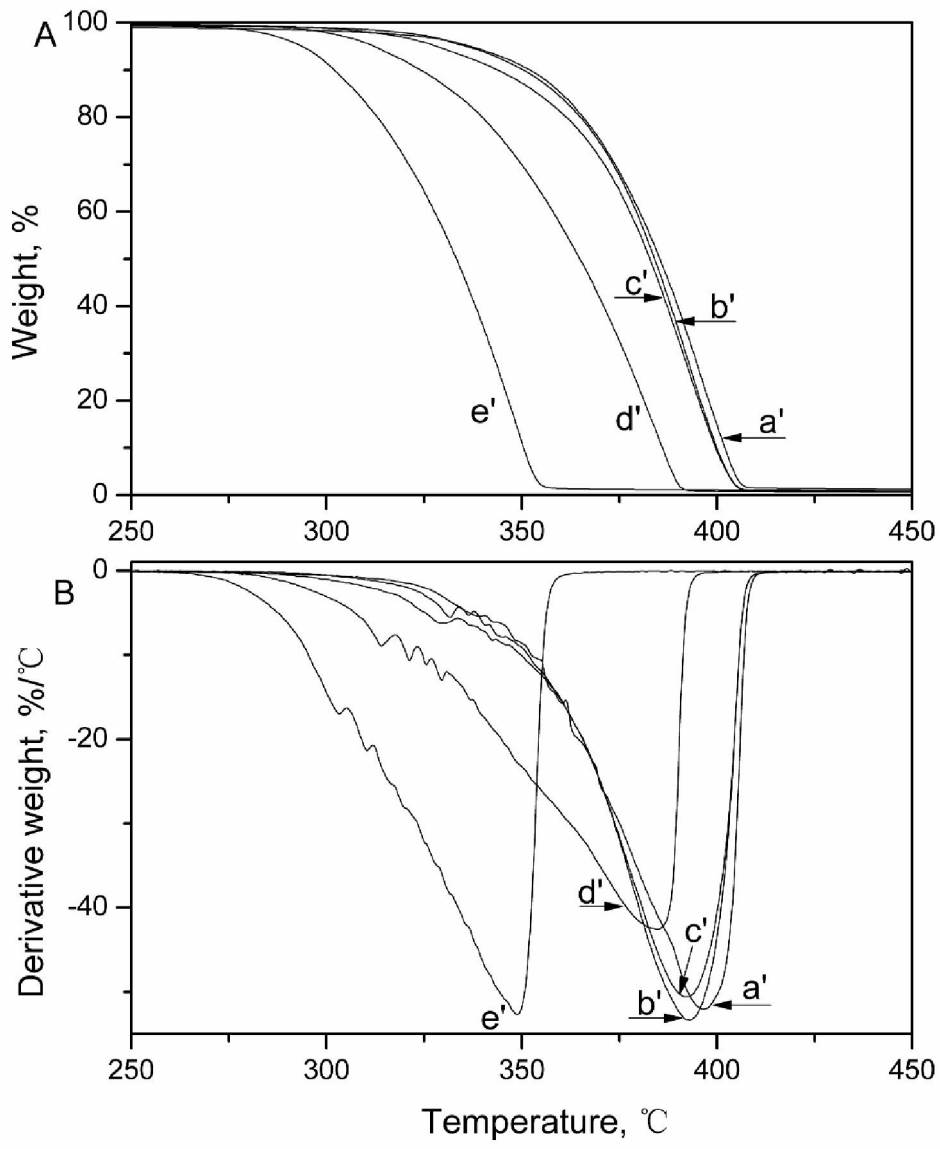

Figure 3.7 TGA (A) and derivative TGA (B) thermograms of PLA/g-MgO nanocomposites with various amounts of g-MgO (a, 0.0125%; b, 0.025%; c, 0.05%; d, 0.2%; e, 0.8%).

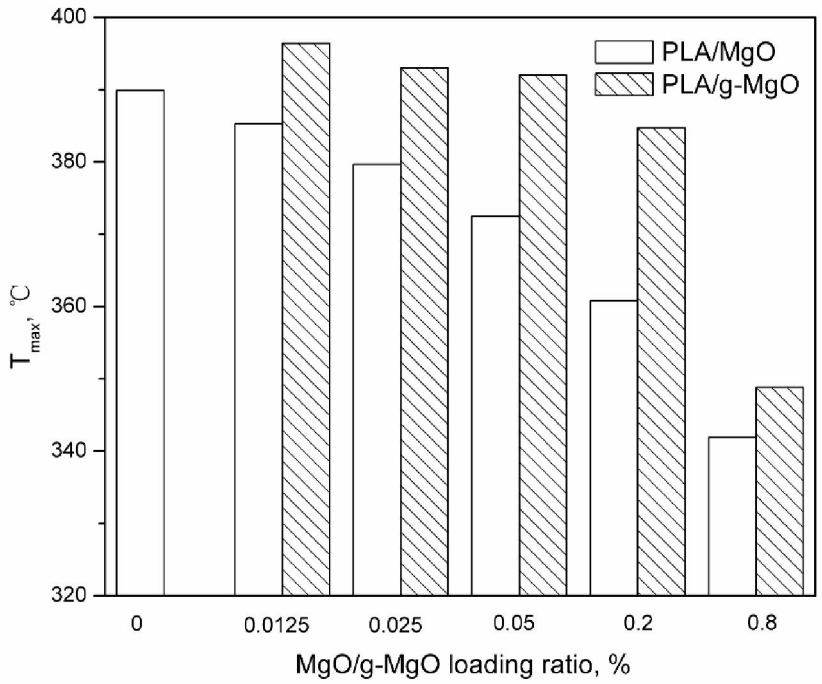

Figure 3.8 Temperatures of maximum decomposition rate (T_{max}) of PLA/MgO and PLA/g-MgO nanocomposites.

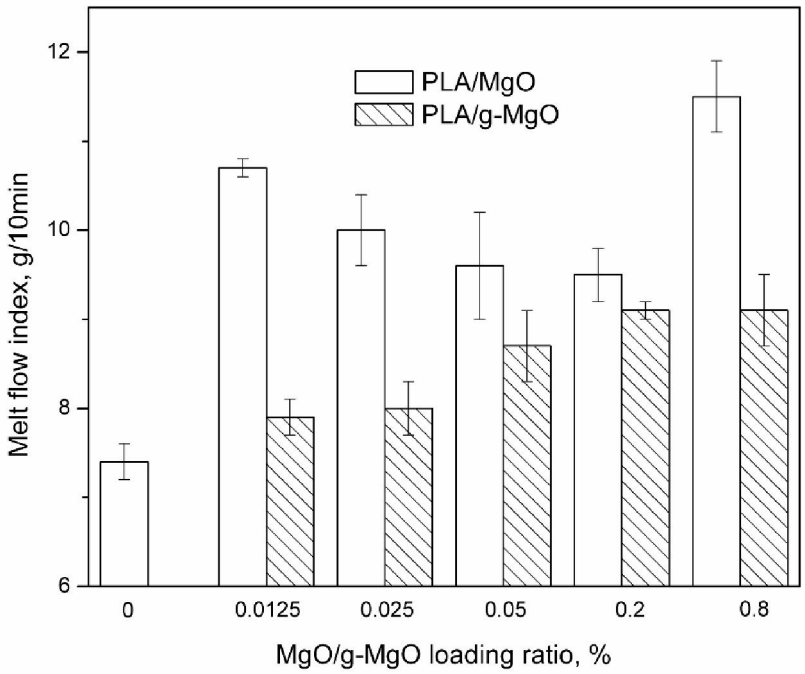

Figure 3.9 Melt flow index of PLA/MgO and PLA/g-MgO nanocomposites.

Table 3.1 DSC results of PLA/MgO and PLA/g-MgO nanocomposites with various nanoparticle loading levels

Sample	MgO/g-MgO ratio (wt%)	T_g ºC	ΔC_p J/(g·ºC)	T_m ºC	ΔH_m J/g	X_m %
PLA	0	59.4	0.53	149.4	22.2	23.7
PLA/MgO	0.0125	58.9	0.53	148.4	21.1	22.5
	0.025	59.0	0.54	148.9	19.7	21.0
	0.05	59.1	0.52	147.6	23.6	25.2
	0.2	59.1	0.53	148.4	21.7	23.2
	0.8	59.4	0.54	148.6	21.9	23.4
PLA/g-MgO	0.0125	59.3	0.52	147.6	21.7	23.2
	0.025	59.0	0.54	148.4	11.1	11.9
	0.05	59.2	0.53	149.0	23.8	25.4
	0.2	59.1	0.52	148.0	26.2	28.0
	0.8	59.1	0.52	149.2	16.6	17.7

Chapter 4 - Synthesis and Characterization of Bionanocomposites of Poly(lactic Acid) and TiO_2 Nanowires by *in situ* Polymerization[3]

4.1 Abstract

Bionanocomposites from biopolymers and inorganic nanoparticles are of great interest for packaging materials due to their enhanced physical, thermal, mechanical, and processing characteristics. In this study, poly(lactic acid) (PLA) nanocomposites with covalent bonding between TiO_2 nanowire surface and PLA chains were synthesized through *in situ* melt polycondensation. Molecular weight, structure, morphology, and thermal properties were characterized. Fourier transform infrared spectroscopy confirmed that PLA chains were covalently grafted onto TiO_2 nanowire surface. Transmission electron microscopy images also revealed clearly a third phase presence on the nanowires after the grafting process. Those grafted PLA chains exhibited significantly increased glass transition temperature and thermal stability, compared with pure PLA. The weight-average molecular weight of PLA/2% TiO_2 nanowire bulk nanocomposites increased by 66% compared with that of pure PLA. The electron microscopy results showed that strong interfacial interaction and homogeneous distribution were achieved between inorganic nanowires and organic PLA matrix in the bulk nanocomposites. The PLA matrix in bulk nanocomposites exhibited elevated glass transition temperature and decreased crystallization ability as the TiO_2 nanowire concentrations were increased from 0 to 2%.

---

[3] Results have been published. Li, Y., Chen, C., Li, J., & Sun, X. S. (2011). Synthesis and characterization of bionanocomposites of ploy(lactic acid) and TiO_2 nanowires by *in situ* polymerization. *Polymer*, doi: 10.1016/j.polymer.2011.03.050, in press. (Reuse by permission of Elsevier).

4.2 Introduction

Packaging has been one of the rapidly growing areas for the use of plastics. Out of total plastics production, 41% are used in packaging industry, and 47% are used for food packaging (Fomin & Guzeev, 2001), which are mainly short-term and single use items. The currently used plastics are mainly made from petroleum based polymers, of which the major concerns are their issues of being non-biodegradable and having non-renewable sources. Poly(lactic acid) (PLA), derived from renewable sugar based resources (starch, sugar cane, cellulose, etc.), has shown great potential as a biodegradable packaging plastic (Auras et al., 2004; Gupta & Kumar, 2007). However, the low glass transition/heat distortion temperatures around 60 ºC and slow biodegradation rate have severely limited its broad disposable applications (Benabdillah et al., 2001; Ray & Bousmina, 2005).

Inspired by Toyota researchers in the early 1990s who added 4.7% nano-clay into nylon 6 resulting in about 50% increase in the strength/modulus and 87 ºC increase in the heat distortion temperature (Kojima et al., 1993; Usuki et al., 1993), synthesizing polymer nanocomposites (PNCs) offers a new approach to enhancing the physical, thermal, and mechanical properties of pristine polymers (Crosby & Lee, 2007; Moczo & Pukanszky, 2008; Paul & Robeson, 2008; Zon et al., 2008). PLA nanocomposites have been reported using various nanoparticles, including carbon nanotubes, layered silicates or clays, silica, graphite, polyhedral oligomeric silsesquioxane, magnesium oxide, etc. (Gnanasekaran et al., 2009; Kim et al., 2010; Liao, 2007; Nakayama & Hayashi, 2007; Ray et al., 2003; Wang et al., 2009; Wu & Yan et al., 2007). Though those nanocomposites exhibited enhanced mechanical strength, very few nanoparticles could efficiently improve the glass transition temperature (T_g) and degradation rate of PLA (Tsuji et al., 2007; Wu & Liao, 2007) because of the lack of strong interfacial interactions between nanoparticles and PLA matrix and the lack of effective degradation promoters.

Because of the capability of absorbing UV light ($\lambda < 388$ nm) to generate oxygen species (Long et al., 2009; Zan et al., 2006a), TiO_2 nanoparticles have been applied to promote the photodegradation of various organic chemicals such as aldehyde, toluene, and benzene (Xu et al., 2010). Once TiO_2 nanoparticles are incorporated into polymer matrix,

these active oxygen species will lead to photodegradation reaction by attacking the interfacial polymer chains, forming carbon-centered radicals, and accelerating chain cleavage. Zan and co-workers incorporated TiO_2 nanoparticles into PE and PS, and they reported significant photodegradation of polymer matrix after UV irradiation for a period of time (Zan et al., 2006a; Zan et al., 2006b). Although biodegradation of PLA can be advanced in the ground with appropriate moisture and bacteria, it still requires a long period of time (Kumar et al., 2010; Shogren et al., 2003), and this biodegradation does not advance in the air. By adding photosensitive TiO_2 nanoparticles into biodegradable PLA, PLA nanocomposites can possess both photodegradability and biodegradability (Nakayama & Hayashi, 2007), and thus the degradation can be promoted under any conditions. Recent advances make it possible to synthesize considerable quantities of TiO_2 nanowires (Kobayashi et al., 2000; Li et al., 1999; Zhang et al., 2001). The extended nanoparticles (i.e., nanowires) can more easily form network structures through either direct interaction between the nanoparticles or chain bridging between the nanoparticles, which is believed to play a significant role in property enhancement (Knauert et al., 2007; Moczo & Pukanszky, 2008), compared with conventional nanospheres. Furthermore, large quantities of hydroxyl groups on the TiO_2 nanoparticle surface enable it to be functionalized with organic monomers or grafted with polymer chains (Al-Abadleh & Grassian, 2003; Hojjati et al., 2007; Khaled et al., 2007; Luo et al., 2009a&b; Lu et al., 2008).

The two challenges of synthesizing PNCs with targeted properties are the difficulties in achieving nanoscale homogeneous dispersion and strong interfacial interaction between nanoparticles and polymer matrix because nanoparticles typically agglomerate due to their hydrophilic nature and high surface area, and they are not miscible with hydrophobic polymer phase (Haque et al., 2007; Zou et al., 2008). In order to solve these problems, we first dispersed TiO_2 nanowires into hydrophilic lactic acid with the aid of ultrasonic treatment and mechanical stirring. Carboxylic acid was known to bond to TiO_2 with each of its oxygen atoms to a Ti^{IV} center of the surface in a bridging bidentate mode (Hojjati et al., 2007; Khaled et al., 2007; Rotzinger et al., 2004). Once the carboxyl group of lactic acid is covalently bonded to the surface of TiO_2 nanowires, the remaining hydroxyl group can form ester bonds

with another lactic acid. The polymer chains continue growing on the nanowire surface with removal of resultant water during condensation polymerization (as illustrated in Figure 4.1). Using the similar approach, we previously grafted PLA chains onto hydroxylated MgO nanocrystals and synthesized PLA/MgO bulk nanocomposites with satisfied interfacial interaction and nanoscale dispersion of nanocrystals into PLA matrix (Li & Sun, 2010). The specific objectives of this study are to (1) synthesize photocatalytic TiO_2 nanowires and characterize the properties; (2) synthesize PLA/TiO_2 nanowire nanocomposites via *in situ* melt polycondensation from lactic acid with different TiO_2 nanowire loadings; (3) characterize the properties of PLA-grafted TiO_2 (PLA-g-TiO_2) nanowires isolated from free PLA in the PLA/2%TiO_2 nanowire bulk nanocomposites to confirm the surface polymerization; and (4) characterize the molecular weight, structure, morphology, and thermal properties of the bulk nanocomposites.

4.3 Experimental Section

4.3.1 Materials

L-lactic acid was supplied as a 90 wt% aqueous solution by Acros Organics. Sodium hydroxide (NaOH) and hydrochloric acid (HCl) was purchased from Fisher Scientific. Absolute ethanol was obtained from Decon Laboratories. Titanium dioxide (TiO_2) nanopowders (< 100nm, mixture of rutile and anatase TiO_2), Tin (II) chloride dihydrate ($SnCl_2 \cdot H_2O$) (98%, reagent grade), and *p*-toluenesulfonic acid monohydrate (TSA) (98.5+%, ACS reagent grade) were purchased from Sigma-Aldrich Co. All materials were used as received.

4.3.2 TiO_2 Nanowires Synthesis and Characterization

Several ways have been indicated in the literatures to synthesize TiO_2 nanowires (Li et al., 1999; Kobayashi et al., 2000; Zhang et al., 2001). We followed a simple chemical approach described by Zhang et al. (2002). For a typical preparation, 0.1 g TiO_2 nanopowders were placed into a Teflon-lined autoclave of 50 ml capacity. It was then filled with 40 ml 10 M NaOH aqueous solution, sealed into a stainless steel tank and maintained at 200 ºC for 24

h without stirring. After cooling down, the sample was washed with 1 M aqueous HCl solution, deionized water, and absolute ethanol several times and dried at 80 ºC for 12 h. Finally, we obtained soft fibrous TiO_2 nanowires with white color. The Brunauer-Emmett-Teller (BET) surface area and porosity structure were determined with a Micromeritics instrument (TriStar-3000). The nitrogen adsorption isotherms were obtained at 77 K. The X-ray diffraction (XRD) patterns were recorded on a Shimadzu XRD-6000 instrument, using Cu-Kα radiation set at a voltage of 40 kV and a current of 40 mA. The scans ranged from 10 to 90°, with a scanning rate of 6°/min. The optical absorption of the synthesized TiO_2 nanowires was measured on a UV-vis spectrophotometer (U-3010, Hitachi, Japan).

4.3.3 Dehydration/Oligomerization

Our preliminary results showed that the addition of TiO_2 nanowires should be less than 2 wt% to achieve homogeneous dispersion in the LA monomer. A determined amount of TiO_2 nanowires (0.25, 0.5, 1, and 2 wt%, based on the weight of pure lactic acid) were added gradually to 30 g of a 90 wt% aqueous solution of LA and ultrasonically treated for 30 min. The mixture was then transferred into a 100-ml three-neck flask equipped with a mechanical stirrer and a reflux condenser that was connected with a vacuum system through a liquid nitrogen cold trap. The mixture was first dehydrated at 110 °C under atmospheric pressure for 2 h, then at 130 °C under a reduced pressure of 100 torr for 3 h, and finally at 150 °C under a reduced pressure of 10 torr for another 4 h. Then a viscous oligomer with TiO_2 nanowires was obtained. Oligomer without TiO_2 nanowires was also prepared as a control following the same procedures. The oligomer yield (weight of oligomer divided by the weight of pure lactic acid and TiO_2 nanowires) resulting from this step was about 72% on average.

4.3.4 Polymerization

After cooling down, the oligomer from the previous step was mixed with $SnCl_2 \cdot H_2O$ (0.4% wt relative to oligomer) and TSA (an equimolar ratio to $SnCl_2 \cdot H_2O$) as a binary catalyst (Moon et al., 2000). The mixture was gradually heated to 180 °C with stirring speed of 200 rpm. The pressure was reduced gradually to 10 torr in 1.5 h. Then the reaction was continued at 180 °C/10 torr for 10 h with stirring speed of 150 rpm. At the end of the

reaction, the flask was cooled, and the product was dissolved in chloroform and subsequently precipitated into methanol. The resulting solid was washed with methanol three times and dried under vacuum at 80 ℃ for 24 h. Bulk nanocomposites were labeled according to the concentrations of TiO_2 nanowires as PLA/0.25%TiO_2, PLA/0.5%TiO_2, PLA/1%TiO_2, and PLA/2%TiO_2. Pure PLA without TiO_2 nanowires was prepared following the same procedures and used as a control.

4.3.5 Isolation of PLA-g-TiO_2 Nanowires

The bulk nanocomposite is a mixture of free PLA and PLA grafted TiO_2 (PLA-g-TiO_2) nanowires (Figure 4.1). For characterization purposes, a repeated dispersion/centrifugation process was used to separate some PLA-g-TiO_2 nanowires from free PLA in the bulk nanocomposite. Briefly, a portion of chloroform dispersed PLA/2%TiO_2 nanowire bulk nanocomposite resulting from the previous step before precipitation into methanol was centrifugated at 8500 rpm for 30 min. The supernatant solution was precipitated into methanol to obtain free PLA. For the precipitant of PLA-g-TiO_2 nanowires, the dispersion/centrifugation operation was performed repeatedly five times to ensure physically absorbed free polymers were completely removed. The PLA-g-TiO_2 nanowires and free PLA were dried in a vacuum oven at 80 ℃ for 24 h to remove residual solvent and stored for future characterization.

4.3.6 Gel Permeation Chromatography (GPC) Analysis

The weight- (M_w) and number-average molecular (M_n) weight as well as the molecular weight distribution (PDI, equals to M_w/M_n) were determined through GPC (Waters 2695 Separation Module). Samples were dissolved in chloroform. Because of the larger size of some TiO_2 nanowires, all the solutions were filtered with 0.45 μm teflon filters before conducting GPC measurements. Measurement was performed at room temperature and a flow rate of 2 ml/min. The molecular weight was calibrated according to polystyrene standard.

4.3.7 Fourier-transform Infrared (FTIR) Spectroscopy

FTIR spectra were acquired with a PerkinElmer Spectrum 400 FT-IR/FT-NIR Spectrometer (Waltham, MA). Spectra were collected in the region of 4000 to 800 cm^{-1} with a spectral resolution of 4 cm^{-1} and 32 scans co-added.

4.3.8 Scanning Electron Microscopy (SEM) and Transmission Electron Microscopy (TEM) Analysis

SEM (Hitachi S-3500N, Hitachi Science Systems, Ltd., Japan) and TEM (H-7100, Hitachi Co.) were used to study the morphology of the samples. For SEM, the samples were glued to aluminum specimen mounts, and the surface was coated with a mixture of 60% gold particles and 40% palladium with a sputter coater (Desk II Sputter/ Etch Unit, NJ) before observation. For TEM, fine powders of each sample were absorbed onto Formvar/Carbon-coated 200-mesh copper grids (Electron Microscopy Sciences, Fort Washington, PA, USA) and observed without staining.

4.3.9 Differential Scanning Calorimetry (DSC) Analysis

Thermal transitions were measured with a TA DSC Q200 instrument. About 5 mg of dried sample was sealed in a standard aluminum pan. An empty sealed pan was used as a reference. The sample was heated from 0 °C to 190 °C at a rate of 10 °C/min, isothermally conditioned at 190 °C for 3 min, quenched to 0 °C, isothermally conditioned at 0 °C for 3 min, and then heated again to 190 °C at the same rate. The sample was characterized in an inert environment by using nitrogen with a gas flow rate of 50 ml/min. Results were obtained from the second DSC heating scan except when otherwise specified. Heat capacity (ΔC_p), T_g, cold crystallization temperature (T_c), melting temperature (T_m), heat of melting (ΔH_m), and heat of crystallization (ΔH_c) were determined from the DSC thermograms. The T_g was determined from the half width midpoint in the step change between the onset and the end temperatures of the transition. Crystallinity (X_m) was estimated according to the following equation:

$$X_m(\%) = \frac{\Delta H_m}{\Delta H_0 \times X_{PLA}} \times 100 \qquad (1)$$

where ΔH_m and ΔH_0 are heats (J/g) of melting of PLA nanocomposites and of PLA crystals of infinite size with a value of 93.6 J/g (Fischer et al., 1973), respectively, and X_{PLA} is the PLA fraction in the bulk nanocomposites.

4.3.10 Thermogravimetric Analysis (TGA)

Decomposition characteristics of the samples were determined with a PerkinElmer Pyris1 TGA (Norwalk, CT). About 5 mg of each sample was placed in the pan and heated from 40 °C to 700 °C at a heating rate of 20 °C/min under a nitrogen or air atmosphere.

4.4 Results and Discussion

4.4.1 Synthesized TiO_2 Nanowires

BET surface analysis gave a specific surface area of ~26.6 m^2/g, average pore size of 12.1 nm, and pore volume of 0.081 cm^3/g. Powder X-ray diffraction indicated that the TiO_2 nanowires were dominated by anatase crystal structure. The UV-vis spectrum indicated that the TiO_2 nanowires had a strong UV absorption ability with absorption peak at 294 nm (Figure 4.2). The threshold of UV absorption is ~380 nm, with the energy slightly higher than the bandgap of bulk anatase TiO_2 crystals (~388 nm or 3.2 eV).

4.4.2 Molecular Weight

Molecular weight and PDI of PLA and PLA/TiO_2 nanowire bulk nanocomposites are listed in Table 4.1. The M_w and M_n of pure PLA were 63,000 and 33,500, respectively, with PDI of 1.9. The M_n of bulk nanocomposites with 0.25% TiO_2 nanowires was increased by 12% compared with pure PLA, with a broader PDI of 2.2. Similar molecular weight values to pure PLA were obtained for bulk nanocomposites with 0.5 and 1% TiO_2 nanowires. PLA/2%TiO_2 bulk nanocomposites showed significantly increased molecular weight, with M_w and M_n increased by 66 and 65%, respectively, compared with those of pure PLA. A similar increment of molecular weight was obtained for free PLA, which was isolated from PLA/2%TiO_2 bulk nanocomposites. As observed under TEM (not shown), quite a lot TiO_2 nanowires were noticed in free PLA, indicating that some TiO_2 nanowires were dispersed into chloroform during the centrifugation process. The increase of molecular weight might be

explained by two reasons. First, although the nanocomposite solution was filtered with 0.45 μm teflon filter before GPC measurement, some nanowires could still pass the filter due to the significantly decreased size, as will be discussed in the morphology section, contributing to the higher molecular hydrodynamic volume. Second, the grafted PLA chains on the nanowire surface formed polymer brushes (Figure 4.1), which also resulted in increased molecular weight.

4.4.3 FTIR

The FTIR spectra of PLA, pristine TiO_2 nanowires, PLA-g-TiO_2 nanowires, and PLA/2% TiO_2 nanowire bulk nanocomposites before isolating are presented in Figure 4.3. Pristine TiO_2 nanowires showed bands around 3200 and 1640 cm^{-1}, corresponding to the stretching and bending vibrations of hydroxyl groups on the TiO_2 nanowire surface. The strong absorption band between 1000 and 400 cm^{-1} were attributed to the Ti-O and Ti-O-Ti vibrations (Bezrodna et al., 2003). PLA showed strong C=O stretching band at 1758 cm^{-1}, and C-O stretching band at 1182, 1128, and 1090 cm^{-1}. The asymmetric and symmetric stretching bands of C-H from CH_3 groups of the side chains were observed at 2996 and 2878 cm^{-1}, whereas their bending vibration was observed at 1455 cm^{-1}. The band at 2946 cm^{-1} was attributed to the stretching of C-H groups in the main chain of PLA, and its bending vibrations appeared at 1384 and 1358 cm^{-1} (Li & Sun, 2010). After surface grafting of TiO_2 nanowires, the bands at 1756, 1184, 1130, 1090 cm^{-1} were caused by the vibrations of C=O and C-O groups from grafted PLA chains. Besides, new bands appeared at 1554 and 1421 cm^{-1} due to the bidentate coordination between Ti atoms and the carboxylic groups of lactic acid (Khaled et al., 2007; Luo et al., 2009a&b). FTIR results indicated that PLA chains were successfully grafted onto TiO_2 nanowire surface. PLA/TiO_2 nanowire bulk nanocomposites showed similar spectra as pure PLA, and the typical spectrum of nanocomposites containing 2% TiO_2 nanowires was presented in Figure 4.3. We did not observe the Ti-O band for the bulk nanocomposites because of the relatively low concentrations of TiO_2 nanowires.

4.4.4 Morphology

Figure 4.4 illustrated the SEM micrographs of pristine TiO_2 nanowires and PLA-g-TiO_2 nanowires. The pristine nanowires exhibited quite clean surface. The diameter was ~50-200 nm and length from a few micrometers to ~20 micrometers (Figure 4.4A), which is consistent with the literature (Zhang et al., 2002). The pristine nanowires were aggregated but were still discernible as single wires at higher magnification. Such nanowires were easily dispersed into lactic acid monomer homogeneously at the beginning of polymerization. Appreciable differences in morphology and size were observed between PLA-g-TiO_2 nanowires and pristine TiO_2 nanowires (Figure 4.4B). In contrast to the pristine TiO_2 nanowires, PLA-g-TiO_2 nanowires seemed much thicker, but still kept the wire-like structure. The length of PLA-g-TiO_2 nanowires was also reduced significantly, compared with pristine nanowires. The nanowires are fragile, and they were broken down during the polymerization processes. Decreased length of TiO_2 nanofibers was also reported by Khaled et al. (2007) when polymerizing methyl methacrylate monomers onto the surface of TiO_2 nanofibers in synthesizing poly(methyl methacrylate)/TiO_2 nanocomposites.

As an additional evidence for the existence of PLA chains on nanowire surface, analysis of TEM was conducted and the typical results are shown in Figure 4.5. Similar to SEM, significant reduction of size was also noticed for PLA-g-TiO_2 nanowires under TEM, compared with that of pristine TiO_2 nanowires (Figure 4.5A and B). The individual TiO_2 nanowires before and after surface grafting were clearly observed at higher magnification (Figure 4.5A' and B'). The surface of pristine TiO_2 nanowires seemed to be smooth and clear without any extra phase adhering to them (Figure 4.5A'). In contrast, the PLA-g-TiO_2 nanowires shown in Figure 4.5B' appeared stained with extra phase (dark area on the nanowire surface) that is presumed to come from grafted PLA molecules.

The SEM micrographs of PLA and bulk nanocomposites are presented in Figure 4.6. The surface of pure PLA was quite flat and smooth (Figure 4.6a). As the concentration of TiO_2 nanowires increased, much more coarse and uneven surfaces were observed for the bulk nanocomposites (Figure 4.6b-e). The nanowires were not discernible from the surface morphology by SEM imaging. We did not observe any phase separation in the bulk

nanocomposites. In general, chemical grafting of polymer chains that are compatible with the polymer matrix on the inorganic nanoparticles provides strong interfacial interaction between the inorganic and the organic phases (Hong et al., 2005).

TEM is a powerful tool for studying the dispersion of nanoparticles embedded within a polymer matrix. The typical TEM micrographs of PLA and bulk nanocomposites are shown in Figure 4.7. No nanowire aggregation was observed in the polymer matrix. The individual nanowires appeared to be distributed homogeneously throughout the polymer matrix (Figure 4.7c/c'). At higher magnification, we observed that the nanowire surface was covered with a third phase due to the presence of PLA (inserted image of Figure 4.7c'). TEM images indicated that the distinct phase on TiO_2 nanowire surfaces prevented the hydrophilic aggregation of pristine nanowires and resulted in a better dispersion of nanowires. The surface grafting could also improve the hydrophobic entanglements of grafted PLA chains with surrounding free PLA matrix.

4.4.5 Thermal Properties

DSC thermograms showing the T_g of pure PLA and PLA-g-TiO_2 nanowires are presented in Figure 4.8. The T_g was determined from the half width midpoint between the onset and the end temperatures of the transition, as indicated by the dash lines in the thermograms. About a 7 ºC increment of T_g was observed for those PLA chains grafted onto TiO_2 nanowire surface compared with pure PLA, as obtained from the first DSC heating scan (Figure 4.8A). After erasing the thermal history, although the T_g of both PLA and PLA-g-TiO_2 nanowires decreased due to the loss of the chain conformational ordering, T_g of the latter was still 6 ºC higher (Figure 4.8B). The very small heat capacity change at the glass transition for PLA-g-TiO_2 nanowires was probably because of the low PLA ratios (~ 30%) in the sample and relatively short grafted PLA chains. The increased T_g sustained the evidence that strong bonding exited between the grafted PLA chains and TiO_2 nanowires, which led to permanent attachment of PLA chain segments onto the TiO_2 nanowire surface. The increased T_g was caused by the restrictions on the mobility of chains in the vicinity of the surface (Oh & Green, 2009). The reduction of chain mobility was possibly caused by crowding and/or local ordering of chains at the interface as well as loss of configurational entropy of the PLA

segments near the nanowire surface (Tsagaropoulos & Eisenberg, 1995). Molecular dynamics simulations also showed that the relaxations of chain segments in the immediate vicinity of the nanoparticles were slower (Starr et al., 2002).

Figure 4.9 shows the DSC thermograms of PLA/TiO_2 nanowire bulk nanocomposites, and quantified results are summarized in Table 4.2. All the thermograms were obtained from the second DSC heating scan after erasing the thermal history, and they exhibited three thermal transitions, i.e., glass transition, cold crystallization, and melting of PLA. Pure PLA showed a T_g of 54.7 ºC, while the bulk nanocomposites exhibited elevated T_g as the TiO_2 nanowire concentrations were increased from 0 to 2%. Maximum T_g was obtained for PLA/2%TiO_2 nanowire bulk nanocomposites, which was 4 ºC higher than that of pure PLA. As discussed before, the permanent graft of PLA chains onto the nanowire surface leads to restricted mobility of chain segments; therefore, T_g increased. With higher concentrations of nanowires in bulk nanocomposites, more grafted chain segments onto nanowire surface were expected, leading to larger T_g.

The T_c and T_m of pure PLA was 110 and 153/160 ºC, respectively, with crystallinity of 47%. Decreased crystallinity was observed for all the bulk nanocomposites with TiO_2 nanowires. Bulk nanocomposites with 0.5 and 2% nanowires exhibited lowest crystallinity. More than a 10 ºC increment of T_c was observed for these two bulk nanocomposites, implying their lowest crystallization ability. These phenomena were probably caused by the reduction of the diffusion of the PLA chains to the growing crystalline lamella and disruption of the regularity of the chain structures in PLA in the presence of TiO_2 nanowires. The incontinuous decrease of crystallinity with increasing nanowire loadings might be related with an inhomogeneous dispersion of TiO_2 nanowires in samples with the lowest crystallinity, and improved nanowire dispersion for the other ones. PLA and bulk nanocomposites with less than 1% TiO_2 nanowires exhibited double melting behaviors, which were caused by the separate melting of the PLA crystals with low structural perfection and normal PLA crystals and the melting-recrystallization to the higher perfection-remelting process of PLA crystals (Li et al., 2010; Yasuniwa et al., 2004). Decreased T_m was obtained for bulk nanocomposites with increased concentration of TiO_2 nanowires. Double melting

peaks merged into one single peak at 149 ºC for PLA/2%TiO_2 nanowire bulk nanocomposites, indicating the difficulties in forming PLA crystals with higher perfection at high concentration of nanowires, which might be caused be the presence of more grafted PLA chains.

The TGA thermograms of intensively dried PLA, pristine TiO_2 nanowires, and PLA-g-TiO_2 nanowires are presented in Figure 4.10. These thermograms were obtained under air atmosphere to quantitatively estimate the grafting ratio of organic PLA chains on the TiO_2 nanowire surface. The weight loss of TiO_2 nanowires and PLA-g-TiO_2 nanowires were 9 and 40% respectively, after achieving the thermogram plateaus during heating. Based on the differences of weight loss between TiO_2 nanowires before and after surface grafting, more than 30% PLA in weight were certainly grafted onto nanowire surface. The grafted PLA chains exhibited two-stage thermal decomposition behaviors. The first decomposition occurred at the peak temperature of 308 ºC, which was related to the polymer chains far away from the nanowire surfaces. The first decomposition temperature was slightly higher than that of pure PLA (300 ºC). The second decomposition occurred at the peak temperature of 560 ºC, which was probably caused by the polymer chains in the vicinity of the nanowires. Similar increments of thermal decomposition temperatures were also reported for *in situ* polymerized poly(3-hexylthiophene) grafted TiO_2 nanotube nanocomposite and polystyrene grafted TiO_2 nanocomposite (Dzunuzovic et al., 2009; Lu & Yang, 2009). The dramatically increased thermal decomposition temperature of those grafted PLA chains was probably caused by its different structure once covalently bonded to nanowire surface and restricted thermal motion of the chains in the gallery (Blumstein, 1965).

The thermal stability of PLA and bulk nanocomposites with TiO_2 nanowires was studied via TGA under an inert nitrogen atmosphere. The TGA thermograms are shown in Figure 4.11, and the decomposition data are summarized in Table 4.3. Pure PLA exhibited a peak decomposition temperature (T_{max}) of 297 ºC and onset (T_{onset}) and end (T_{end}) decomposition temperatures of 276 and 308 ºC. Broader decomposition ranges (T_{end} - T_{onset}) were observed for all the bulk nanocomposites, due to their more complex structures (i.e., free PLA chains, grafted chains in the vicinity of nanowire surfaces, grafted chains far away

from nanowire surfaces, chains entangled with nanowires, etc.) compared with pure PLA (Figure 4.1). Decreased T_{onset} was obtained for bulk nanocomposites with less than 1% TiO_2 nanowires, which might be caused by the accelerated decomposition of PLA chains with the aid of extra hydroxyl groups from TiO_2 nanowires (Wang et al., 2009). PLA/2%TiO_2 nanowire bulk nanocomposites showed highest T_{max} and T_{end} among pure PLA and other bulk nanocomposites. This might be explained by the fact that more grafted PLA chains resulting from higher concentrations of nanowires played a dominant role in enhancing the thermal stability, while the catalytic effect from extra hydroxyl groups played a subordinate role. Moreover, the high concentration of TiO_2 nanowires could act as a superior insulator and mass transport barrier to the volatile products generated during decomposition (Ray & Okamoto, 2003). Significantly increased thermal decomposition temperatures were also reported for PLA/multi-walled carbon nanotube nanocomposites (MWNTs) at higher concentrations of MWNTs (Wu & Liao, 2007).

4.5 Conclusions

Bionanocomposites with covalent bonding between TiO_2 nanowire surface and PLA chains were synthesized through *in situ* melt polycondensation. The covalent grafting of PLA chains onto the nanowire surfaces was confirmed by FTIR spectroscopy and TGA. TEM micrographs and DSC results also sustained the presence of the third phase on the nanowire surfaces. Those PLA on the nanowire surfaces exhibited significantly increased T_g and thermal stability, compared with pure PLA. TGA results also showed that more than 30% of PLA in weight were certainly grafted onto the nanowire surfaces. Increased molecular weight was obtained for PLA/2%TiO_2 nanowire bulk nanocomposites, of which the M_w was 66% higher than that of pure PLA. TEM micrographs indicated that homogeneous dispersion of TiO_2 nanowires in the PLA matrix was achieved. The T_g of bulk nanocomposites increased, whereas the crystallization ability decreased, as the nanowire concentrations increased from 0 to 2%.

4.6 Acknowledgments

The authors gratefully acknowledge the following individuals for their contributions: Dr. Krystyna Brzezinska of Materials Research Laboratory of UCSB for performing GPC measurements, Dr. Donghai Wang of Department of Biological and Agricultural Engineering for allowance of using FTIR, Mr. Kent Hampton of Department of Entomology for performing SEM analysis, and Dr. Dan Boyle of Department of Biology for performing TEM analysis. Contribution No. 11-153-J from the Kansas Agricultural Experiment Station.

4.7 References

Al-Abadleh, H. A., & Grassian, V. H. (2003). Oxide surfaces as environmental interfaces. Surf. Sci. Rep., 52, 63-161.

Auras, R., Harte, B., & Selke, S. (2004). An overview of polylactides as packaging materials. Macromol. Biosci., 4, 835-864.

Benabdillah, K. M., Boustta M., Coudane J., &Vert M. (2001). Chap. 14 Can the Glass Transition Temperature of PLA Polymers Be Increased? In Polymers from Renewable Resources: Biopolyesters and Biocatalysis, ed. by Carmen Scholz, Richard A. Gross, ACS publication, pp 200-220.

Bezrodna, T., Puchkovska, G., Shimanovska, V., Chashechnikova, I., Khalyavka, T., & Baran, J. (2003). Pyridine−TiO2 surface interaction as a probe for surface active centers analysis. Appl. Surf. Sci., 214, 222-231.

Blumstein, A. (1965). Polymerization of adsorbed monolayers: II. thermal degradation of the inserted polymers. J. Polym. Sci., A 3, 2665-2673.

Crosbya, A. J., & Lee, J. Y. (2007). Polymer nanocomposites: the “nano” effect on mechanical properties. Polym. Rev., 47, 217-229.

Džunuzović, E., Vodnik, V., Jeremić, K., & Nedeljković J. M. (2009). Thermal properties of PS/TiO2 nanocomposites obtained by in situ bulk radical polymerization of styrene. Mater. Lett., 63, 908-810.

Fischer, E. W., Sterzel, H. J., & Wegner, G. (1973). Investigation of the structure of solution grown crystals of lactide copolymers by means of chemical reactions. Kolloid Z. Z. Polym., 251, 980-990.

Fomin, V. A., & Guzeev, V. V. (2001). Biodegradable polymers, their present state and future aspects. Prog. Rubb. Plastics Tech., 17, 186-204.

Gnanasekaran, D., Madhavan, K., & Reddy, B. S. R. (2009). Developments of polyhedral oligomeric silsesquioxanes (POSS), POSS nanocomposites and their applications: a review. J. Sci. Ind. Res., 68, 437-464.

Gupta, A. P., & Kumar, V. (2007). New emerging trends in synthetic biodegradable polymers – polylactide: a critique. Eur. Polym. J., 43, 4053-4074.

Haque, S., Rehman, I., & Darr, J. A. (2007). Synthesis and characterization of grafted nanohydroxyapatites using functionalized surface agents. Langmuir, 23, 6671-6676.

Hojjati, B., Sui, R., & Charpentier, P. A. (2007) Synthesis of TiO2/PAA nanocomposite by RAFT polymerization. Polymer, 48, 5850-5858.

Hong, Z., Zhang, P., He, C., Qiu, X., Liu, A., Chen, L., Chen, X., & Jing, X. (2005). Nano-composte of poly(L-lactide) and surface grafted hydroxyapatite: mechanical properties and biocompatibility. Biomaterials, 26, 6296-6304.

Khaled, S. M., Sui, R., Charpentier, P. A., & Rizkalla, A. S. (2007). Synthesis of TiO2−PMMA nanocomposite: using methacrylic acid as a coupling agent. Langmuir, 23, 3988-3995.

Kim, H., Abdala, A. A., & Macosko, C. W. (2010). Graphene/polymer nanocomposites. Macromolecules, 43, 6515-6530.

Knauert, S. T, Douglas, J. F., & Starr, F. W. (2007). The effect of nanoparticle shape on polymer-nanocomposite rheology and tensile strength. J. Polym. Sci. Part B-Polym. Phys., 45, 1882-1897.

Kobayashi, S., Hanabusa, K., Hamasaki, N., Kimura, M., & Shirai, H. (2000). Preparation of TiO2 hollow-fibers using supramolecular assemblies. Chem. Mater., 12, 1523-1525.

Kojima, Y., Usuki, A., Kawasumi, M., Okada, A., Fukushima, Y., Kurauchi, T., & Kamigaito, O. (1993). J. Mater. Res., 8, 1185-1189.

Kumar, R., Yakubu, M. K., & Anandjiwala, R. D. (2010). Biodegradation of flax fiber reinforced poly lactic acid. Express Polym. Lett., 4, 423-430.

Li, G. L., Wang, G. H., & Hong, J. M. (1999). Synthesis and characterization of rutile TiO2 nanowhiskers. J. Mater. Res., 14, 3346-3354.

Li, Y., & Sun, X. S. (2010). Preparation and characterization of polymer−inorganic nanocomposites by in situ melt polycondensation of L-lactic acid and surface-hydroxylated MgO. Biomacromolecules, 11, 1847–1855.

Li Y., Venkateshan, K., & Sun, X. S. (2010). Mechanical and thermal properties, morphology, and relaxation characteristics of poly(lactic acid) and soy flour/wood flour blends. Polym. Int., 59, 1099-1109.

Long, Y., Lu, Y., Huang, Y., Peng, Y., Lu, Y., Kang, S., & Mu, J. (2009). Effect of C60 on the photocatalytic activity of TiO2 nanorods. J. Phys. Chem. C, 113, 13899–13905.

Lu, X., Lv, X., Sun, Z., & Zheng, Y. (2008). Nanocomposites of poly(L-lactide) and surface-grafted TiO2 nanoparticles: synthesis and characterization. Eur. Polym. J., 44, 2476-2481.

Luo, Y. B., Li, W. D., Wang, X. L., Xu, D. Y., & Wang, Y. Z. (2009). Preparation and properties of nanocomposites based on poly(lactic acid) and functionalized TiO2. Acta. Mater., 57, 3182-3191.

Luo, Y., Wang, X., Xu, D., & Wang, Y. (2009). Preparation and characterization of poly(lactic acid)-grafted TiO2 nanoparticles with improved dispersions. Appl. Surf. Sci., 255, 6795-6801.

Móczó, J., & Pukánszky, B. (2008). Polymer micro and nanocomposites: structure, interactions, properties. J. Ind. Eng. Chem., 14, 535-563.

Moon, S. I., Lee, C. W., Miyamoto, M., & Kimura, Y. (2000). Melt polycondensation of L-lactic acid with Sn(II) catalysts activated by various proton acids: a direct manufacturing route to high molecular weight poly(L-lactic acid). J. Polym. Sci. Pol. Chem., 38, 1673-1679.

Nakayama, N., & Hayashi, T. (2007). Preparation and characterization of poly(L-lactic acid)/TiO2 nanoparticle nanocomposites films with high transparency and efficient photodegradability. Polym. Degrad. Stab., 92, 1255-1264.

Oh, H., & Green, P. F. (2009). Polymer chain dynamics and glass transition in athermal polymer/nanoparticle mixtures. Nat. Mater., 8, 139-143.

Paul, D. R., & Robeson, L. M. (2008). Polymer nanotechnology: nanocomposites. Polymer, 49, 3187-3204.

Ray, S. S., & Bousmina, M. (2005). Biodegradable polymers and their layered silicate nanocomposites: in greening the 21st century materials world. Prog. Mater. Sci., 50, 962-1079.

Ray, S. S., & Okamoto, M. (2003). Polymer/layered silicate nanocomposites: a review from preparation to processing. Prog. Polym. Sci., 28, 1539-1641.

Ray, S. S., Yamada, K., Okamoto, M., & Ueda, K. (2003). New polylactide/layered silicate nanocomposites. 2. Concurrent improvements of material properties, biodegradability, and melt rheology. Polymer 44, 857-866.

Rotzinger, F. P., Kesselman-Truttmann, J. M., Hug, S. J., Shklover, V., & Graetzel, M. (2004). Structure and vibrational spectrum of formate and acetate adsorbed from aqueous solution onto the TiO2 rutile (110) surface. J. Phys. Chem. B, 108, 5004-5017.

Shogren, R. L., Doane, W. M., Garlotta, D., Lawton, J. W., & Willett, J. L. (2003). Biodegradation of starch/polylactic acid/poly(hydroxy ester ether) composite bars in soil. Polym. Degrad. Stab., 79, 405-411.

Starr, F W., Schrøder, T. B., & Glotzer, S. C. (2002). Molecular dynamics simulation of a polymer melt with a nanoscopic particle. Macromolecules 35, 4481-4492.

Tsagaropoulos, G., & Eisenberg, A. (1995). Direct observation of two glass transitions in silica-filled polymers. Implications to the morphology of random ionomers. Macromolecules, 28, 396-398.

Tsuji, H., Kawashima, Y., Takikawa, H., & Tanaka, S. (2007). Poly(l-lactide)/nano-structured carbon composites: conductivity, thermal properties, crystallization, and biodegradation. Polymer, 48, 4213-4225.

Usuki, A., Kojima, Y., Kawasumi, M., Okada, A., Fukushima, Y., Kurauchi, T., & Kamigaito, O. (1993). Synthesis of nylon 6-clay hybrid. J. Mater. Res., 8, 1179-1184.

Wang, B., Sun, X. S., Klabunde, K. J. (2009). Poly(lactic acid)/multi-hydroxyl magnesium oxide nanocomposites prepared by melt compounding. J. Biobased Mater. Bioenergy, 3, 130-138.

Wu, C. S., & Liao, H. T. (2007). Study on the preparation and characterization of biodegradable polylactide/multi-walled carbon nanotubes nanocomposites. Polymer, 48, 4449-4458.

Xu, Y., Zhuang, Y., & Fu. X. (2010). New insight for enhanced photocatalytic activity of TiO2 by doping carbon nanotubes: a case study on degradation of benzene and methyl orange. J. Phys. Chem. C, 114, 2669-2676.

Yan, S., Yin, J., Yang, Y., Dai, Z., Ma, J., & Chen, X. (2007). Surface-grafted silica linked with L-lactic acid oligomer: a novel nanofiller to improve the performance of biodegradable poly(L-lactide). Polymer, 48, 1688-1694.

Yasuniwa, M., Tsubakihara, S., Sugimoto, Y., & Nakafuku, C. (2004). Thermal analysis of the double-melting behavior of poly(L-lactic acid). J. Polym. Sci. Part B Polym. Phys., 42, 25-32.

Zan, L., Wang, S. L., Fa, W. J., Hu, Y. H., Tian, L. H., & Deng, K. J. (2006a). Solid-phase photocatalytic degradation of polystyrene with modified nano-TiO2 catalyst. Polymer, 47, 8155-8162.

Zan, L., Fa, W., & Wang, S. (2006b). Novel photodegradable low-density polyethylene-TiO2 nanocomposite film. Environ. Sci. Technol., 40, 1681-1685.

Zhang, X. Y., Zhang, L. D., Chen, W., Meng, G. W., Zheng, M. J., & Zhao, L. X. (2001). Electrochemical fabrication of highly ordered semiconductor and metallic nanowire arrays. Chem. Mater., 13, 2511-2515.

Zhang, Y. X., Li, G. H., Jin, Y. X., Zhang, Y., Zhang, J., & Zhang, L. D. (2002). Hydrothermal synthesis and photoluminescence of TiO2 nanowires. Chem. Phys. Lett., 365, 300-304.

Zou, H., Wu, S., & Shen, J. (2008). Polymer/silica nanocomposites: preparation, characterization, properties, and applications. Chem. Rev., 108, 3893-3957.

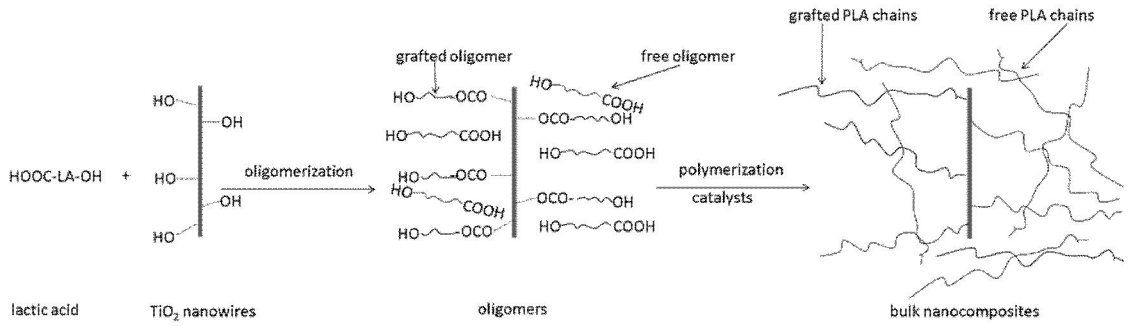

Figure 4.1 Illustration of the synthesis approach for PLA/TiO_2 nanowire nanocomposites.

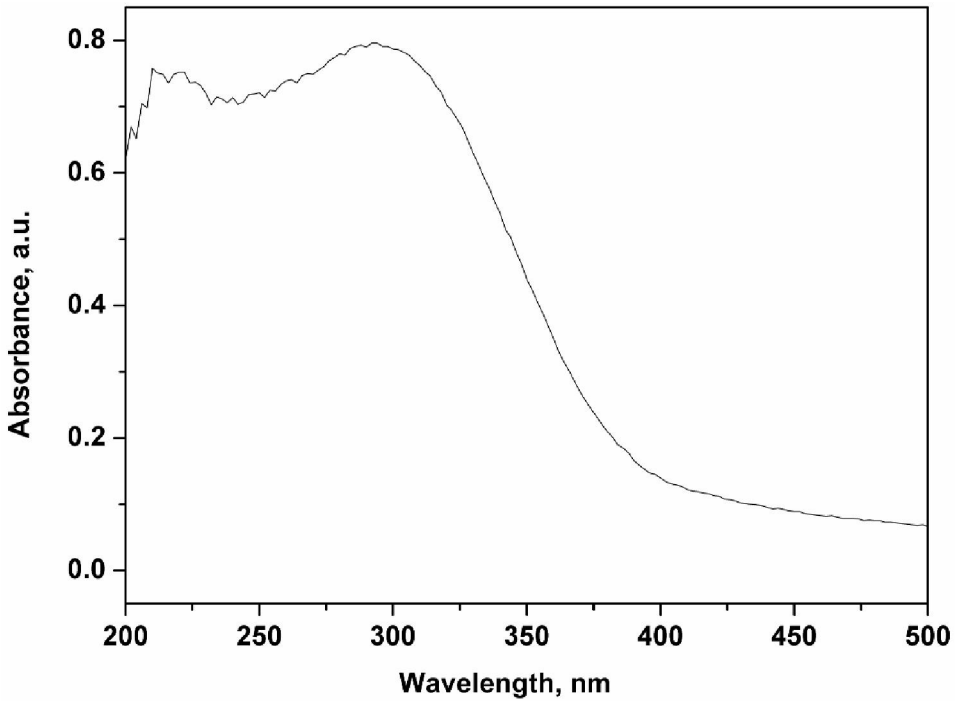

Figure 4.2 UV-vis spectrum of pristine TiO_2 nanowires.

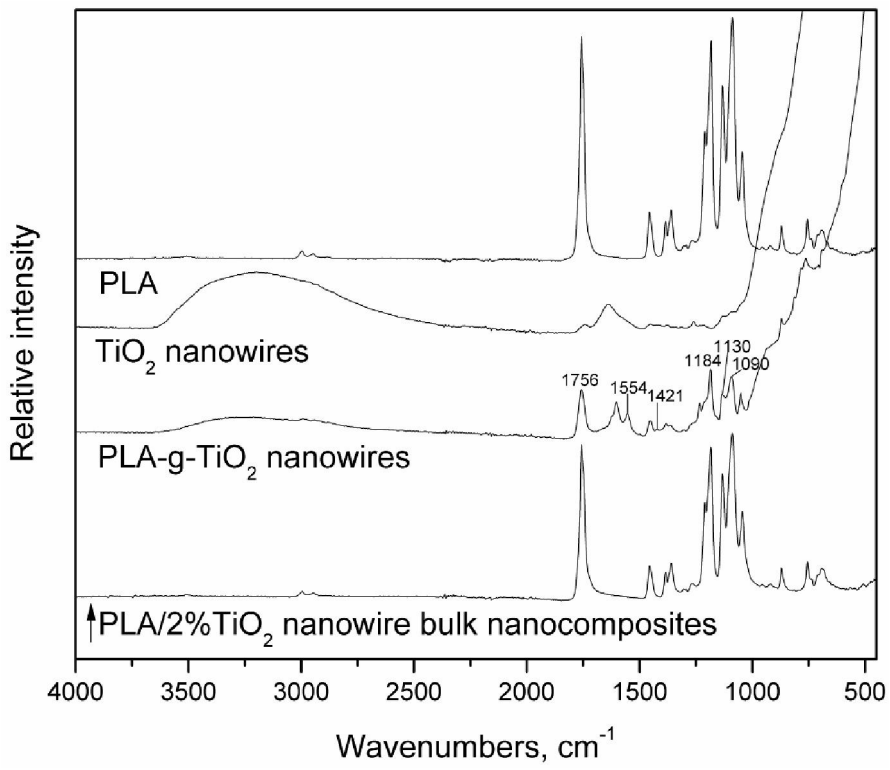

Figure 4.3 FTIR spectra of PLA, pristine TiO_2 nanowires, PLA-g-TiO_2 nanowires, and PLA/2% TiO_2 nanowire bulk nanocomposites.

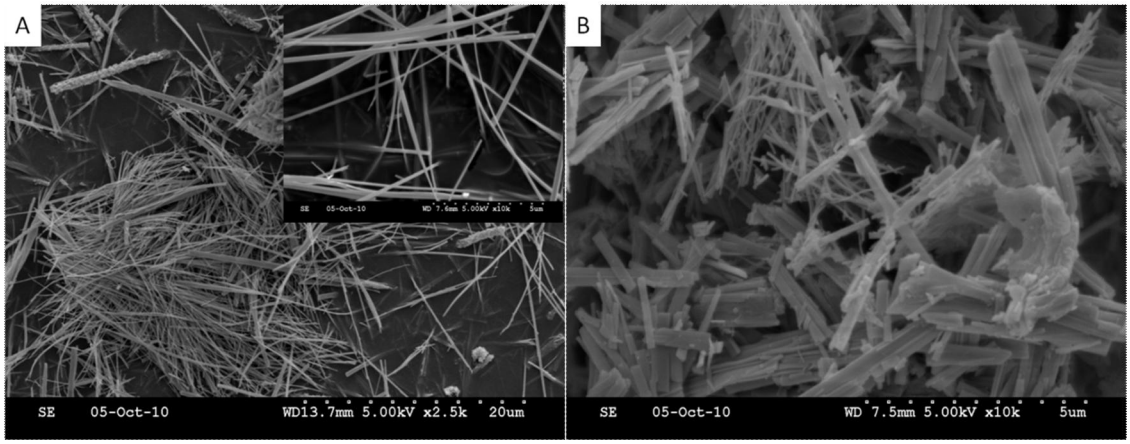

Figure 4.4 SEM micrographs of (A) pristine TiO_2 nanowires and (B) PLA-g-TiO_2 nanowires (scale bar is indicated at the bottom of each image).

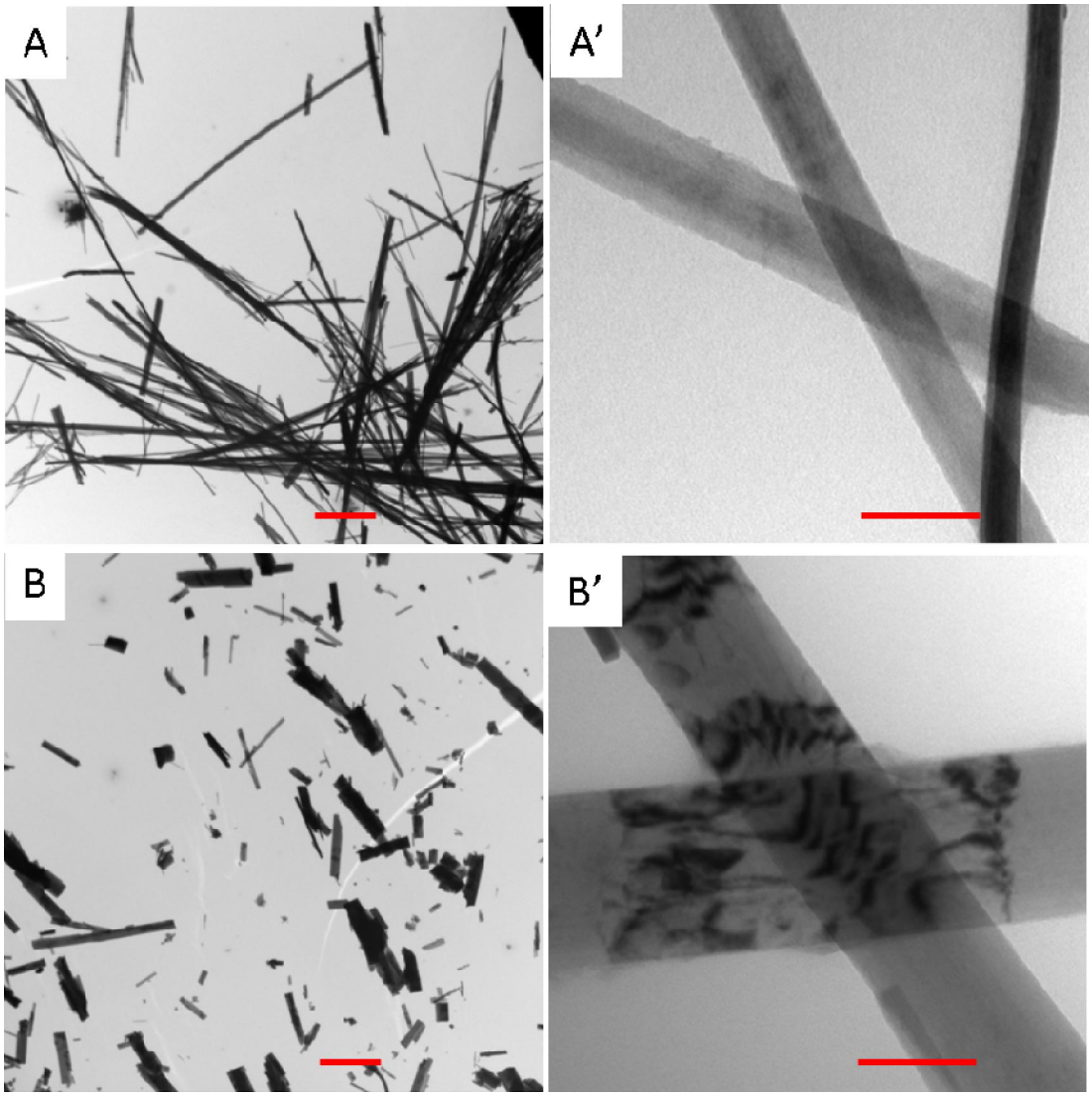

Figure 4.5 TEM micrographs of (A and A') synthesized TiO_2 nanowires and (B and B') PLA-g-TiO_2 nanowires (scale bar: left, 2 µm; right, 100 nm).

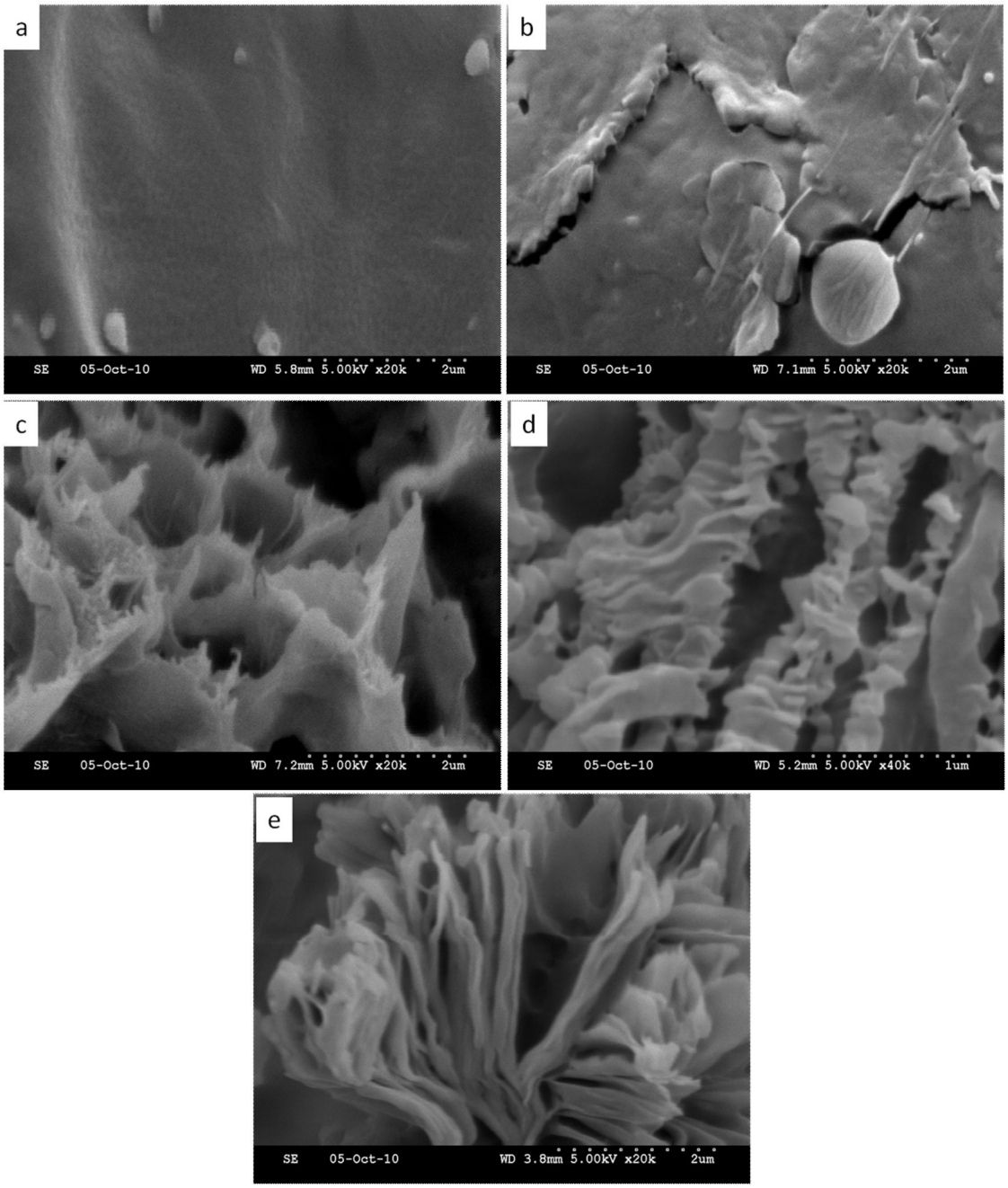

Figure 4.6 SEM micrographs of PLA/TiO_2 nanowire bulk nanocomposites (a, PLA; b, PLA/0.25%TiO_2; c, PLA/0.5%TiO_2; d, PLA/1%TiO_2; e, PLA/2%TiO_2; scale bar is indicated at the bottom of each image).

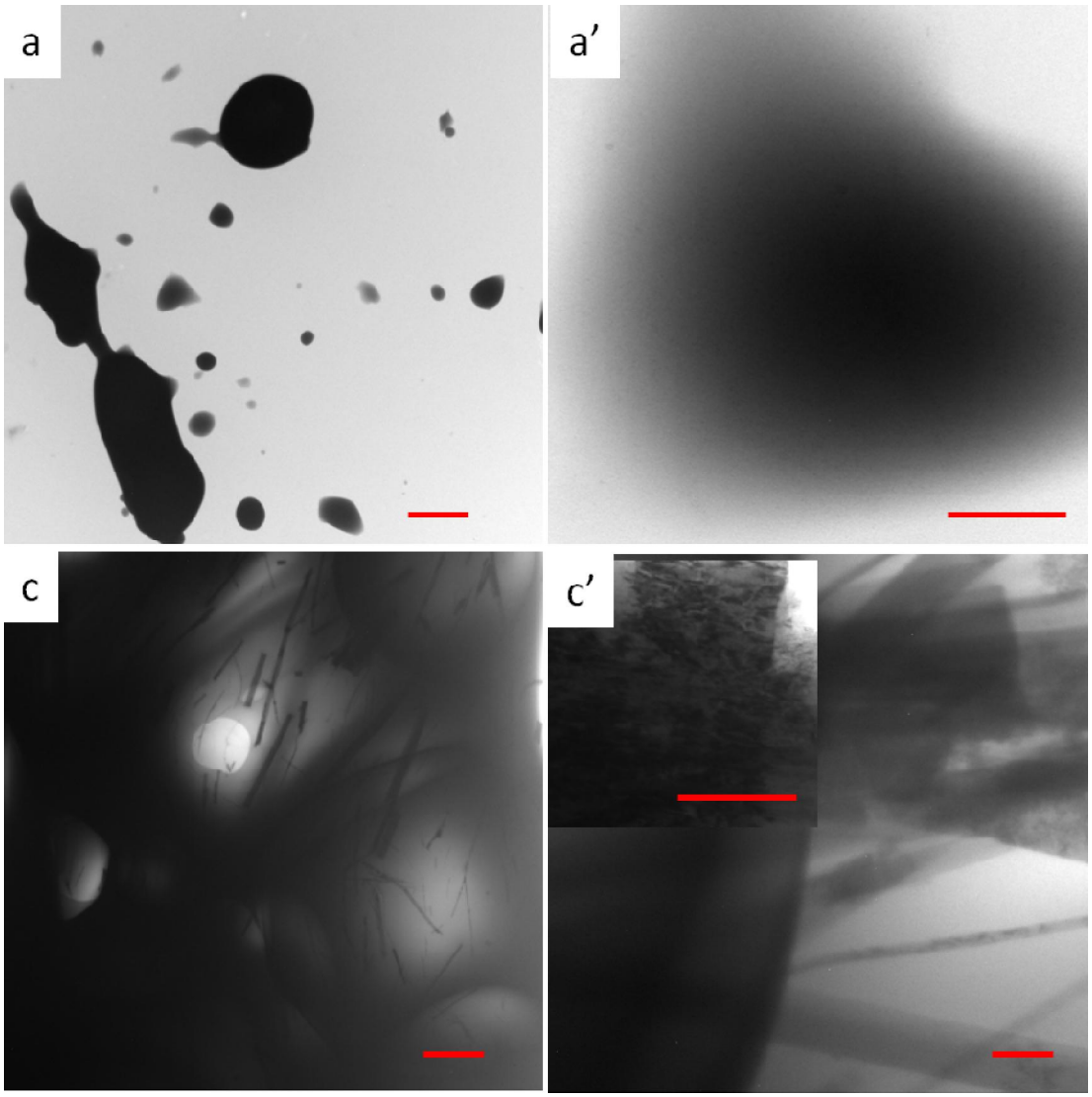

Figure 4.7 Typical TEM micrographs of PLA and PLA/TiO_2 nanowire bulk nanocomposites (a/a', PLA; c/c', PLA/0.5%TiO_2; scale bar: left, 2 µm; right, 200 nm).

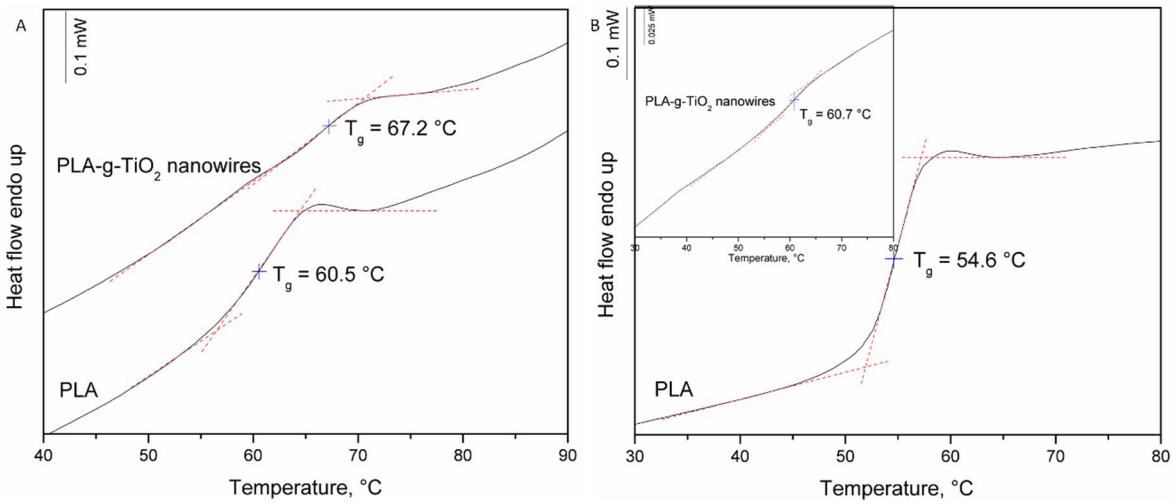

Figure 4.8 DSC thermograms of PLA and PLA-g-TiO_2 nanowires (A, first heating scan; B, second heating scan).

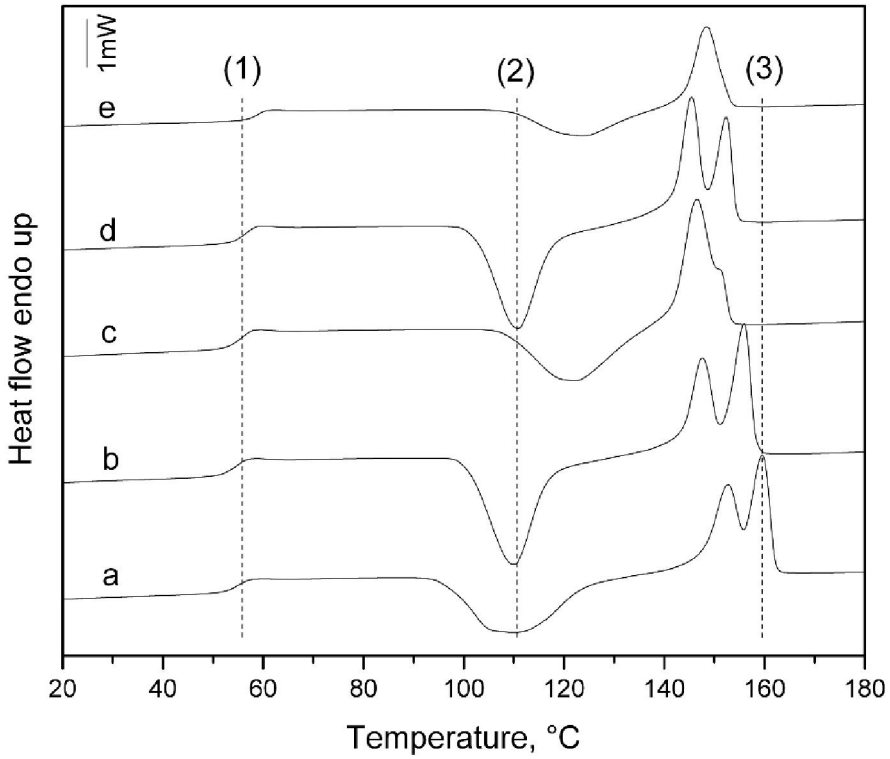

Figure 4.9 DSC thermograms of PLA/TiO_2 nanowire bulk nanocomposites (a, PLA; b, PLA/0.25%TiO_2; c, PLA/0.5%TiO_2; d, PLA/1%TiO_2; e, PLA/2%TiO_2). (1) Glass transition, (2) cold crystallization, and (3) melting.

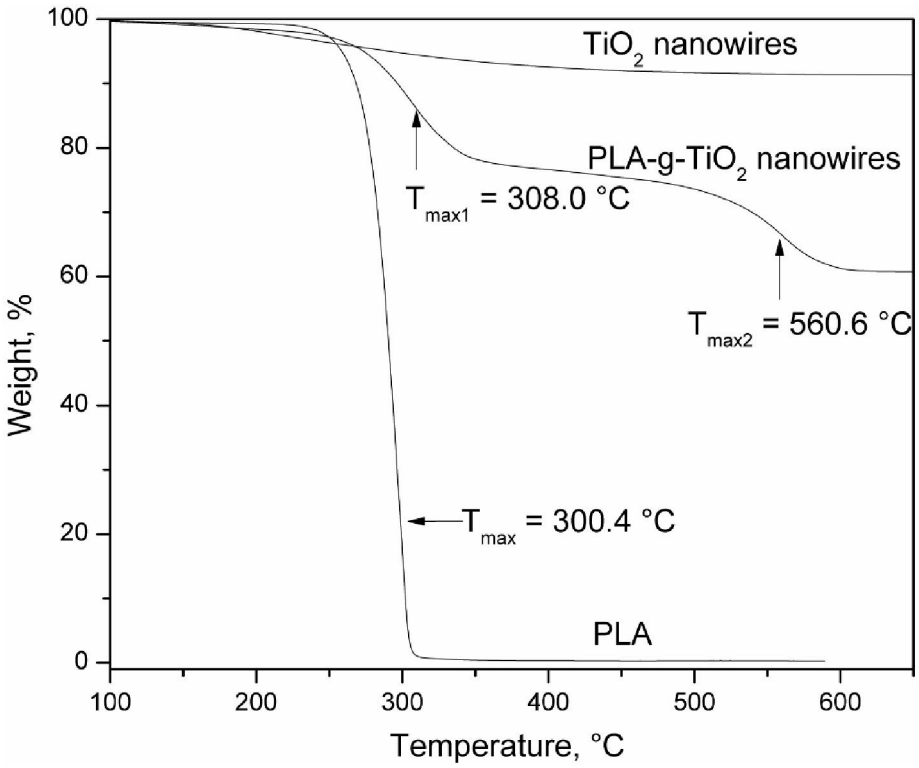

Figure 4.10 TGA thermograms of PLA, pristine TiO_2 nanowires, and PLA-g-TiO_2 nanowires under air atmosphere.

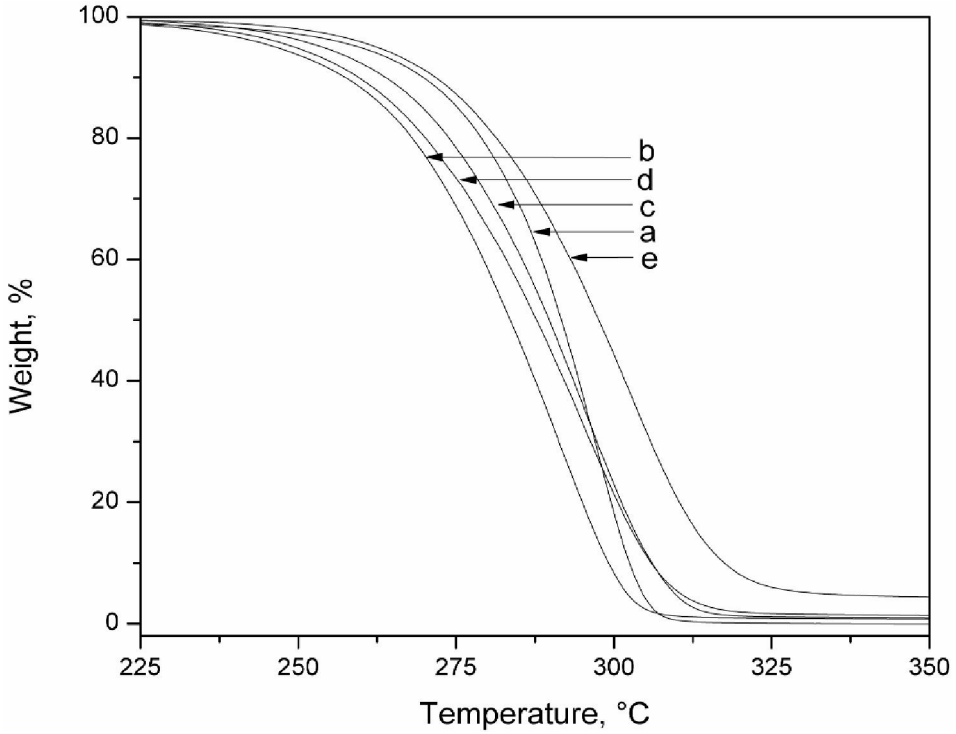

Figure 4.11 TGA thermograms of PLA/TiO_2 nanowire bulk nanocomposites under nitrogen atmosphere (a, PLA; b, PLA/0.25%TiO_2; c, PLA/0.5%TiO_2; d, PLA/1%TiO_2; e, PLA/2%TiO_2).

Table 4.1 Molecular weight of PLA and bulk nanocomposites containing TiO_2 nanowires determined by GPC measurement

Sample	M_w	M_n	[a]PDI
PLA	63,000	33,500	1.9
PLA-0.25%TiO_2	83,300	37,500	2.2
PLA-0.5% TiO_2	66,800	34,500	1.9
PLA-1% TiO_2	66,100	31,300	2.1
PLA-2% TiO_2	104,800	55,200	1.9
free PLA	104,300	59,200	1.8

[a]PDI –Molecular weight distribution (M_w/ M_n)

Table 4.2 Thermal properties of PLA and bulk nanocomposites containing TiO_2 nanowires determined from DSC thermograms

Sample	T_g ºC	ΔC_p J/(g·ºC)	T_c ºC	ΔH_c J/g	T_m ºC	ΔH_m J/g	X_m %
PLA	54.7	0.55	110.0	43.1	152.7, 159.5	43.5	46.5
PLA-0.25%TiO_2	54.9	0.52	110.1	36.5	147.6, 155.9	36.9	39.5
PLA-0.5% TiO_2	55.1	0.55	122.1	25.8	146.5, 151.0	26.8	28.8
PLA-1% TiO_2	56.2	0.49	110.8	34.0	145.5, 152.2	35.1	37.9
PLA-2% TiO_2	58.4	0.50	123..7	21.4	148.5	24.5	26.7

Table 4.3 Thermal decomposition temperatures of PLA and bulk nanocomposites containing TiO_2 nanowires derived from TGA thermograms

Sample	T_{onset} °C	T_{end} °C	T_{max} °C
PLA	276.2	308.3	296.6
PLA-0.25%TiO_2	254.7	306.4	291.3
PLA-0.5% TiO_2	263.4	314.9	295.7
PLA-1% TiO_2	261.9	314.2	295.7
PLA-2% TiO_2	274.5	322.6	302.3

Chapter 5 - Isothermal Crystallization and Melting Behaviors of Bionanocomposites from Poly(lactic acid) and TiO_2 Nanowires[4]

5.1 Abstract

Two representative poly(lactic acid) (PLA) nanocomposites with 1% TiO_2 nanowires were prepared through *in situ* melt polycondensation and easy solution-mixing approaches, respectively. The former was denoted as ISPLANC, and the latter as SMPLANC. The isothermal crystallization kinetics and melting behaviors of pure PLA, ISPLANC, and SMPLANC were comparatively investigated by differential scanning calorimetry in the temperature range of 80–115°C. Maximum crystallization growth rate (G_{exp}) was observed at 100°C for all three samples. The well dispersed TiO_2 nanowires acted as effective nucleation agents in ISPLANC, which exhibited much higher G_{exp} in compared to pure PLA and SMPLANC below 110°C. However, much smaller crystallization enthalpy of ISPLANC was obtained because of its restricted chain mobility in forming crystalline lamellar. The crystallization behavior of all three samples fit the Avrami equation quite well, with most of the R^2 values larger than 0.9990. Double-melting behaviors were observed after heating the samples after isothermal crystallization at various temperatures, which was explained by the melt recrystallization of the smaller and imperfect crystals formed at lower isothermal crystallization temperatures. We also obtained the equilibrium melting temperatures of the three samples by carrying out Hoffman-Weeks plots.

[4] Results have been accepted to publish. Li, Y., Chen, C., Li, J., & Sun, X. S. (2011). Isothermal crystallization and melting behaviors of bionanocomposites from ploy(lactic Acid) and TiO_2 nanowires. *J. Appl. Polym. Sci.*, submitted.

5.2 Introduction

Poly(lactic acid) (PLA) is a biodegradable polymer derived from renewable resources such as corn starch, sugar beets, cellulosic materials, etc. It is a most promising environmental-friendly thermoplastic that has potential applications in service utensils, packaging materials, appliance components, textiles, films, and biomedical materials (Drumright et al., 2000; Jamshidian et al., 2010). In recent years, PLA nanocomposites have been intensively studied to improve PLA properties. Nanoparticles including carbon nanotubes, layered silicates or clays, and silica have been investigated widely to enhance the physical, thermal, and mechanical properties of pristine PLA (Chang et al., 2003; Fukushima et al., 2010; Kuan et al., 2008; Lahiri et al., 2009; Ray et al., 2005; Wen et al., 2010; Wu et al., 2007; Yan et al., 2007; Zhang et al., 2008). PLA nanocomposites with nanoparticles such as graphite, polyhedral oligomeric silsesquioxane, TiO_2, MgO, hydroxyapatite, etc., also have been reported (Gnanasekaran et al., 2009; Kim et al., 2010; Li et al., 2010; Nakayama et al., 2007; Wang et al., 2009; Zheng et al., 2006).

In addition to the dispersion of nanoparticles in the PLA matrix and interfacial interaction between these two phases, the crystalline properties and melting behaviors of the PLA matrix and the effect of nanoparticles on them are of great importance for the properties and end use of PLA nanocomposites. For PLA and its nanocomposites prepared via melt polycondensation, a subsequent solid-state polymerization (SSP) is often necessary to increase further the molecular weight (Moon et al., 2000; Moon et al., 2001a, 2001b). Therefore, a thorough understanding of the crystallization kinetics and melting behaviors of PLA nanocomposites is crucial in the effort to optimize SSP process conditions and control of molecular weight of the final products. Additionally, control of crystallization factors allows for the design of polymeric materials with desirable properties (Iannace & Nicolais, 1997; Wu et al., 2007). The rate of hydrolytic degradation of PLA also has been reported to be strongly affected by the degree of crystallinity (Kawai et al., 2007; Tsuji et al., 2001). Therefore, the crystalline lamellar organization of PLA plays an important role for controlling its degradation. Recent studies have examined the crystallization kinetics of PLA and its composites and nanocomposites (Krikorian & Pochan, 2004; Liu et al., 2009;

Lorenzo, 2005; Nam et al., 2003; Papageorgiou et al., 2010), and the overall crystallization rate or crystallinity of PLA has been increased with the incorporation of various microparticles and nanoparticles (Ke & Sun, 2003; Li et al., 2010; Nam et al., 2003; Papageorgiou et al., 2010; Shieh & Liu, 2007).

In a previous study, we prepared PLA nanocomposites with TiO_2 nanowires through an *in situ* melt polycondensation approach (Li et al., 2011). PLA chains were covalently bonded to the nanowire surface, and the resultant nanocomposites showed a satisfactory dispersion of nanowires and interfacial interaction. Significantly improved glass transition temperature and thermal stability were observed for the bonded PLA chains. In this study, we will report the isothermal crystallization kinetics and melting behaviors of such nanocomposites and pure PLA. For comparison purposes, the nanocomposites prepared by easy solution-mixing of PLA and TiO_2 nanowires also were studied and reported.

5.3 Experimental Section

5.3.1 Materials

TiO_2 nanowires were synthesized in our lab following previously described procedures (Zhang et al., 2002). Pure PLA and *in situ* polymerized PLA/1% TiO_2 nanowire nanocomposites were prepared via melt polycondensation of L-lactic acid without and with TiO_2 nanowires, respectively, as reported previously (Li et al., 2011). The weight-average molecular weights of the pure PLA and the nanocomposites were 63,000 and 66,000 (based on polystyrene standard), respectively, with polydispersity of about 2. Chloroform was purchased from Fisher Scientific.

5.3.2 Preparation of Nanocomposite Films

The solution-mixing PLA/1% TiO_2 nanowire nanocomposites were prepared by using the solution-intercalation film-casting technique as follows: 0.02 g of TiO_2 nanowires was added to 20 ml chloroform, and the mixture was sonicated for 30 min to achieve a uniform dispersion. Meanwhile, 2 g of synthesized pure PLA was completely dissolved in 20 ml chloroform. The PLA solution and nanowire dispersion were stirred for 1 h and sonicated for

1 h. The mixture was cast on a Petri dish at room temperature, kept in a fume hood with controlled evaporation of the solvent for 1 week, then dried in a vacuum oven for 24 h at 80°C to evaporate any residual solvent. Eventually, the solution-mixing nanocomposite (SMPLANC) film was obtained. Pure PLA and *in situ* polymerized nanocomposites (ISPLANC) also were dissolved in chloroform, and films were obtained similarly. The crystallization and melting behaviors of these three types of samples (PLA, ISPLANC, and SMPLANC) were compared. All the samples for microscopy and crystallization studies were cut from these cast films.

5.3.3 Optical Microscopy

The dispersion of TiO_2 nanowires in the ISPLANC and SMPLANC films was examined with an Olympus BX50 microscope. The images were captured with a Nikon Digital Camera DXM 1200F using Nikon ACT-1 version 2.62 software.

5.3.4 Differential Scanning Calorimetry (DSC) Analysis

The isothermal crystallization and melting behaviors of PLA, ISPLANC, and SMPLANC were studied with a TA DSC Q200 instrument under a nitrogen atmosphere. The DSC instrument was calibrated using the melting temperature and enthalpy of indium. The sample films were weighed (around 8 mg) in a standard aluminum pan and sealed. An empty sealed pan was used as a reference. For crystallization characterization, a sample was heated from 0°C to 190°C at a rate of 10°C/min, and maintained at 190°C for 5 min. Subsequently, it was rapidly cooled (~60°C/min) to the isothermal crystallization temperature (T_c). T_c for the samples ranged from 80–115°C at 5°C intervals; samples were held at each T_c for 30 to 50 min, allowing complete crystallization. To observe melting behavior, the completely crystallized sample was reheated from T_c to 190°C at a rate of 10°C/min. Heat of melting (ΔH_m) and melting temperature (T_m) were determined from the DSC thermograms. Crystallinity (X_m) was estimated according to the following equation (1):

$$X_m = \frac{\Delta H_m}{\Delta H_0 \times X_{PLA}} \qquad (1)$$

where ΔH_m and ΔH_0 are heats of melting (J/g) of the measured sample and of PLA crystals of infinite size with a value of 93.6 J/g (Fischer et al., 1973), respectively, and X_{PLA} is the PLA fraction in the sample (X_{PLA}=1 for PLA, and X_{PLA}=0.99 for ISPLANC and SMPLANC).

5.4 Results and Discussion

5.4.1 Morphology

Figure 5.1 shows the microscopy images of ISPLANC (left image) and SMPLANC (right image) films. No nanowire aggregate was observed for ISPLANC film. The individual nanowires were distributed homogeneously throughout the polymer matrix, indicating that *in situ* polymerization was an effective approach to achieve nanocomposites with uniform distributions. Because of the ease of dispersion of TiO_2 nanowires in the aqueous L-lactic acid monomer and *in situ* grafting of lactic acid oligomer on to the surface of nanowires, the nanowires could be well dispersed in the PLA matrix. However, for the nanocomposites prepared by easy solution-mixing of PLA and TiO_2 nanowires (SMPLANC), severe aggregation of TiO_2 nanowires occurred because of the hydrophilic nature and high surface area of nanowires.

5.4.2 Isothermal Crystallization Behavior

Figure 5.2 (A–C) shows the DSC thermograms of PLA, ISPLANC, and SMPLANC at T_c's from 80–115°C. Generally, the T_c is chosen in the range between the glass transition temperature (T_g) and equilibrium melting temperature (T_m^0), at which temperature polymer can crystallize. When the melted semi-crystalline polymer is cooled down and maintained at T_c, its crystallization rate depends on its degree of supercooling (i.e. $\Delta T = T_m^0 - T_c$) (Fraïsse et al., 2007). Shortest crystallization peak time was noticed at T_c of 100°C for all the samples. Upon increasing or decreasing T_c beyond 100°C in the investigated temperature range, the isothermal crystallization peaks became broader; therefore, the time required for the complete crystallization became longer. Furthermore, ISPLANC exhibited a much narrower crystallization peak with lower peak position at each T_c compared with pure PLA and

SMPLANC, which will be discussed later as crystallization half-time and crystallization growth rate.

Based on the samples' DSC exotherms in terms of the heat flow per gram of the sample (dH/dt) as a function of crystallization time, t, we plotted the relative crystallinity, $\alpha(t)$, as a function of t (Figure 5.3, A–C). The relative crystallinity is defined as follows:

$$\alpha(t) = \frac{\Delta H(t)}{\Delta H_\infty} \qquad (2)$$

where $\Delta H(t)$ is the enthalpy of isothermal crystallization at time t (Eq. (3)) and ΔH_∞ is the value after complete crystallization (Eq.(4)). In this study, ΔH_∞ is the total area under the crystallization curve, as listed in Table 5.1.

$$\Delta H(t) = \int_0^t (\frac{dH}{dt})dt \qquad (3)$$

$$\Delta H_\infty = \int_0^\infty (\frac{dH}{dt})dt \qquad (4)$$

All the $\alpha(t)$ vs. t plots exhibited similar sigmoidal profiles. A relevant kinetic characterization, obtained by the intersection of the $\alpha(t)$ vs. t plots and the horizontal line at $\alpha(t) = 0.5$, as shown in Figure 5.3(A–C), is the experimental crystallization half-time ($t_{0.5\text{exp}}$). The $t_{0.5\text{exp}}$ corresponds to the time necessary for the sample to reach 50% of its maximum crystallinity. The reciprocal value of $t_{0.5\,\text{exp}}$ is assumed to be equal to the experimental crystallization growth rate (G_{exp}). Table 5.1 summarizes the $t_{0.5\text{exp}}$ and G_{exp} values as derived from Figure 5.3. The change of G_{exp} as a function of T_c was plotted in Figure 5.4 to provide a better visualization. Increasing the crystallization temperature for each sample initially caused G_{exp} values to increase and then to decrease. Such behavior is common for polymers due to the balance between two opposing effects on the crystallization (Huang et al., 2006). As T_c decreases and approaches T_g, the crystallization growth rate is greatly retarded by the significant decrease in chain mobility. When T_c increases and approaches the T_m^0, although chain mobility increases, it is overcome by the great decrease of the formed nucleation density, and the crystallization growth rate decreases at low degrees of supercooling (i.e., smaller ΔT).

The minimum $t_{0.5\,exp}$ was observed at 100°C for both PLA and nanocomposites, with $t_{0.5exp}$ of 9.0 min and G_{exp} of 0.11 min^{-1} for PLA, $t_{0.5exp}$ of 6.1 min and G_{exp} of 0.16 min^{-1} for ISPLANC, and $t_{0.5exp}$ of 9.8 and G_{exp} of 0.10 min^{-1} for SMPLANC. The G_{exp} of ISPLANC was much higher than that of pure PLA at T_c below 110°C because of the nucleation effects of TiO_2 nanowires. At T_c above 110°C, the G_{exp} of ISPLANC decreased faster than that of pure PLA; at 115°C it was even lower. This can be explained by its much lower T_m^0 (161.7°C) than that of pure PLA (188.4°C). At the same T_c, the ISPLANC system was subjected to more decrease of formed nucleation density because of its lower degree of supercooling than pure PLA. As a result, its crystallization growth rate decreased.

The G_{exp} of SMPLANC was larger than that of pure PLA at T_c of 90°C and below, but smaller at T_c of 95°C and above. Polymer crystallization generally involves nucleation and crystalline growth processes. At lower T_c, the TiO_2 nanowires acted as additional nucleation sites in the SMPLANC system compared with pure PLA, and nucleation was the dominant factor in determining the G_{exp}. While at higher T_c, due to the high concentration and poor dispersion of nanowires in the SMPLANC system, the mobility of PLA chains was restricted and the crystalline growth process was retarded. Furthermore, the effect of TiO_2 nanowires on PLA crystallization in SMPLANC system was much less obvious than that in ISPLANC system. The nanocomposites prepared through solution mixing did not have strong interfacial interaction between PLA matrix and TiO_2 nanowires, and the dispersion of TiO_2 nanowires was not satisfying. Therefore, the effect of TiO_2 nanowires on the crystallization of surrounding PLA chains for SMPLANC became less significant. Although ISPLANC crystallized more rapidly than pure PLA and SMPLANC, its crystallization enthalpy (ΔH_∞) was much smaller at each T_c (Table 5.1) because of its restricted chain mobility in forming crystalline lamellar.

Avrami analysis is the most popular and easiest methodology to achieve relevant parameters for characterizing the crystallization kinetics of polymers (Supaphol, 2001). The fundamental Avrami equation (5) below was used to analyze the increase of the relative crystallinity with time (Avrami, 1939, 1940, 1941):

$$\alpha(t) = 1 - \exp(-kt^n) \qquad (5)$$

where k is the Avrami rate constant and n is the Avrami exponent. The values of k and n are diagnostic of the crystallization mechanism. They are related to the crystallization half-time and to the type of nucleation together with the geometry of the crystal growth, respectively.

Applying the natural logarithmic properties to both sides of Eq. (5), obtains the following equation:

$$\ln(-\ln(1-\alpha(t))) = \ln(k) + n\ln(t) \qquad (6)$$

This equation was used to construct the Avrami fit plots as shown in Figure 5.5 (A–C) to calculate the k and n. The experimental data was also drawn as scatter plots in Figure 5.5 (A–C). Because the Avrami equation rarely describes the whole conversion process, we drawn only the plots for $\alpha(t)$ from 0.03–0.8 based on the literature (Lorenzo et al., 2007). If the experimental data obey the Avrami theory, the Avrami fitting lines should fit the experimental data quite well, yielding $\ln(k)$ as an intercept and n as a slope. The Avrami constants k and n and correlation coefficient of the fit R^2 were summarized in Table 5.1. Most of the R^2 values were larger than 0.9990, indicating a very good Avrami fit of the data (Lorenzo et al., 2007).

The Avrami exponent n differed from sample to sample, and it also varied with T_c. The average n value of 3.5–3.6 in the T_c range evaluated for PLA and SMPLANC indicated that the crystal growing mechanism was intermediate between the instantaneous (n = 3) and sporadic (n = 4) types of nucleation, and the growing of spherulites was three-dimentional (Iannace & Nicolais, 1997). The average n value of ISPLANC was 4.3, which can be theoretically explained by the introduction of a nucleation index m ($m = n - 4$) (Supaphol, 2001). The values of m between 0 and 1 indicated that the nature of the nucleation rate increased with time with sporadic nucleation mechanism during crystallization process. The n values can be affected by many factors, such as the mechanism of nucleation, nucleation density, the form of crystalline growth, restriction of crystalline formation due to surrounding fillers, and even the detecting techniques used. PLA n values in the range of 2–5.4 have been reported (Iannace & Nicolais, 1997; Liao et al., 2007; Mano et al., 2004; Zhang et al., 2004). The rate constant k is determined by the balance of two factors, the rate of nucleation and the crystalline growth. The former increases with supercooling, but the latter decreases;

consequently, a maximum value of k exists at a given supercooling. As shown in Table 5.1, for all the samples, the k values first increased as T_c increased and then decreased generally, similar to the tendency of G_{exp}.

To further confirm whether the crystallization of PLA and nanocomposites follows the Avrami model, the crystallization half-time values also were calculated from the knowledge on k and n as follows (Fraïsse et al., 2007):

$$G_{cal} = \frac{1}{t_{0.5cal}} = \frac{1}{(\frac{\ln 2}{k})^{\frac{1}{n}}}$$

where $t_{0.5cal}$ is the calculated crystallization half-time and G_{cal} is the calculated crystallization rate, which are shown in Table 5.1. Figure 5.4 illustrates the comparison between the isothermal crystallization rate as calculated from the Avrami parameters and the same kinetic parameter as directly derived from the experimental relative crystallinity data. The agreement observed between the two series of data revealed that the crystallization kinetics of all the samples followed the Avrami model.

5.4.3 Melting Behaviors

The melting thermograms of PLA and its nanocomposites (ISPLANC and SMPLANC) after isothermal crystallization at various T_c's are presented in Figure 5.6 (A–C), and the data are summarized in Table 5.2. All the samples exhibited double-melting behaviors, except for ISPLANC after isothermal crystallization at T_c of 115°C. L and H are used for the names of the low-temperature and high-temperature melting peaks. On the basis of this notation, the peak melting temperatures of L and H are denoted as T_m(L) and T_m(H), respectively. For both PLA and nanocomposites, the area of L increased with increasing T_c, whereas the area of H decreased. In other words, the ratio of peak area of H to that of L was dependent on T_c, which could be explained by the melt-recrystallization model (Wunderlich, 1980; Yasuniwa et al., 2004). The melt-recrystallization model suggests that small and imperfect crystals change successively into more stable crystals through the melt-recrystallization mechanism. That is, the melting and recrystallization are competitive in the heating process (Yasuniwa et al., 2004). When the samples were crystallized at lower T_c's,

the mobility of polymer chains was restricted, resulting in smaller crystallite structures and more defect-ridden crystalline lamellar. Such crystals recrystallized in the melt-recrystallization process during heating, leading to a higher melting peak. While at higher T_c's, forming more perfect and larger crystal lamellae was easier, and therefore it was more difficult for the recrystallization process to occur. As a result, the area of peak H became smaller or even disappeared for the samples crystallized at higher T_c. In summary, peak H is a result of the melting of the crystallites recrystallized during the heating process, whereas peak L refers to the melting of the primary crystallites formed during the isothermal crystallization process.

As shown in Table 5.2, the heat of melting (ΔH_m) and crystallinity (X_m) of PLA and nanocomposites also are affected by T_c. The X_m of PLA and nanocomposites increased in general as the T_c increased in the evaluated temperature range. This is because additional crystallization occurred during isothermal crystallization at higher T_c, corresponding to the higher ΔH_∞ as reported in Table 5.1. The much lower X_m in the ISPLANC compared with pure PLA was due to the inability of polymer chains to be incorporated fully into growing crystalline lamella. In other words, the presence of high concentrations of dispersed TiO_2 nanowires and strong covalent bonding between nanowire surface and PLA chains prevented large crystalline domains from forming due to limited space and restricted mobility imposed on PLA chains. SMPLANC also exhibited lower X_m compared with pure PLA, but to a much smaller extent than ISPLANC. As expected, the nanocomposites prepared through solution mixing did not have strong interfacial interaction between PLA matrix and TiO_2 nanowires. Because of the lack of efficient interfacial interaction and homogeneous dispersion of nanowires, the effect of nanowires on the mobility of PLA chains in forming crystalline lamellar was expected to be much smaller compared with ISPLANC. Decreased crystallinity also was reported for other PLA nanocomposites in the literature (Nakayama & Hayashi, 2007; Wu & Liao, 2007; Wu et al., 2007).

The values of T_m(L) and T_m(H) of PLA and its nanocomposites are plotted as a function of T_c in Figure 5.7. As can be observed clearly, T_m(L) increased continuously with increasing T_c in the evaluated temperature range, whereas T_m(H) remained almost unchanged.

Increased T_m(L) indicated that the perfection and thickness of the growing PLA lamella crystals increased at higher T_c's (Krikorian & Pochan, 2004). PLA and SMPLANC exhibited nearly the same T_m(L) and T_m(H) at each T_c, whereas melting temperatures in the case of ISPLANC were much lower, suggesting thinner lamella crystals or defective crystalline regions in the nanocomposites in the presence of well dispersed TiO_2 nanowires. Many works on nanocomposites report a decrease of melting temperature compared with pristine polymers (Hao et al., 2002; Maio et al., 2004; Nakayama & Hayashi, 2007; Wu & Liao, 2007). Two possible reasons explain the decreased melting temperatures of nanocomposites: One is that the mobility of polymer chains is greatly restricted by the nanoparticles in forming perfect and larger crystalline lamellar. Another is that the presence of the nanoparticles increases greatly the nucleation rate, whose characteristic time is much lower than the time required for chain disentanglement, thus disallowing the growth of well developed lamellar crystals (Maio et al., 2004).

The equilibrium melting temperature can be measured by isothermal crystallization at various temperatures by carrying out a Hoffman-Weeks plot (Weeks, 1963; Hoffman & Weeks, 1965). By fitting the data points of T_m(L) to a straight line (Hoffman-Weeks plot) and extrapolating it to $T_m = T_c$, the T_m^0 was determined (Figure 5.7). PLA and SMPLANC showed the same T_m^0 of 188.4°C, whereas the T_m^0 of ISPLANC was much lower, only 161.7°C. The explanation for the T_m^0 reduction of ISPLANC was similar to that described above for melting temperatures.

5.5 Conclusions

In situ polymerization was a more effective approach than solution mixing in preparing PLA/TiO_2 nanowires nanocomposites. Crystallization growth rate first increased then decreased in the temperature range of 80–115°C, with maximum G_{exp} observed at 100°C. The TiO_2 nanowires acted as nucleation agents in the ISPLANC, which exhibited much higher G_{exp} than either pure PLA or SMPLANC below 110°C. But the ISPLANC had much smaller crystallization enthalpy at each T_c because of its restricted chain mobility in

forming crystalline lamellar. The crystallization behavior of all the three samples fit the Avrami equation quite well. Double-melting behaviors were observed. The overall crystallinity of both PLA and nanocomposites increased in general as T_c increased in the evaluated temperature range. Equilibrium melting temperature of the ISPLANC was 161.7°C, and that of the SMPLANC was 188.4°C, same as PLA. The knowledge obtained about crystallization kinetics and melting behaviors of PLA and its nanocomposites could be useful references for optimizing the solid-state polymerization process and designing PLA thermoplastics with desirable properties.

5.6 References

Avrami, M. (1939). Kinetics of phase change. I. General theory. J. Chem. Phys., 7, 1103-1112.

Avrami, M. (1940). Kinetics of phase change. II. Transformation-time relations for random distribution of nuclei. J. Chem. Phys., 8, 212.

Avrami, M. (1941). Kinetics of phase change. III. Granulation, phase change, and microstructure. J. Chem. Phys., 9, 177.

Chang, J. H, Uk-An, Y., & Sur, G. S. (2003). Poly(lactic acid) nanocomposites with various organoclays. I. thermomechanical properties, morphology, and gas permeability. J. Polym. Sci. Part B: Polym. Phys., 41, 94-103.

Drumright, R. E., Gruber, P. R., & Henton, D. E. (2000). Polylactic acid technology. Adv. Mater., 12, 1841–1846.

Fischer, E. W., Sterzel, H. J., & Wegner, G. (1973). Investigation of the structure of solution grown crystals of lactide copolymers by means of chemical reactions. Kolloid Z. Z. Polym., 251, 980-990. Fraïsse, F.; Nedelec, J. M.; Grolier, J. P. E.; Baba, M. Phys Chem Chem Phys 2007, 9, 2137–2141.

Fukushima, K., Murariu, M., Camino, G., & Dubois, P. (2010). Effect of expanded graphite/layered-silicate clay on thermal, mechanical and fire retardant properties of poly(lactic acid). Polym. Degrad. Sta., 95, 1063-1076.

Gnanasekaran, D., Madhavan, K., & Reddy, B. S. R. (2009). Developments of polyhedral oligomeric silsesquioxanes (POSS), POSS nanocomposites and their applications: a review. J. Sci. Ind. Res., 68, 437-464.Hao, J.; Yuan, M.; Deng, X. J Appl Polym Sci 2002, 86, 676–683.

Hoffman, J. D., & Weeks, J. J. (1965). X-ray study of isothermal thickening of lamellae in bulk polyethylene at the crystallization temperature. J. Chem. Phys., 42, 4301-4302.

Huang, C.-I., Tsai, S.-H., & Chen, C.-M. (2006). Isothermal crystallization behavior of poly(L-lactide) in poly(L-lactide)-*block*-poly(ethylene glycol) diblock copolymers. J. Polym. Sci. Part B Polym. Phys., 44, 2438–2448.

Iannace S., & Nicolais L. (1997). Isothermal crystallization and chain mobility of poly(L-lactide). J. Appl. Polym. Sci., 64, 911–919.

Jamshidian, M., Tehrany, E. A., Imran, M., Jacquot, M., & Desobry, S. (2010). Poly-lactic acid: production, applications, nanocomposites, and release studies. Compr. Rev. Food Sci. F, 9, 552–571.

Kawai, T., Rahman, N., Matsuba, G., Nishida, K., Kanaya, T., Nakano, M., Okamoto, H., Kawada, J., Usuki, A., Honma, N., Nakajima, K., & Matsuda, M. (2007). Crystallization and melting behavior of poly (l-lactic acid). Macromolecules, 40, 9463–9469.

Ke, T., & Sun, X. S. (2003). Melting behavior and crystallization kinetics of starch and poly(lactic acid) composites. J. Appl. Polym. Sci., 89, 1203–1210.

Kim, I., & Jeong, Y. G. (2010). Polylactide/exfoliated graphite nanocomposites with enhanced thermal stability, mechanical modulus, and electrical conductivity. J. Polym. Sci. Part B Polym. Phys., 48, 850–858.

Krikorian, V., & Pochan, D. J. (2004). Unusual crystallization behavior of organoclay reinforced poly(l-lactic acid) nanocomposites. *Macromolecules*, 37, 6480–6491.

Kuan, C., Kuan, H., Ma, C. M., & Chen, C. (2008). Mechanical and electrical properties of multi-wall carbon nanotube/poly(lactic acid) composites. J. Phys. Chem. Solids, 69, 1395-1398.

Lahiri, D., Rouzaud, F., Namin, S., Keshri, A. K., Valdes, J. J., Kos, L., Tsoukias, N., & Agarwal, A. (2009). Carbon nanotube reinforced polylactide−caprolactone copolymer: mechanical strengthening and interaction with human osteoblasts in vitro. ACS Appl. Mater. Interfaces, 1, 2470–2476.

Li, Y., Chen, C., Li, J., & Sun, X. S. (2011). Synthesis and characterization of bionanocomposites from L-lactic acid and TiO2 nanowires by in situ polymerization. Polymer, under review.

Li, Y., & Sun, X. S. (2010). Preparation and characterization of polymer−inorganic nanocomposites by in situ melt polycondensation of L-lactic acid and surface-hydroxylated MgO. Biomacromolecules, 11, 1847–1855.

Li, Y., & Sun, X. S. (2011). Mechanical and thermal properties of biocomposites from poly(lactic acid) and DDGS. J. Appl. Polym. Sci., n/a, doi: 10.1002/app.33681.

Li Y., Venkateshan, K., & Sun, X. S. (2010). Mechanical and thermal properties, morphology, and relaxation characteristics of poly(lactic acid) and soy flour/wood flour blends. Polym. Int., 59, 1099-1109.Liao, R.; Yang, B.; Yu, W.; Zhou, C. J Appl Polym Sci 2007, 104, 310–317.

Liu, Y., Wang, L., He, Y., Fan, Z., & Li, S. (2010). Non-isothermal crystallization kinetics of poly(L-lactide). Polym. Int., 59, 1616–1621.

Lorenzo, A. T., Arnal, M. L., Albuerne, J., & Muller, A. J. (2007). DSC isothermal polymer crystallization kinetics measurements and the use of the Avrami equation to fit the data: Guidelines to avoid common problems. Polym. Test, 26, 222-231.

Lorenzo, M. L. D. (2005). Crystallization behavior of poly(L-lactic acid). Eur. Polym. J., 41, 569–575.

Maio, E. D., Iannace, S., Sorrentino, L., & Nicolais, L. (2004). Isothermal crystallization in PCL/clay nanocomposites investigated with thermal and rheometric methods. Polymer, 45, 8893–8900.

Mano, J. F., Wang, Y., Viana, J. C., Denchev, Z., & Oliveira, M. J. (2004). Cold crystallization of PLLA studied by simultaneous SAXS and WAXS. Macromole. Mater. Eng., 289, 910–915.

Moon, S. I., Lee, C. W., Miyamoto, M., & Kimura, Y. (2000). Melt polycondensation of L-lactic acid with Sn(II) catalysts activated by various proton acids: a direct manufacturing route to high molecular weight poly(L-lactic acid). J. Polym. Sci. Pol. Chem., 38, 1673-1679.Moon, S. I.; Lee, C. W.; Taniquchi, I.; Miyamoto, M.; Kimura, Y. Polymer 2001, 42, 5059–5062.

Moon, S. I., Taniquchi, I., Miyamoto, M., Kimura, Y., & Lee, C. W. (2001). Synthesis and properties of high-molecular-weight poly(L-lactic acid) by melt/solid polycondensation under different reaction conditions. High Perform. Polym., 13, S189–S196.

Nakayama, N., & Hayashi, T. (2007). Preparation and characterization of poly(L-lactic acid)/TiO2 nanoparticle nanocomposites films with high transparency and efficient photodegradability. Polym. Degrad. Stab., 92, 1255-1264.Nam, J. Y.; Ray, S. S.; Okamoto, M. Macromolecules 2003, 36, 7126–7131.

Papageorgiou, G. Z., Achilias, D. S., Nanaki, S., Beslikas, T., & Bikiaris, D. (2010). PLA nanocomposites: effect of filler type on non-isothermal crystallization. Thermochim. Acta., 511, 129–139.

Ray, S. S., & Bousmina, M. (2005). Biodegradable polymers and their layered silicate nanocomposites: in greening the 21st century materials world. Prog. Mater. Sci., 50, 962-1079.Shieh, Y. T.; Liu, G. L. J Polym Sci B Polym Phys 2007, 45, 1870–1881.

Supaphol, P. (2001). Application of the Avrami, Tobin, Malkin, and Urbanovici-Segal macrokinetic models to isothermal crystallization of syndiotactic polypropylene. Thermochim. Acta., 370, 37–48.

Tsuji, H., Nakahara, K., & Ikarashi, K. (2001). Poly(L-lactide), 8. high-temperature hydrolysis of poly(L-lactide) films with different crystallinities and crystalline thicknesses in phosphate-buffered solution. Macromol. Mater. Eng., 286, 398–406.

Wang, B., Sun, X. S., Klabunde, K. J. (2009). Poly(lactic acid)/multi-hydroxyl magnesium oxide nanocomposites prepared by melt compounding. J. Biobased Mater. Bioenergy, 3, 130-138.Weeks, J. J. J Res Nat Bur Stand 1963, 67A, 441.

Wen, X., Lin, Y., Han, C., Han, L., Li, Y., & Dong, L. (2010). Dramatic improvements in mechanical properties of poly(L-lactide)/silica nanocomposites by addition of hyperbranched poly(ester amide). Macromol. Mater. Eng., 295, 415–419.

Wu, C. S., & Liao, H. T. (2007). Study on the preparation and characterization of biodegradable polylactide/multi-walled carbon nanotubes nanocomposites. Polymer, 48, 4449-4458.Wu, D.; Wu, L.; Wu, L.; Xu, B.; Zhang, Y.; Zhang, M. J Polym Sci B Polym Phys 2007, 45, 1100–1113.

Wunderlich, B. (1980). Macromolecular Physics; Academic: New York, Vol. 3.

Yan, S., Yin, J., Yang, Y., Dai, Z., Ma, J., & Chen, X. (2007). Surface-grafted silica linked with L-lactic acid oligomer: a novel nanofiller to improve the performance of biodegradable poly(L-lactide). Polymer, 48, 1688-1694.

Yasuniwa, M., Tsubakihara, S., Sugimoto, Y., & Nakafuku, C. (2004). J. Polym. Sci. Part B Polym. Phys., 42, 25–32.

Zhang, J.; Lou, J.; Ilias, S.; Krishnamachari, P.; Yan, J. Thermal properties of poly(lactic acid) fumed silica nanocomposites: Experiments and molecular dynamics simulations. Polymer 2008, 49, 2381–2386.

Zhang, J.; Tsuji, H.; Noda, I.; Ozaki, Y. Structural Changes and Crystallization Dynamics of Poly(l-lactide) during the Cold-Crystallization Process Investigated by Infrared and Two-Dimensional Infrared Correlation Spectroscopy. Macromolecules 2004, 37, 6433–6439.

Zhang, Y. X., Li, G. H., Jin, Y. X., Zhang, Y., Zhang, J., & Zhang, L. D. (2002). Hydrothermal synthesis and photoluminescence of TiO2 nanowires. Chem. Phys. Lett., 365, 300-304.

Zheng, X.; Zhou, S.; Li, X.; Weng, J. Shape memory properties of poly(d,l-lactide)/hydroxyapatite composites. Biomaterials 2006, 27, 4288–4295.

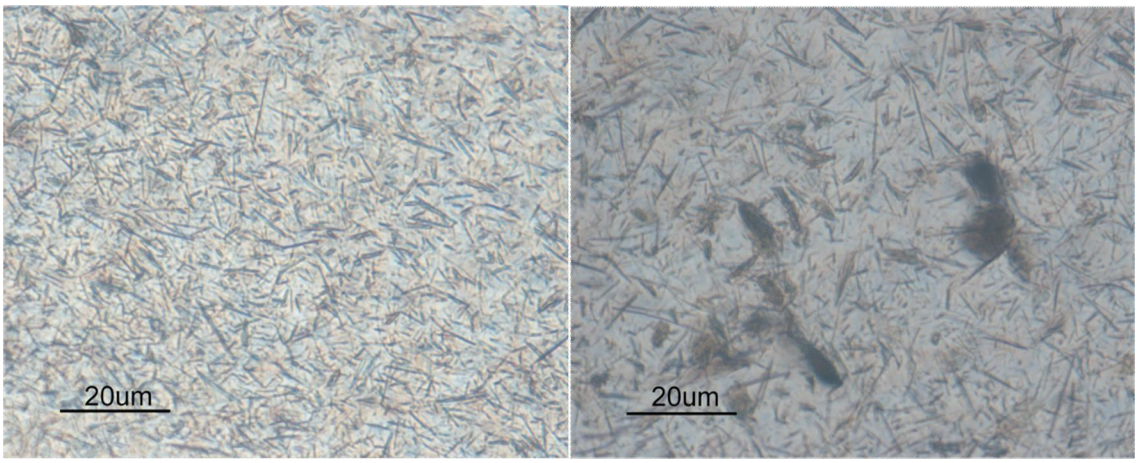

Figure 5.1 Microscope images of PLA nanocomposite films (left: ISPLANC; right: SMPLANC).

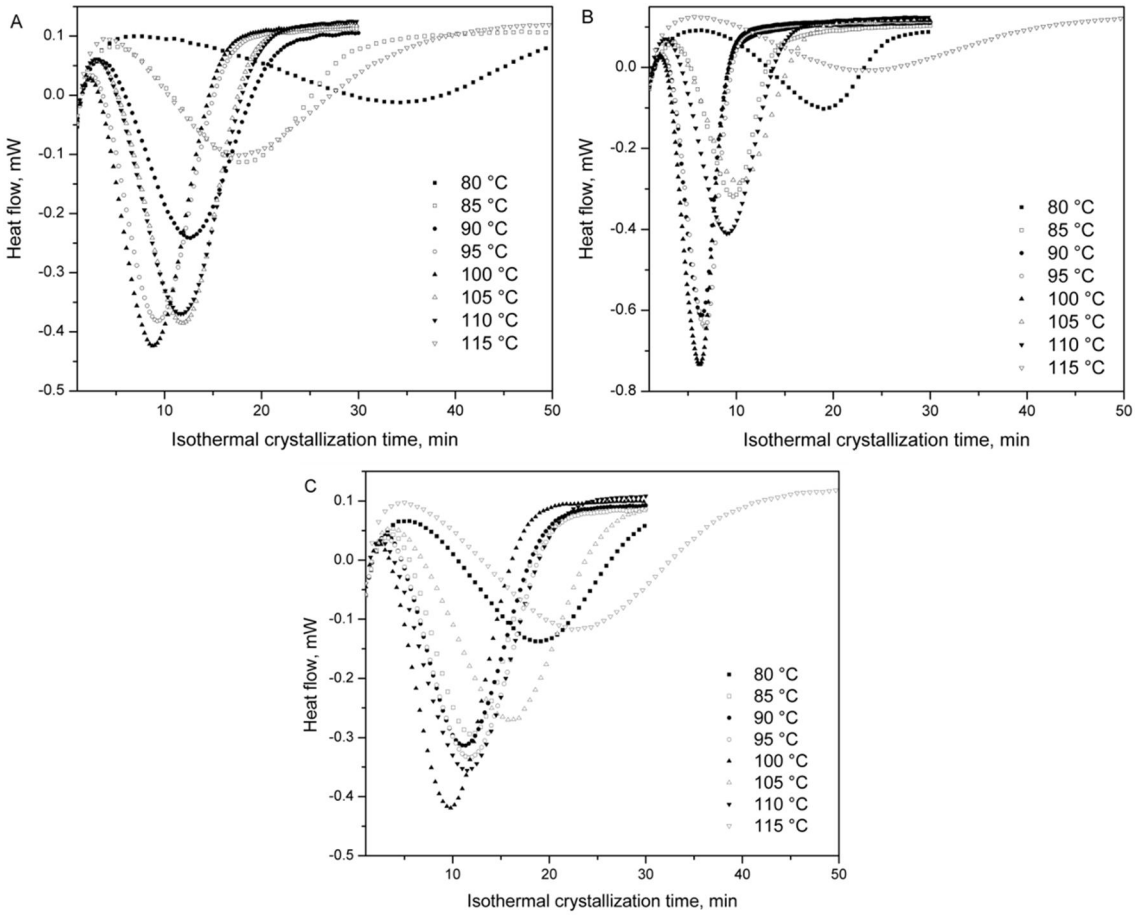

Figure 5.2 Isothermal crystallization thermograms of PLA (A) and its nanocomposites (B, ISPLANC; C, SMPLANC) at various temperatures.

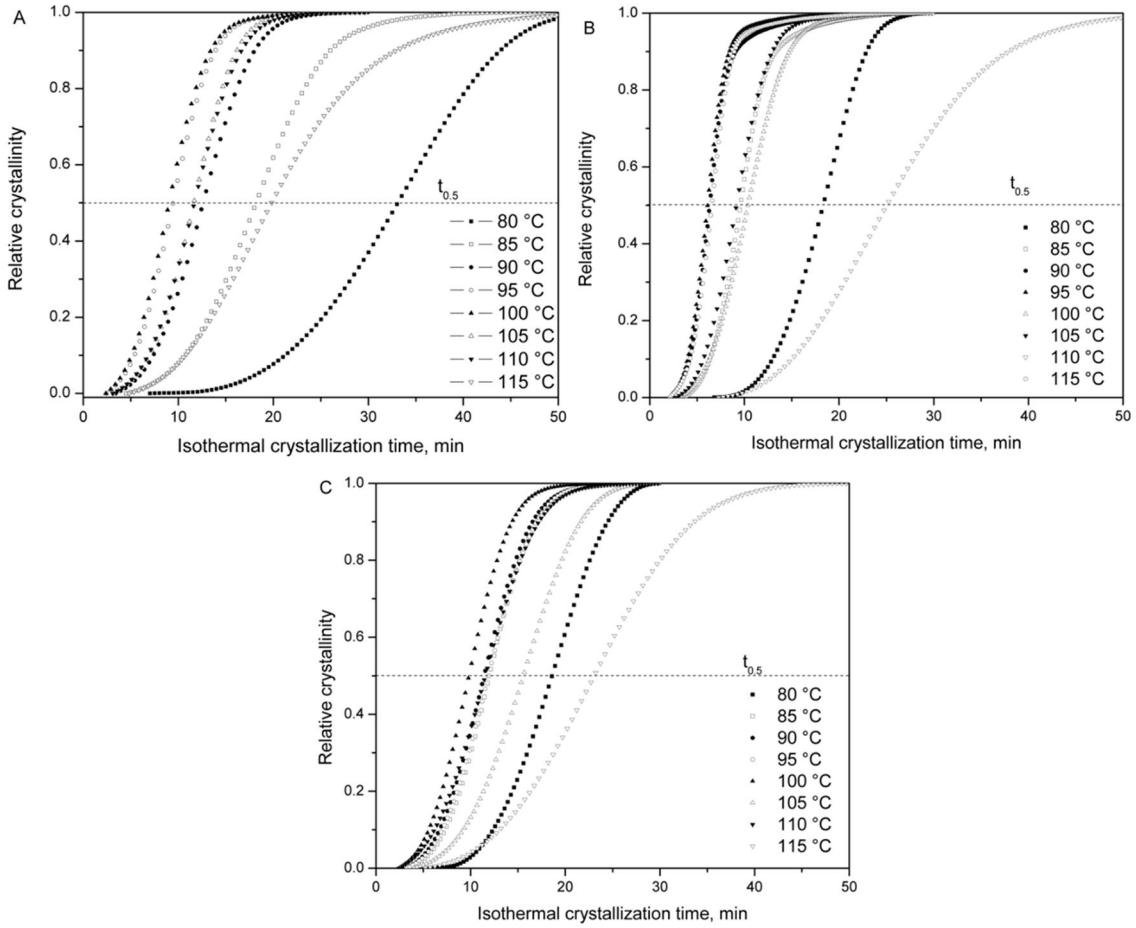

Figure 5.3 Relative crystallinity as a function of isothermal crystallization time for PLA (A) and its nanocomposites (B, ISPLANC; C, SMPLANC) at various temperatures.

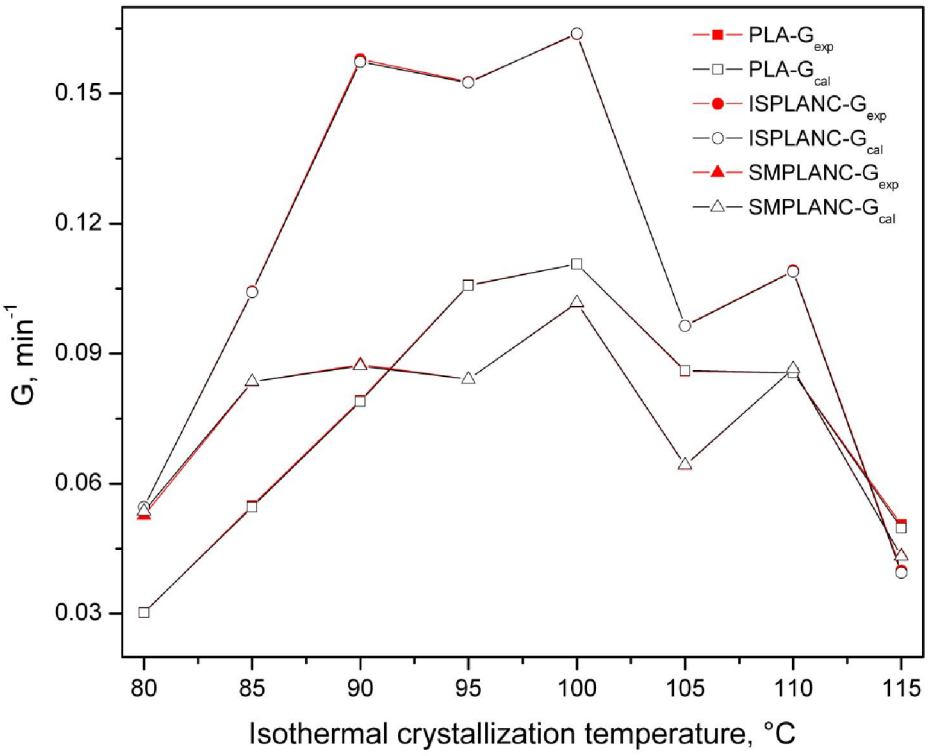

Figure 5.4 Experimental (G_{exp}) and calculated (G_{cal}) crystallization rate of PLA and its nanocomposites (ISPLANC and SMPLANC) as a function of temperatures.

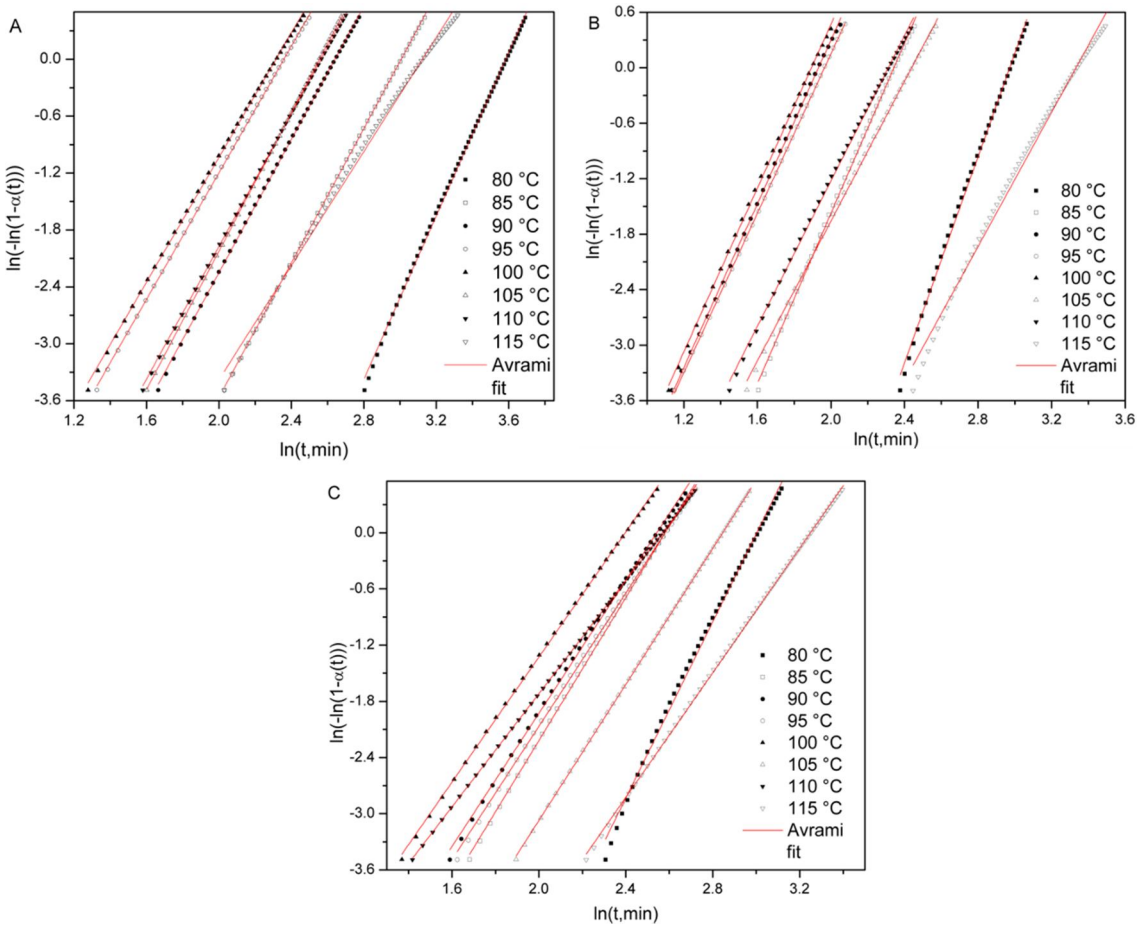

Figure 5.5 Avrami analysis of the isothermal crystallization data of PLA (A) and its nanocomposites (B, ISPLANC; C, SMPLANC) at various temperatures.

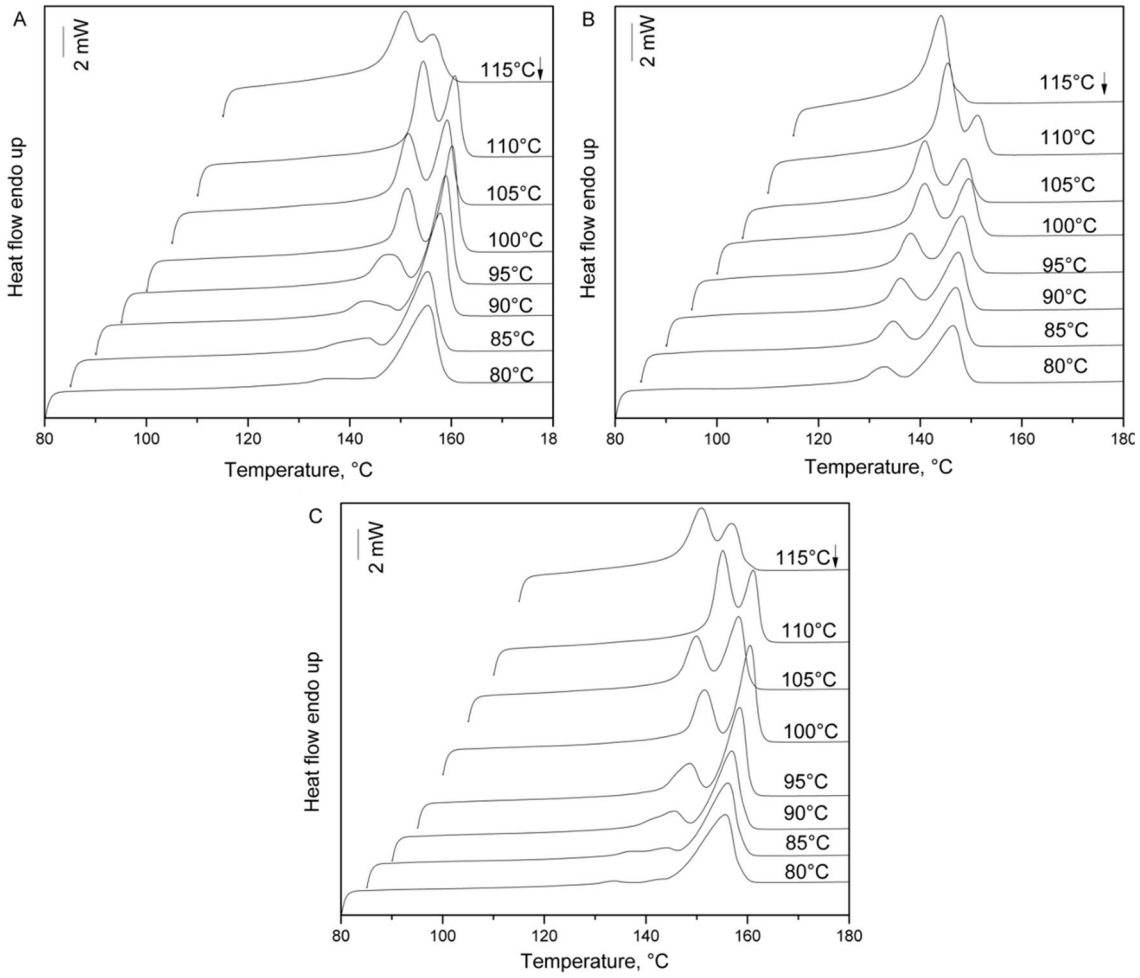

Figure 5.6 DSC melting thermograms of PLA (A) and its nanocomposites (B, ISPLANC; C, SMPLANC) after isothermal crystallization at various temperatures.

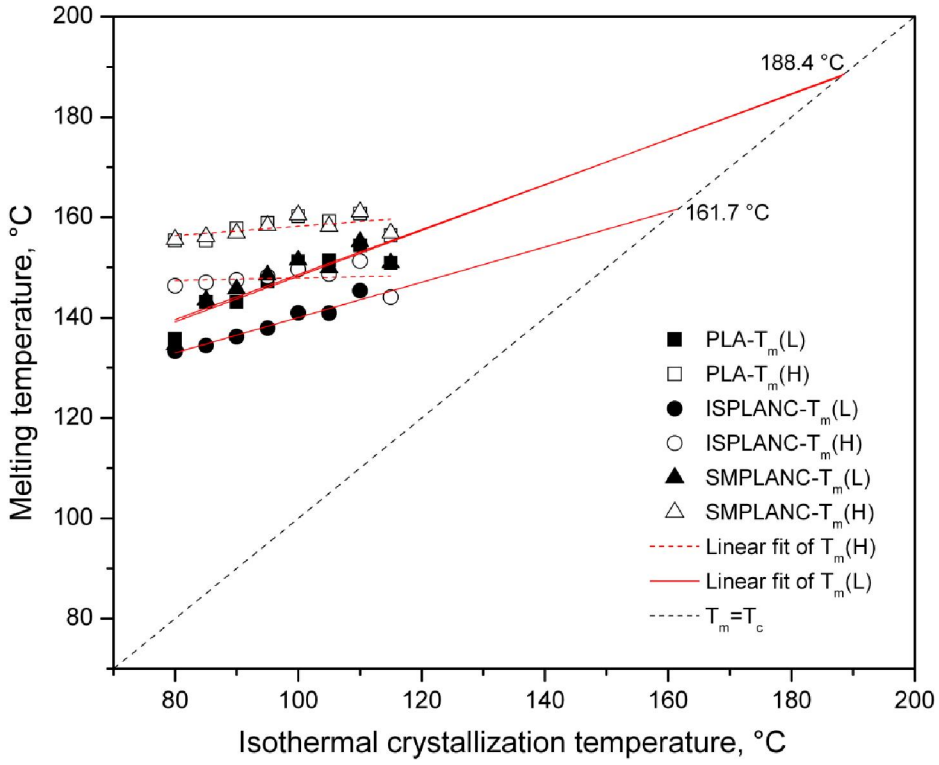

Figure 5.7 Melting temperatures of PLA and its nanocomposites as a function of isothermal crystallization temperature and Hoffman-Weeks analysis.

Table 5.1 Summary of isothermal crystallization data of PLA and its nanocomposites (ISPLANC and SMPLANC)

Sample	T_c (°C)	ΔH_∞ (J/g)	$t_{0.5exp}$ (min)	G_{exp} (min^{-1})	K (min^{-1})	n	n_{ave}	R^2	$t_{0.5cal}$ (min)	G_{cal} (min^{-1})
PLA	80	23.9	33.1	3.02E-02	1.97E-07	4.31	3.52	0.9992	33.0	3.03E-02
	85	25.5	18.2	5.49E-02	2.35E-05	3.54		0.9999	18.3	5.46E-02
	90	28.1	12.6	7.92E-02	9.33E-05	3.51		0.9998	12.7	7.89E-02
	95	30.6	9.5	1.06E-01	3.82E-04	3.34		0.9999	9.5	1.06E-01
	100	32.5	9.0	1.11E-01	4.95E-04	3.29		0.9997	9.0	1.11E-01
	105	36.1	11.6	8.59E-02	8.96E-05	3.65		0.9999	11.6	8.60E-02
	110	37.7	11.7	8.55E-02	1.27E-04	3.50		0.9999	11.7	8.56E-02
	115	32.8	19.8	5.05E-02	8.27E-05	3.01		0.9965	20.1	4.97E-02
ISPLANC	80	14.3	18.3	5.46E-02	6.24E-08	5.58	4.34	0.9982	18.3	5.46E-02
	85	15.6	9.6	1.04E-01	2.10E-05	4.60		0.9992	9.6	1.04E-01
	90	17.2	6.3	1.58E-01	1.92E-04	4.43		0.9997	6.4	1.57E-01
	95	19.5	6.6	1.53E-01	2.10E-04	4.31		0.9999	6.6	1.53E-01
	100	21.6	6.1	1.64E-01	2.29E-04	4.43		0.9995	6.1	1.64E-01
	105	21.0	10.4	9.64E-02	1.00E-04	3.78		0.9992	10.4	9.64E-02
	110	24.2	9.2	1.09E-01	1.14E-04	3.93		0.9992	9.2	1.09E-01
	115	26.2	25.1	3.99E-02	5.56E-06	3.63		0.9942	25.3	3.95E-02
SMPLANC	80	21.0	19.0	5.26E-02	7.37E-07	4.70	3.62	0.9971	18.7	5.36E-02
	85	25.2	12.0	8.35E-02	5.27E-05	3.82		0.9997	12.0	8.35E-02
	90	28.0	11.4	8.75E-02	1.20E-04	3.55		0.9993	11.5	8.71E-02
	95	30.4	11.9	8.41E-02	1.03E-04	3.56		0.9995	11.9	8.41E-02
	100	31.6	9.8	1.02E-01	3.35E-04	3.34		0.9998	9.8	1.02E-01
	105	33.4	15.6	6.42E-02	3.26E-05	3.63		0.9999	15.6	6.43E-02
	110	34.8	11.6	8.65E-02	4.26E-04	3.02		0.9999	11.6	8.65E-02
	115	35.8	23.1	4.34E-02	2.04E-05	3.32		0.9998	23.2	4.32E-02

Table 5.2 Melting parameters of PLA and its nanocomposites (ISPLANC and SMPLANC) derived from DSC melting thermograms after isothermal crystallization at various temperatures

Sample	T_c (°C)	T_m(L) (°C)	T_m(H) (°C)	ΔH_m (J/g)	X_m
PLA	80	135.8	155.4	36.6	0.39
	85	143.1	155.3	37.2	0.40
	90	143.1	157.8	40.4	0.43
	95	147.2	158.9	41.9	0.45
	100	151.2	160.2	43.3	0.46
	105	151.4	159.2	43.7	0.47
	110	154.4	160.7	45.8	0.49
	115	150.9	156.4	43.9	0.47
ISPLANC	80	133.3	146.4	20.2	0.22
	85	134.4	147.0	21.4	0.23
	90	136.2	147.5	22.0	0.24
	95	137.9	148.2	23.5	0.25
	100	141.0	149.6	25.1	0.27
	105	140.9	148.7	23.9	0.26
	110	145.4	151.3	27.5	0.30
	115	144.1	144.1	30.5	0.33
SMPLANC	80	134.6	155.6	35.5	0.38
	85	143.5	156.2	35.5	0.38
	90	145.7	156.9	36.9	0.40
	95	148.5	158.4	39.1	0.42
	100	151.5	160.5	41.8	0.45
	105	150.0	158.2	40.0	0.43
	110	155.2	161.1	45.5	0.49
	115	150.9	156.9	40.9	0.44

Chapter 6 - Mechanical and Thermal Properties, Morphology, and Relaxation Characteristics of Poly(lactic acid) and Soy Flour/Wood Flour Blends[5]

6.1 Abstract

Poly(lactic acid) (PLA) is a biodegradable polymer derived from sugar-based materials, and its applications are varied. PLA blends are commonly employed to overcome disadvantages such as, poor impact strength, low heat distortion temperature, poor processability and relatively high cost. In this study, blending PLA with SF, WF and sodium bisulfite modified SF (MSF) was used to improve its adhesion to PLA. In all cases, 0.5% methylene diphenyl diisocyanate (MDI) was used as a coupling agent. Mechanical and thermal properties, morphology, and relaxation characteristics of the blends were investigated. Results showed that MDI was an effective coupling agent for the WF/PLA system in improving tensile strength and elongation. Differential scanning calorimetry results indicated that SF and modified SF act as nucleation agents and facilitate the crystallization behavior of PLA by increasing the percentage of crystallinity. From mechanical relaxation of the temperature-variant system, we determined how the mechanical relaxation time evolves during the course of heating and obtained Kohlrausch-Williams-Watts parameter and activation energy (ΔE). Poly(lactic acid) and its blends exhibited highly homogeneous relaxational dynamics in their transition from glass to liquid, and the ΔE of PLA and its blends is mainly affected by their densities and compositions.

---

[5]Results have been published. Li, Y., Venkateshan, K., & Sun, X. S. (2010). Mechanical and thermal properties, morphological, and relaxation characteristics of poly(lactic acid) and soy flour / wood flour blends. *Polym. Int.,* 59, 1099-1109. (Reuse by permission of John Willey and Sons).

6.2 Introduction

The development of synthetic polymers from petroleum-based products has benefited humankind for decades but has also led to severe problems including overexploitation of fossil resources and environmental pollution. Therefore, there is a great interest in the development of alternatives and biodegradable polymers. Several bio-based polymers such as poly(lactic acid) (PLA), polyhydroxyalkanoates, and functionalized vegetable/plant starch- and protein-based resins have been created from renewable resources (Bhardwaj & Mohanty, 2007; Yu et al., 2006). Poly(lactic acid) is a biodegradable polymer derived from sugar-based materials. It exhibits mechanical properties similar to those of synthetic polymers such as polyethylene, polypropylene, polystyrene, and polyethylene terephthalate (Anderson et al., 2008; Bhardwaj & Mohanty, 2007). However, the application of PLA has been limited by its relatively high cost.

In past decades, blending PLA resin with low-cost, natural biopolymers, such as starch (Jacobsen & Fritz, 1996; Ke & Sun, 2000; Wu, 2008; Zhang & Sun, 2004), protein (Zhang et al., 2006), wood flour (WF), and fibers (Huda et al., 2006; Jiang et al., 2007; Takatani et al., 2008), received lots of attention. These biopolymers are abundant, relatively inexpensive, renewable, and biodegradable. Wang et al. (2001&2002) successfully prepared PLA/starch blends by using methylene diphenyl diisocyanate (MDI) as a coupling agent. The blends showed enhanced mechanical properties, with the improvement of storage modulus at temperatures above the glass transition temperature (T_g) when the ratio of starch to PLA was up to 45:55 (w/w) with 0.5% MDI. Compared with starch (~$0.1-$0.2 per pound), which is also consumed in the production of fuel ethanol, WF is more attractive, available, and affordable (~$0.1 per pound). Studies involving WF, polymers and MDI have been reported extensively and includes WF-Polyurethane-MDI prepolymer (Aranguren et al., 2007; Marcovich et al., 2006; Mosiewichi et al., 2008) and WF-High density polyethylene-MDI functionalized polyethylene prepolymer (Zhang et al., 2006) systems. An improvement in thermo-mechanical and interfacial properties with the exception of impact strength has been reported for both systems. Furthermore, Pilla et al. (2008) investigated the properties of PLA/pine wood flour (PWF) composites by varying the percentage of PWF with and without

a silane coupling agent. They concluded that the addition of PWF (up to 40%) increased the modulus but decreased toughness and elongation; tensile strength remained the same (about 51–57 MPa), and the effects of silane on the mechanical properties were not significant. Lee et al. (2008) conducted a similar study of a WF/talc mixture-filled PLA and found that tensile strength decreased slightly with the addition of talc but increased with the addition of 1 wt% silane. In our study, we hypothesize that MDI can enhance the mechanical and interfacial properties of WF/PLA and soy flour/PLA (SF/PLA) blends and be an effective coupling agent based on the high reactivity of isocyanate groups of MDI with nucleophiles, such as hydroxyl groups present in soy flour (SF) and WF, in forming urethane linkages (Dieteroch et al., 1985).

Soy protein is another natural biopolymer that has been used extensively as a biodegradable adhesive (Kalapathy et al., 1995; Kuo et al., 2003; Liu & Li, 2004; Sun & Bian, 1999), but not as extensively as thermoplastics (Paetau et al., 1994; Sue et al., 1997; Sun et al., 1999). When modified with sodium bisulfite ($NaHSO_3$), soy protein adhesive had adhesion strength and water resistance similar to that of phenol formaldehyde resin-based adhesives (Sun et al., 2008). Zhang et al. (2006) prepared PLA/soy protein isolate (SPI) and PLA/soy protein concentrate (SPC) blends with poly(2-ethyl-2oxazoline) as a compatibilizer and found that PLA/SPC blends had a higher tensile strength than PLA/SPI blends prepared at the same ratio. They concluded that the compatibility of PLA/SPC was higher than that of PLA/SPI and attributed this to the higher carbohydrate content in SPC (Zhang et al., 2006). Because soy flour (SF) contains about 50% soy protein and is less expensive (~$0.1 per pound) than SPI and SPC, we decided to use SF and modified SF (MSF) in addition to WF as fillers. For the WF/PLA blends, we expected to obtain improved mechanical performance and improved interface adhesion with SF/PLA and MSF/PLA blends. We hypothesized that with modification with $NaHSO_3$, the protein in the SF would provide improved adhesion function at the interface between the PLA matrix and SF particles and that the higher carbohydrate content in SF compared with SPI and SPC would provide better compatibility with PLA.

Based on our literature studies, hypotheses and expectations of biocompatibility, biodegradability, effective compatibilization and interfacial adhesion, the objectives of this

research are to: (1) develop novel high-performance biodegradable blends from PLA and natural biopolymer fillers such as SF and MSF and thereby explore the possibility of hydrophobic bonding reinforcement between high molecular weight protein chains and PLA chains. Soy protein and its derivatives have been proven to be effective in pressure sensitive adhesive, binder and filler applications (Sun et al., 2008); (2) investigate the mechanical and thermal properties and morphology of the blends with different fillers with and without MDI as a coupling agent; and (3) study the relaxation characteristics, such as mechanical relaxation time (τ_{mech}), dynamic heterogeneity, Kohlrausch-Williams-Watts parameter (β), and activation energy (ΔE), from dynamic mechanical analysis (DMA) measurements. To our knowledge, the analysis of DMA results to calculate τ_{mech} and determine ΔE using the method described in this paper has not been reported previously.

6.3 Experimental Section

6.3.1 Materials

Poly(lactic acid) (2002D) in pellet form was obtained from NatureWorks LLC (Minnetonka, MN). Soy flour, composed of 50% protein, was provided by Cargill (Cedar Rapids, IA), and the density was 500 kg/m^3. To prepare MSF, a known amount of SF was suspended in water at a weight ratio of 1 to 16 (SF/water). The suspension was continuously stirred, and the pH was adjusted to 9.5. After 1 h, an accurately weighed amount of $NaHSO_3$ (Fisher Scientific, Pittsburgh, PA) was added to the suspension. The concentration of $NaHSO_3$ in the SF solution was 6 g/L ($NaHSO_3$/water). After setting the suspension containing $NaHSO_3$ for 15 min, the pH was adjusted to 9.5 again. The mixtures were stirred continuously for another 2 h, the pH was again adjusted to 7.0, and mixtures were then freeze-dried at 233 K. The freeze-dried mixtures were milled into powder by using a mill (UDY Corp., Fort Collins, CO) with a U.S. #100 mesh screen. Wood particles were provided by Georgia-Pacific LLC (Atlanta, GA) and milled into WF with the same mill. The WF had a density of 200 kg/m^3. The MDI was purchased from ICI Polyurethanes Group (West Deptford, NJ) and was obtained in a dark brown, viscous, liquid form.

6.3.2 Blends Preparation

The PLA pellets were ground through a 1 mm screen in a laboratory mill (Thomas-Wiley Company, Philadelphia, PA). Ground PLA and the fillers (WF, SF, and MSF) were dried in a vacuum oven at 353 K for at least 3 h before blends were prepared. The ratio of PLA to filler was 80 to 20 by weight. We selected the filler content of 20% by weight in consideration of the degree of hydrophilicity of the fillers and its compatibility with PLA which is primarily hydrophobic. It was reported that for PLA-fiber composites which contained 30% by weight or greater amounts of hydrophilic filler, the consequences were poor interfacial compatibility and mechanical properties (Yu et al., 2007). To make blends with MDI, 0.5% MDI, based on 100 parts of the blend, was added as a coupling agent. Each blend was mixed in a stand mixer (Ultra Power Kitchen Aid, St. Joseph, MI) for 10 min and then transferred to an intensive mixer (Rheomix 600, Haake, Paramus, NJ) equipped with two corotating rollers with a gap. Blends were hot-mixed for 2.5 min at 443 K and 120 rpm. After cooling, blends were ground into 1 mm powder for tensile bar preparation. Pure PLA was treated with the same procedures as the control. Dog-bone-type tensile bars according to ASTM Method D 638-91 (1992), were compression molded at 443 K, 8000 lb for 5 min with a Carver hot press (model 3889, Auto "M", Carver Inc., Wabash, IN), cooled to room temperature in air, and then removed from the mold. Pure PLA and its blends with different fillers with and without MDI were prepared and labeled as PLA, WF/PLA, WF/PLA/MDI, SF/PLA, SF/PLA/MDI, MSF/PLA, and MSF/PLA/MDI. At least five specimens were prepared for each sample type.

6.3.3 Mechanical Measurements

The tensile bars were conditioned at 298 K with a relative humidity of 50% for 48 h prior to mechanical testing. The mechanical tests were performed with an Instron testing system (model 4465, Canton, MA) at a crosshead speed of 5 mm/min with a 30 mm gauge length. Five replicates were tested for each sample type.

6.3.4 Differential Scanning Calorimetry (DSC)

The thermal properties of the blends were measured with a PerkinElmer differential scanning calorimeter (Norwalk, CT). About 5 mg of dried blend powder was sealed in an aluminum pan. A sealed empty pan was used as a reference. The sample was heated from 253 K to 463 K at a rate of 10 K/min, isothermally conditioned at 463 K for 5 min, cooled to 253 K at 10 K/min, isothermally held at 253 K for 5 min, and then heated again to 463 K. The specimen was characterized in an inert environment by using nitrogen. Results were obtained from the second DSC heating scan. The heat capacity (ΔCp, equals to $Cp,l - Cp,g$), glass transition temperature (T_g), heat of melting (ΔH_m), and heat of crystallization (ΔH_c) were determined from the DSC curve. The T_g was determined on the curve where the specific heat change is half of the change in the completed transition. The crystallinity of PLA (X_m) in the blend was estimated according to the following equation (Zhang & Sun, 2004):

$$X_m(\%) = \frac{\Delta H_m}{\Delta H_0 \times X_{PLA}} \times 100 \qquad (1)$$

where ΔH_m and ΔH_0 are heats (J/g) of melting of the blend and a PLA crystal of infinite size with a value of 93.6 J/g (Zhang & Sun, 2004), respectively, and X_{PLA} is the PLA fraction in the blend.

6.3.5 Thermogravimetric Analysis (TGA)

Decomposition temperature of both fillers and composites was determined via TGA (PerkinElmer Pyris1 TGA, Norwalk, CT). About 5 mg of each sample was placed in the pan and heated from 313 K to 873 K at a heating rate of 20 K/min under a nitrogen atmosphere.

6.3.6 Morphology

Morphological studies of the fractured surfaces of samples obtained from tensile tests were conducted using scanning electron microscopy (SEM) (Hitachi S-3500N, Hitachi Science Systems, Ltd., Japan). Each specimen was mounted on an aluminum stub, and the fractured surface was coated with an alloy of 60% gold and 40% palladium with a sputter coater (Desk II Sputter/ Etch Unit, NJ) before observation. The SF, MSF, and WF were also observed in a similar fashion.

6.3.7 Dynamic Mechanical Analysis (DMA)

Dynamic mechanical experiments were conducted using a PerkinElmer dynamic mechanical analyzer 7e (Norwalk, CT) in a three-point flexural mode at 1 Hz frequency. The specimens (about 10 mm × 6 mm × 2 mm) were obtained from tensile bars with a saw, and the edges were polished carefully with grade 240 abrasive sandpaper. Specimens were heated from 253 K to 432 K at a heating rate of 3 K/min under a helium atmosphere. The experimental methods used to perform the DMA and the corresponding relaxation behaviors were explained in detail (McCrum et al., 1991). Briefly, the sample was subjected to an oscillating stress of known amplitude and frequency in a 3-point flexural mode within the approximation of linear response. The flexural storage modulus, B', and flexural loss modulus, B'', were determined from the changes in the amplitude and phase angle of the observed oscillating strain response of the specimen.

6.4 Results and Descussion

6.4.1 Mechanical Properties

The mechanical behaviors of PLA and its blends were characterized by tensile tests, and the results are summarized in Table 6.1. The PLA exhibited a tensile strength (σ) of about 76 MPa, elongation (ε) of 6.2%, and Young's modulus (E) of 1.9 GPa. For WF/PLA, the σ showed a deduction (54 MPa), with ε of 4% and E of 2.3 GPa. However, with the addition of 0.5% MDI, the σ of WF/PLA increased to 69 MPa, and ε and E changed slightly. The improvement of σ is a consequence of increased WF/PLA interfacial adhesion due to the formation of urethane linkages between MDI-PLA and MDI-WF because MDI acts as a coupling agent.

The σ, ε, and E values obtained for SF/PLA were similar to those of WF/PLA. However, with the addition of MDI, SF/PLA did not exhibit an improvement in mechanical performance, indicating that MDI is not an effective coupling agent. The ineffectiveness of MDI as a coupling agent in SF/PLA blends is attributed to the following: (1) increased PLA-MDI-PLA and SF-SF interactions instead of SF-MDI-PLA possibly due to significant differences in the kinetics of PLA-MDI and SF-MDI reactions. As mentioned previously, SF

comprises of high molecular weight protein chains which contribute to diffusional constraints and decreased rate of reaction kinetics; and (2) the coupling mechanism of SF-MDI-PLA is mainly based on the reaction of isocyanate groups from MDI and hydroxyl groups from SF and PLA to form urethane linkages. However, the lower amount of hydroxyl groups in SF leads to a higher degree of PLA-MDI reaction in forming PLA-MDI-PLA network. Furthermore, increased PLA-MDI-PLA and SF-SF interactions lead to phase separation of PLA and SF phases resulting in aggregation and formation of larger size PLA-PLA and SF-SF particles as shown in Figure 6.4. The aggregation of SF particles into larger size particles instead of binding with PLA clusters is further discussed in the morphology section.

For MSF/PLA, the σ was 59 MPa, a 12.5% increase from SF/PLA. The protein structure in SF was partially unfolded during modification, which resulted in increased molecule mobility and exposure of the hydrophobic groups, leading to enhanced hydrophobic interaction between MSF and PLA. When MDI was added to the MSF-PLA system, mechanical properties remained unchanged.

6.4.2 Thermal Properties

Figure 6.1 shows the DSC thermograms of PLA and its blends. The thermograms were obtained from the second heating scan to avoid heat history effects. Table 6.2 shows the summary of DSC results, which reveal the glass transition and crystallization/melting behaviors of the PLA component in the blends. The T_g of PLA in the blends was slightly lower than that of pure PLA. Cold crystallization was observed for pure PLA and the blends, except for WF/PLA (Figure 6.1). Compared with pure PLA, the cold crystallization of PLA in the blends occurred at lower temperatures in a narrower temperature range. The depression of cold crystallization temperature (T_c) indicates an enhanced crystalline ability of PLA. Furthermore, PLA in the SF/PLA and MSF/PLA with and without MDI showed much higher crystallization enthalpy (ΔH_c) and melting enthalpy (ΔH_m) than pure PLA, indicating a higher crystallinity (X_m) for those blends (Table 6.2). We attribute this to the increased nucleation and accelerated crystallization of PLA induced by SF and MSF. Similar results were reported by Zhang et al.[8] for PLA and SPI/SPC blends. Also, the T_c of MSF/PLA and MSF/PLA/MDI was further reduced by 5 K and 10 K, respectively, compared with that of SF/PLA.

The WF/PLA without and with MDI showed differences in cold crystallization and melting compared with other types of blends. For WF/PLA, no cold crystallization was observed and the X_m was quite low (3.5%) (Table 6.2). When MDI was added, a small cold crystallization peak was observed and the X_m increased to 15.41%, which is still much lower than that of PLA in other blends. Because WF is much larger than SF and MSF, WF is less likely to act as a nucleation agent in the formation of PLA crystallites (Sun et al., 1999). Moreover, the larger size of WF acts as a diffusion barrier that reduces the mobility of PLA chains, and this inhibits crystal growth. The effect of filler size on crystal growth was reported by Sun et al. (2007) in PLA/starch/MDI (55/45/0.5 w/w/w) blends. Also, Pilla et al. (2008) reported that the surface chemistry of fibers might be another important factor for crystal formation in PLA-based composites.

The double melting behavior of PLA in the blends (SF/PLA, SF/PLA/MDI, MSF/PLA, MSF/PLA/MDI) observed in the current study has been explained previously by the melt-recrystallization model (Yasuniwa et al., 2004). The lower temperature peaks (~411 -417 K) and the higher temperature peaks (~418–423 K) are due to the melting of a certain amount of previously formed PLA crystals and the melting of crystals formed through a melt-recrystallization process, respectively. For pure PLA, double melting peaks were also observed previously when the melt-crystallizing samples were heated at a heating rate below 10 K/min (Yasuniwa et al., 2004). Multiple melting behaviors of many semicrystalline polymers, such as poly(ethylene terephthalate) and poly(butylenes terephthalate), have be reported elsewhere (Tan et al., 2000; Yasuniwa et al., 2000).

The TGA thermograms of the fillers, PLA, and its blends are presented in Figures 6.2A and 6.2B, and the thermogravimetric data are summarized in Table 6.3. The onset and end decomposition temperatures (T_{onset} and T_{end}) of SF, MSF, and WF were 513 K and 645 K, 513 K and 628 K, and 566 K and 672 K, respectively (Figure 6.2A). The maximum rate of decomposition (T_{max}) for WF was 645 K, which was about 50 K higher than the T_{max} for SF and MSF. The TGA results of the fibers indicate that WF possesses higher thermal stability than SF and MSF. For pure PLA, the thermal decomposition ranged from 608 K to 657 K, with T_{max} of 646 K (Figure 6.2B). Both SF/PLA and SF/PLA/MDI showed similar

decomposition characteristics, with T_{onset}, $T_{end,}$ and T_{max} of 591 K, 631 K, and 620 K, respectively. The MSF/PLA and MSF/PLA/MDI exhibited a lower T_{max} of 596 K. In summary, the T_{onset}, T_{end}, and T_{max} for SF/PLA and MSF/PLA without and with MDI were similar. This indicates that the effect of MDI on the decomposition behavior was minimal. On the basis of T_{onset}, T_{end}, and T_{max} values, WF/PLA blends exhibited higher degree of thermal stability. Furthermore, for WF/PLA with MDI, the T_{max} was 10 K higher than that of WF/PLA. The increased thermal stability of WF/PLA/MDI is due to the improved coupling effects between PLA and WF facilitated by MDI. Because the tar and ash content of the fibers is higher, the residual sample weight of PLA blends at temperatures above 660 K is higher than that of pure PLA.

6.4.3 Morphology

Among the three fillers, SF had the smallest average size (~5–15 μm) and was more particulate and conventional (spherical) in shape (Figure 6.3). After modification, the compact spherical structure of SF was partially unfolded, resulting in more irregular shapes and a larger size (~10–20 μm). The WF existed in spherical, rod, and nonconventional geometric forms and was the largest in size (~25 μm in diameter and ~150–250 μm in length) compared with SF and MSF. Poly(lactic acid) exhibits a smooth and continuous fracture surface corresponding to the absence of ductility. This demonstrates that the fracture mode was predominantly brittle and is supported by the low elongation values shown in Table 6.1.

The SF/PLA and MSF/PLA blends showed pores of average size of 5–20 μm (Figure 6.4) that could be caused by the poor packing properties of SF and MSF. With the addition of MDI, the degree of porosity decreased significantly in both SF/PLA and MSF/PLA. Furthermore, PLA and SF phases formed larger aggregates in SF/PLA/MDI than in SF/PLA. We attribute this to the interpenetration of MDI leading to increased PLA-MDI-PLA and SF-SF interactions and resulting in formation of large aggregations of PLA and SF particles. The aggregation of PLA and SF phases is a consequence of differences in the kinetics of PLA-MDI and SF-MDI reactions and the relatively higher rate of consumption of MDI in forming PLA-MDI-PLA phase and its phase separation from the SF phase as shown in Figure 6.4. Moreover, increased SF-SF interaction and aggregation with the addition of MDI are also

possible due to pH changes of the environment surrounding the protein molecules. The modification of ionic environment with the addition of salts, acids and bases and the resulting protein-protein interaction and aggregation has been reported for pea proteins (Shand et al., 2007).

Because of the difference between the hydrophobic PLA and hydrophilic WF and the irregularity in size and geometry, WF particles are unevenly distributed throughout the PLA matrix. For WF/PLA, features corresponding to fiber pull-out from PLA matrix were observed, and the fiber surface appeared smooth. With the addition of MDI, some broken WF fibers were observed on the fracture surface, and the fibers were partially coated with PLA matrix, indicating an improved interfacial adhesion between PLA and WF. For MSF/PLA, because of increased irregularity in shape and the larger size of MSF compared with SF, the packing was poor as observed by the large number of heterogeneous interfaces between MSF and PLA in the micrograph. With the addition of MDI, the modification and reduction of the heterogeneous interfaces between MSF and PLA was minimal. We attribute the lack of coupling effect of MDI to the diffusional constraints at the interfaces between MSF and PLA to increased dynamic heterogeneity of MSF, which is due to modification and partial unfolding of proteins. In summary, an absence of the conventional coupling mechanism in SF/PLA/MDI and MSF/PLA/MDI was observed.

6.4.4 DMA and Relaxation Characteristics

Figures 6.5 and 6.6 show direct measurements of B' and B'' during the course of heating the specimen from 275 K to 363 K. For PLA and PLA blends, B' increased gradually with heating between 275 K and 323 K, reached a peak value, and then declined sharply toward an asymptotic value at temperatures higher than 350K (Figures 6.5A and 6.6A). The peak appeared at different temperatures for different samples. The measured initial B' at 275 K, $B'_{initial}$, the peak value, B'_{peak}, the final asymptotic value, B'_{final}, $\Delta B'_1$ (= B'_{peak} - $B'_{initial}$), and $\Delta B'_2$ (=B'_{peak} - B'_{final}) are listed in Table 6.4.

Briefly, because a low heating rate (3 K/min) and sinusoidal frequency (1 Hz) were used in these experiments, for the temperature range from 275 K to 323 K for a nonequilibrium state, the measured B' varied ($\Delta B'_1$, equals to B'_{peak} - $B'_{initial}$) during the

oscillation time and is, therefore, time dependent. It is phenomenologically equivalent to the time-dependent heat capacity in a study of thermal relaxation (Andersson, 1997). The time-dependent behavior of B' during the oscillation measurements was also observed for other composite materials in a study of thermal relaxation (Andersson, 1997). The consequences of time dependency of B' are relaxation of the nonequilibrium structure, densification of molecular structure and aging, decrease of fictive temperature (Tool, 1946) and, thus, increase of the relaxation time. Furthermore, the densification and aging effects contribute to the increase in B', which is due to the decrease in the vibrational part of B' and analogous to the decrease in the vibrational part of heat capacity with temperature, as observed from fixed sinusoidal frequency measurements (Tombari et al., 2002). In summary, the increase in B' in the temperature range of 275 K to 323 K is considered as a characteristic of kinetic unfreezing of a nonequilibrium disordered structure on heating and the resulting densification and aging effects. The PLA and PLA blends exhibited different values of $\Delta B'_1$ (Table 6.4). Because the $\Delta B'_1$ values vary substantially for different samples because of the effect of different degrees of aging, the relative values of B' at 298 K (Table 6.4) were used to correlate with the Young's modulus (E) (Table 6.1), which was also measured at 298K. The moduli (B' and E) measured at 298K correlate fairly well, with a regression value of r^2 = 0.64, with the exception of SF/PLA/MDI and MSF/PLA/MDI samples. The lack of correlation in these two samples suggests the absence of a conventional coupling mechanism of MDI with PLA, SF, and MSF. This fact was discussed previously in the morphology section. In addition, the correlation between B' and E was also affected by the differences in thermal and aging histories between samples obtained for DMA and tensile characterization before and during testing. Furthermore, the sinusoidal oscillation stimulus of 1 Hz was used in the flexural mode for the DMA test, and a constant displacement rate of 5 mm/min was used in uniaxial tensile mode for the tensile test.

In Figures 6.5A and 6.6A, for PLA and PLA blends, B' decreased ($\Delta B'_2$, equals to $B'_{peak} - B'_{final}$) between 323 K and 363 K. The shapes of these plots resemble the B' and B'' spectra of the irreversible structural changes that occur with (1) polymerization at a constant temperature and (2) relaxation in the frequency, ω, domain (Alves et al., 2004; Li et al.,

2000), where ω is varied at a constant temperature. The B'_{peak} in Figures 6.5A and 6.6A represents the unrelaxed flexural modulus, B_U, of the sample and does not contain all contributions from molecular modes that fail to relax within the observation time. The high temperature plateau value of B', B'_{final}, represents the relaxed flexural modulus, B_R, of the sample when the characteristic relaxation times of the PLA molecular modes are shorter than the experimental window and contains contributions from all the relaxed modes. In contrast to the aging effects, for which B' increases with heating, the decrease in B' in the temperature range of 323 K to 363 K is attributed to relaxational effects. The competing effects of aging and relaxation lead to the appearance of a peak in B' measurements, and the degree of aging determines the peak size. For PLA, SF/PLA/MDI, and MSF/PLA samples that exhibit a high degree of aging, the peak in B' is high, which results in the absence of a distinct plateau value of B_U. For WF/PLA, WF/PLA/MDI, SF/PLA, and MSF/PLA/MDI samples that exhibit a lower degree of aging, the peak in B' becomes vanishingly small and gives the appearance of a clear plateau value of B_U.

To explain the relaxational effects on dynamic B of the samples with increasing temperature, T, the T dependent complex flexural modulus, B^*, for a constant frequency according to Boltzmann superposition principle can be expressed as: (McCrum et al., 1991)

$$B^*(T) = B'(T) + iB''(T)$$
$$B^*(T) = B_R(T) + \left(B_U(T) - B_R(T)\right)\left[1 - \int_0^\infty e^{-i\omega t}\left(\frac{\partial \phi(t)}{\partial t}\right)_T dt\right] \qquad (2)$$

For the dynamics of molecular motions which are activated on heating and are responsible for the vibrational and configurational contributions and that involves a summation or distribution of relaxation modes with various relaxation amplitude and relaxation time components, the phenomenological expression for the relaxation function, $\phi(t)$, is generally defined as:

$$\left[\phi(t)\right]_T = \exp\left\{-\left[\frac{t}{\tau(T)}\right]^{\beta(T)}\right\} \qquad (3)$$

Equation 3 is known as the stretched exponential function, or Kohlrausch-Williams-Watts function (KWW) (Kohlrausch, 1854; Williams & Watts, 1970), where τ is the characteristic relaxation time, β ($0 < \beta < 1$) is the stretch parameter describing the non-exponential nature of the relaxation, and t is the time for the observation of the perturbation's relaxation. The various relaxation modes are an indication of dynamic heterogeneity arising from the existence of different physical and chemical states in a material. Each mode corresponds to heterogeneity of number of hydrogen bonds, covalent bonds, ions, or ion-pairs, to a certain flexibility of a molecule, chemical structures, local environments, interfaces, cooperativity length scales and size and different molecular modes or mechanisms (Goldstein, 1969; Stillinger & Weber, 1982; Wales, 2003). The KWW function has been used to explain the linear relaxation behavior of materials, the motion of carriers in amorphous semiconductors and a variety of chemical physics problems (Dishon et al., 1985).

In this case, B' and B'' can be measured accurately only when $\frac{dT}{dt}$ and $\frac{d\tau}{dt}$ are insignificant during the acquisition of successive data points ($\Delta T \sim 0.25$ K, $\Delta t \sim 5$ seconds between successive data points). The KWW expression in Eq. 3 is used in Eq. 2 because the KWW function has been transformed and numerically integrated (Dishon et al., 1985) to obtain the flexural complex, storage and loss moduli components. The expressions for the separated storage and loss components can be written as:

$$B'(T) = B_R(T) + (B_U(T) - B_R(T))N' \quad \textit{and} \quad B''(T) = (B_U(T) - B_R(T))N'' \tag{4}$$

where N' and N'' are the normalized real and imaginary parts of the integral in Eq. 2. The numerical solutions of N' and N'' obtained by using series expressions have been reported for a set of $\omega\tau$ values (Dishon et al., 1985). For the small range of T in which the relaxation features are shown in Figures 6.5 and 6.6, the terms $[B_U(T) - B_R(T)]$ and $\beta(T)$ change with T negligibly in comparison with the many orders of decrease in $\tau(T)$. By assuming the B_U, B_R, and β in Eqs. 2, 3, and 4 are T independent, Eq. 2 can also be rewritten as:

$$B^*(T) = B_R + (B_U - B_R)\left[1 - \int_0^\infty e^{-i\omega t}\left(\frac{\partial \phi(t)}{\partial t}\right)_T dt\right] \quad (5a)$$

where $[\phi(t)]_T = \exp\left\{-\left[\frac{t}{\tau(T)}\right]^\beta\right\}$ (5b)

Because N' and N'' in Eq. 4 have been solved for a set of $\omega\tau$ values, Eq. 4 becomes invariant of one's choice of ω or τ. In this manner, each data point for a single frequency is described by $\omega\tau(T)$, Kramers-Kronig relations are obeyed, and the entire curve in Figures 6.5 and 6.6 is described by β and $\omega\tau(T)$.

By analyzing the data from Figures 6.5 and 6.6 according to Eq. 4, we determined β, ΔB (equals to $B_U - B_R$), and B_R for each set of B' and B''; results are shown in Table 6.5. As an example, B' and B'' obtained using Eq. 4 are plotted with the experimental data for MSF/PLA and shown in Figures 6.7A and 6.7B. The calculated values of B' and B'' match the experimental data reasonably well. The characteristic relaxation time, τ, was calculated for each point by determining the product, $\omega\tau(T)$, for each calculated value of B' and B'' as described previously for the dielectric data (Ferrari et al., 1996; Venkateshan & Johari, 2004). Because ω is a constant, this yields a value of τ for each value of B^* calculated for a certain T during the course of heating. The resulting values of τ in natural logarithmic scale (ln) are plotted against T^{-1} for the seven samples and are shown in Figures 6.8A and 6.8B. Because the dynamic heterogeneity of the seven samples is low, as indicated by the higher β values, the nonlinearity of the evolution of ln τ with T^{-1} is expected to be low. To determine the linearity of ln τ vs. T^{-1} plots, the calculated τ data in Figures 6.8A and 6.8B were fit using a linear equation; the regression values (r^2) ranged from 0.93 to 0.99 (Table 6.5), evidence of an adequate degree of linearity. By considering the definition of T_g as the temperature at which the mechanical, structural, or viscosity relaxation times attain a value of 100 sec (Bohmer et al., 1993; Bohmer & Angell, 1994) and by using the linear fits for the seven samples in Figures 6.8A and 6.8B, we calculated the temperatures at which the τ values were equal to 100 sec; results are tabulated in Table 6.5. The temperatures determined for τ = 100 sec from the DMA analysis are in close agreement with the T_g determined from DSC experiments (Table 6.5). Because the samples exhibited a low degree of dynamic

heterogeneity and the plots of ln τ vs. T^{-1} are linear, we conclude that the degree of deviation of the fictive temperature from T is low, and thus ln τ as a function of T^{-1} can be expressed in the Arrhenius form (Aou et al., 2007):

$$\ln \tau = \ln A + \frac{\Delta E}{RT} \qquad (6)$$

where A is the pre-exponential factor, ΔE is the activation energy for mechanical relaxation, and R is the universal gas constant. The ΔE determined from the slopes of ln τ vs. T^{-1} plots for the seven samples are listed in Table 6.5. The calculated ΔE for the seven samples are in the range of 461 to 637 kJ/mol, which is in close agreement with the literature values for PLA of varying tacticity and other polymers (Aou et al., 2007; Li et al., 2000).

6.4.4.1 Dynamic Heterogeneity and KWW Parameter (β)

For PLA, $\beta = 0.75$ and is higher than that for other polymers (Aou et al., 2007; Ferrari et al., 1996; Mano & Gomez-Ribelles, 2003), an indication that the glass-liquid transition dynamics of the relaxing moieties are homogeneous and the evolution of τ with temperature is Arrheniun in nature, where densification effects dominate. For WF/PLA, $\beta = 0.71$, and the disconnected nature of the heterogeneous WF fibers with interfaces are observed in the micrograph (Figure 6.4). For WF/PLA/MDI, $\beta = 0.80$, an indication of the coupling effect of MDI in binding PLA and WF resulting in a lower heterogeneity compared with that of WF/PLA. For SF/PLA, $\beta = 0.78$, an indication of homogeneous relaxational dynamics. For SF/PLA/MDI, $\beta = 0.74$, and, as discussed previously, the interpenetration of MDI leads to lower compatibility between PLA and SF particles and increased dynamic heterogeneity. For MSF/PLA and MSF/PLA/MDI, $\beta = 0.72$ and 0.70, respectively. Because the protein molecules in MSF are partially unfolded, additional dynamic heterogeneity is incorporated. Furthermore, the increased configurational contribution arising from the partial unfolding of protein molecules increases the heterogeneity at PLA and MSF interfaces and makes the coupling effect of MDI minimal.

Though the β values among PLA and its blends are not consistent with all the microstructures shown in Figure 6.4, it was expected that incorporating various fillers would significantly change the dynamic heterogeneity because of different physical and chemical

states at the interphase regions between amorphous clusters of different cooperativity sizes and length scales and the amorphous phases of PLA, WF, SF, and MSF (Guo et al., 2005; Ngai & Paluch, 2004).

In general, β values for PLA and its blends ranged from only 0.71 to 0.81, which is higher than β values obtained for other composites (Aou et al., 2007; Ferrari et al., 1996; Mano & Gomez-Ribelles, 2003). We conclude that PLA and its blends exhibit a highly homogeneous relaxational dynamics mechanism in their transition from glass to liquid that is due to the high degree of hydrophobicity of PLA, SF, and MSF, where densification effects dominate.

The values of ΔB and ΔC_p (Tables 6.5 and 6.2) for the seven samples correlate fairly well ($r^2 = 0.79$), which was expected from the correlation between the mechanical and thermal responses measured with DMA and DSC, respectively, as the material evolved from a glassy to liquid state during heating. The thermal and mechanical modes would contain both vibrational and configurational contributions (Venkateshan & Johari, 2006).

6.4.4.2 Activation Energy (ΔE)

The calculated ΔE for PLA is higher than those for its blends (Table 6.5), which is predominantly dependent on the composition and overall composite material density. The densities of PLA, SF, and WF are 1.24, 0.5, and 0.2 g/cm^3, respectively, showing that the densities of both PLA and SF are much higher than the density of the WF. Therefore, PLA had higher ΔE value than its blends. The SF/PLA blends with or without MDI had similar ΔE values, but values were higher than those of WF/PLA blends or MSF/PLA blends; this is a result of the higher density of SF and partially due to the large protein molecules in SF. The protein molecules in MSF were partially unfolded and would need less thermal energy to activate molecular mobility; thus, the ΔE values of MSF/PLA with or without MDI were lower than that of the SF/PLA blend. Comparing the ΔE values of WF/PLA blends with or without MDI, the coupling mechanism of MDI reinforcing the fiber-PLA interface resulted in an increase in ΔE from 461 to 521 kJ/mol.

In semicrystalline polymeric materials, the presence of crystalline regions influences the landscape because they will explore the lowest possible minima with a higher curvature,

similar to densification effects. Because the lowest energy minima of greater curvature have a higher vibrational frequency (Goldstein, 1969; Stillinger & Weber, 1982; Wales, 2003) and the curvature determines the instantaneous elastic moduli, the energy barrier (ΔE) to another minimum would be higher (Goldstein, 1969; Stillinger & Weber, 1982; Wales, 2003). In addition to influencing ΔE between different minima, the presence of crystalline regions and densification may influence the number of minima and the overall dynamic heterogeneity. However, the effect of crystallinity was not considered in the ΔE discussion because the crystallinity of PLA and its blends was similar (~25%), based on the DSC first scan data (data not shown). Furthermore, the ΔE of PLA and its blends did not correlate with the dynamic heterogeneity, as reported for other materials (Vyazovkin et al., 2006). The lack of correlation between ΔE and β indicates that the effects of dynamic heterogeneity and the coupling between the different minima do not influence the barrier height in the landscape.

6.5 Conclusions

Poly(lactic acid) blends with improved tensile mechanical properties were successfully prepared by intensive mixing followed by compression molding. Methylene diphenyl diisocyanate was an effective coupling agent for the WF/PLA system, resulting in improved tensile strength and elongation. Modification of SF with $NaHSO_3$ was also an effective way to increase the mechanical properties of the SF/PLA system. Results from DSC revealed that SF and MSF, but not WF, could act as nucleation agents to induce and accelerate the crystallization of PLA in the blends, resulting in much higher crystallinity.

Mechanical relaxation behaviors were well characterized on the basis of DMA results. The temperature-dependent mechanical relaxations of PLA and its blends with WF, SF, and MSF with and without MDI were analyzed using the KWW relaxation function, and information such as τ, β, and ΔE were obtained. Poly(lactic acid) and its blends exhibited highly homogeneous relaxational dynamics in their transition from glass to liquid during heating because of the high degree of hydrophobicity and densification effects of PLA, SF, and MSF. The homogeneous relaxation is evidenced by the high values of β (0.70 to 0.80) obtained for PLA and its blends and the corresponding linearity of the $\ln \tau$ vs. T^{-1} plots.

The thermal and mechanical behavior of PLA and its blends correlated well as shown by the good agreement between (1) ΔC_p and ΔB and (2) T_g values determined by DSC and DMA (τ = 100 sec) techniques. Activation energy of PLA and its blends with WF, SF, and MSF is mainly affected by their densities and compositions.

6.6 Acknowledgments

The authors gratefully acknowledge the financial support of USDA/NRI. Contribution No. 09-382-J from the Kansas Agricultural Experiment Station.

6.7 References

Alves, N. M., Gomez-Ribelles, J. L., Gomez Tejedor, J. A., & Mano, J. F. (2004). Viscoelastic behavior of poly(methyl methacrylate) networks with different cross-linking degrees. Macromolecules, 37, 3735-3744.

Anderson, K. S., Schreck, K. M., & Hillmyer, M. A. (2008). Toughening polylactide. Polym. Rev., 48, 85-108.

Andersson, O. (1997). Simulation of a glass transition in a hot-wire experiment using time-dependent heat capacity. Intl. J. Thermophys, 18, 195-208.

Aou, K., Hsu, S. L., Kleiner, L. W., Tang, F. W. (2007). Roles of conformational and configurational defects on the physical aging of amorphous poly(lactic acid). J. Phys. Chem. B, 111, 12322-12327.

Aranguren, M. I., Racz, I., & Marcovich, N. E. (2007). Microfoams based on castor oil polyurethanes and vegetable fibers. J Appl Polym Sci, 105, 2791-2800.

ASTM D 638-91 (1992). In Annual Book of ASTM Standards; American Society for Testing and Materials: Philadelphia, Vol.8.01, p 161.

Bhardwaj, R., & Mohanty, A. K. (2007). Advances in the properties of polylactides based materials: A review. J Biobased Mater Bioenergy, 1, 191-209.

Bohmer, R., & Angell, C. A. (1994). In Disorder Effects on Relaxational Processes; Richert, R. and Blumen, A., Ed.; Springer, Berlin.

Bohmer, R., Ngai, K. L., Angell, C. A., & Plazek, D. J. (1993). Nonexponential relaxations in strong and fragile glass formers. J. Chem. Phys., 99, 4201-4209.

Dieteroch, D., Grigat, E., & Hahn, W. (1985). Polyurethane Handbook; Oertel, G., Ed.; Hanser: New York, p 7.

Dishon, M., Weiss, G. H., & Bendler, J. T. (1985). Stable law densities and linear relaxation phenomena. J. Research of National Bureau of Standards, 90, 27-39.

Ferrari, C., Salvetti, G., Tombari, E., & Johari, G. P. (1996). Specific heat relaxation during macromolecule growth. Phys. Rev. E: Stat. Phys., Plasmas, Fluids 54, R1058-R1061.

Goldstein, M. J. (1969). Viscous liquids and the glass transition: a potential energy barrier picture. Chem. Phys., 51, 3728-3739.

Guo, Z., Sautereau, H., & Kranbuehl, D. E. (2005). Evidence for spatial heterogeneities observed by frequency dependent dielectric and mechanical measurements in vinyl/dimethacrylate systems. Polymer, 46, 12452-12459.

Huda, M. S., Drzal, L. T., Misra, M., & Mohanty, A. K. (2006). Wood-fiber-reinforced poly(lactic acid) composites: Evaluation of the physicomechanical and morphological properties. J. Appl. Polym. Sci., 102, 4856-4869.

Jacobsen, S., & Fritz, H. G. (1996). Filling of poly(lactic acid) with native starch. Polym. Eng. Sci., 36, 2799-2804.

Jiang, L., Wolcott, M. P., Zhang, J. W., & Englund, K. (2007). Flexural properties of surface reinforced wood/plastic deck board. Polym. Eng. Sci., 47, 281-288.

Johari, G. P. (1994). In Disorder Effects on Relaxational Processes; Richert, R. & Blumen, A., Ed.; Springer, Berlin.

Kalapathy, U., Hettiarachchy, N. S., Myers, D., & Hanna, M. A. (1995). Modification of soy proteins and their adhesive properties on woods. J. Am. Oil Chem. Soc., 72, 507-510.

Ke, T. Y., & Sun, X. S. (2000). Physical properties of poly(lactic acid) and starch composites with various blending ratios. Cereal. Chem., 77, 761-768.

Kohlrausch, R. (1854). Theorie des elektrischen Rückstandes in der Leidener Flasche. Annalen der Physik, 91, 179-214.

Kuo, M. L., Myers, D. J., Heemstra, H., Curry, D., Adams, D. O., & Stokke, D. D. (2003). Soybean-based adhesive resins and composite products utilizing such adhesives. U.S. Patent 6518387.

Lee, S. Y., Kang, I. A., Doh, G. H., Yoon, H. G., Park, B. D., & Wu, Q. L. (2008). Thermal and mechanical properties of wood flour/talc-filled polylactic acid composites: Effect of filler content and coupling treatment. J. Thermoplast. Compos. Mater., 21, 209-223.

Li, G., Lee-Sullivan, P., & Thring, R. W. (2000). Determination of activation energy for glass transition of an epoxy adhesive using dynamic mechanical analysis. J. Therm. Anal. Calorim., 60, 377-390.

Liu, Y., & Li, K. C. (2004). Modification of soy protein for wood adhesives using mussel protein as a model: The influence of a mercapto group. Macromol. Rapid Commun., 25, 1835-1838.

Mano, J. F., & Gomez-Ribelles, J. L. (2003). Mechanical Spectroscopy studies on a side-chain liquid crystalline polysiloxane. Comparison with dielectric and DSC data. Macromolecules, 36, 2816-2824.

Marcovich, N. E., Bellesi, N. E., Auad, M. L., Nutt, S. R. & Aranguren, M. I. (2006). Cellulose micro/nanocrystals reinforced polyurethane. J. Mater. Res., 21, 870-881.

McCrum, N. G., Read, B. E., & Williams, G. (1991). Anelastic and Dielectric Effects in Polymeric Solids; Dover, NY.

Mosiewichi, M. A., Casado, U., Marcovich, N. E., & Aranguren, M. I. (2008). Vegetable oil based-polymers reinforced with wood flour. Mol. Cryst. Liq. Cryst., 484, 509-516.

Ngai, K. L., & Paluch, M. (2004). Classification of secondary relaxation in glass-formers based on dynamic properties. J. Chem. Phys., 120, 857-873.

Paetau, I., Chen, C. Z., & Jane, J. L. (1994). Biodegradable plastic made from soybean products. 1. Effect of preparation and processing on mechanical properties and water absorption. Ind. Eng. Chem. Res., 33, 1821-1827.

Pilla, S., Gong, S., O'Neill, E., Rowell, R. M., & Krzysik, A. M. (2008). Polylactide-pine wood flour composites. Polym. Eng. Sci., 48, 578-587.

Shand, P. J., Ya, H., Pietrasik, Z. & Wanasundara, P. K. J. P. D. (2007). Physicochemical and textural properties of heat-induced pea protein isolate gels. Food Chem., 102: 1119-1130.

Stillinger, F., & Weber, T. (1982). Hidden structure in liquids. Phys. Rev. A, 25, 978-989.

Sue, H. J., Wang, S., & Jane, J. L. (1997). Morphology and mechanical behaviour of engineering soy plastics. Polymer, 38, 5035-5040.

Sun, X. S., Acioli-Moura, R., & Li, W. (2007). Effects of starch types on mechanical properties of poly(lactic acid)/starch composites. Int. Polym. Proc., 22, 410-417.

Sun, X. S., & Bian, K. (1999). Shear strength and water resistance of modified soy protein adhesives. J. Am. Oil Chem. Soc., 76, 977-980.

Sun, X. S., Zhu, L., & Wang, D. (2008). Latex adhesives derived from ionic strength induced soy protein complexes. U.S. Patent 20080287635 A1.

Sun. X. S., Kim, H. R., & Mo, X. Q. (1999). Plastic performance of soybean protein components. J. Am. Oil Chem. Soc., 76, 117-123.

Takatani, M., Ikeda, K., Sakamoto, K., & Okamoto, T. (2008). Cellulose esters as compatibilizers in wood/poly(lactic acid) composite. J. Wood Sci., 54, 54-61.

Tan, S. S., Su, A. H., Li, W. H., & Zhou, E. (2000). New insight into melting and crystallization behavior in semicrystalline poly(ethylene terephthalate). J. Polym. Sci. Part B Polym. Phys., 38, 53-60.

Tombari, E., Presto, S., Salvetti, G., & Johari, G. P. (2002). Spontaneous decrease in the heat capacity of a glass. J. Chem. Phys., 117, 8436-8441.

Tool, A. Q. (1946). Relation between inelastic deformability and thermal expansion of glass in its annealing range. J. Am. Ceram. Soc., 29, 240-253.

Venkateshan, K., & Johari, G. P. (2006). Dielectric relaxation and elasticity during polymerization. J. Chem. Phys., 125, 054907/1-054907/12.

Venkateshan, K., & Johari, G. P. (2004). Dielectric polarization and the stages of a macromolecule's growth. J. Phys. Chem. B, 108, 15049-15056.

Vyazovkin, S., Sbirrazzuoli, N., & Dranca, I. (2006). Variation in activation energy of the glass transition for polymers of different dynamic fragility. Macromol. Chem. Phys., 207, 1126-1130.

Wales, D. J. (2003). Energy Landscapes, Cambridge University Press, Cambridge.

Wang, H., Sun, X. S., & Seib, P. (2001). Strengthening blends of poly(lactic acid) and starch with methylenediphenyl diisocyanate. J. Appl. Polym. Sci., 82, 1761-1767.

Wang, H., Sun, X. S., & Seib, P. (2002). Mechanical properties of poly(lactic acid) and wheat starch blends with methylenediphenyl diisocyanate. J. Appl. Polym. Sci., 84, 1257-1262.

Williams, G., & Watts, D. C. (1970). Non-symmetrical dielectric relaxation behaviour arising from a simple empirical decay function. Trans. Faraday Soc., 66, 80-85.

Wu, C. S. (2008). Characterizing biodegradation of PLA and PLA-g-AA/starch films using a phosphate-solubilizing Bacillus species. Macromol. Biosci., 8, 560-567.

Yasuniwa, M., Tsubakihara, S., & Murakami, T. (2000). High-pressure DTA of poly(butylene terephthalate), poly(hexamethylene terephthalate), and poly(ethylene terephthalate). J. Polym. Sci. Part B Polym. Phys., 38, 262-272.

Yasuniwa, M., Tsubakihara, S., Sugimoto, Y., & Nakafuku, C. (2004). Thermal analysis of the double-melting behavior of poly(L-lactic acid). J. Polym. Sci. Pol. Phys., 42, 25-32.

Yu, L., Petinaki, S., Dean, K., Bilyk, A., & Wu, D. (2007). Green polymeric blends and composites from renewable resources. Macromol. Symp., 249-250, 535-539.

Yu, L., Dean, K., & Li, L. (2006). Polymer blends and composites from renewable resources. Prog. Polym. Sci., 31, 576-602.

Zhang, C., Li, K., & Simonsen, J. (2006). Terminally functionalized polyethylenes as compatibilizers for wood-polyethylene composites. Polym. Eng. Sci., 46, 108-113.

Zhang, J., & Sun, X.S. (2004). Mechanical properties of poly(lactic acid)/starch composites compatibilized by maleic anhydride. Biomacromolecules, 5, 1446-1451.

Zhang, J. W., Jiang, L., & Zhu, L. Y. (2006). Morphology and properties of soy protein and polylactide blends. Biomacromolecules, 7, 1551-1561.

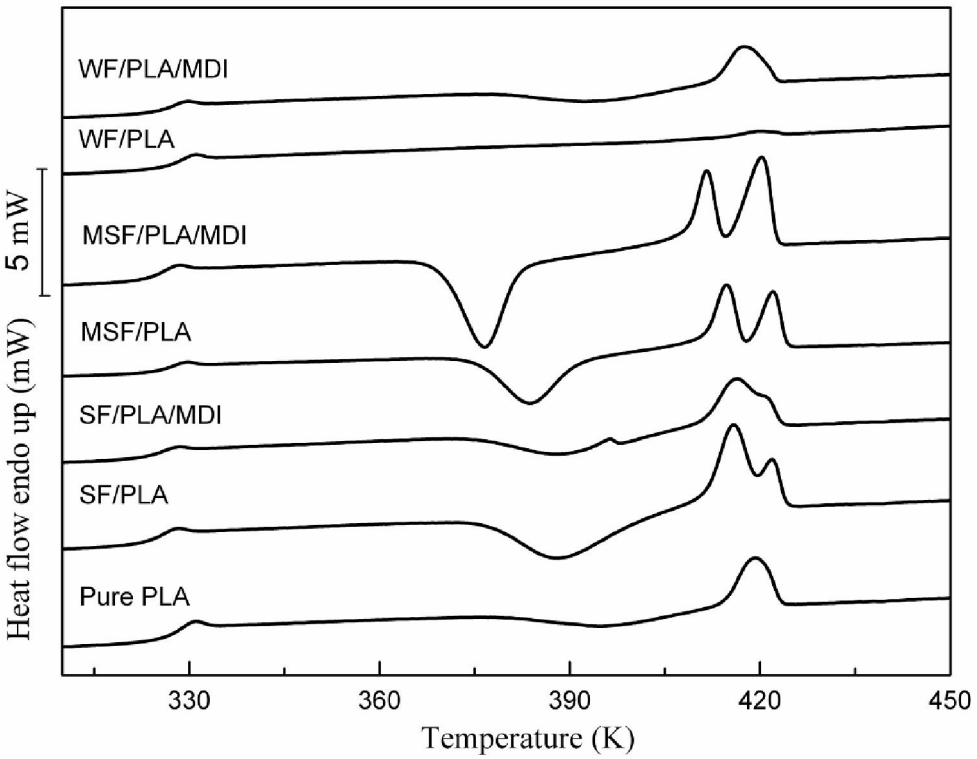

Figure 6.1 DSC thermograms of PLA and PLA blends with WF, SF, and MSF with or without MDI.

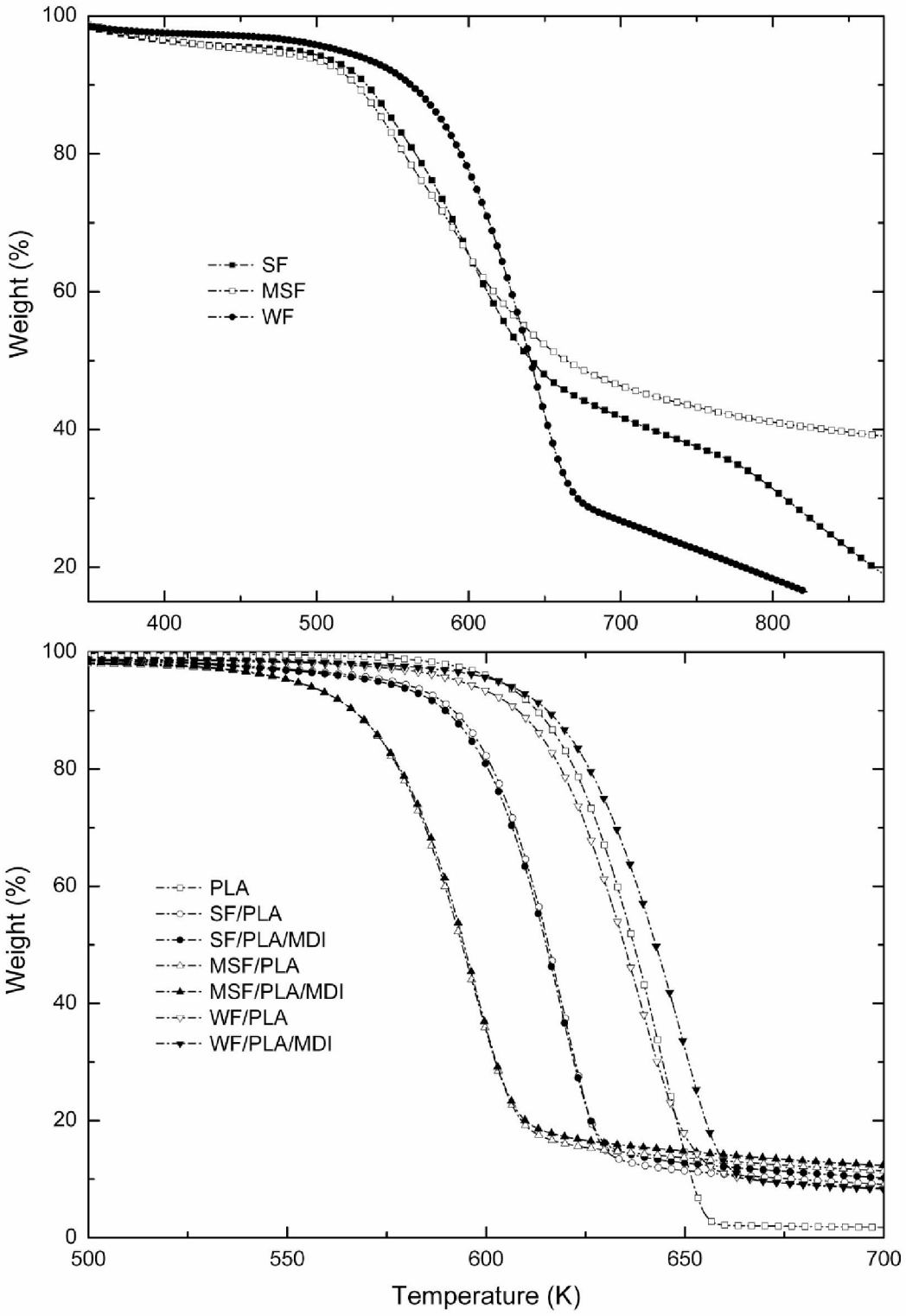

Figure 6.2 TGA thermograms of (A) fillers (SF, MSF, and WF) and (B) PLA and PLA blends with WF, SF, and MSF with or without MDI.

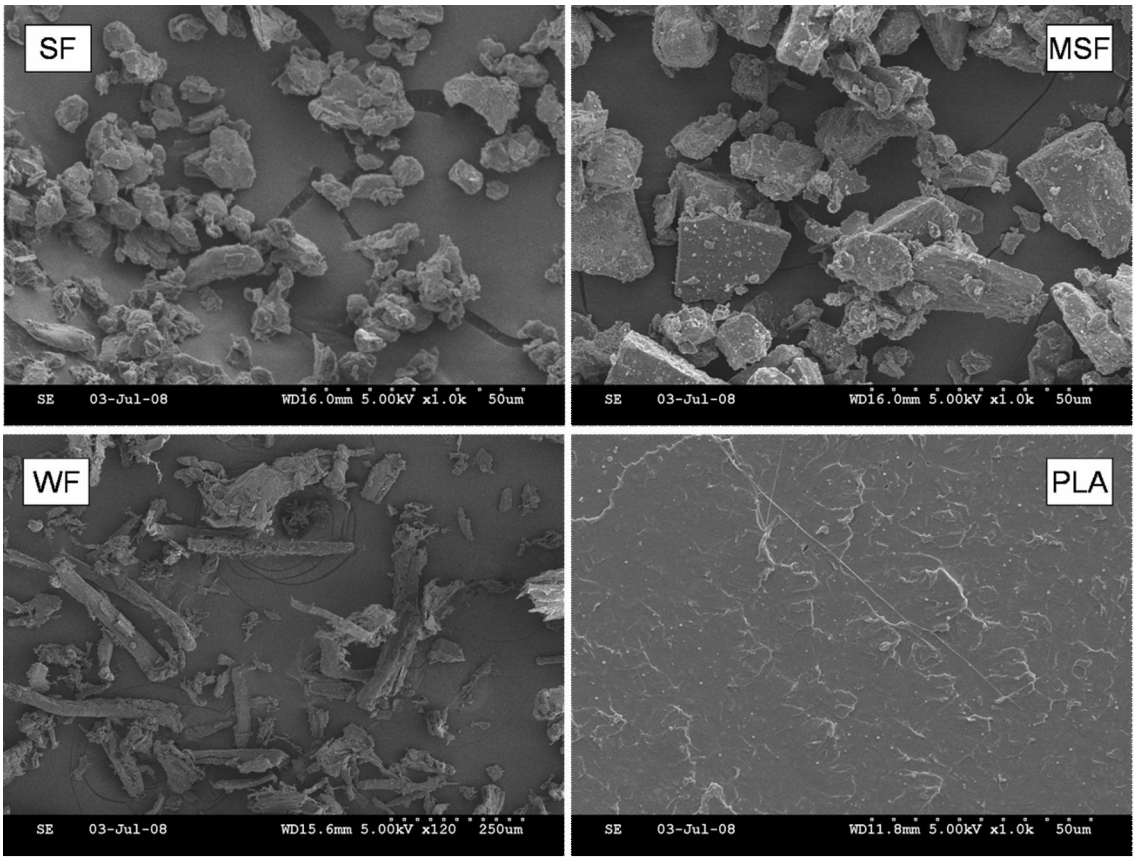

Figure 6.3 SEM micrographs of fillers (SF, MSF, and WF) and PLA. Scale bar is shown at the bottom of each micrograph.

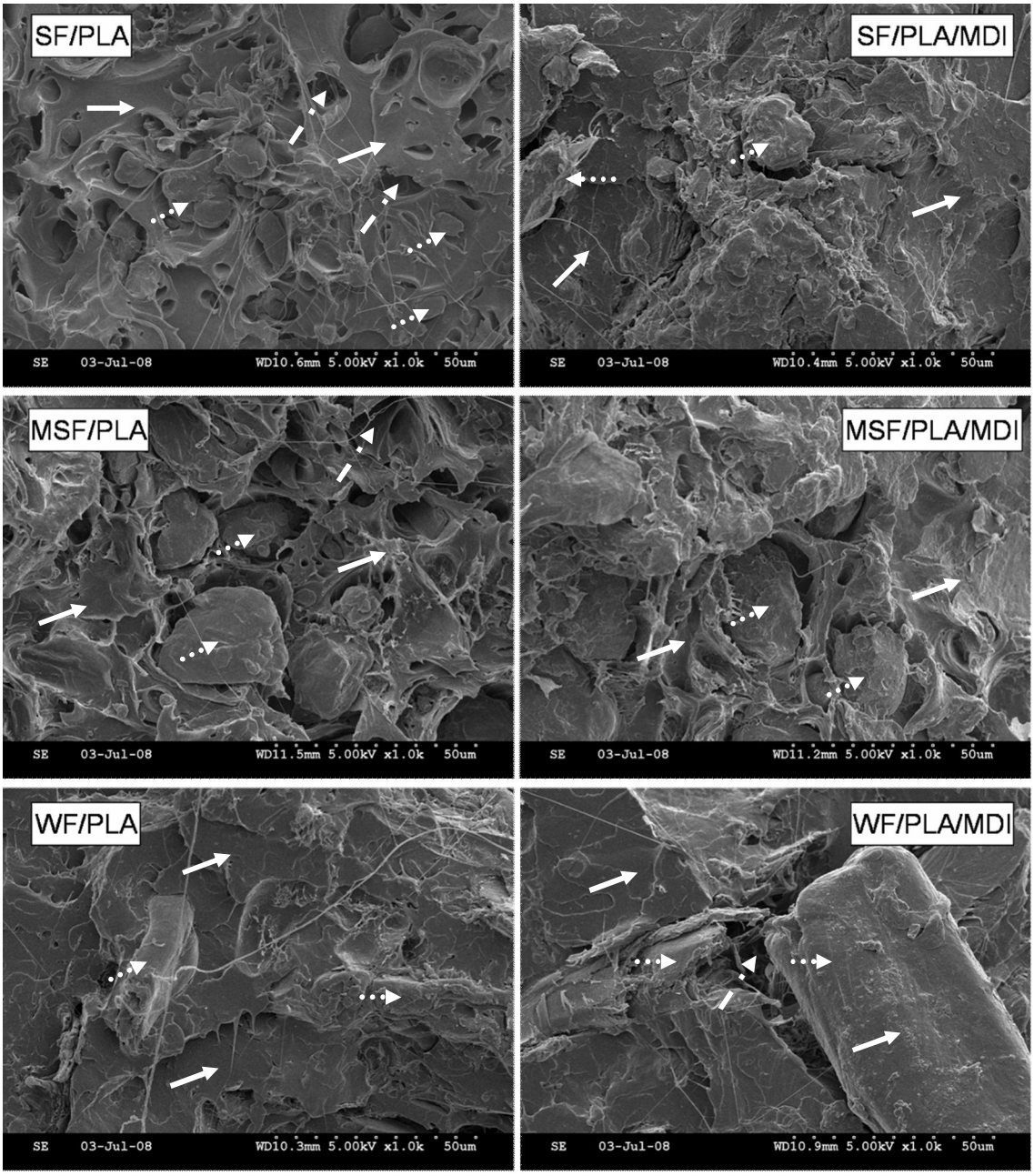

Figure 6.4 SEM micrographs of PLA blends with WF, SF, and MSF with or without MDI. Solid arrow indicates PLA phase; dot arrow indicates fillers; dash dot arrow indicates the air-induced pores. Scale bar is shown at the bottom of each micrograph.

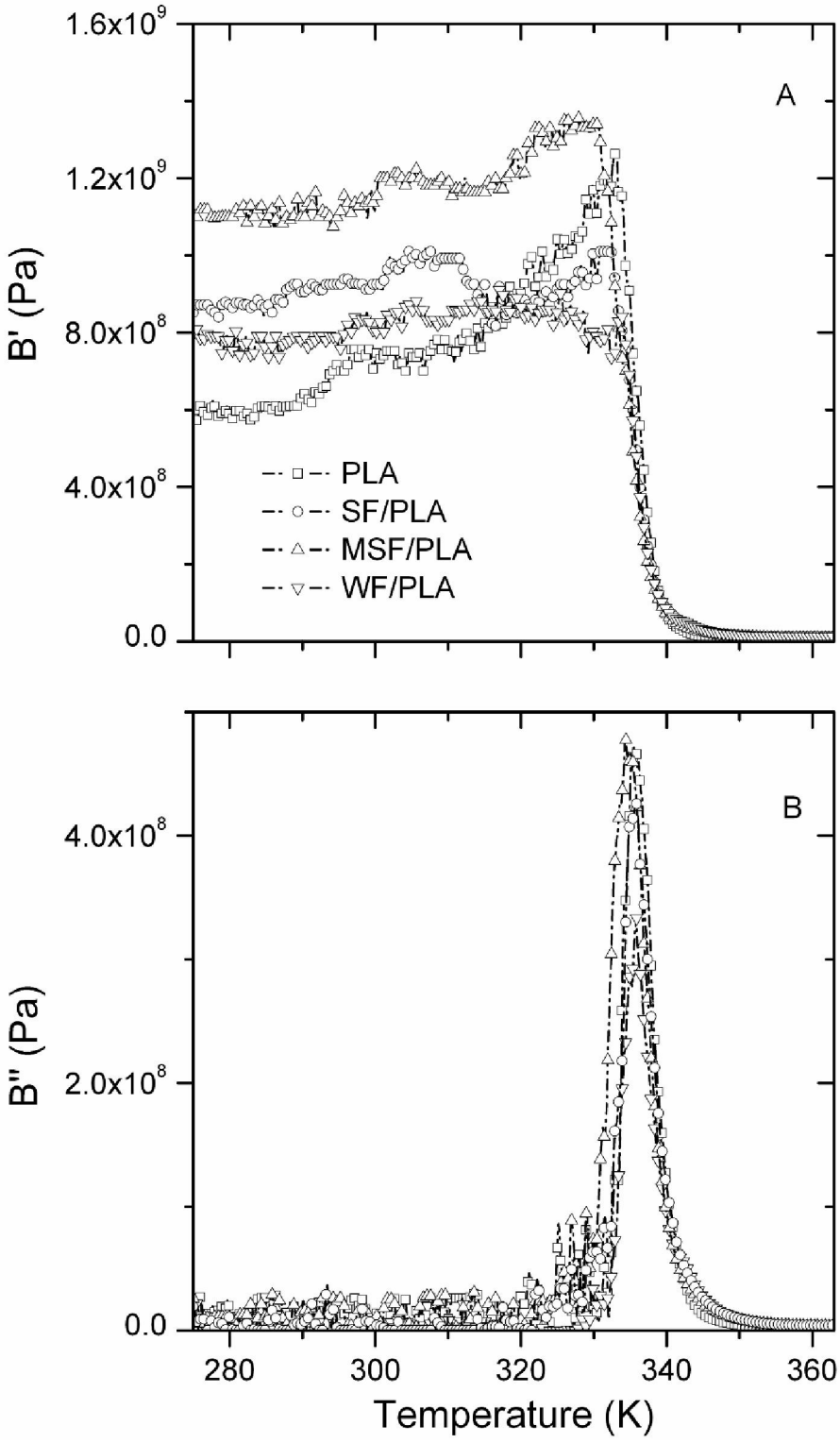

Figure 6.5 (A) Flexural storage modulus (*B′*) and (B) loss modulus (*B′′*) of PLA and PLA blends with WF, SF, and MSF.

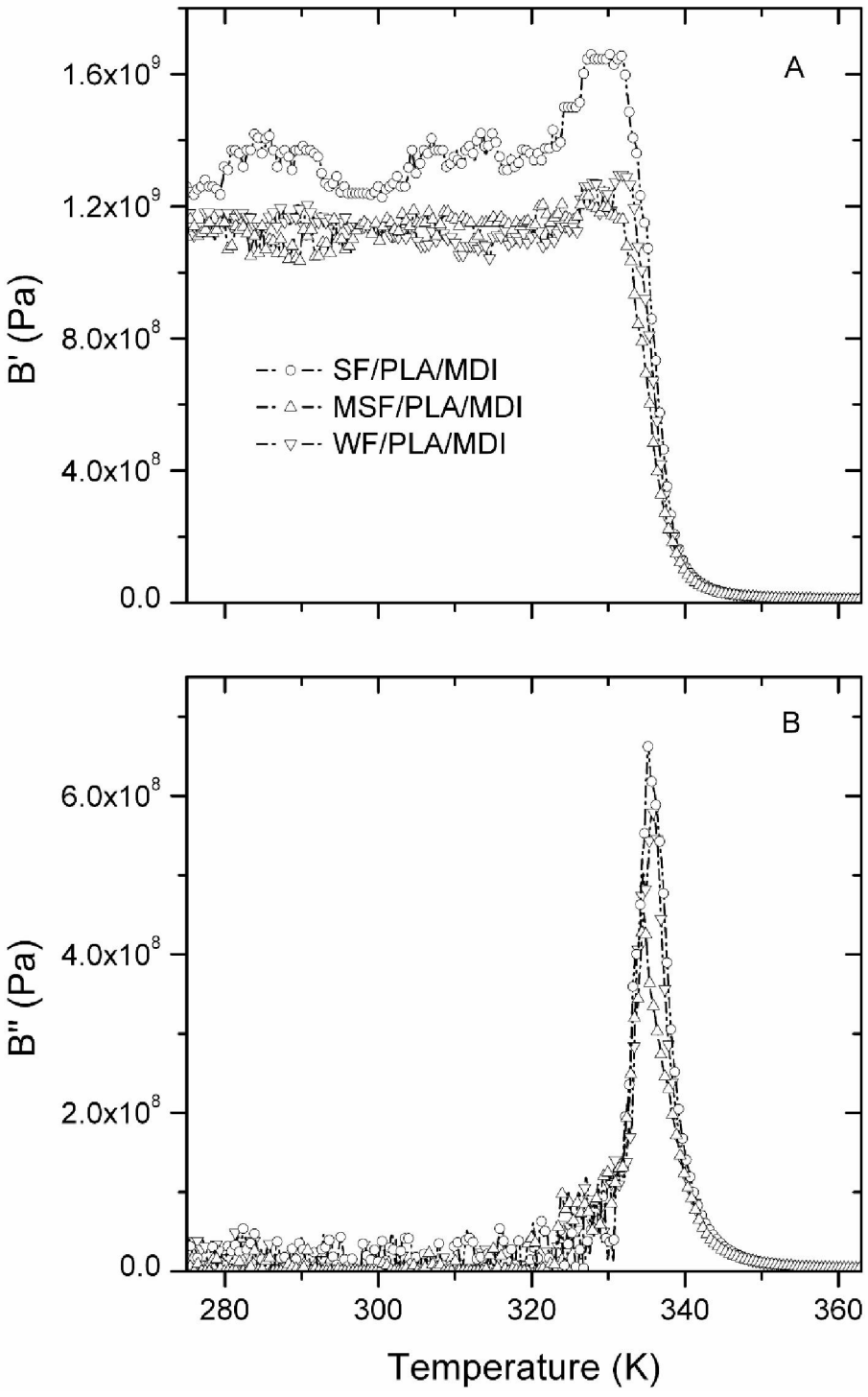

Figure 6.6 (A) Flexural storage modulus (*B′*) and (B) loss modulus (*B″*) of PLA blends with WF, SF, and MSF in the presence of MDI.

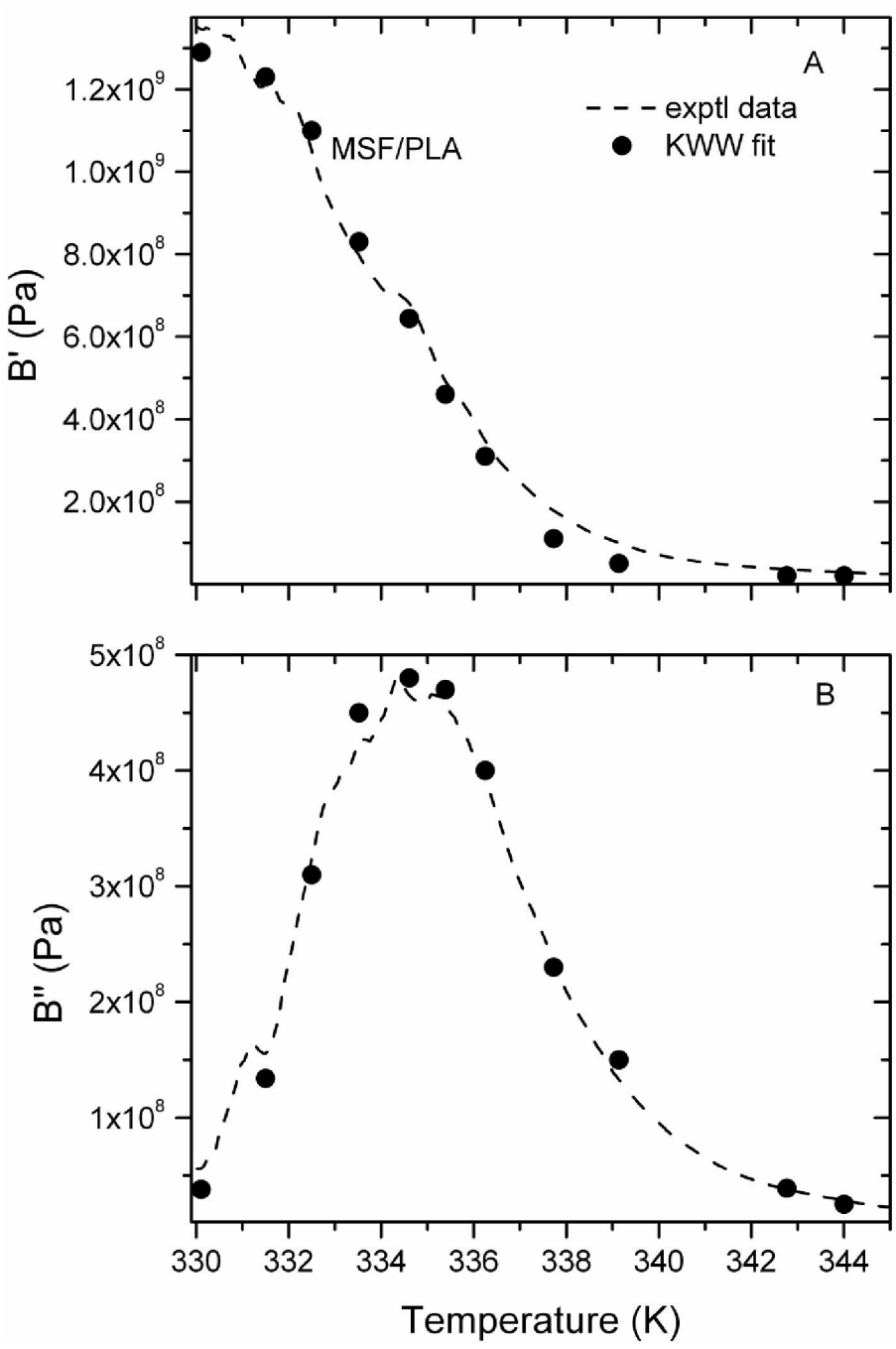

Figure 6.7 Plots of (A) flexural storage modulus (*B′*) and (B) loss modulus (*B″*) against temperature for MSF/PLA. Dotted lines represent experimental data, and filled circles represent data points calculated from Eq. 4.

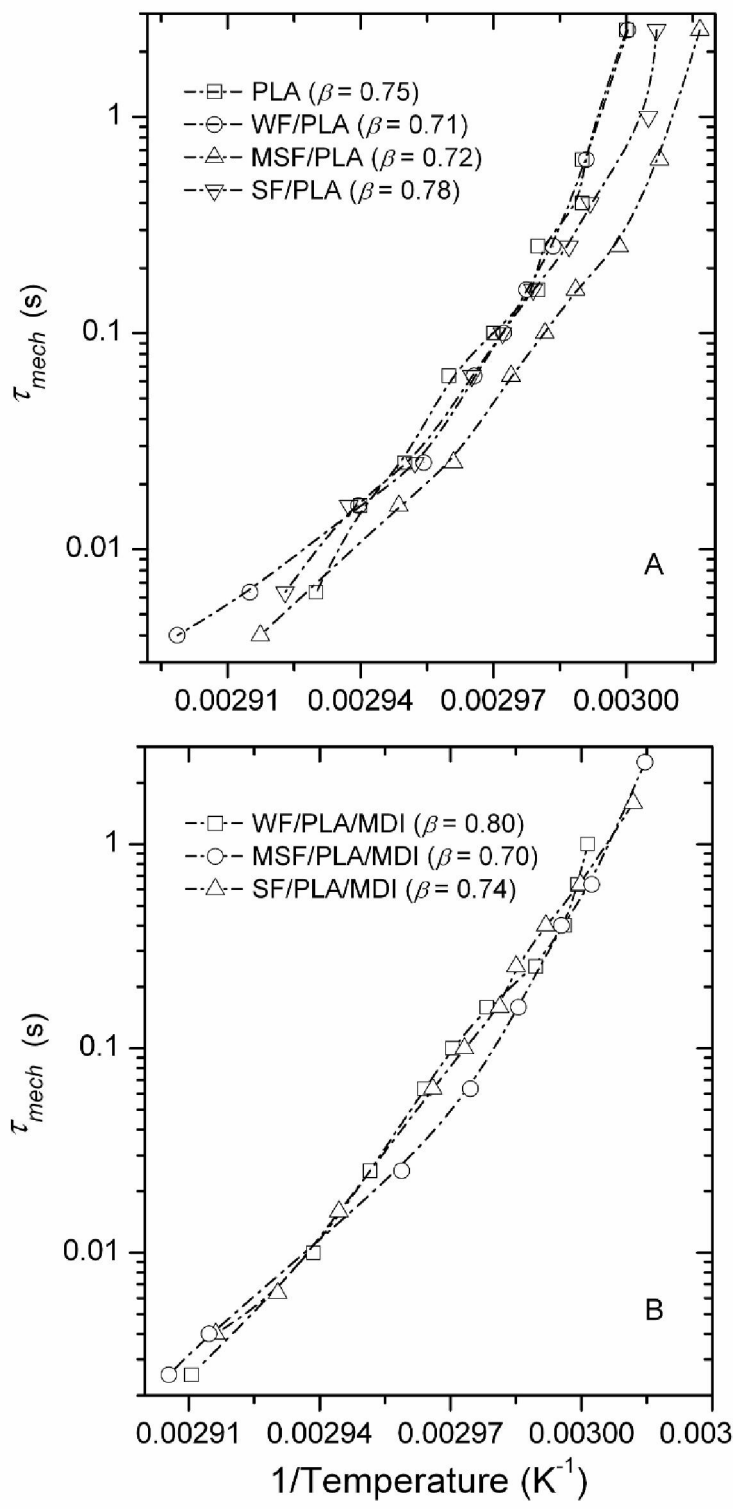

Figure 6.8 Plots of the relaxation time calculated from the *B′* and *B″* data against the inverse of temperature for PLA and PLA blends with WF, SF, and MSF (A and B).

Table 6.1 Mechanical properties of PLA and its blends with WF, SF, and MSF

Samples	Tensile Strength, σ (MPa)	Elongation at Break, ε (%)	Young's Modulus, E (GPa)
PLA	75.9 ± 3.2	6.2 ± 0.8	2.0 ± 0.1
WF/PLA	53.7 ± 1.1	4.0 ± 0.2	2.3 ± 0.1
WF/PLA/MDI	69.3 ±1.7	4.7 ± 0.1	2.4 ± 0.1
SF/PLA	52.2 ± 2.9	3.6 ± 0.1	2.3 ± 0.1
SF/PLA/MDI	51.5 ± 2.7	4.4 ± 0.4	2.1 ± 0.2
MSF/PLA	58.8 ± 1.5	4.0 ± 0.1	2.3 ± 0.1
MSF/PLA/MDI	61.0 ± 1.6	4.3 ± 0.1	2.2 ± 0.1

Table 6.2 Thermal behaviors of PLA and its blends with WF, SF, and MSF determined from DSC curves

Samples	ΔCp *(J/g*K)*	T_g (K)	T_c (K)	ΔH_c (J/g)	T_{m1} (K)	T_{m2} (K)	ΔH_m (J/g)	X_m (%)
PLA	0.48	328.0	394.5	-3.6	-	419.3	9.2	9.8
WF/PLA	0.37	327.9	-	0	-	419.1	2.6	3.5
WF/PLA/MDI	0.54	327.4	392.5	-1.7	-	417.9	11.5	15.4
SF/PLA	0.41	325.3	388.2	-30.1	415.9	422.0	30.9	41.4
SF/PLA/MDI	0.57	326.3	388.0	-12.9	416.4	418.2	16.6	22.2
MSF/PLA	0.54	327.4	383.6	-22.1	414.8	422.2	24.6	32.9
MSF/PLA/MDI	0.43	325.4	376.6	-26.4	411.8	420.1	27.5	36.7

Table 6.3 Decomposition temperatures of WF, SF, MSF, PLA and PLA blends with WF, SF, and MSF determined from TGA curves

Samples	T_{onset} (K)	T_{end} (K)	T_{max} [a] (K)
WF	566.3	671.8	646.7
SF	512.9	644.9	595.2
MSF	512.8	628.3	592.8
PLA	607.5	657.4	645.4
WF/PLA	610.7	656.1	638.7
WF/PLA/MDI	609.9	663	649.8
SF/PLA	590.8	631.5	619.9
SF/PLA/MDI	592.4	630.8	619.4
MSF/PLA	565.6	612.6	595.7
MSF/PLA/MDI	566.9	611.6	596.9

[a] Maximum rate of decomposition.

Table 6.4 Flexural storage modulus $B'_{initial}$, B'_{peak}, B'_{final}, $\Delta B'_1$ (= B'_{peak} - $B'_{initial}$), $\Delta B'_2$ (= B'_{peak} - B'_{final}), and B'_{298K} for PLA and PLA blends with WF, SF, and MSF determined from DMA curves

Samples	$B'_{initial}$[a] (GPa)	B'_{peak}[b] (GPa)	B'_{final}[c] (GPa)	$\Delta B'_1$[d] (GPa)	$\Delta B'_2$[e] (GPa)	B'_{298K}[f] (GPa)
PLA	0.60	1.26	0.004	0.66	1.26	0.75
WF/PLA	0.80	0.84	0.020	0.04	0.82	0.83
WF/PLA/MDI	1.16	1.29	0.031	0.13	1.26	1.14
SF/PLA	0.87	1.01	0.025	0.14	0.99	0.92
SF/PLA/MDI	1.25	1.66	0.032	0.41	1.63	1.24
MSF/PLA	1.10	1.35	0.021	0.25	1.33	1.14
MSF/PLA/MDI	1.15	1.20	0.027	0.05	1.17	1.16

[a] B' at 275 K.

[b] B' of the peak value.

[c] B' of the final asymptotic value.

[d] Defined as B'_{peak} - $B'_{initial.}$

[e] Defined as B'_{peak} - $B'_{final.}$

[f] B' at 298 K.

Table 6.5 β, ΔB, B_R, r^2, $T_{g,DMA}$, $T_{g,DSC}$ and ΔE obtained for PLA and PLA blends with WF, SF, and MSF determined from KWW fit (except for $T_{g,DSC}$)

Samples	β_{KWW}	ΔB[a] (GPa)	B_R (GPa)	r^2[b]	$T_{g,DMA}$[c] (K)	$T_{g,DSC}$ (K)	ΔE[d] (kJ/mol)
PLA	0.75	1.21	0.004	0.96	327	328.0	637±43
WF/PLA	0.71	0.89	0.017	0.93	324	327.9	461±43
WF/PLA/MDI	0.80	1.33	0.035	0.99	325	327.4	521±14
SF/PLA	0.78	1.03	0.025	0.96	326	325.3	583±41
SF/PLA/MDI	0.74	1.68	0.045	0.98	326	326.3	560±23
MSF/PLA	0.72	1.29	0.017	0.96	323	327.4	483±34
MSF/PLA/MDI	0.70	1.25	0.025	0.97	325	325.4	518±32

[a] Defined as $B_U - B_R$.

[b] Regression value of ln τ vs. T^{-1} plots (Figs. 3 and 4).

[c] Determined at relaxation time τ = 100 sec.

[d] Relaxation activation energy.

Chapter 7 - Mechanical and Thermal Properties of Biocomposites from Poly(lactic acid) and DDGS[6]

7.1 Abstract

Distillers dried grains with solubles (DDGS), an ethanol industry coproduct, is used mainly as a low-value feedstuff. Poly(lactic acid) (PLA) is a leading biodegradable polymer, but its applications are limited by its relatively high cost. In this study, low-cost, high-performance biodegradable composites were prepared through thermal compounding of DDGS and PLA with methylene diphenyl diisocyanate (MDI) as a coupling agent. Mechanical, morphological, and thermal properties of the composites were studied. The coupling mechanism of MDI in the PLA/DDGS system was confirmed via Fourier-transform infrared spectra. The PLA/20%DDGS composite with 1% MDI showed tensile strength (77MPa) similar to that of pure PLA, but its Young's modulus was 25% higher than that of pure PLA. With MDI, strong interfacial adhesion was established between the PLA matrix and DDGS particles, and the porosity of the composites decreased dramatically. Crystallinity of PLA in the composites was higher than that in pure PLA. Composites with MDI had higher storage moduli at room temperature than pure PLA. This novel application of DDGS for biocomposites has significantly higher economic value than its traditional use as a feedstuff.

[6] Results have been published. Li, Y., & Sun, X. S. (2011). Mechanical and thermal properties of biocomposites from poly(lactic acid) and DDGS. *J. Appl. Polym. Sci.,* 121, 589-597. (Reuse by permission of John Wiley and Sons).

7.2 Introduction

The U.S. ethanol industry has grown exponentially in recent years, and the supply of distillers dried grains with solubles (DDGS) has subsequently increased dramatically. In 2006, about 13.2 million metric tons of DDGS were produced in the United States, and this number may increase to 25 million metric tons by 2011(Robinson et al., 2008). DDGS contains about 26.8-33.7% protein (dry weight basis), 39.2-61.9% carbohydrates (including fibers), 3.5-12.8% oils, and 2.0-9.8% ash (Rosentrater & Muthukumarappan, 2006). Currently, the ethanol industry's only outlet for DDGS is animal feed ingredients (Cheesbrough et al., 2008; Wu & Mohanty, 2007). Most research publications about DDGS focus on its feed applications (Chevanan et al., 2008; Li et al., 2010a; Xu et al., 2010).

In recent years, DDGS production has far exceeded its consumption rate as feed. It is predicted that DDGS may have to be disposed of via landfilling, creating an environmental burden (Wu & Mohanty, 2007). Consequently, development of new outlets for DDGS has become an urgent need and is crucial to maintaining economic viability of the ethanol industry. Several potential alternatives have been proposed including extracting higher value protein and cellulose from DDGS (Wang et al., 2009; Xu et al., 2007, 2009) and using DDGS for phenolic/DDGS composites (Tatara et al., 2007, 2009), biocomposites (Schilling et al., 2009; Wu & Mohanty, 2007;), and bioadhesives (Mohanty et al., 2007). In this study, we explore the feasibility of using DDGS for biodegradable composites with poly(lactic acid) (PLA).

PLA is derived from sugar-based materials. It is the leading biodegradable polymer and considered a sustainable alternative to petroleum-based plastics. PLA exhibits mechanical properties similar to those of some traditional polymers. However, its applications are limited by several unsatisfactory characteristics, such as modest strength and modulus, brittleness, low heat distortion temperature, and relatively high cost (~80 cents per pound). Therefore, PLA has been compounded with various low-cost natural biopolymers including wood flour, sugar cane, lignin, flax, soy flour, soy protein, and starch to reduce its cost and enhance its modulus and biodegradability (Chen et al., 2008; Duhovic et al., 2009; Fang et al., 2009; Ke & Sun, 2000; Li et al., 2003; Li et al., 2010b; Ren et al., 2009; Wang et al., 2008; Zhang et al., 2006; Zhang & Sun, 2004). Our group has made achievements in preparing PLA/starch composites. When a mixture of 55% PLA and 45% starch (w/w) was thermally compounded with 0.5% methylene

diphenyl diisocyanate (MDI) as coupling agent, the composite showed enhanced mechanical properties and storage modulus above glass transition temperature (Wang et al., 2001, 2002).

DDGS is a multiple-component biopolymer that has not been studied for use in PLA composites but exhibits several advantages over other fillers. First, the cost of DDGS is only 4-6 cents per pound, which is lower than the cost of starch (10-20 cents per pound), wood fibers (~10 cents per pound), and soy flour (~10 cents per pound). Second, DDGS contains about 30% zein, which is a hydrophobic protein and has been considered a candidate for adhesives (Parris & Dickey, 2003). For that reason, zein might provide extra hydrophobic interactions and adhesion with the PLA matrix in PLA/DDGS composites. MDI used as a coupling agent for the PLA/DDGS system could further improve compatibility and interfacial adhesion. MDI has two isocyanate groups, which react with nucleophiles such as hydroxyl groups, carboxyl groups, and amino groups to form urethane or urea linkages (Chen et al., 2008; Dieteroch et al., 1985; Li et al., 2010b). Consequently, MDI can act as a chain extender for pure PLA, which has been reported in detail by Chen et al. (2008). However, no significant effect of MDI on the thermal and mechanical properties of pure PLA were observed. Therefore, the coupling reaction of pure PLA with MDI was not included in this study. The proposed coupling mechanism between PLA and DDGS with MDI is shown in Figure 7.1. Potential applications for these novel composites include vehicle interiors, appliance components, service utensils, and packaging materials. The objectives of this study were to develop value-added biocomposites from DDGS with PLA matrix and investigate the composites' mechanical, morphological, and thermal properties.

7.3 Experimental Section

7.3.1 Materials

PLA (2002D) in pellet form was obtained from NatureWorks LLC (Minnetonka, MN). Corn DDGS was provided by Abengoa Bioenergy Corporation (York, NE) and contained 57% carbohydrates, 31% crude protein, and 9% crude fat based on dry matter. MDI was purchased from ICI Polyurethanes Group (West Deptford, NJ).

7.3.2 Preparation of PLA/DDGS Composites

PLA pellets were ground through a 2 mm screen in a laboratory mill (Thomas-Wiley Company, Philadelphia, PA). DDGS was also ground with the same mill through a 1 mm screen.

Ground PLA and DDGS were dried in a vacuum oven at 80 ºC for 24 h. Mixtures of ground PLA with 20, 30, 40, or 50% DDGS (based on total weight) were mixed in a stand mixer (Ultra Power Kitchen Aid, St. Joseph, MI) for 10 min and then transferred to an intensive mixer (Rheomix 600, Haake, Paramus, NJ) equipped with two corotating rollers with a gap. The mixtures were thermal blended for 3 min at 180 ºC and 130 rpm. When cool, mixtures were ground into 2 mm powder. Pure PLA was treated with the same procedures as the control. Composites of PLA/20%DDGS with varying ratios of MDI (0.25, 0.5, 1, and 2% based on 100 parts of PLA/DDGS mixture) were prepared similarly to further investigate the effectivity of MDI as coupling agent. Dog-bone-type tensile bars were compression molded at 180 ºC and 8000 lb for 5 min with a Carver hot press (model 3889, Auto "M", Carver Inc., Wabash, IN) according to ASTM Method D 638-91 (1992), cooled to room temperature in air, and then removed from the mold. Five tensile bars were prepared for each type of composite, and bars were conditioned at 25 ºC with a relative humidity of 50% for at least 48 h prior to characterization.

7.3.3 Fourier-transform Infrared (FTIR) Spectroscopy

FTIR spectra of the samples were acquired with a PerkinElmer Spotlight 300 spectrometer. Spectra were collected in the region of 4000 to 800 cm^{-1} with a spectral resolution of 8 cm^{-1} and 64 scans co-added. At least three replicates were collected for each sample type.

7.3.4 Mechanical Measurements

The tensile tests were performed with an Instron testing system (model 4465, Canton, MA) at a crosshead speed of 5 mm/min with a 30 mm gauge length. Five replicates were tested for each sample type.

7.3.5 Scanning Electron Microscopy (SEM)

Morphology of the fractured surfaces of composites obtained from tensile tests was observed via SEM (Hitachi S-3500N, Hitachi Science Systems, Ltd., Japan). Each specimen was mounted on an aluminum stub, and the fractured surface was coated with an alloy of 60% gold and 40% palladium with a sputter coater (Desk II Sputter/ Etch Unit, NJ) before observation. DDGS was observed similarly.

7.3.6 Differential Scanning Calorimetry (DSC)

Thermal transitions of the composites were measured with a TA DSC Q200 instrument in an inert environment by using nitrogen with gas flow rate of 50 ml/min. About 5 mg of each sample obtained from a tensile bar was crimp sealed in an aluminum pan. An empty pan was used as a reference. The sample was heated from 0 °C to 190 °C at a rate of 10 °C/min to examine the glass transition temperature (T_g) and crystallinity of PLA in the test specimens. Crystallinity (X_m) was estimated according to the following equation:

$$X_m(\%) = \frac{\Delta H_m}{\Delta H_0 \times X_{PLA}} \times 100 \qquad (1)$$

ΔH_m and ΔH_0 are heats (J/g) of melting of composite and PLA crystal of infinite size with a value of 93.6 J/g (Fischer et al., 1973), respectively, and X_{PLA} is the PLA fraction in the composite.

7.3.7 Thermogravimetric Analysis (TGA)

Thermal stability of the samples was determined with a PerkinElmer Pyris1 TGA instrument (Norwalk, CT). About 5 mg of each sample obtained from a tensile bar was placed in the pan and heated from 40 °C to 600 °C at a heating rate of 20 °C /min under a nitrogen atmosphere.

7.3.8 Dynamic Mechanical Analysis (DMA)

Dynamic mechanical experiments were conducted using a PerkinElmer DMA 7e instrument (Norwalk, CT) in a three-point flexural mode at 1 Hz frequency. Specimens (about 10 mm × 6 mm × 2 mm) were obtained from tensile bars with a saw, and the edges were polished carefully with grade 240 abrasive sandpaper. Specimens were heated from 0 °C to 150 °C at a heating rate of 3 °C/min under a helium atmosphere. Flexural storage modulus and flexural loss modulus were determined from the changes in the amplitude and phase angle of the observed oscillating strain within the approximation of linear response of the specimen.

7.4 Results and Discussion

7.4.1 FTIR

Figure 7.2 shows the representative FTIR spectra of MDI, DDGS, PLA, and the PLA/20%DDGS/1%MDI composite. The strong absorption peak at 2292 cm^{-1} for MDI was attributed to the free –N=C=O groups. For DDGS, the broad band centered at 3364 cm^{-1} was assigned to the stretching vibration of –OH and –NH from carbohydrates and protein, the peak at 2930 cm^{-1} to the stretching of –CH from lipids, the peak at 1654 cm^{-1} to the amide Ⅰ absorption of corn protein, and the peaks at the region of 1250-1000 cm^{-1} to carbohydrates. These results confirm that DDGS is composed of carbohydrates, protein, and lipids. PLA exhibited –OH vibration bands at 3500 cm^{-1}; –CH stretching and bending vibration bands at 2994, 2944, and 1454 cm^{-1}; and –C=O vibration bands at 1772 cm^{-1} (Li & Sun, 2010). After thermal compounding of PLA and DDGS with MDI, the peak of –N=C=O in the composites totally disappeared, indicating that all free isocyanate groups from MDI were consumed during thermal compounding. Moreover, the strong absorption peak of –OH and –NH observed in DDGS became very weak, indicating that most –OH and –NH groups were reacted with MDI in forming urethane and urea linkages. The urea-urethane and alcohol-urethane groups were expected to be found at 1647 cm^{-1} and 1704-1727 cm^{-1} (Wu & Mohanty, 2007), respectively, which were overlapped with amide Ⅰ and –C=O absorption.

7.4.2 Mechanical Properties

Pure PLA exhibited tensile strength (σ) of 77 MPa, elongation (ε) of 6.2%, and Young's modulus (E) of 2.0 GPa (Table 7.1). With 20% DDGS, σ and E decreased to 27 MPa and 1.8 GPa, respectively, whereas ε increased significantly to 16%, as shown in the stress-strain curve (Figure 7.3). As the DDGS loading further increased, σ and E kept decreasing, whereas ε remained higher than that of pure PLA. When DDGS content reached 50% in the composite, σ and E decreased to about 10 MPa and 0.8 GPa, respectively, and ε was 7.8% (Table 7.1). These results indicated that interfacial adhesion between the PLA matrix and DDGS particles was poor because of their immiscible characteristics. The loading ratio of DDGS was then fixed at 20% to investigate the effect of coupling agent (MDI) on mechanical properties of composites (Table 7.2). The σ and E of PLA/20% DDGS composites increased dramatically by incorporating MDI,

compared with composites without MDI, whereas ε decreased slightly compared with that of pure PLA. With 0.25% MDI, σ and E increased to 54 MPa and 2.4 GPa, respectively. For composites with 0.5% MDI, σ further increased to 68 MPa, whereas E remained almost unchanged. Optimum mechanical properties were obtained at 1% MDI, at which σ (77 MPa) was the same as that of pure PLA, E (2.5 GPa) was 25% higher, and ε (5.0%) was slightly decreased. As MDI ratio further increased to 2%, mechanical properties decreased.

As expected, DDGS particles in the PLA matrix without a coupling agent acted as stress concentrators under tensile stress, often inducing fractures and resulting in low tensile strength. Moreover, because of the poor packing properties of DDGS, some pores were observed in the tensile bars without MDI, which also resulted in low strength. However, in contrast to the immediate fracture after reaching maximum load for PLA, the PLA/20%DDGS composite showed distinct yielding and stable neck growth (Figure 7.3), which were induced by the debonding of DDGS particles from the PLA matrix during fracturing. This is further discussed in the morphology section.

Because of the formation of covalent linkages between hydroxyl or carboxyl groups from PLA into PLA-MDI and hydroxyl or amine groups from DDGS into DDGS-MDI (Figure 7.1), interfacial adhesion between the PLA matrix and DDGS particles was greatly improved, resulting in increased strength and modulus. Meanwhile, with formation of DDGS-MDI, packing properties of DDGS were improved, and porosity of the composites significantly decreased as indicated in the SEM images (Figure 7.4), which also enhanced mechanical properties. However, excess PLA-MDI and DDGS-MDI segments were formed with extra MDI (2%), and these segments might interfere with effective entanglements or segmental crystallization between DDGS particles and the PLA matrix (Zhang et al., 2006), resulting in decreased strength and modulus. Similar results were reported for PLA/sugar beet pulp composites with MDI ranging from 0 to 3% (Chen et al., 2008).

7.4.3 Morphology

As shown in Figure 7.4, DDGS exists in irregular shapes and various sizes (20-200 μm) and has coarse surfaces. Pure PLA has a smooth and continuous fracture surface, indicating a brittle fracture behavior that corresponds to its low elongation value shown in Table 7.1. Surface roughness of the PLA matrix obviously increased with inclusion of 20% DDGS as observed

from SEM images (Figure 7.4, a and a'), indicating that remarkable plastic deformation occurred. As discussed previously, because there was not sufficient interfacial adhesion, DDGS particles debonded from the PLA matrix at the interface during fracturing. Void formation due to cavitation localized at the particle/matrix interfaces was visible together with PLA matrix strands surrounding voids (Figure 7.4, a and a'), and the stress state in the PLA matrix was altered. During the debonding process, these PLA matrix strands were plastically stretched, fibrillized, and finally broken down. The toughening mechanism of particle-filled semicrystalline polymers has been explained in detail (Kim & Michler, 1998a, 1998b). With the naked eye and SEM, we also observed some pores attributed to the poor packing properties of DDGS. As DDGS loading ratio further increased, more pores were observed (SEM images not shown), which corresponds to the decreased strength and elongation of composites.

With 0.25% MDI added, fracturing extending through DDGS particles was observed in addition to debonding, and the porosity decreased obviously (Figure 7.4, b), indicating the greatly improved wettability of DDGS particles by the PLA matrix and penetration of PLA into the porous DDGS. With increasing amounts of MDI, almost no evidence of debonding could be observed at the fracture surfaces (Figure 7.4, c-e). Instead, DDGS particles ruptured together with the PLA matrix at the plane of the fracturing surfaces. For composites with 1% and 2% MDI, few individual DDGS particles could be observed, and those that were distinguishable appeared to be completely coated and penetrated by the PLA matrix (Figure 7.4, d-e). Moreover, no pores could be observed in the tensile bars. The SEM images provide clear evidence that MDI addition established strong interfacial bonding between the PLA matrix and DDGS particles that led to greatly improved stress transfer between the matrix and fillers, corresponding to measurements of the mechanical properties.

7.4.4 Thermal Properties

Figure 7.5 shows DSC thermograms of compression-molded PLA and PLA/20%DDGS composites. The thermograms were obtained from the first heating scan to reveal the glass transition and crystalline status of the PLA component in the composites. Table 7.3 summarizes the DSC results. The T_g of the composite without MDI was 3 ºC lower than that of pure PLA (62.1 ºC). With addition of MDI, T_g increased slightly, indicating that some coupling effects from MDI occurred. An endothermic peak around the glass transition region was observed for

PLA and composites because of physical aging during storage at ambient temperature. The peak area of PLA, PLA composites without MDI and with 0.25% MDI was larger than that of composites with a higher MDI loading ratio. During sample storage, molecular mobility reduces free volume. Samples with a higher degree of aging have smaller free volume as well as smaller enthalpy and potential energy than samples with a lower degree of aging (Pan et al., 2007). Therefore, when the aged samples are heated, more energy is required for the glass transition, thus increasing the area of the endothermic peak. Crystallinity of PLA in the composites was higher than that of pure PLA. However, crystallinity of the composite with 2%MDI was slightly lower than that of other composites. This might be caused by the excess PLA-MDI and DDGS-MDI segments that occurred with extra MDI loading, which would interfere with segmental crystallization, as discussed previously in the mechanical properties section.

TGA and derivative TGA thermograms of DDGS, PLA, and PLA/20%DDGS composites are shown in Figure 7.6 (A) and (B), and the TGA data are summarized in Table 7.4. Because of its multiple components (carbohydrates, protein, lipids, etc.), DDGS exhibited a much broader decomposition range than PLA; onset, end, and peak decomposition temperatures (T_{onset}, T_{end}, and T_{max}) of DDGS were 298.8, 418.6, and 383.1 ºC, respectively, and T_{onset}, T_{end}, and T_{max} of PLA were 344.5, 388.9, and 381.7 ºC, respectively. The composite without MDI showed slightly higher decomposition temperatures than PLA with T_{end} and T_{max} of 401.2 and 385.5 ºC, respectively. All composites with MDI showed similar decomposition temperatures with T_{max} values slightly lower than that of PLA. Because DDGS has higher tar and ash content than PLA, the residue weight of PLA/DDGS composites above 425 ºC is higher than that of PLA but lower than that of DDGS.

For PLA and PLA/20%DDGS composites with and without MDI, storage modulus (E') increased gradually with heating between 20 and 61 ºC, reached a peak value, dropped sharply at the glass transition region, and then reached a rubbery plateau (Figure 7.7, A). The increase of E' between 20 and 61 ºC was a kinetic unfreezing of a nonequilibrium disordered structure at the low heating rate (3 ºC /min) and sinusoidal frequency (1 Hz) and a consequence of molecular structure densification and aging (Li et al., 2010b). For all samples, the competing effects of aging and relaxation led to the fluctuation of E' before its sharp drop. An increase in E' around 100 ºC was attributed to cold crystallization of PLA components. When the E' values of PLA and composites at room temperature (25 ºC) were compared, composites without MDI showed a

smaller E' (1.02 GPa) than PLA (1.12 GPa), corresponding to its lower mechanical strength. With MDI, an obvious increase in E' was observed for all composites, indicating effective coupling between PLA and DDGS.

The loss factor (tan δ) of PLA and PLA/20%DDGS composites during heating is presented in Figure 7.7 (B). The peak that appeared at about 69 ºC is known as T_g from DMA measurement. Pure PLA had the largest tan δ (1.65) at T_g, indicating that it contains a greater amorphous phase portion than the composites, which corresponds to the lowest crystallinity value of pure PLA determined from DSC. In a composite system with filler, the filler would limit mobility of the matrix molecular chain, thereby affecting relaxation of the matrix chains and causing a lower damping in the transition zone compared with a pristine polymer (Nielsen & Landel, 1994).

7.5 Conclusions

PLA/DDGS composites with mechanical properties similar to those of pure PLA were successfully prepared via thermal compounding. FTIR spectroscopy verified that MDI was an effective coupling agent for the PLA/DDGS system. Without a coupling agent, tensile strength and Young's modulus of composites decreased dramatically as DDGS content increased. For PLA/20%DDGS composites, as MDI loading ratio gradually increased from 0.25 to 1%, tensile strength and Young's modulus increased and approached values similar to those of pure PLA. Morphology of the fracture surfaces showed that addition of MDI established strong interfacial bonding between the PLA matrix and DDGS particles and decreased the porosity of composites. Crystallinity of PLA in the composites was higher than that of pure PLA. Composites with MDI had higher storage moduli at room temperature than pure PLA. These results indicate that using low-cost DDGS as filler can result in biodegradable composites that have properties similar to those of pure PLA but cost significantly less. This novel application of DDGS for biocomposites has significantly higher economic value than its traditional use as a feedstuff.

7.6 References

ASTM D 638-91. (1992). In Annual book of ASTM standards (Vol.8.01, p. 161). Philadelphia, PA: American Society for Testing and Materials.

Cheesbrough, V., Rosentrater, K. A., & Visser, J. (2008). Properties of distillers grains composites: a preliminary investigation. J. Polym. Environ., 16, 40-50.

Chen, F., Liu, L., Cooke, P. H., Hicks, K. B., & Zhang, J. (2008). Performance enhancement of poly(lactic acid) and sugar beet pulp composites by improving interfacial adhesion and penetration. Ind. Eng. Chem. Res., 47, 8667-8675.

Chevanan, N., Rosentrater, K. A., & Muthukumarappan, K. (2008). Effect of DDGS, moisture content, and screw speed on physical properties of extrudates in single-screw extrusion. Cereal Chem., 85, 132-139.

Dieteroch, D., Grigat, E., & Hahn, W. (1985). Polyurethane handbook (p. 7); G. Oertel (Ed.). New York: Hanser..

Duhovic, M., Horbach, S., & Bhattacharyya, D. (2009). Improving the interface strength in flax fiber poly(lactic) acid composites. J. Biobased Mater. Bioenergy, 3, 188-198.

Fang, K., Wang, B. B., Sheng, K. C., & Sun, X. S. (2009). Properties and morphology of poly(lactic acid)/soy protein isolate blends. J. Appl. Polym. Sci., 114, 754-759.

Fischer, E. W., Sterzel, H. J., & Wegner, G. (1973). Investigation of the structure of solution grown crystals of lactide copolymers by means of chemical reactions. Kolloid Z. Z. Polym., 251, 980-990.

Ke, T. Y., & Sun, X. S. (2000). Physical properties of poly(lactic acid) and starch composites with various blending ratios. Cereal Chem., 77, 761-768.

Kim, G. M., & Michler, G. H. (1998a). Micromechanical deformation processes in toughened and particle-filled semicrystalline polymers: Part 1. Characterization of deformation processes in dependence on phase morphology. Polymer, 39, 5689-5697.

Kim, G. M., & Michler, G. H. (1998b). Micromechanical deformation processes in toughened and particle filled semicrystalline polymers: Part 2. model representation for micromechanical deformation processes. Polymer, 39, 5699-5703.

Li, J. C., He, Y., & Inoue, Y. (2003). Thermal and mechanical properties of biodegradable blends of poly(L-lactic acid) and lignin. Polym. Int., 52, 949-955.

Li, M. H., Robinson, E. H., Oberle, D. F., & Lucas, P. M. (2010a). Effects of various corn distillers by-products on growth, feed efficiency, and body composition of channel catfish, Ictalurus punctatus. Aquacult. Nutr., 16, 188-193.

Li, Y., & Sun, X. S. (2010). Preparation and characterization of polymer−inorganic nanocomposites by in situ melt polycondensation of L-lactic acid and surface-hydroxylated MgO. Biomacromolecules, 11, 1847–1855.

Li, Y., Venkateshan, K., & Sun, X. S. (2010b). Mechanical and thermal properties, morphology and relaxation characteristics of poly(lactic acid) and soy flour/wood flour blends. Polym. Int., 59, 1099-1109.

Mohanty, A. K., Wu, Q., & Singh, A. (2007). Bioadhesive from distillers' dried grains with solubles (DDGS) and the methods of making those. US Patent Office, Pat. No. 20070196521 A1.

Nielsen, L. E., & Landel, R. F. (1994). Mechanical Properties of Polymers and Composites, 2nd ed. (p. 425). New York: Marcel Dekker.

Pan, P., Zhu, B., & Inoue, Y. (2007). Enthalpy relaxation and embrittlement of poly(L-lactide) during physical aging. Macromolecules, 40, 9664-9671.

Parris, N., & Dickey, L. C. (2003). Adhesive properties of corn zein formulations on glass surfaces. J. Agr. Food Chem., 51, 3892-3894.

Ren, J., Fu, H. Y, Ren, T. B., & Yuan, W. Z. (2009). Preparation, characterization and properties of binary and ternary blends with thermoplastic starch, poly(lactic acid) and poly(butylene adipate-co-terephthalate). Carbohydr. Polym., 77, 576-582.

Robinson, P. H., Karges, K., & Gibson, M. L. (2008). Nutritional evaluation of four co-product feedstuffs from the motor fuel ethanol distillation industry in the Midwestern USA. Anim. Feed Sci. Tech., 146, 345-352.
Rosentrater, K. A., & Muthukumarappan, K. (2006). Corn ethanol coproducts: generation, properties, and future prospects. Int. Sugar J., 108, 648-657.
Schilling, C. H, Karpovich, D. S., & Tomasik, P. (2009). Biodegradable Plastics from Soy Protein and Polysaccharide Carboxylates. J. Biobased Mater. Bioenergy, 3, 408-417.
Tatara, R. A., Rosentrater, K. A., & Suraparaju, S. (2009). Design properties for molded, corn-based DDGS-filled phenolic resin. Ind. Crop. Prod., 29, 9-15.
Tatara, R. A., Suraparaju, S., & Rosentrater, K. A. (2007). Compression molding of phenolic resin and corn-based DDGS blends. J. Polym. Environ., 15, 89-95.
Wang, H., Sun, X. S., & Seib, P. (2001). Strengthening blends of poly(lactic acid) and starch with methylenediphenyl diisocyanate. J. Appl. Polym. Sci., 82, 1761-1767.
Wang, H., Sun, X. S., & Seib, P. (2002). Mechanical properties of poly(lactic acid) and wheat starch blends with methylenediphenyl diisocyanate. J. Appl. Polym. Sci., 84, 1257-1262.
Wang, N., Yu, J. G., Chang, P. R., & Ma, X. F. (2008). Influence of formamide and water on the properties of thermoplastic starch/poly(lactic acid) blends. Carbohydr. Polym., 71, 109-118.
Wang, Y., Tilley, M., Bean, S., Sun, X. S., & Wang, D. (2009). Comparison of methods for extracting kafirin proteins from sorghum distillers dried grains with solubles. J. Agr. Food Chem., 57, 8366-8372.
Wu, Q., & Mohanty, A. K. (2007). Renewable resource based biocomposites from coproduct of dry milling corn ethanol industry and castor oil based biopolyurethanes. J. Biobased Mater. Bioenergy, 1, 257-265.
Xu, G., Baidoo, S. K., & Johnston, L. J., Bibus, D., Cannon, J. E., & Shurson, G. C. (2010). The effects of feeding diets containing corn distillers dried grains with solubles, and withdrawal period of distillers dried grains with solubles, on growth performance and pork quality in grower-finisher pigs. J. Anim. Sci., 88, 1388-1397.
Xu, W., Reddy, N. & Yang, Y. Q. (2009). Extraction, characterization and potential applications of cellulose in corn kernels and distillers' dried grains with solubles (DDGS). Carbohydr. Polym., 76, 521-527.
Zhang, C., Li, K., & Simonsen, J. (2006). Terminally functionalized polyethylenes as compatibilizers for wood-polyethylene composites. Polym. Eng. Sci., 46, 108-113.
Zhang, J. F., & Sun, X. S. (2004). Mechanical properties of poly(lactic acid)/starch composites compatibilized by maleic anhydride. Biomacromolecules, 5, 1446-1451.
Zhang, J. W., Jiang, L., & Zhu, L. Y. (2006). Morphology and properties of soy protein and polylactide blends. Biomacromolecules, 7, 1551-1561.

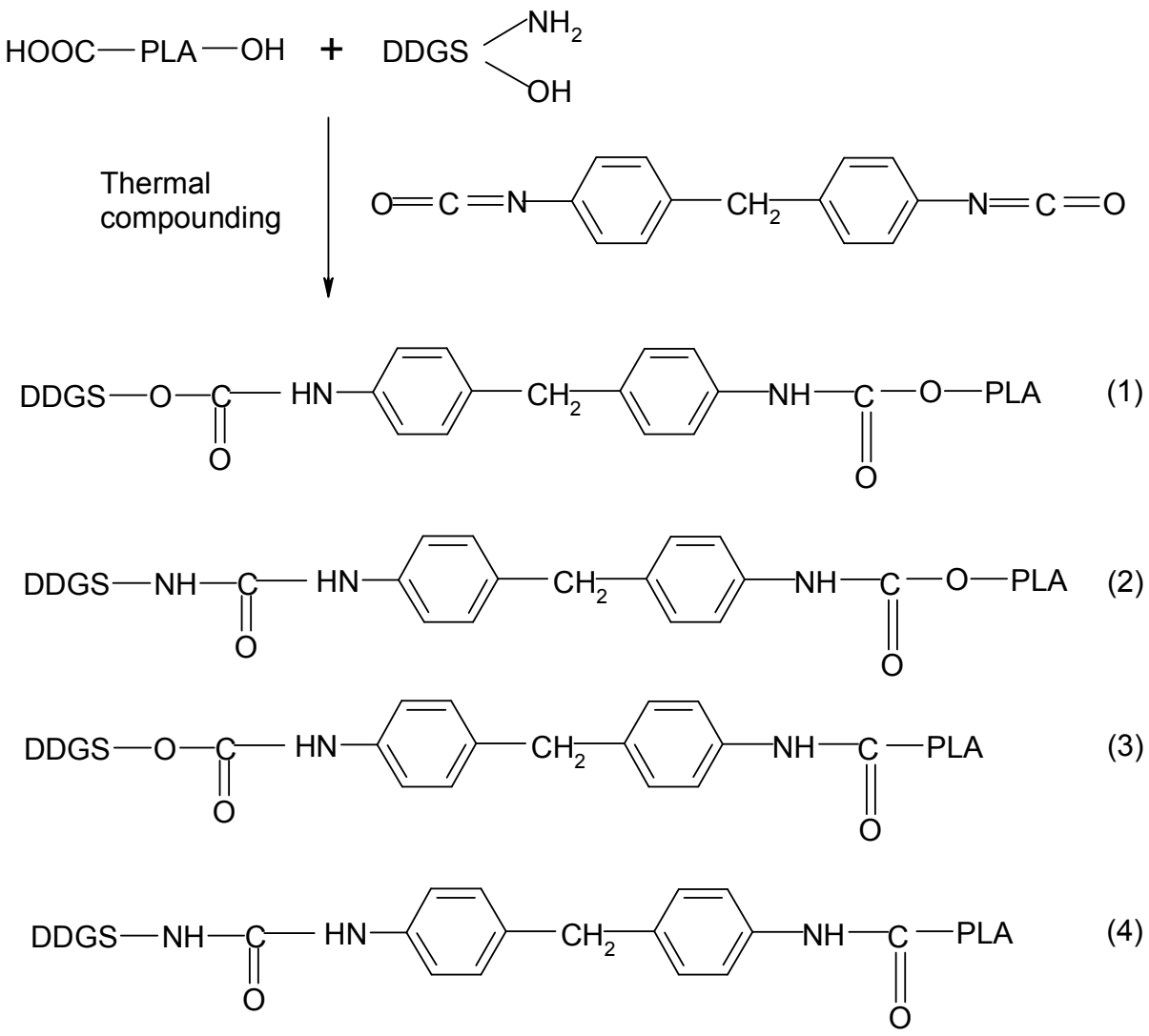

Figure 7.1 Proposed coupling mechanism between PLA and DDGS with MDI.

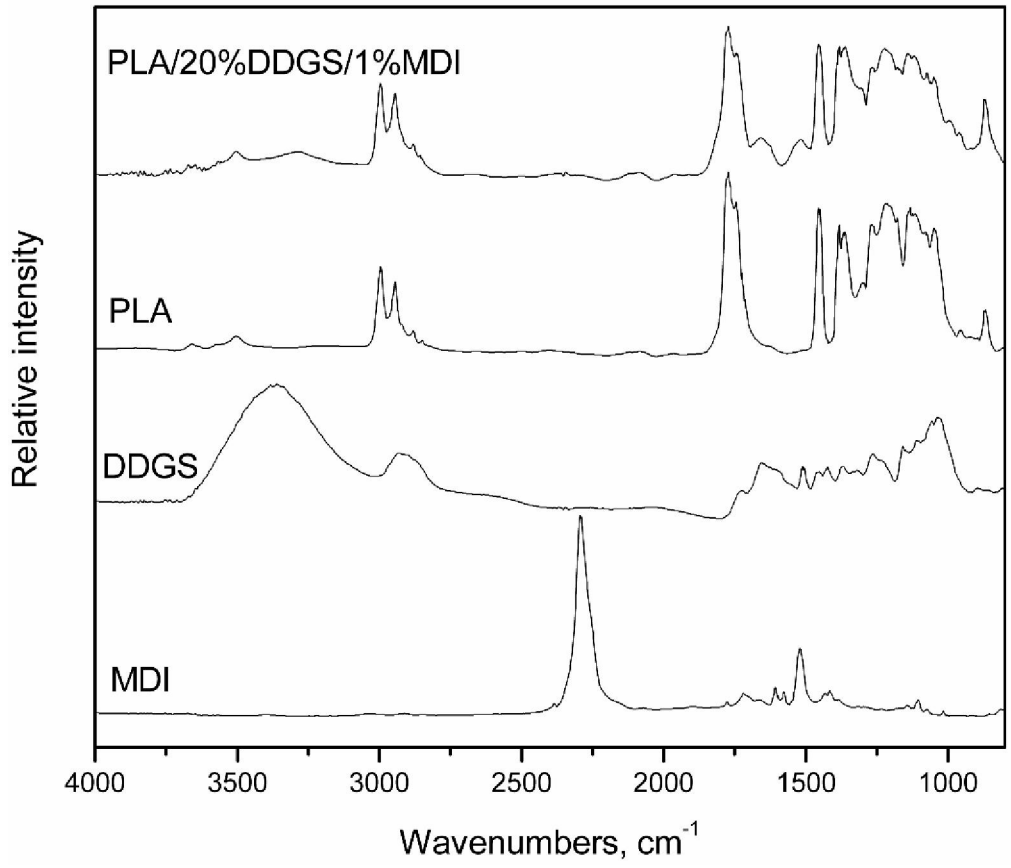

Figure 7.2 FTIR spectra of MDI, DDGS, PLA, and PLA/20%DDGS/1%MDI composite.

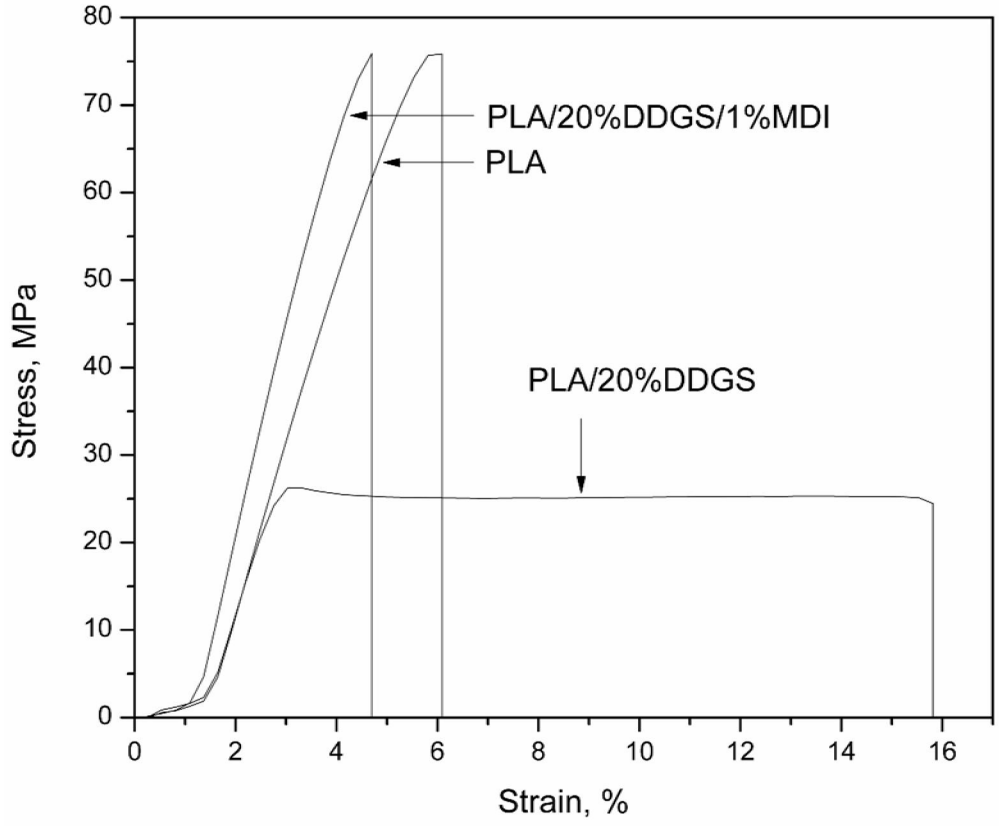

Figure 7.3 Tensile stress-strain curves of PLA and typical PLA/DDGS composites.

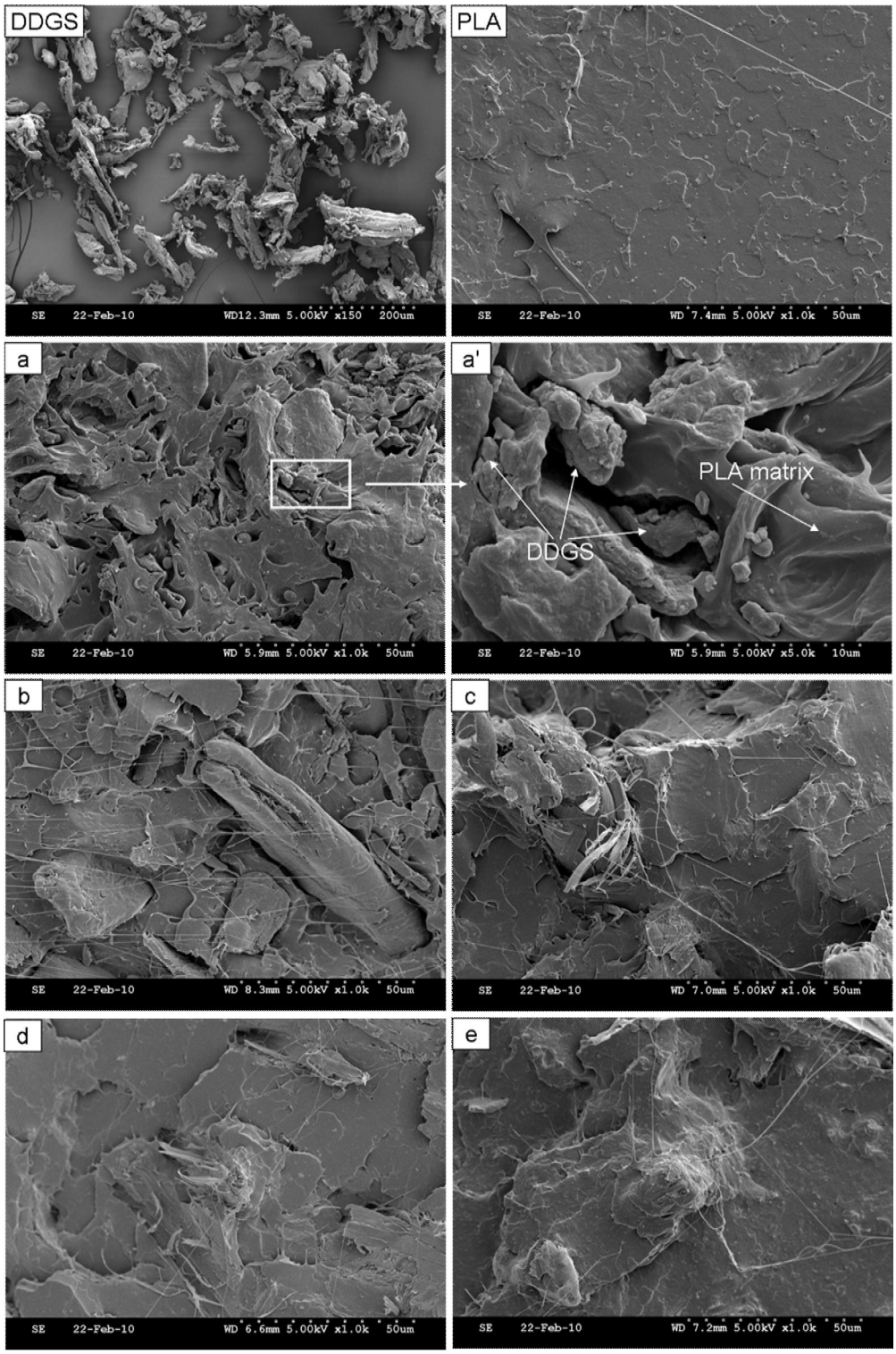

Figure 7.4 SEM images of PLA and PLA/20%DDGS composites with (a and a') 0%MDI, (b) 0.25%MDI, (c) 0.5%MDI, (d) 1%MDI, (e) 2%MDI.

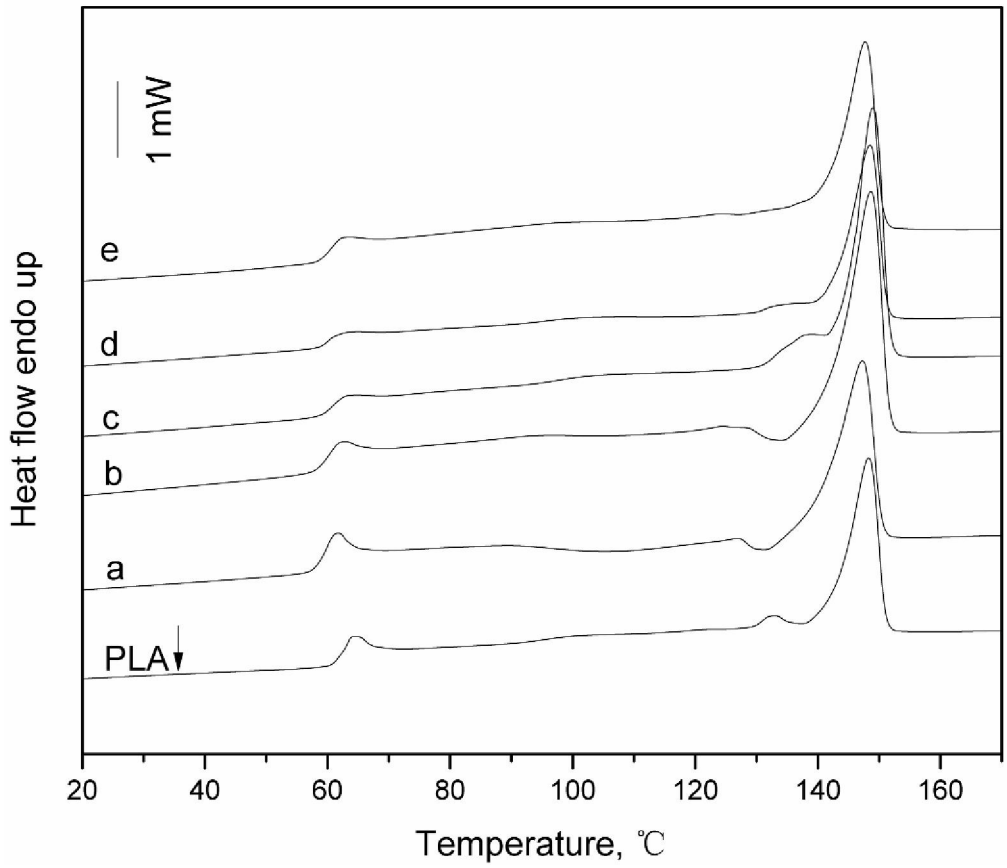

Figure 7.5 DSC thermograms of PLA and PLA/20%DDGS composites with (a) 0%MDI, (b) 0.25%MDI, (c) 0.5%MDI, (d) 1%MDI, (e) 2%MDI (first scan).

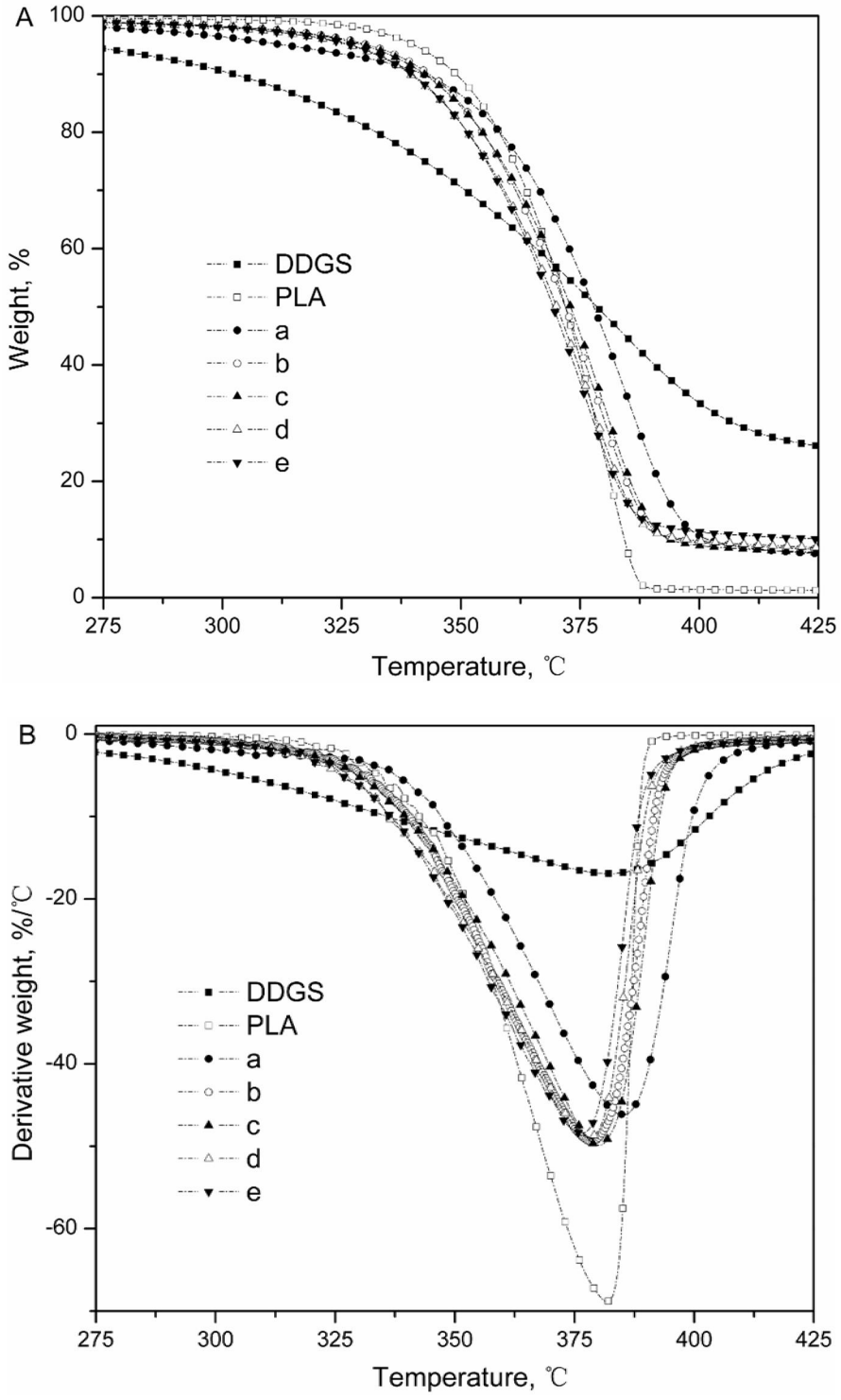

Figure 7.6 TGA (A) and derivative TGA (B) thermograms of DDGS, PLA, and PLA/20%DDGS composites with (a) 0%MDI, (b) 0.25%MDI, (c) 0.5%MDI, (d) 1%MDI, (e) 2%MDI.

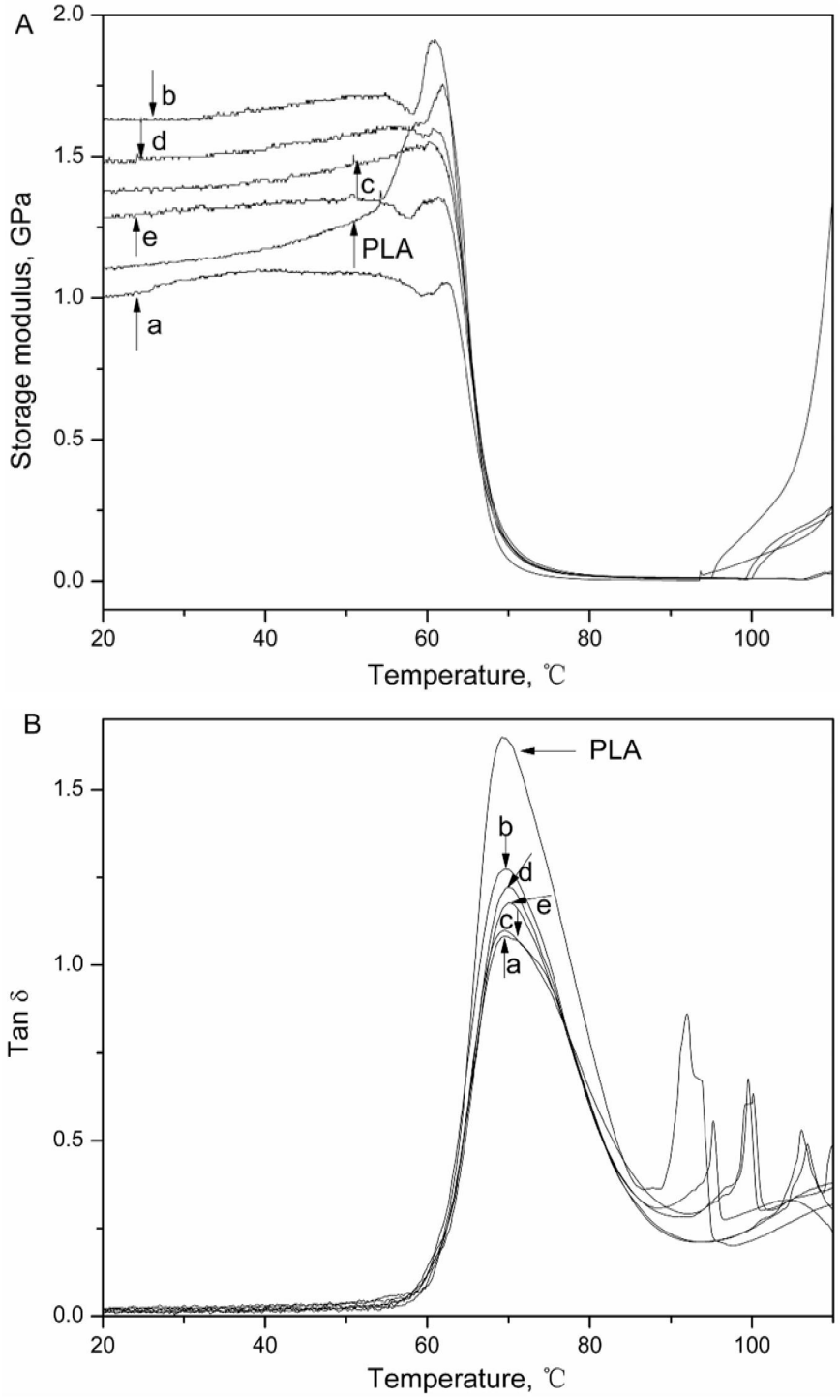

Figure 7.7 Flexural storage modulus (A) and tan δ (B) of PLA and PLA/20%DDGS composites with (a) 0%MDI, (b) 0.25%MDI, (c) 0.5%MDI, (d) 1%MDI, (e) 2%MDI.

Table 7.1 Mechanical properties of PLA/DDGS composites without coupling agent

Sample	Tensile strength (MPa)	Elongation at break (%)	Young's modulus (MPa)
Pure PLA	77.10 ± 0.76	6.18 ± 0.37	2.04 ± 0.02
20% DDGS	27.44 ± 0.68	15.65 ± 2.36	1.81 ± 0.04
30% DDGS	20.24 ± 1.11	11.62 ± 2.08	1.51 ± 0.05
40% DDGS	13.55 ± 0.94	10.95 ± 3.57	1.20 ± 0.14
50% DDGS	9.72 ± 0.51	7.77 ± 1.90	0.80 ± 0.05

Table 7.2 Mechanical properties of PLA/20%DDGS composites with varying amount of MDI as coupling agent

Sample	Tensile strength (MPa)	Elongation at break (%)	Young's modulus (MPa)
0.25% MDI	54.47 ± 1.34	3.92 ± 0.12	2.36 ± 0.09
0.5% MDI	68.13 ± 0.79	4.56 ± 0.16	2.41 ± 0.05
1% MDI	77.05 ± 1.70	4.96 ± 0.16	2.52 ± 1.26
2% MDI	68.77 ± 0.45	4.84 ± 0.36	2.36 ± 0.04

Table 7.3 DSC results of PLA and PLA/20%DDGS composites with varying amount of MDI

Sample	T_g ºC	ΔC_p J/(g·ºC)	T_m ºC	ΔH_m J/g	X_m %
PLA	62.1	0.35	148.3	19.01	20.3
0%MDI	58.9	0.38	147.3	19.94	26.6
0.25%MDI	59.7	0.30	148.6	19.69	26.3
0.5%MDI	60.8	0.27	148.9	19.66	26.3
1%MDI	60.3	0.26	148.5	18.72	25.0
2%MDI	60.5	0.35	147.7	16.96	22.7

Table 7.4 Decomposition temperatures of DDGS, PLA, and PLA/20%DDGS composites with varying amount of MDI determined from derivative TGA thermograms

Sample	T_{onset} ºC	T_{end} ºC	T_{max} ºC
DDGS	298.8	418.6	383.1
PLA	344.5	388.9	381.7
0%MDI	343.0	401.2	385.5
0.25%MDI	340.2	394.2	379.9
0.5%MDI	341.7	393.2	378.4
1%MDI	335.5	391.2	377.8
2%MDI	337.2	389.7	376.5

Chapter 8 - Conclusions and Recommendations

8.1 Conclusions

Inorganic nanoparticles and low-cost agricultural residues reinforced poly(lactic acid) (PLA) nanocomposites/composites with improved thermal stability, glass transition temperature (T_g), mechanical properties, and reduced cost were reported in this dissertation. Both *in situ* polymerization and melt blending approaches were employed.

PLA-MgO nanocomposites were synthesized by *in situ* melt polycondensation of lactic acid and surface-hydroxylated MgO nanocrystals at MgO loading level of 0.005-0.2%. The covalent grafting of PLA chains onto MgO nanocrystal surfaces was confirmed by Fourier transform infrared spectroscopy (FTIR), thermalgravimetric analysis (TGA), and solid-state ^{1}H and ^{13}C nuclear magnetic resonance spectroscopy. The nanocomposites exhibited continuous morphology with small convexities uniformly distributed in PLA matrix because of surface grafting and hydrogen bonding between PLA chains and hydroxylated MgO, while pure PLA exhibited an incontinuous particle morphology with a flat, smooth surface. MgO crystals acted as nucleation agents to induce and accelerate crystallization of the PLA-MgO nanocomposite. Thermal stability of the PLA-MgO nanocomposite was significantly increased compared with that of pure PLA.

PLA nanocomposites with bare MgO crystals and surface grafted MgO nanocrystals with PLA chains (g-MgO) were prepared via melt blending, respectively. For PLA/MgO nanocomposites, maximum tensile strength and Young's modulus were obtained at a 0.0125% MgO loading level and increased by 14% and 26%, respectively, compared with values for pure PLA. For PLA/g-MgO nanocomposites, maximum tensile strength was obtained at a 0.025% g-MgO loading level and was slightly higher than the tensile strength value of the PLA/0.0125%MgO nanocomposite. Morphology of the fracture surfaces showed that PLA/g-MgO nanocomposites had stronger interfacial interaction than PLA/MgO nanocomposites.

PLA nanocomposites were also synthesized with high anisotropy TiO_2 nanowires through *in situ* melt polycondensation. The covalent grafting of PLA chains onto the nanowire surfaces

was confirmed by FTIR spectroscopy and TGA. TEM micrographs and DSC results also sustained the presence of the third phase on the nanowire surfaces. Those PLA on the nanowire surfaces exhibited significantly increased T_g and thermal stability, compared with pure PLA. TGA results also showed that more than 30 wt.% PLA was grafted onto the nanowire surfaces. The T_g of bulk nanocomposites increased, whereas the crystallization ability decreased, as the nanowire concentrations increased from 0 to 2%.

In situ polymerization was a more effective approach than solution mixing in preparing PLA/TiO_2 nanowires nanocomposites. Crystallization growth rate first increased then decreased in the temperature range of 80–115°C, with maximum rate observed at 100°C. The TiO_2 nanowires acted as nucleation agents in the ISPLANC, which exhibited much higher G_{exp} than either pure PLA or SMPLANC below 110°C. The crystallization behavior of all the three samples fit the Avrami equation quite well. The overall crystallinity of both PLA and nanocomposites increased in general as crystallization temperature increased in the evaluated range.

PLA composites with wood flour (WF) and soy flour (SF) were prepared by thermal blending followed by compression molding. Methylene diphenyl diisocyanate (MDI) was an effective coupling agent for the WF/PLA system, resulting in improved tensile strength and elongation. Modification of SF with $NaHSO_3$ was also an effective way to increase the mechanical properties of the SF/PLA system. Results from DSC revealed that SF and modified SF, but not WF, could act as nucleation agents to induce and accelerate the crystallization of PLA in the composites, resulting in much higher crystallinity. The temperature-dependent mechanical relaxations of PLA and its composites with WF, SF, and modified SF with and without MDI were analyzed using the KWW relaxation function, and information such as τ, β, and ΔE were obtained. PLA and its composites exhibited highly homogeneous relaxational dynamics in their transition from glass to liquid during heating because of the high degree of hydrophobicity and densification effects of PLA, SF, and MSF.

PLA/DDGS composites with mechanical properties similar to those of pure PLA were successfully prepared via thermal compounding. FTIR spectroscopy verified that MDI was an effective coupling agent for the PLA/DDGS system. For PLA/20%DDGS composites, as MDI loading ratio gradually increased from 0.25 to 1%, tensile strength and Young's modulus increased and approached values similar to those of pure PLA. Morphology of the fracture

surfaces showed that addition of MDI established strong interfacial bonding between the PLA matrix and DDGS particles and decreased the porosity of composites. These results indicate that using low-cost DDGS as filler can result in biodegradable composites that have properties similar to those of pure PLA but cost significantly less. This novel application of DDGS for biocomposites has significantly higher economic value than its traditional use as a feedstuff.

Overall, the results from this dissertation are promising. These results provide new insights into fundamentals and structure-property relationships of polymer nanocomposites and composites. These novel PLA thermoplastic nanocomposites and composites with enhanced properties have potential applications in packaging materials, textiles, appliance components, autoparts, medical implants, etc. Commercialization of such products in the future would accelerate the use of biopolymers (starch, cellulose, hemicelluloses, etc.) and reduce our reliance on fossil resources.

8.2 Recommendations on Future Studies

Based on the experiences and results of this study, future research on the following topics should be considered:

(1) To compare the reinforcing differences of TiO_2 nanowires, nanosheets, and nanospheres on the properties of PLA nanocomposites. Though it is expected that the reinforcing effect of nanoparticles in nanocomposites increases with the anisotropy (aspect ratio) of nanoparticles, there is lack of experiment data on such hypothesis using nanoparticles from the same origin.

(2) To investigate the effects of TiO_2 nanoparticles on photodegradation and biodegradation of PLA nanocomposites. TiO_2 is a well known photocatalyst. The wide band gap of TiO_2 ($E_g > 3.2$ eV) makes it capable of absorbing UV light ($\lambda < 388$ nm) and generating active oxygen species, which are expected to induce the photodegradation of interfacial polymers. PLA has the limitation of slow biodegradation rate. By incorporating photoactive TiO_2 nanoparticles, PLA nanocomposites would possess both photodegradability and biodegradability, thus a higher degradation rate.

(3) To further understand the basic relationships between nanoscale structural variables and the macroscale properties of polymer nanocomposites. Although it is believed

that the substantial improvements in bulk material properties stem from the dramatically increased polymer chain-nanoparticle interface area in the case of nanocomposites, we are still far from fully understanding molecular mechanisms responsible for the observed bulk behaviors.